UNITED NATIONS UNIVERSITY
UNU-GTP
Geothermal Training Programme

Orkustofnun, Grensasvegur 9,
IS-108 Reykjavik, Iceland

Reports 2019
Number 1

THE BORINQUEN GEOTHERMAL AREA, COSTA RICA: 1D AND 3D INVERSION OF RESISTIVITY DATA GEOLOGICAL/GEOTHERMAL INTERPRETATION

MSc thesis
School of Engineering and Natural Sciences
Faculty of Earth Sciences
University of Iceland

by

Diego Badilla Elizondo
Costa Rican Electric Company (ICE)
Department of Geophysics
P.O. Box 10032, San José
COSTA RICA
dbadillae@ice.go.cr

United Nations University
Geothermal Training Programme
Reykjavík, Iceland
Published in September 2019

ISBN 978-9979-68-320-9

ISSN 1670-7427

This MSc thesis has also been published in September 2019 by the
School of Engineering and Natural Sciences, Faculty of Earth Sciences
University of Iceland

INTRODUCTION

The Geothermal Training Programme of the United Nations University (UNU) has operated in Iceland since 1979 with six month annual courses for professionals from developing countries. The aim is to assist developing countries with significant geothermal potential to build up groups of specialists that cover most aspects of geothermal exploration and development. During 1979-2012, 515 scientists and engineers from 53 developing countries have completed the six month courses. They have come from Asia (40%), Africa (32%), Central America (16%), Central and Eastern Europe (12%), and Oceania (0.4%) There is a steady flow of requests from all over the world for the six month training and we can only meet a portion of the requests. Most of the trainees are awarded UNU Fellowships financed by the UNU and the Government of Iceland.

Candidates for the six month specialized training must have at least a BSc degree and a minimum of one year practical experience in geothermal work in their home countries prior to the training. Many of our trainees have already completed their MSc or PhD degrees when they come to Iceland, but several excellent students who have only BSc degrees have made requests to come again to Iceland for a higher academic degree. In 1999, it was decided to start admitting UNU Fellows to continue their studies and study for MSc degrees in geothermal science or engineering in co-operation with the University of Iceland. An agreement to this effect was signed with the University of Iceland. The six month studies at the UNU Geothermal Training Programme form a part of the graduate programme.

It is a special pleasure to introduce the 29th UNU Fellow to complete the MSc studies at the University of Iceland under the co-operation agreement. Andemariam Teklesenbet, BSc in Geology, of the Geological Survey of Eritrea, completed the six month specialized training in Geophysical Exploration at the UNU Geothermal Training Programme in October 2007. His research report was entitled: „Transient electromagnetic and magnetotelluric geophysical methods in the Hengill area, SW-Iceland". After two years of geothermal research work in Eritrea, he came back to Iceland for MSc studies at the Faculty of Earth Sciences of the University of Iceland in August 2009. In January 2012, he defended his MSc thesis presented here, entitled "Multidimensional inversion of MT data from Alid geothermal area, Eritrea; comparison with geological structures and identification of a geothermal reservoir". His studies in Iceland were financed by the Government of Iceland through a UNU-GTP Fellowship from the UNU Geothermal Training Programme. We congratulate him on his achievements and wish him all the best for the future. We thank the Faculty of Earth Sciences at the School of Engineering and Natural Sciences of the University of Iceland for the co-operation, and his supervisors for the dedication. It must be mentioned here that this MSc thesis is an evidence of unsual courage and determination. Two months after starting his MSc studies, Andemariam was diagnosed with a life-threatening cancer and had to undergo an extremely difficult operation. He has since been undergoing a treatment unique in the world. Despite this, Andemariam managed to complete his MSc studies in only 2½ year, which is a major achievement.

Finally, I would like to mention that Andemariam's MSc thesis with the figures in colour is available for downloading on our website *www.unugtp.is* under publications.

With warmest wishes from Iceland,

Ingvar B. Fridleifsson, director
United Nations University
Geothermal Training Programme

ACKNOWLEDGEMENTS

I sincerely thank the United Nations University Geothermal Training Programme (UNU-GTP) for granting the scholarship of this study at the University of Iceland. I would like to thank the Costa Rican Electricity Company (ICE) for the study leave, allowing use of the data; the University of Iceland and Iceland GeoSurvey (ÍSOR) for providing access to facilities and training required for successful completion of this study.

I wish to express my gratefulness to my advisors Gylfi Páll Hersir, Ásdís Benediktsdóttir and Halldór Geirsson for the knowledge, guidance and support towards the successful completion of this degree. My sincere gratitude to Mr. Lúdvík S. Georgsson, Director of UNU-GTP, and Mr. Ingimar G. Haraldsson, Deputy Director of UNU-GTP, Mrs. Málfríður Ómarsdóttir, Environmental Scientist, Ms. Thórhildur Ísberg and Mr. Markús Wilde for personal and technical support throughout my studies.

Many thanks to the fellows at UNU-GTP and friends at the University of Iceland for the valuable time and friendship.

Many thanks to the field crew at the Department of Geophysics at ICE, for the big effort and the excellent job done in collecting all the field data.

There are no words to express the gratitude to my wife Adriana and my two kids, Luciana and Mateo, and to our families for their sacrifice, support and encouragement.

DEDICATION

This thesis is dedicated to my family, especially to my wife and two kids
that have been my support during this time

ABSTRACT

This work consists of modelling and interpretation of resistivity data from the Borinquen Geothermal Area in Costa Rica through 1D joint inversion of Time Domain Electromagnetic (TDEM) and magnetotelluric (MT) data and 3D inversion of static shift corrected MT data. A comparison of the results with gravity, geochemistry, geological investigation and well log data is done.

A total of 97 co-located MT/TDEM sounding pairs were used to carry out the 1D resistivity inversion. Resistivity cross sections and depth slices were created based on the 1D and 3D inversion results to compare both approaches. The subsurface resistivity structure shows a clear image of the main elements associated with the different stages of alteration mineralogy present in a typical high temperature geothermal system in a volcanic environment. On top, a high resistivity zone is seen, reflecting unaltered rocks. Then, a shallow lying conductive layer is found reflecting smectite alteration mineralogy. Below the low resistivity cap, a high resistivity core is found, reflecting chlorite-epidote alteration. Good correlation is observed between the subsurface resistivity structure and the alteration mineralogy revealed in borehole cuttings.

A new constraint to the Cañas Dulces Caldera is suggested here by slightly modifying some of the previously proposed boundaries and by suggesting the missing boundaries to the north. Based on this work, the north and northeast boundary of the Cañas Dulces Caldera is proposed. It is suggested here that the Borinquen and Las Pailas Geothermal Areas are mostly controlled by the north and northeast boundaries of the inferred Cañas Dulces and San Vicente Caldera structures and other secondary tectonic structures or fractures.

The results are important for a better understanding of the geothermal system and the geological setting which is most essential for ICE (Instituto Costarricense de Electricidad, Costa Rican Electricity Company) in developing future geothermal projects in the country.

TABLE OF CONTENTS

LIST OF FIGURES

LIST OF TABLES

ABBREVIATIONS

1D	One dimensional
2D	Two dimensional
3D	Three dimensional
AMT	Audiomagnetotelluric
A/MT	Audiomagnetotelluric/Magnetotelluric
BGF	Borinquen Geothermal Field
PGF	Pailas Geothermal Field
CR	Costa Rica
CAVA	Central American Volcanic Arc
CDC	Cañas Dulces Caldera
EDI	Electrical Data Interchange
EM	Electromagnetic
ICE	Instituto Costarricense de Electricidad
ISOR	Iceland GeoSurvey
Kya	Thousand years ago
HI	Háskóli Íslands (University of Iceland)
m a.s.l.	Metres above sea level
m b.s.l.	Metres below sea level
MAT	Middle America Trench
Ma	Million years ago
MT	Magnetotelluric(s)
TEM	Transient Electromagnetic
TDEM	Time Domain Electromagnetic
TE	Transverse Electric
TM	Transverse Magnetic
USF	Universal Sounding Format
WSINV3DMT	3D inversion program written by Dr. Weerachai Siripunvaraporn

MEANING OF SYMBOLS

$\boldsymbol{E}$ $[\mathrm{Vm}^{-1}]$	Electric field intensity
$\boldsymbol{B}$ [T]	Magnetic induction
$\boldsymbol{H}$ $[\mathrm{Am}^{-1}]$	Magnetic field intensity
$\boldsymbol{D}$ $[\mathrm{Cm}^{2}]$	Electric displacement
η $[\mathrm{Cm}^{-3}]$	Electric charge density of free charges
$\boldsymbol{J}$ $[\mathrm{Am}^{2}]$	Electric current density
σ $[\mathrm{Sm}^{-1}]$	Electric conductivity
μ $[\mathrm{H/m}]$	Magnetic permeability
ε $[\mathrm{F/m}]$	Electric permittivity
δ [m]	Electromagnetic skin depth
T [s]	Period
f [Hz]	Frequency
t $[s]$	Time
ω $[rad/s]$	Angular frequency
ρ [Ωm]	Resistivity
$\boldsymbol{Z}$ [Ω]	Impedance tensor (2x2 matrix)
ρ_a [Ωm]	Apparent resistivity
$i = \sqrt{-1}$	Imaginary number
κ $[\mathrm{m}^{-1}]$	Propagation constant (wave number)

$\mathcal{T}$	Tipper
$\Re$	Real part of the Tipper
$\Im$	Imaginary part of the Tipper
M_q	Length of the real part of the Induction arrow
M_q	Length of the imaginary part of the Induction arrow

1 INTRODUCTION

Exploration and rational use of natural resources for energy generation is of high importance in Costa Rica (CR), a country aiming to be carbon neutral by 2021. Geothermal energy plays an important role as it has a small environmental impact and its productivity is stable throughout the year. According to the energy expansion plan for the next decade in CR (ICE, 2018a), geothermal power plants are going to be important energy contributors for the country.

Preliminary exploration studies of the geothermal potential in CR were performed in the 70s in Guanacaste Volcanic Range located in the northwestern part of the country, resulting in recommendations to investigate the areas on the slopes of Rincon de la Vieja, Miravalles and Tenorio volcanoes (Moya and Yock, 2007; Figure 20). Currently, two geothermal power plants located in Miravalles and Las Pailas geothermal areas are generating electricity of a total of ~253 MWe. Borinquen I will add 55 MWe more by 2024 and Borinquen II 55 MWe by 2030 resulting in a total of ~363 MWe.

The geology of the Rincón de la Vieja Volcano complex has been investigated and discussed (Kempter, 1997; Zamora et al., 2004; Deering et al., 2007; Denyer et al., 2009; Molina et al., 2014). Local geological structures and regional lineaments have been proposed as well as generalized conceptual models of Borinquen and Las Pailas Geothermal areas. Due to the interest of the ICE in the exploration and exploitation of geothermal resources, studies in geochemistry, geophysics, drilling and more detailed analysis were performed.

The present work has quite positive impacts for the country and for the Costa Rican Electricity Company. It is based on the newest electromagnetic (EM) data package from the Borinquen Geothermal area including static shift correction of all MT sounding data which guarantees a realistic up to date resistivity model of the Borinquen Geothermal area. It is also important that the whole process from the planning of the campaign up to 3D inversion and interpretation is performed by the department of geophysics, supported by senior geophysicists from Iceland GeoSurvey. It ensures the success at this stage allowing us to perform other 3D resistivity modelling for future projects thanks to this great contribution from UNU-GTP, University of Iceland and Iceland GeoSurvey.

The overall objective of the work is to contribute to a better understanding of the geological setting of the Rincón de la Vieja Volcano Complex as well as the two geothermal areas located south and southwest of the edifice. This is key information for ICE in order to improve knowledge and expertise for future developments. It generates more possibilities for the country to produce energy from renewables.

Specifically, the objectives of this work are three folded: to better comprehend the EM methods used in geothermal exploration, to understand the procedure related to 3D electrical resistivity inversion, and consequently, we can execute it for any other geothermal area in the country and, to generate 1D and 3D resistivity inversion models for Borinquen Geothermal area to update the conceptual model and contribute to the current exploration/drilling stage.

2 ELECTROMAGNETIC (EM) METHODS

2.1 Electromagnetic theory

2.1.1 Maxwell's equations

The electromagnetic methods for subsurface resistivity measurements rely on electromagnetic theory, of which Maxwell's equations form the central part. The four Maxwell equations taken in aggregate are a complete description of the relationships between electric and magnetic fields in any medium (Chave and Jones, 2012).

Faraday's law: It states that time variations of the magnetic field induce corresponding fluctuations in the electric field flowing in a closed loop with its axis oriented in the direction of the induced field (Figure 1):

$$\nabla \times \boldsymbol{E} = -\frac{\partial \boldsymbol{B}}{\partial t} \tag{2.1a}$$

Ampère's law: The magnetic field induced around a closed loop is proportional to the electric current density plus the derivative of the electric displacement current with respect to time (rate of change of electric field or displacement current density) that the loop encloses (Figure 1):

$$\nabla \times \boldsymbol{H} = \boldsymbol{j} + \frac{\partial \boldsymbol{D}}{\partial t} \tag{2.1b}$$

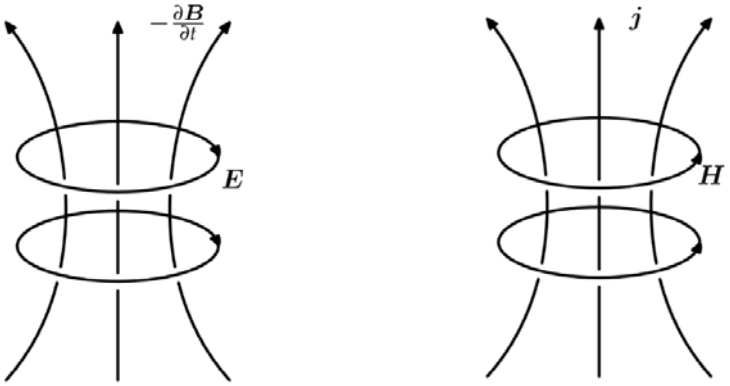

FIGURE 1: Representation of Faraday's and Ampere's law (from Simpson and Bahr, 2005)

Gauss's law for magnetism: There are no magnetic monopoles; the total magnetic flux through a closed surface is zero.

$$\nabla \cdot \boldsymbol{B} = 0 \tag{2.1c}$$

Gauss's law: The electric flux leaving a volume is proportional to the electric charge density inside.

$$\nabla \cdot \boldsymbol{D} = \eta \tag{2.1d}$$

where $\boldsymbol{E}$ - represents the electric field $[\mathrm{Vm}^{-1}]$, $\boldsymbol{B}$ - refers to the magnetic induction [T], $\boldsymbol{H}$ is the magnetic intensity $[\mathrm{Am}^{-1}]$, $\boldsymbol{j}$ - is the electric current density $[\mathrm{Am}^{-2}]$, $\boldsymbol{D}$ is the electric displacement current $[\mathrm{Cm}^{-2}]$, η represents the electric charge density owing to free charges $[\mathrm{Cm}^{-3}]$.

The operators $\nabla \times$ and $\nabla \cdot$ are vector calculus expressions, curl and divergence, respectively.

For a linear and isotropic medium, the relations between **E**, **D**, **B** and **H** are specified by the constitutive equations:

$$\boldsymbol{B} = \mu \boldsymbol{H} \tag{2.2a}$$

$$\boldsymbol{D} = \varepsilon \boldsymbol{E} \tag{2.2b}$$

$$\boldsymbol{j} = \sigma \boldsymbol{E} \tag{2.2c}$$

Where, μ is the magnetic permeability $[\mathrm{Hm}^{-1}]$;

ε is the dielectric permittivity $[\mathrm{Fm}^{-1}]$;

σ is the electrical conductivity of the sounding medium $[\mathrm{Sm}^{-1}]$;

$\mu = \mu_0 \mu_r$

$\varepsilon = \varepsilon_0 \varepsilon_r$

The relative dielectric permittivity (ε_r) for most materials within the Earth vary between 1 and approximately 100. In vacuum ($\varepsilon_r = 1$) the electric permittivity equals to $\varepsilon_0 = 8{,}85 \cdot 10^{-12}\ [F/m]$ and increases to $100\varepsilon_0$ for water (Keller, 1987). The magnetic permeability (μ) of most Earth materials can be approximated to its value in vacuum, $\mu_0 = 4\pi \cdot 10^{-7}\ [H/m]$, meaning that the relative magnetic permeability (μ_r) is close to 1, but can be greater for highly magnetized materials.

2.1.2 The EM field in a homogeneous conductive medium

Considering the case of a homogeneous and isotropic medium, assuming the harmonic dependence of the oscillating electromagnetic field, a harmonic temporal variation $e^{i\omega t}$, and substituting the relations from equations (2.2) into Maxwell's equations (equations (2.1)) we get:

$$\nabla \times \boldsymbol{E} = -i\omega\mu \boldsymbol{H} \tag{2.3a}$$

$$\nabla \times \boldsymbol{H} = (\sigma + i\omega\mu)\boldsymbol{E} \tag{2.3b}$$

$$\nabla \cdot \boldsymbol{H} = 0 \tag{2.3c}$$

$$\nabla \cdot \boldsymbol{E} = \frac{\eta}{\varepsilon} \cong 0 \tag{2.3d}$$

Where, $\omega = 2\pi f$ is the angular frequency;

$f = \frac{1}{T}$ is the frequency of oscillation;

T is the period of the oscillation;

$i = \sqrt{-1}$ is the imaginary unit of the complex number

Let's consider an EM wave of angular frequency ω and with an angle of incidence θ_i traveling through the air and approaching the surface of the homogeneous Earth of conductivity σ. When the wave hits the surface it is both reflected back and refracted into the half space at an angle of refraction θ_t. The relation between the angles of the incident and refracted waves is given by Snell's law:

$$\frac{1}{v_0} sin\theta_i = \frac{1}{v} sin\theta_t \tag{2.4}$$

Where, v_0 is the velocity of an EM wave traveling in the free air with speed of light (c)

$v = \frac{1}{\sqrt{\mu\varepsilon}}$ is the velocity of an EM wave traveling in a homogeneous Earth

From equation (2.4),

$$sin\theta_t = \frac{v}{v_0} sin\theta_i \tag{2.5}$$

Where, $sin\theta_i \leq 1$

$$\frac{v}{v_0} = \frac{1}{\sqrt{\varepsilon_r \mu_r}} << 1$$

By evaluating these values in equation (2.5) we see that the angle of the refracted wave in the homogeneous half space must be close to zero. This indicates that EM waves are predominantly vertically incident plane waves and therefore $\frac{\partial}{\partial x} = \frac{\partial}{\partial y} = 0$.

Applying the definition of curl together with the *Faraday's law* (equation (2.1a)), gives:

$$\frac{\partial E_z}{\partial y} - \frac{\partial E_y}{\partial z} = -\mu \frac{\partial H_x}{\partial t} \quad \Rightarrow \quad \frac{\partial E_y}{\partial z} = i\omega\mu H_x \tag{2.6a}$$

$$\frac{\partial E_x}{\partial z} - \frac{\partial E_z}{\partial x} = -\mu \frac{\partial H_y}{\partial t} \quad \Rightarrow \quad \frac{\partial E_x}{\partial z} = -i\omega\mu H_y \tag{2.6b}$$

$$\frac{\partial E_y}{\partial x} - \frac{\partial E_x}{\partial y} = -\mu \frac{\partial H_z}{\partial t} = 0 \tag{2.6c}$$

In a similar way, applying the definition of curl with *Ampère's law* (equation (2.1b)), it gives:

$$\frac{\partial H_z}{\partial y} - \frac{\partial H_y}{\partial z} = \sigma E_x + \varepsilon \frac{\partial E_x}{\partial t} \quad \Rightarrow \quad -\frac{\partial H_y}{\partial z} = (\sigma + i\omega\varepsilon) E_x \tag{2.7a}$$

$$\frac{\partial H_x}{\partial z} - \frac{\partial H_z}{\partial x} = \sigma E_y + \varepsilon \frac{\partial E_y}{\partial t} \quad \Rightarrow \quad \frac{\partial H_x}{\partial z} = (\sigma + i\omega\varepsilon) E_y \tag{2.7b}$$

$$\frac{\partial H_y}{\partial x} - \frac{\partial H_x}{\partial x} = \sigma E_z + \varepsilon \frac{\partial E_z}{\partial t} = 0 \tag{2.7c}$$

Relating the second derivative of the electric field with respect to z (derivative of equations (2.6a), (2.6b)) with the first derivative of the magnetic field (equations (2.7a) and (2.7b)) and after that, by relating the second derivative of the magnetic field with respect to z (derivative of equations (2.7a) and (2.7b)) with the first derivative of the electric field (equations (2.6a) and (2.6b)) we have:

$$\frac{\partial^2 E_x}{\partial z^2} = -i\omega\mu \frac{\partial H_y}{\partial z} = i\omega\mu(\sigma + i\omega\varepsilon) E_x \tag{2.8a}$$

$$\frac{\partial^2 E_y}{\partial z^2} = \quad i\omega\mu \frac{\partial H_x}{\partial z} = i\omega\mu(\sigma + i\omega\varepsilon) E_y \tag{2.8b}$$

$$\frac{\partial^2 H_x}{\partial z^2} = (\sigma + i\omega\varepsilon) \frac{\partial E_y}{\partial z} = i\omega\mu(\sigma + i\omega\varepsilon) H_x \tag{2.9a}$$

$$\frac{\partial^2 H_y}{\partial z^2} = -(\sigma + i\omega\varepsilon) \frac{\partial E_x}{\partial z} = i\omega\mu(\sigma + i\omega\varepsilon) H_y \tag{2.9b}$$

The four equations above can be expressed as:

$$\frac{\partial^2 E_{x,y}}{\partial z^2} = \kappa^2 E_{x,y} \tag{2.10}$$

$$\frac{\partial^2 H_{x,y}}{\partial z^2} = \kappa^2 H_{x,y} \tag{2.11}$$

Where

$$\kappa^2 = i\omega\mu(\sigma + i\omega\varepsilon) \tag{2.12}$$

At the frequencies used and for the targets of interest in magnetotellurics, the magnetic permeability may be taken as the free-space value μ_0 in nearly all Earth materials (Chave and Jones, 2012). The typical ranges of the variables for MT studies are:

$$\sigma \approx 10^{-4} - 1\ [S/m]$$

$$f \approx 10^{-4} - 10^{4}\ Hz$$

$$\varepsilon_r \approx 1 - 100$$

By evaluating the term $(\omega\varepsilon)$ in equation (2.12) for the extreme values we get:

$$(\omega\varepsilon_r\varepsilon_0)_{max} = 2\pi f_{max} 100\varepsilon_0$$

$$(\omega\varepsilon)_{max} = 2\pi 10^4 \cdot 100 \cdot 8{,}85 \cdot 10^{-12} \approx 5 \cdot 10^{-5}$$

Therefore, $\sigma \gg \omega\varepsilon$ and equation (2.12) representing the wave number or complex propagation constant κ is reduced to:

$$\kappa^2 \approx i\omega\mu\sigma \tag{2.13}$$

Equations (2.10) and (2.11) are second order differential equations which describe the electric and magnetic field for a homogeneous and conductive medium. Their solution can be written in a general form as:

$$E_{x,y}(z,t) = \left(A_{x,y}e^{\kappa z} + B_{x,y}e^{-\kappa z}\right)e^{i\omega t} \tag{2.14}$$

$$H_x(z,t) = \frac{\kappa}{i\omega\mu}\left(A_y e^{\kappa z} - B_y e^{-\kappa z}\right)e^{i\omega t} \tag{2.15}$$

$$H_y(z,t) = \frac{-\kappa}{i\omega\mu}(A_x e^{\kappa z} - B_x e^{-\kappa z})e^{i\omega t} \tag{2.16}$$

where $A_{x,y}$ and $B_{x,y}$ are constants to be determined. Because the Earth does not generate electromagnetic energy, but only dissipates or absorbs it (Simpson and Bahr, 2005), we can evaluate the constants $A_{x,y}$ by considering that at $z \to \infty, \boldsymbol{H}\ \&\ \boldsymbol{E} \to 0$, therefore we must have $A_{x,y} = 0$ and we can rewrite equations (2.14) to (2.16) as:

$$E_x(z,t) = B_x e^{-\kappa z} e^{i\omega t} \tag{2.17}$$

$$E_y(z,t) = B_y e^{-\kappa z} e^{i\omega t} \tag{2.18}$$

$$H_x(z,t) = \frac{-\kappa}{i\omega\mu} B_y e^{-\kappa z} e^{i\omega t} = \frac{-\kappa}{i\omega\mu} E_y(z,t) \tag{2.19}$$

$$H_y(z,t) = \frac{\kappa}{i\omega\mu} B_x e^{-\kappa z} e^{i\omega t} = \frac{\kappa}{i\omega\mu} E_x(z,t) \tag{2.20}$$

The propagation of electromagnetic waves through a medium with homogeneous physical properties is proportional to $e^{-\kappa z}$ under the assumption of $e^{i\omega t}$ time dependence (see equations (2.17) to (2.20)) meaning that electromagnetic fields are governed by a diffusion equation (Chave and Jones, 2012). The characteristic length scale for electromagnetic induction is the distance over which the electromagnetic field decays to 1/e ≈ 0.37 of its initial amplitude at the surface or:

$$e^{-1} = e^{-\kappa z} \Rightarrow 1 = \kappa z$$

$$z = \delta = \frac{1}{\kappa} \tag{2.21}$$

Equation (2.21) represents the *skin depth* (δ) in terms of the wave number (κ). It's a function of frequency and conductivity of the medium according to equation (2.13) where lower frequencies can sense deeper due to there is less energy transferred to the medium. By using the real part of equation (2.13) and inserting it into equation (2.21) we can calculate the skin depth as:

$$\delta = \sqrt{\frac{2}{\omega\mu_0\sigma}} = 503\sqrt{\frac{1}{f\sigma}} \ [m] \tag{2.22}$$

For homogeneous earth, when electromagnetic plane waves propagate vertically downward, the ratio between the components of electric and magnetic fields is a characteristic measurement of the electromagnetic properties of the medium, known as impedance **Z** (Keller and Frischknecht, 1966). The unit for impedance is given in Ohm [Ω].

Z is a complex tensor and can be written in matrix form as:

$$\begin{bmatrix} E_x \\ E_y \end{bmatrix} = \begin{bmatrix} Z_{xx} & Z_{xy} \\ Z_{yx} & Z_{yy} \end{bmatrix} \begin{bmatrix} H_x \\ H_y \end{bmatrix} \tag{2.23}$$

or in the general expression,

$$\boldsymbol{E} = \boldsymbol{Z}\boldsymbol{H} \tag{2.24}$$

The linear relations of the fields can be written as:

$$E_x = Z_{xx}H_x + Z_{xy}H_y \tag{2.25}$$

$$E_y = Z_{yx}H_x + Z_{yy}H_y \tag{2.26}$$

The reader is referred to section 2.2.3 for the different cases of the MT impedance tensor.

2.2 The magnetotelluric (MT) method

2.2.1 Overview

The magnetotelluric method is an exploration technique that utilises a broad spectrum of naturally occurring geomagnetic variations as a power source for electromagnetic induction in the Earth. The advantage of using natural field is to have power available throughout the frequency range of interest ($\sim 10^{-4}$ to $10^{4}\ Hz$). This situation is particularly important for the low frequencies (< 0,01 Hz), where a large power source and equipment set up would be needed to generate signals (Vozoff, 1991). Within that frequency range two sources are important:

- Meteorological activity occurring at the atmosphere, such as world-wide thunderstorm discharges usually near equator produces EM fields with periods shorter than 1 s (Simpson and Bahr, 2005).

- For higher periods (low frequencies), generally higher than 1s, the signal is due to interactions between solar wind and the Earth's magnetosphere and ionosphere (Simpson and Bahr, 2005). The most visible forms of this interaction are the northern lights.

By Faraday's Law of induction, the time varying magnetic field induces an electric current within the Earth, and by Ohm's Law this current generates an electric ("telluric") field. The strength of the electric field is dependent on the conductivity of the medium and the strength of the inducing source magnetic field. Hence, by determining the magnetic and electric field ratios at varying frequencies together with appropriate data inversion procedures one can estimate the resistivity distribution of the subsurface, on depth scales ranging from a few tens of meters to hundreds of kilometres (Tikhonov, 1950; Cagniard, 1953).

For the purposes of considering electromagnetic induction in the Earth, a number of simplifying assumptions (stated by Cagniard, 1953; Keller and Frischknecht, 1966) are considered applicable (Simpson and Bahr, 2005):

i. Maxwell's general electromagnetic equations are obeyed.

ii. The Earth does not generate electromagnetic energy, but only dissipates or absorbs it.

iii. All fields may be treated as conservative and analytic away from their sources.

iv. The natural electromagnetic source fields utilised, being generated by large-scale ionospheric current systems that are relatively far away from the Earth's surface, may be treated as uniform, plane-polarised electromagnetic waves impinging on the Earth at near-vertical incidence. This assumption may be violated in polar and equatorial regions.

v. No accumulation of free charges is expected to be sustained within a horizontal layered Earth. In a two dimensional or three dimensional Earth, charges can accumulate along discontinuities. This generates a non-inductive phenomenon known as *static shift*.

vi. Charge is conserved, and the Earth behaves as an Ohmic conductor, obeying the equation:

$$\boldsymbol{j} = \sigma \boldsymbol{E} \tag{2.27}$$

vii. The electric displacement field is quasi-static for MT sounding periods. Therefore, time-varying displacement currents (arising from polarisation effects) are negligible compared with time-varying conduction currents, which promotes the treatment of electromagnetic induction in the Earth purely as a diffusion process.

viii. Any variations in the electrical permittivity and magnetic permeability of rocks are assumed negligible compared with variations in bulk rock conductivities.

MT generally refers to recording time series of electric and magnetic fields of periods from 0,0025 s (400 Hz) to 1000 s (0,001 Hz) or as high as 10000 s (0,0001 Hz). Audio magnetotellurics (AMT) refers to 'audio' frequencies, generally recording frequencies of 100 Hz to 10 kHz (Flóvenz et al., 2012).

There are two frequency bands that are problematic for A/MT data acquisition. The most well-known one is the so-called *MT dead band*, and it is located at frequencies between 0,5 Hz - 5 Hz (Simpson and Bahr, 2005). Not only is there low power at these frequencies – which are the cross-over frequencies between lightning-induced energy and ionospheric-induced energy – but also a natural maximum in the near surface microseismic noise due to coupling of the wind and ocean to the ground. This range is located in Band 3 on Figure 2 where a decay in the power spectra density curve is seen. This low power and high noise can be compensated at great extend with an overnight data acquisition and by improving the contact resistance between the electrodes and the ground, for instance. The other problems occur at frequencies around 1 kHz – 5 kHz (Christopherson et al., 2002) and it is the so- called *AMT dead band*. The energy from distant lightning storms comes from cloud to stratosphere at about 10 Hz to 1 kHz frequencies, and cloud to ground at 5 kHz to 100 kHz and higher frequencies. There is a natural minimum in energy at 1 kHz – 5 kHz due to this. This range is located around Band 1 (Figure 2) with a decay in the power spectra density curve.

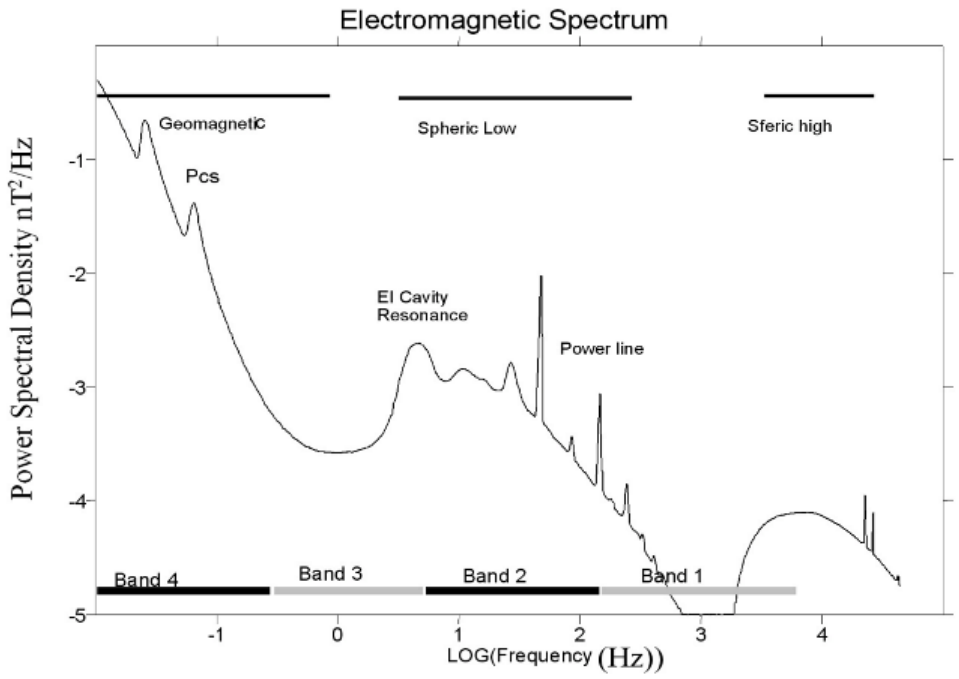

FIGURE 2: The EM power spectra (Manoj, 2003)

On the Earth's surface the time variations of the three components of the magnetic field (H_x, H_y *and* H_z), and the two horizontal components of the Earth's electric field (E_x *and* E_y) are measured simultaneously and orthogonally. All these signals are recorded by a receiver for a period of time that can vary according to the desired depth of investigation. The typical configuration for a MT sounding survey is shown in Figure 3 where the electric dipole length is ~100 m, the separation of the magnetic coils should be at least 10 m from the transmitter and 5 m away from the electric dipoles wires. The reader is referred to section 5.1 for details in the MT field set up.

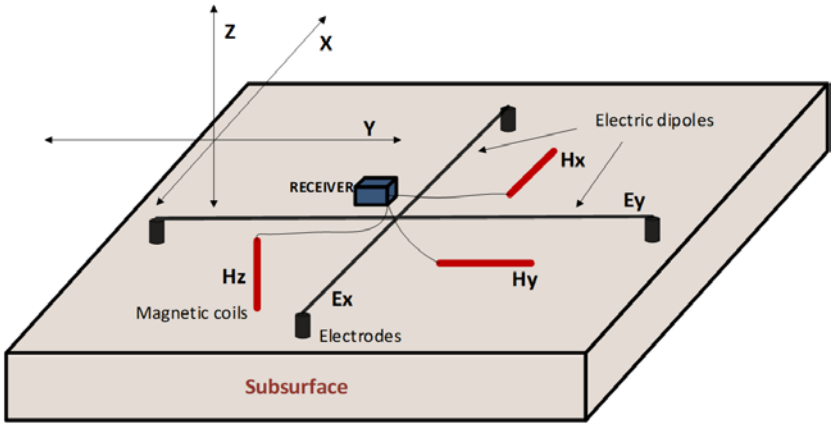

FIGURE 3: Typical MT field configuration (modified from Phoenix Geophysics, 2015)

Obtaining MT data for great depths requires to measure for long periods at each station in order to get enough samples at those frequencies. For instance, to sample a frequency of 0,001 Hz or 1 cycle per 1000 s, it is necessary to record for at least 16,67 min to get one data sample! That means we really need to record for several hours to get enough samples that can represent significant statistical average of the data.

An example of the variation for the five components measured with the MT method over a twenty-hours period is shown in Figure 4 from a site in the northern Costa Rica, next to Borinquen Geothermal Area, on the 25th October 2016 (UCT).

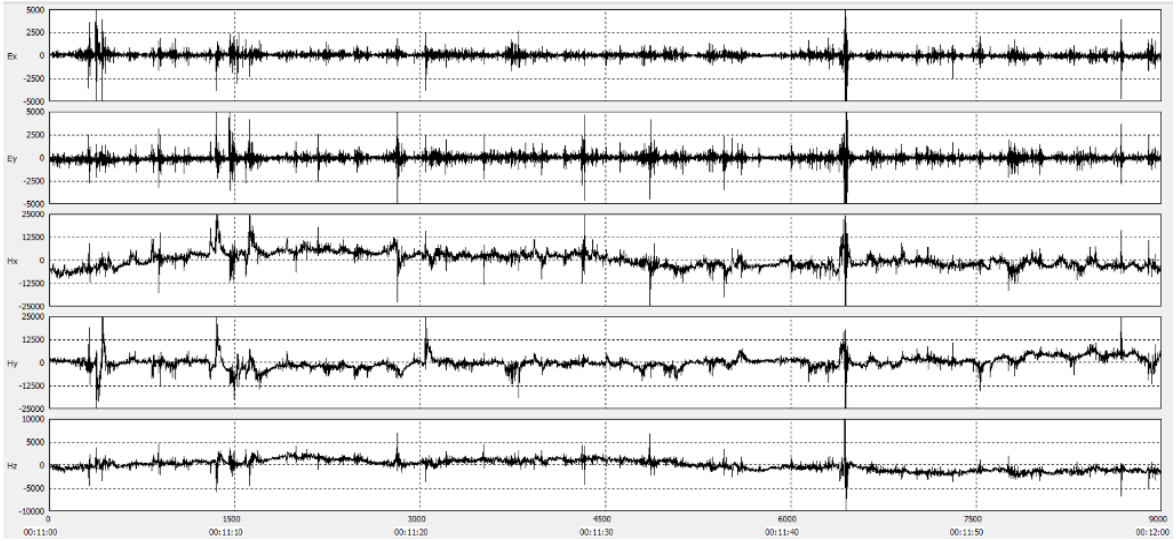

FIGURE 4: Typical magnetotelluric time series. The time variations are shown for one minute of recordings of channels Ex, Ey, Hx, Hy and Hz at site RPN323, southern flank of Rincon de la Vieja Volcano, CR

2.2.2 Resistivity (ρ)

The electrical resistivity (ρ) is defined by Ohm's law (equation (2.27)). It is measured in [Ωm] and is the reciprocal value of conductivity (σ). Resistivity is defined for a piece of a specific material as the ratio of the potential difference, ΔV [V], to the current I [A], across a material which has a cross sectional area A [m^2] and length L [m] (Figure 5):

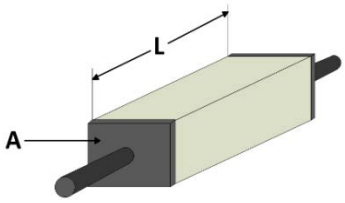

FIGURE 5: Material with specific resistivity ρ

$$\rho = \frac{\Delta V}{L}\frac{A}{I} = R\frac{A}{L} \tag{2.28}$$

2.2.3 The MT impedance tensor (Z)

The impedance tensor (**Z**) relates the components of the Earth's electric and magnetic fields as shown in equation (2.24) and it is a function of the Earth's resistivity (ρ), therefore, we can calculate the apparent resistivity from the impedance tensor. It is called apparent resistivity since we don't measure rock resistivity directly at certain depth, but indirectly on the surface. The apparent resistivity and phase from MT sounding data are inverted in order to obtain a resistivity model of the subsurface by using 1D, 2D or 3D resistivity inversion models.

In the specific case of 1D earth, the conductivity varies only with depth and the diagonal elements of the impedance tensor presented in equation (2.23) Z_{xx} and Z_{yy} are zero. Those diagonal elements couple parallel electric and magnetic field components. Whilst the off-diagonal components (which couple orthogonal electric and magnetic field components) are equal in magnitude, but have opposite signs (Simpson and Bahr, 2005). The impedance tensor $\boldsymbol{Z}$ can be written as:

$$\boldsymbol{Z} = \begin{bmatrix} 0 & Z_{xy} \\ Z_{yx} & 0 \end{bmatrix} \tag{2.29}$$

where $Z_{xy} = -Z_{yx} \neq 0$.

For a homogeneous earth as discussed in section 2.1.2, by using the results from equations (2.17) to (2.20) the orthogonal impedance tensor components can be related and expressed as:

$$Z_{xy} = \frac{E_x}{H_y} = \frac{i\omega\mu}{k} = \sqrt{\frac{\omega\mu}{\sigma}}\, e^{i\pi/4} \tag{2.30a}$$

$$Z_{yx} = \frac{E_y}{H_x} = \frac{-i\omega\mu}{k} = -Z_{xy} \tag{2.31b}$$

Equations (2.30a) and (2.31b) have a constant phase of $\theta = \pi/4$; the magnetic field is 45° behind the electric field.

We can calculate the resistivity of the half-space by:

$$\rho = \frac{1}{\omega\mu}\left|Z_{xy}\right|^2 = \frac{1}{\omega\mu}\left|Z_{yx}\right|^2 \quad [\Omega m] \tag{2.32}$$

For a two dimensional (2D) Earth the conductivity is constant along one principal horizontal direction while changing both along the vertical and one of the two principal horizontal directions.

In this case the diagonal elements of $\boldsymbol{Z}$ vanish and the off diagonal elements become unequal. The direction along which the conductivity is constant is called the geoelectric strike (Zstrike).

$$\boldsymbol{Z} = \begin{bmatrix} 0 & Z_{xy} \\ Z_{yx} & 0 \end{bmatrix} \tag{2.33}$$

However, if the MT measurement axes are not in alignment with the geological strike, the diagonal elements will not become equal to zero. Usually, the MT field layout is not set up in the strike direction. However, the tensor can be rotated to an angle θ according to the polarization direction that the diagonal elements become ~0 under this rotation angle.

The rotation of $\boldsymbol{Z}$ implicates the decomposition of the electric and magnetic field components into E-polarization (Transverse electric mode, TE) and B-polarization (Tranverse Magnetic mode, TM) as explained by Berdichevsky and Dmitriev (2008). In the TE mode the electric field is aligned parallel to the electric strike and in the TM mode the magnetic field is aligned with the strike. If x-axis is in the strike direction, i.e. E_x is parallel to the strike and E_y is perpendicular, the off-diagonal components of equation (2.33) become:

$$Z_{xy} = \frac{E_x}{H_y} = Z_{TE} \tag{2.34}$$

$$Z_{yx} = \frac{E_y}{H_x} = Z_{TM} \tag{2.35}$$

The apparent resistivity for each mode is then:

$$\rho_{xy} = \frac{1}{\omega\mu}\left|Z_{xy}\right|^2 \tag{2.36}$$

$$\rho_{yx} = \frac{1}{\omega\mu}\left|Z_{yx}\right|^2 \tag{2.37}$$

and the phase is given by

$$\theta_{xy} = \arg\left(Z_{xy}\right), \qquad \theta_{yx} = \arg\left(Z_{yx}\right) \tag{2.38}$$

In the 3D case, conductivity varies in all three directions, x, y and z. We have, $Z_{xy} \neq Z_{yx}\ and\ Z_{xx} \neq Z_{yy}$. The impedance tensor takes the general form:

$$\boldsymbol{Z} = \begin{bmatrix} Z_{xx} & Z_{xy} \\ Z_{yx} & Z_{yy} \end{bmatrix} \tag{2.39}$$

There is no rotational direction through which the two diagonal components of the impedance tensor become zero simultaneously, so all the elements in the tensor need to be considered in the analysis.

2.2.4 Rotation of the impedance tensor

The impedance tensor can be rotated to an angle θ with the rotation matrix R and its transpose, R^T to align it with the geological strike. The rotation operator is:

$$R(\theta) = \begin{bmatrix} cos\,\theta & sin\,\theta \\ -sin\,\theta & cos\,\theta \end{bmatrix} \tag{2.40}$$

with θ positive clockwise from the x-axis.

The Cartesian rotation matrix operates on the impedance tensor to yield rotated versions of each element. In matrix rotation, this is given by:

$$\boldsymbol{Z}(\theta) = R(\theta)\boldsymbol{Z}R(\theta)^T \tag{2.41}$$

where $\boldsymbol{Z}(\theta)$ represents the rotated impedance.

The elements of the impedance tensor (**$\boldsymbol{Z}$**) can be written in terms of elements of the original impedance tensor as:

$$Z_{xx} = Z_{xx}\cos^2(\theta) + \left(Z_{xy} + Z_{yx}\right)\sin(\theta)\cos(\theta) + Z_{yy}\sin^2(\theta) \tag{2.42}$$

$$Z_{xy} = Z_{xy}\cos^2(\theta) + \left(Z_{yy} - Z_{xx}\right)\sin(\theta)\cos(\theta) - Z_{yx}\sin^2(\theta) \tag{2.43}$$

$$Z_{yx} = Z_{yx}\cos^2(\theta) + \left(Z_{yy} + Z_{xx}\right)\sin(\theta)\cos(\theta) - Z_{xy}\sin^2(\theta) \tag{2.44}$$

$$Z_{yy} = Z_{yy}\cos^2(\theta) - \left(Z_{xy} + Z_{yx}\right)\sin(\theta)\cos(\theta) + Z_{xx}\sin^2(\theta) \tag{2.45}$$

From the above rotated forms of the impedance tensor, we can determine several combinations of the impedance tensors that are *rotationally invariant*, it means they present the same value independent of the angle of rotation.

Consider the sum of the diagonal elements, $Z_{xx} + Z_{yy}$. From the above equations:

$$\begin{aligned} Z_{xx}(\theta) + Z_{yy}(\theta) & \\ &= Z_{xx}\cos^2(\theta) + \left(Z_{xy} + Z_{yx}\right)\sin(\theta)\cos(\theta) + Z_{yy}\sin^2(\theta) \\ &+ Z_{yy}\cos^2(\theta) - \left(Z_{xy} + Z_{yx}\right)\sin(\theta)\cos(\theta) + Z_{xx}\sin^2(\theta) \end{aligned} \tag{2.46}$$

$$= Z_{xx}(\cos^2(\theta) + \sin^2(\theta)) + Z_{yy}(\cos^2(\theta) + \sin^2(\theta))$$

$$= Z_{xx} + Z_{yy}$$

Similarly, it is possible to show that the difference of the off-diagonal elements, $Z_{xy} - Z_{yx}$, is also rotationally invariant.

In the 1D interpretation of MT soundings, combinations of the impedance tensor elements are often used (Ranganayaki, 1984). Park and Livelybrooks (1989) mention three rotationally invariant combinations:

$$Z_{ave} = \frac{Z_{xy} - Z_{yx}}{2} \tag{2.47}$$

$$Z_{gma} = \sqrt{-Z_{xy}Z_{yx}} \tag{2.48}$$

$$Z_{det} = \sqrt{Z_{xx}Z_{yy} - Z_{xy}Z_{yx}} \tag{2.49}$$

where Z_{ave}, Z_{gma} and Z_{det} are the arithmetic average, the geometric average of the off-diagonal elements and the determinant of the impedance tensor, respectively.

The method used is this work for 1D joint inversion is the determinant of the impedance tensor. Resistivity and phase are calculated as:

$$\rho_{det} = \frac{1}{\omega\mu}|Z_{det}|^2; \;\; \theta_{det} = \arg(Z_{det}) \tag{2.50}$$

2.2.5 MT geoelectric strike analysis

The impedance tensor $\boldsymbol{Z}$ apart from containing information about the resistivity structure of the subsurface also provides indications about dimensionality and geoelectrical directions. The impedance geoelectric strike analysis of MT data allows determining the strike of dominant 2D geoelectrical structure. This can be difficult in the presence of both noise and local distortion. Normally, the strike angle is the least stable parameter, which can be resolved from MT data (Groom et al., 1993).

The impedance tensor for a 2D Earth is given by:

$$\boldsymbol{Z} = \begin{bmatrix} 0 & Z_{TE} \\ Z_{TM} & 0 \end{bmatrix} \tag{2.51}$$

The impedance elements Z_{TE} and Z_{TM} relate the fields parallel and perpendicular to the geoelectrical strike (Zstrike), respectively. The strike angle, θ_S is obtained from the measured impedances by maximizing suitable function of off-diagonal impedance, Z_{xy} and Z_{yx} under rotation of the axis.

$$\tan(4\theta_S) = \frac{(Z_{xx} - Z_{yy})(Z_{xy} + Z_{yx})^* + (Z_{xx} + Z_{yy})^*(Z_{xy} - Z_{yx})}{|Z_{xx} - Z_{yy}|^2 - |Z_{xy} + Z_{yx}|^2} \tag{2.52}$$

where * denotes the complex conjugate.

Equation (2.52) gives four angles which maximize the off-diagonal components and forms two principal directions perpendicular to each other.

The computed Zstrike direction has a 90° ambiguity, since rotation by 90° only switches the location of the two principal impedance tensor elements within the tensor. The inherent 90° ambiguity can be resolved by use of Tipper strike (refers to section 2.2.6), which uniquely defines the regional geoelectrical strike under the assumption of 2D regional structure (Zhang et al., 1987).

2.2.6 Geomagnetic transfer function

The geomagnetic transfer function is a complex vector showing the relationship between the horizontal and the vertical components of the magnetic field. The vertical component is generated by lateral conductivity gradients in the earth. This function is known as the *Tipper* $\mathcal{T}$ and is mathematically expressed as:

$$H_z = \mathcal{T}_{zx}H_x + \mathcal{T}_{zy}H_y \tag{2.53}$$

For a homogeneous medium, the Tipper function is zero due to no induced vertical magnetic field, H_z. On the other hand, there is an induced vertical magnetic field (H_z) when we are close to a vertical boundary between low and high conductivity structures, for example, at the boundary between ocean and land. For a 2D earth, the coordinate system can be rotated so that the x-axis is in the strike direction, the so-called *Tipper strike* (Tstrike), to get $\mathcal{T}_{zx} = 0$ and $\mathcal{T}_{zy} \neq 0$. We can do this by minimizing $|\mathcal{T}_{zx}|$.

The Tipper vector, normally called inductions arrows, can be decomposed into two vectors in the horizontal xy plane. The arrows have a real (in-phase) and imaginary (out-of-phase) part. There exist two conventions for the induction arrows called reversed (Parkinson convention; Parkinson, 1959) or non-reversed (Wiese convention; Wiese, 1962). In the Wiese convention, the vectors point away from lateral increase in electrical conductivity. The magnitude of induction arrows depends on both the proximity to the conductor and the conductivity contrast. The bigger the contrast the longer are the arrows and the closer the conductor the longer are the arrows.

The length of the real (M_r) and imaginary (M_q) arrows are given as:

$$M_r = \left(\Re\mathcal{T}_{zx}{}^2 + \Re\mathcal{T}_{zy}{}^2\right)^{1/2} \tag{2.54}$$

$$M_q = \left(\Im\mathcal{T}_{zx}{}^2 + \Im\mathcal{T}_{zy}{}^2\right)^{1/2} \tag{2.55}$$

where $\Re$ and $\Im$ are the real and imaginary parts of the Tipper, respectively.

The directions of the arrows are similarly determined as:

$$\theta_r = tan^{-1}\left(\frac{\Re\mathcal{T}_{zy}}{\Re\mathcal{T}_{zx}}\right) \tag{2.56}$$

$$\theta_q = tan^{-1}\left(\frac{\Im\mathcal{T}_{zy}}{\Im\mathcal{T}_{zx}}\right) \tag{2.57}$$

where θ_r and θ_q are clockwise positive from the x-axis (usually geomagnetic North) along which the coherency between vertical and the horizontal magnetic field is at its maximum.

2.2.7 Data dimensionality

MT data can be used to indicate the geoelectrical dimensionality of the Earth´s subsurface, which can be 1D, 2D or 3D in terms of the resistivity structure as explained in section 2.2.3. The early tools (still used) to estimate data dimensionality developed in MT during the 1960s and 1970s were based on the rotational properties of the magnitudes of the response tensor elements as for example the *skew, ellipticity and polar diagrams*, whereas more modern tools developed since the mid-1980s essentially use the rotational properties of their phases (Chave and Jones, 2012).

The *Swift skew* was one of the most used indicator to estimate data dimensionality. It is a normalized parameter, which is rotationally invariant. This quantity was given by Swift (1967):

$$skew = \frac{\left|Z_{xx} + Z_{yy}\right|}{\left|Z_{xy} - Z_{yx}\right|} \tag{2.58}$$

If the skew is higher than 0.3 it means that we need 3D resistivity models to explain the data, but if this value is below 0.2 it means that data can be explained by 1D or 2D models.

A second dimensionality indicator is the *ellipticity* of the MT response tensor. It is given by the ratio of the minor axis of the impedance ellipse to the major axis (Chave and Jones, 2012):

$$ellipticity = \frac{\left|Z_{xx}(\theta) - Z_{yy}(\theta)\right|}{\left|Z_{xy}(\theta) + Z_{yx}(\theta)\right|} \tag{2.59}$$

Ellipticity, as a function of the rotational angle, is undefined for a pure 1D response, as both the numerator and denominator are zero. It will also be zero for a 2D Earth.

The *polar diagrams* (also known as peanut diagrams) are the third conventional dimensionality (and directionality) indicator that was widely used prior to around 1990 and is still used today. It considers the rotational shape of the magnitudes of the diagonal and off-diagonal impedance tensor elements through plotting $|Z_{xx}(\theta)|$ and $|Z_{xy}(\theta)|$ as a function of θ. Over a 1D Earth, $|Z_{xx}(\theta)|$ is zero for all angles, and $|Z_{xy}(\theta)|$ describes a perfect circle as shown in Figure 6a. For a purely 2D Earth, $|Z_{xy}(\theta)|$ describes a shape that is elliptical for low to moderate anisotropy between Z_{xy} and Z_{yx}, but adopts a "peanut" form for higher anisotropy. The diagonal term $|Z_{xx}(\theta)|$ displays a four-leaf clover pattern, with zeros at the direction of the strike and perpendicular to the strike, where $|Z_{xy}(\theta)|$ reaches maxima and minima. For a 3D Earth symmetry is lost and the diagonal element, $|Z_{xx}(\theta)|$, does not display zeros at four cardinal points 90° apart at the angles where the off-diagonal $|Z_{xy}(\theta)|$ reaches maxima and minima (Figure 6c).

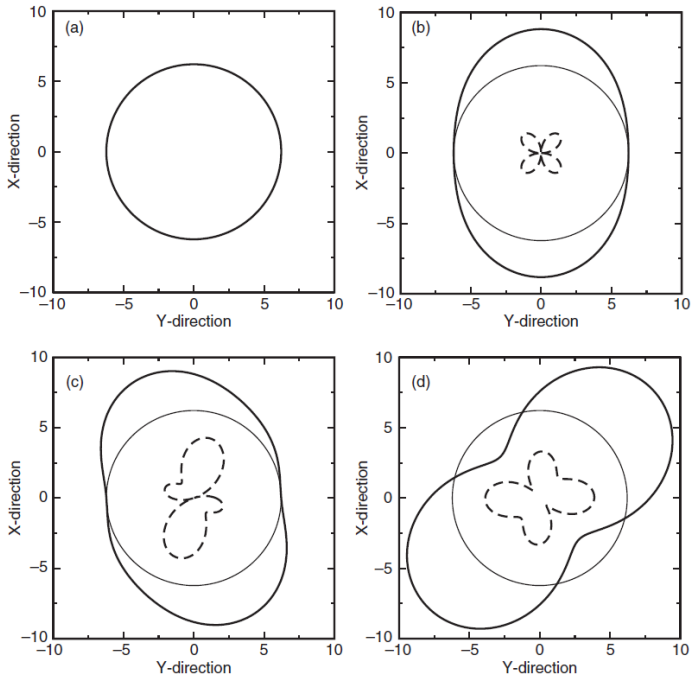

FIGURE 6: Impedance magnitude rotation diagrams ("peanut diagrams") for the synthetic (a) 1D, (b) 2D, (c) 3D and (d) 3D/2D cases (from Chave and Jones, 2012)

Chave and Jones (2012) conclude that all three of the above mentioned dimensionality indicators that are amplitude-based are seriously affected by distortion, i.e. highly sensitive to noise.

The first "modern" dimensionality indicator to be proposed was the phase-sensitive skew, η, of Bahr (1988). It is a measure of the skew of the phases of the impedance tensor, which is unaffected by amplitude distortion effects, and is given by

$$\eta = \frac{|[D_2, S_2] - [S_1, D_2]|^{1/2}}{|D_2|} \tag{2.60}$$

where the S (sum) and D (difference) impedances are the so-called modified impedances (Bahr, 1988) given by

$$S_1 = Z_{xx} + Z_{yy}\,, \quad S_2 = Z_{xy} + Z_{yx}$$
$$D_1 = Z_{xx} - Z_{yy}\,, \quad D_2 = Z_{xy} - Z_{yx} \tag{2.61}$$

Bahr (1988, 1991) gave criteria for interpreting η based on its value. Values of $\eta < 0.1$ are considered to be 1D, 2D or distorted 2D (3D/2D). Values in the range $0.1 < \eta < 0.3$ are considered to be indicative of a modified 3D/2D form called the delta (δ) technique. Values of $\eta > 0.3$ are considered to represent 3D data.

2.3 The transient electromagnetic method

2.3.1 Overview

The Transient Electromagnetic (TEM) method, also known as Time Domain Electromagnetics (TDEM), is a geophysical exploration method used to obtain the subsurface resistivity information, from a few metres to around 1 km.

The development of the TDEM method started in the 1950's, but it was not a common practice due to the lack of instrumentation electronic development. In 1970's, the advance in equipment and methods for interpretation of TDEM data reached important levels and became well known and widely used (Spies and Frischknecht, 1991).

2.3.2 Central loop TDEM sounding

A typical TDEM sounding configuration is the central loop configuration (Figure 7). Here, a transmitter is connected to a square loop of wire that is placed on the surface and a multi turn receiver coil, located at the centre of the transmitter loop is connected to the receiver. A magnetic field of known strength is built up by transmitting a periodic and symmetrical current signal into the loop.

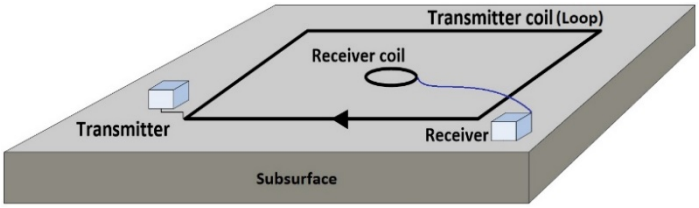

FIGURE 7: Typical central loop TDEM configuration (modified from Phoenix Geophysics, 2015). Transmitter loop size was 100 m x 100 m in the Borinquen survey

A few milliseconds after the constant current is injected into the loop it is abruptly turned off. The resulting decaying magnetic field induces electrical currents in the ground initially called early time currents (Figure 8). These signals diffuse downwards and away from the transmitter forming the late time currents as a response to the time varying magnetic field with a distribution similar to the one shown on Figure 8.

As the transmitter is turned off, the current in the loop decays linearly during the turn off time (Figure 9). This time is also known as "ramp time". The current distribution in the ground generates a secondary magnetic field that decays with time. The decay rate of the magnetic field as a function of time is monitored by measuring the induced voltage in a receiver coil. The current distribution and the decay rate of the magnetic field depend on the resistivity structure of the earth. The decay rate, recorded as a function of time just after the current in the transmitter loop becomes zero (Figure 9), can therefore, be interpreted in terms of the subsurface resistivity structure (Árnason, 1989).

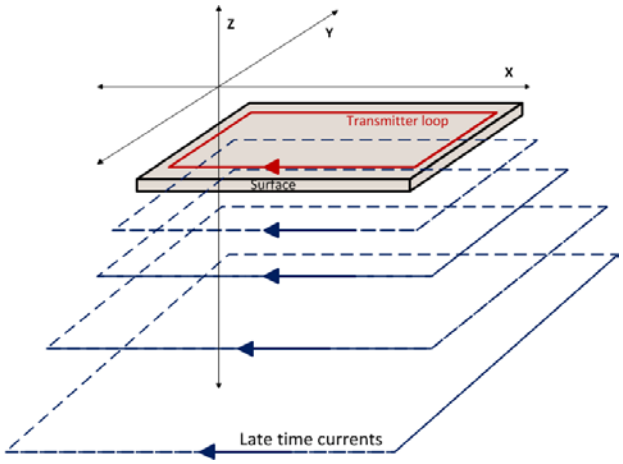

FIGURE 8: Current propagation, early and late times (modified from Rowland, 2002)

The waveform of the transmitter current and an induced EM force as a response of turning off the current in the transmitter are shown in Figure 9a and Figure 9b. The decay rate of the magnetic field is measured as a function of time at so-called time gates that represent prefixed intervals, equally distributed on a log of time scale. It's shown in Figure 9c.

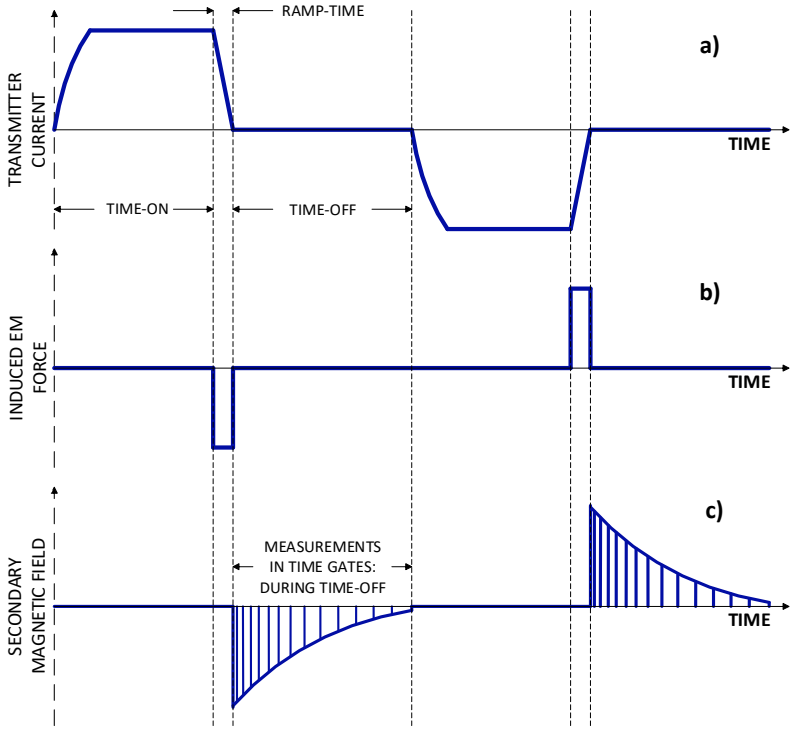

FIGURE 9: TDEM waveforms (modified from Rowland, 2002) showing in a) the signal of the current injected into the transmitter loop, the ramp time and the time on/off; in b) the induced EM force and c) the measurement time gates

2.3.3 TDEM for a homogeneous earth

For a homogeneous half space of conductivity σ, the induced voltage in the receiver coil is given by (Árnason, 1989):

$$V(t,r) = I_0 \frac{C(\mu_0 \sigma r^2)^{\frac{3}{2}}}{10\pi^{\frac{1}{2}} t^{\frac{5}{2}}} \tag{2.62}$$

Where, $C = A_r n_r A_s n_s \frac{\mu_0}{2\pi r^3}$

Furthermore, t is the elapsed time after the transmitter current is turned off (s), A_r is the cross-sectional area of the receiver coil (m^2), n_r is the number of windings in the receiver coil, μ_0 is the magnetic permeability in vacuum (H/m), A_s represents the cross-sectional area of the transmitter loop (m^2), n_s is the number of windings in the transmitter loop, I_0 represents the transmitter current (A), r is the radius of the transmitter loop and $V(t,r)$ the measured voltage (V).

The time behaviour of the diffusing voltage response for different resistivities can be divided into three phases: early times, intermediate times and late times. In Figure 10a, the induced voltage is constant at the early stage and starts to decrease with time in the intermediate stage. For the late times the measured voltage V(t) decays linearly as a function of time (log-log scale). The slope of the curve is -5/2 showing that the voltage is proportional to $t^{-5/2}$ (see equation (2.62)).

The behaviour of the apparent resistivity response for different values of resistivity for a homogeneous half space is shown in Figure 10b. It is possible to see how the apparent resistivity approaches the true resistivity of the half-space at late times. This is an important fact because we can relate it with the voltage response, which reaches the late stage at late times as the resistivity is lower (Figure 10b). Here we can also see how the transition between early time, intermediate and late time depends on the resistivity and it is shifted at early times to higher resistivity values.

Apparent resistivity ρ_a of a homogeneous half-space in terms of induced voltage at late times after the source current is turned off is obtained by rearranging equation (2.62) and it is given by:

$$\rho_a = \frac{\mu_0}{4\pi}\left[\frac{2\mu_0 I_0 A_r n_r A_s n_s}{5t^{\frac{5}{2}} V(t,r)}\right]^{\frac{2}{3}} \tag{2.63}$$

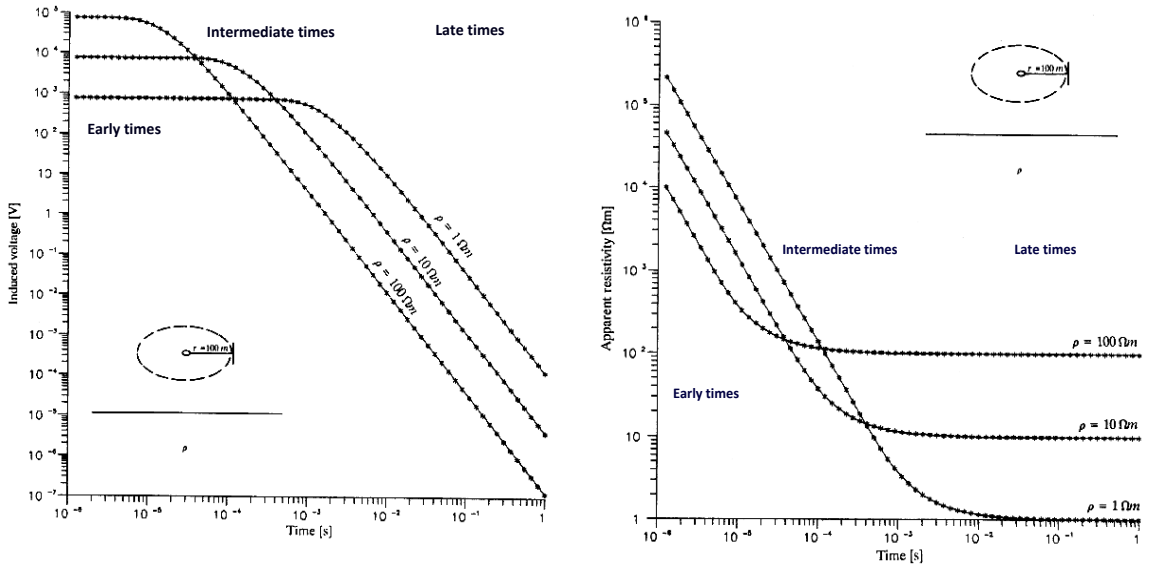

a) b)

FIGURE 10: Voltage response to the left and late time apparent resistivity to the right for a homogeneous half-space of different resistivity (modified from Árnason, 1989)

2.4 Electromagnetic distortion

2.4.1 Static shift problem

As discussed by Árnason (2015) the MT method, like all resistivity methods that are based on measuring the electric field on the surface of the Earth, suffers the so-called telluric or static shift problem. The shift problem comes about because the electromagnetic field is distorted by shallow resistivity anomalies at, or close to, the sounding site and/or topography.

The shift is called "static" because the conservation of current at conductivity discontinuities is not a time-dependent process like, for example, induction. Therefore, the phenomenon of static shift does not affect the phase of the transfer function (Simpson and Bahr, 2005).

Except at very high frequencies, the magnetic field is not much affected (Groom, 1989) but the electric field can be severely affected. Árnason (2015) explains that for very high frequencies the electric field is distorted both by induced eddy currents and galvanic distortion. At lower frequencies (below a few hundred Hz), most commonly used in geothermal exploration, the electric field is practically only subject to galvanic distortion and has an unknown frequency independent multiplier, relative to the undistorted field, causing shifts of the apparent resistivity curves when plotted on log log-scale.

The unknown shift multiplier in the apparent resistivity scales directly the resistivity values obtained by interpretation of the soundings. According to the dependence of the depth of penetration (skin-depth) on the resistivity, depths to resistivity boundaries will also be scaled by the square root of the multiplier. It is therefore, evident that interpretation of un-corrected MT data can lead to drastically wrong resistivity models. In Árnason (2015), it is demonstrated, both by model calculations and by extensive field data that the shifts can be large, both up and down, and they can be systematic in large areas.

The static shift distortion caused by resistivity inhomogeneities can be classified in *electric field distortion* and *current distortion*, *topographic effects* are a part of the second one.

Due to the dependency of the electric field on resistivity of the material where the voltage difference is measured, it leads to local distortion of the amplitudes of electric fields as a result of conservation of electric charge. This causes impedance magnitudes to increase or decrease by real scaling factors.

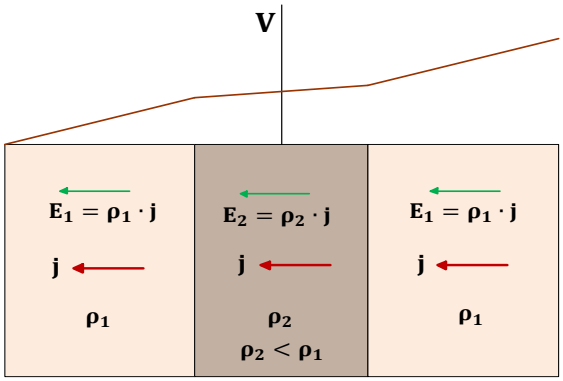

FIGURE 11: Electric field distortion (modified from Sternberg et al., 1988; Árnason, 2015)

Figure 11 shows the variation of the voltage and electric field (slope of the voltage curve) in the surface when a constant current density flows through 2D domains of different resistivity (extending infinitely deep). In this example, $\rho_2 < \rho_1$ and the electric field (or the voltage difference over a given length) is lower in the low resistivity domain. Unless at very high frequencies where eddy currents may be induced, this lowering of the electric field is independent of the frequency of the current. According to the definition, the apparent resistivity will be lower in domain 2 than outside. If $\rho_2 > \rho_1$ the electric field and the apparent resistivity would be higher in the central domain 2 than outside.

When current is flowing in the ground with a localised resistivity anomaly of lower resistivity than the surroundings, then, the current is deflected into the anomaly suffering current channelling. On the other hand, if the resistivity is higher, the current is repelled out of the anomaly. If the anomaly is close to the surface, this will affect the current density at the surface and hence the electric field and apparent resistivity. Like for the voltage distortion, this effect is independent of the frequency of the current density except at very high frequencies (Árnason, 2015).

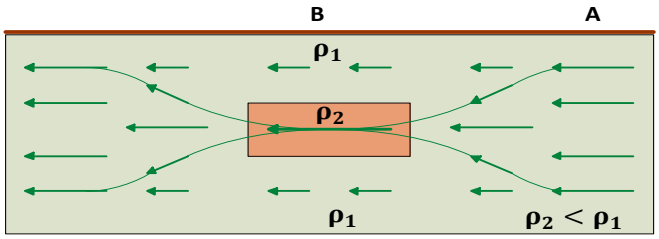

FIGURE 12: Current channelling caused by localised conductive anomalies (modified from Sternberg et al., 1988; Árnason, 2015)

In Figure 12 the superficial body with resistivity ρ_2 is channelling the current because its resistivity is lower than the rest of the subsurface having ρ_1. But if ρ_2 was higher than ρ_1, then the current would be repelled.

Due to topographic effects, the electric field increases in valleys and decreases on hills due to galvanic effects (Figure 13a). It is because the induced current flowing mostly laterally is spread out in local topographic highs but concentrated in topographic lows as shown in Figure 13b). In the case of constant resistivity, this will lead to apparent resistivity lower than the true resistivity on topographic highs and higher in topographic lows.

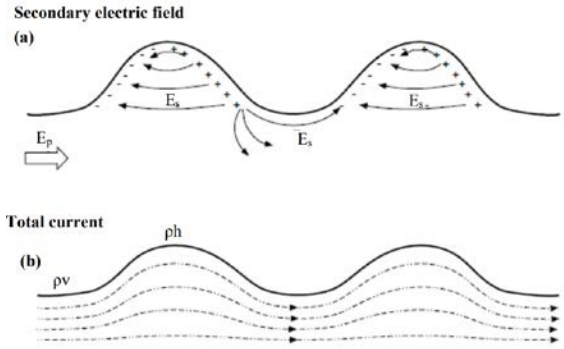

FIGURE 13: Induced current density distortion due to topography

Several studies exist on the effect of topography on MT measurements, most of which adopt a numerical modelling approach (Wannamaker et al., 1984; Jiracek et al., 1986). Any attempts to model topography and incorporate it in an inversion would be to introduce topographic effects again after it has been eliminated by static shift correction. Topographic effects on MT responses in 3D are more complicated than in 2D because they produce both inductive and galvanic effects in any polarization (Nam et al., 2008), hence carrying out 3D inversion might considerably reduce them.

2.4.2 Correction of static shift

The TDEM technique can be visualized as if the induced currents diffuse downwards and outwards with time like a "smoke fringe" (Nabighian, 1979). In this method, the near surface resistivity anomalies only affect the method at very early times. At late times, the current distribution has diffused deep below near surface anomalies and their effects disappear. Similarly, topography can affect the method at early times, but at late times, when the induced currents have diffused down below the topographic regime, the influence of the topography fates out. In the case of MT this is different because the electric field signatures of currents induced at great depths have to be conveyed all the way to the surface and hence are prone to near surface inhomogeneities as demonstrated above and frequently high frequency effects prohibit resolving the resistivity structure in the immediate vicinity of the electric dipoles.

In the late eighties people started to use TDEM soundings to correct for static shifts in MT data (e.g. Sternberg et al., 1988). However, some people still apply the MT method without proper static shift correction. This may be justified in areas with gentle topography and where the near surface rocks are homogeneous, such as sedimentary layers. High temperature geothermal systems in volcanic areas are the other extreme. They are normally characterised by very high resistivity contrast at the surface and shallow depths which are ideal conditions for extreme static shifts. Cumming and Mackie (2010) discuss the use of TDEM for static shift correction of MT data concluding that it should be able to resolve the shallow resistivity structure in resistive environments, but big loops and/or large current may be needed to enable the data to tie in with the MT data. Árnason (2015) mentions how joint inversion of MT and TDEM data at Iceland GeoSurvey has revealed shift multipliers as low as 0.1, meaning that if the static shift problem was not corrected for, interpretation would give ten times too low resistivity values and about three times too shallow depths to resistivity contrasts.

3 THE SIGNIFICANCE OF RESISTIVITY IN GEOTHERMAL EXPLORATION

The application of electromagnetic (EM) methods to image the resistivity structure of geothermal prospects has been demonstrated to be successful. Hersir and Björnsson (1991) give an overview of basic theory and application of geophysical methods for geothermal exploration, among them the MT and TDEM methods, whose combination has the potential to reveal the resistivity structure from the near surface down to great depths. The use of MT and TDEM soundings for geothermal exploration is widely reported (e.g., Árnason et al., 2010; Cumming and Mackie, 2010; Uchida, 2005). During the exploration stage, a resistivity model is key information to decide the location of exploration and possible production wells. This is because hydrothermal processes in geothermal systems affect the electrical resistivity of rocks; hence, models of the subsurface resistivity can be used to identify zones of different alteration, permeability and porosity (Rosenkjær and Oldenburg, 2012).

3.1 Resistivity of rocks

Different authors have discussed resistivity of rocks and the parameters affecting the resistivity of water bearing rocks. Flóvenz et al. (1985); Hersir and Björnsson (1991); Hersir and Árnason (2009) and Flóvenz et al. (2012) make reference about the conduction of electricity in solutions, electrical resistivity of water bearing rocks and the dependence of resistivity on some important parameters. Hersir and Árnason (2009) explain how electrical conduction of water bearing rocks is mostly through water contained in pores and along surface layers at the contact of rocks and solution and depends on the number and mobility of ions and on the rock matrix, because conduction is also defined by the connectivity of the flow paths through the rock.

3.1.1 Conduction of electricity in the rocks

Conduction in the Earth occurs through the transport of several types of charge carriers, including electrons (in metals), ions (in aqueous fluids and melts) or electron “holes” or vacancies (in semiconductors). Electrical conductivity varies over many orders of magnitude (Chave and Jones, 2012).

Since the process that is occurring is conduction, or more correctly for most Earth materials semiconduction (Chave and Jones, 2012), it seems natural to refer to rock conductivity measured in Siemens per meter (S/m). Nevertheless, magnetotelluric models are often presented and discussed in terms of the reciprocal property, resistivity, measured in ohm meters (Ωm), as it is simply easier to compare numbers that are greater than one than those less than one.

There are three main conduction mechanisms of electric current in the subsurface: pore fluid conduction, surface conduction and mineral conduction.

Pore fluid conduction

This mechanism is due to dissolved ions in the pore fluid which are free to move. The mobility of the ions is strongly dependent on viscosity of the fluid and concentration of the electrolyte. Revil and Glover (1998) mention how pore fluid conduction tends to dominate the resistivity of most rocks in the upper parts of the crust, unless high temperature geothermal settings are present facilitating chemical and thermal alteration.

Surface conduction

This conduction process happens on the interface between the pore fluid and the pore walls. It is caused by highly mobile ions that are absorbed by the pore walls and form a conductive layer on the pore surface. Depending on the hydrothermal alteration conditions of the rocks (stage and amount) the ability in forming a conductive layer in the pores will vary. This ability is called cation-exchange

capacity (CEC) (Waxman and Smiths, 1968; Pezard, 1990). CEC varies greatly between minerals. Clay minerals have variable but high CEC, whereas minerals forming normal volcanic rocks have practically no CEC. Revil et al. (1998) mention how the interface conductivity (surface conduction) has been shown to be directly proportional to the cation exchange capacity of the minerals involved. Weisenberger et al. (2016) mention how there is a good correlation between CEC and resistivity. Lévy et al. (2018) presented a contribution in the understanding of this property of minerals and how electrical conduction behaves according to the alteration mineralogy.

Mineral conduction

At very high temperatures and close to the solidus of the rock, the conductivity of the rock matrix becomes important (Flóvenz et al., 2012). The matrix conductivity follows the Arrhenius formula:

$$\sigma_m = \sigma_0 e^{-E/kT} \tag{3.64}$$

Where σ_m is matrix conductivity

σ_0 is the conductivity at infinite temperature

E represents the activation energy (eV)

k corresponds to the Boltzmann constant (~$8.617 \cdot 10^{-5}$ eV·K^{-1}) and

T is the temperature in K

Laboratory measurements of basalts and related material as a function of temperature indicate that the matrix resistivity is in the order of 1000 Ωm at 400 °C and decreases to 10 Ωm at 800 °C. At higher temperature, partial melt will still decrease the resistivity (Scarlato et al., 2004).

Electrical resistivity depends considerably on surface conduction for geothermal reservoirs where temperatures can exceed 300 °C (Flóvenz et al., 2005). For unaltered rocks (fresh water and low temperature) a linear relationship is found between the bulk conductivity and the pore fluid conductivity over almost the whole range of salinities (Flóvenz et al., 2005), showing that the pore fluid conduction is always dominant and the surface conduction is negligible. By understanding the conduction mechanisms governing the geothermal systems allow us to use the resistivity image to predict the temperature of the different alteration zones due to the relationship of surface conduction and the minerals involved according to the CEC (e.g. Revil et al., 1998; Flóvenz et al., 2005; Lévy et al., 2018).

3.1.2 Factors affecting the resistivity of rocks

In water bearing rocks conduction of electricity is mainly affected by salinity, temperature, the degree of fluid saturation, conductivity of the rock matrix, porosity/permeability, water-rock interaction and alteration.

Salinity

Groundwater may have a variety of salts in the solution. Conduction of electricity in solutions depends on the free ions.

Hersir and Björnsson (1991) discuss how equivalent salinity can be used to find out how resistivity depends on salinity for a single salt, such as NaCl in water. As shown in Figure 14, salinity affects the resistivity in a nearly inversely linear manner (Keller and Frischknecht, 1966). In Figure 14 we can see how temperature plays also an important role by decreasing the resistivity of the solution. The relationship between salinity and resistivity is given by:

$$\rho = 9.545\, C^{-0.937} \approx 10/C \tag{3.65}$$

Where C (g/l) is the concentration of NaCl (for C < 100 g/l).

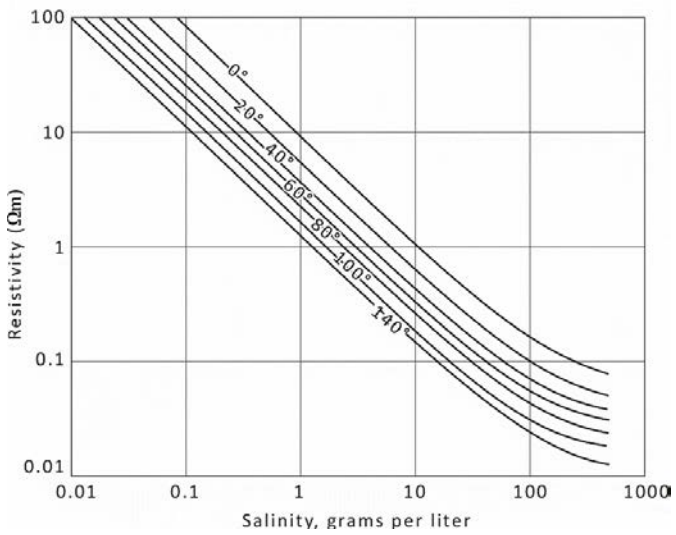

FIGURE 14: Resistivity of solution of sodium chloride as a function of concentration and temperature (modified from Keller and Friscknecht, 1966)

Temperature

At low to moderate temperatures (0 to ~200 °C), where we can have a combination of unaltered rocks, fresh water but also alteration mineralogy, resistivity of aqueous solutions decreases with increasing temperature (Figure 15). The reason is increasing mobility of the ions caused by a decrease in the viscosity of the water. Dakhnov (1962) describes this relationship:

$$\rho_w = \frac{\rho_{w0}}{1 + \alpha(T - T_0)} \tag{3.66}$$

Where ρ_w is resistivity of the fluid at temperature T, ρ_{w0} the resistivity of the fluid at temperature T_0; α the temperature coefficient of resistivity and T_0 is the room temperature ($\alpha \approx 0.023$ °C^{-1} for T_0 = 25 °C, and 0.025 °C^{-1} for T_0 = 0 °C).

At higher temperatures, a decrease in the dielectric permittivity of the water results in a decrease in the number of dissociated ions in the solution. Above 300 °C, this starts to increase the electrical resistivity of the fluid (Quist and Marshall, 1968). At very high temperatures the behaviour depends mostly on the rock matrix and therefore, resistivity is explained through mineral conduction mechanism.

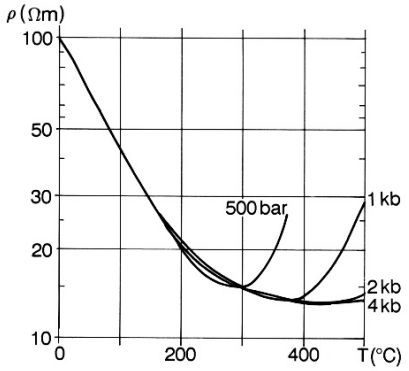

FIGURE 15: The resistivity of a NaCl solution as a function of temperature at different pressures (modified from Quist and Marshall, 1968)

Fluid saturation

Saturation is the fraction of the pore space that is actually filled with fluid. Resistivity soundings are used to find the depth to the groundwater table, since above that level the rocks may be partially saturated only, resulting in relatively high resistivity according to the degree of saturation.

Conductivity of the rock matrix

For most rocks in geothermal systems, the rock matrix itself has very low to extremely low conductivity at reservoir temperature; rock is normally an insulator. This implies that the conduction takes mainly place because of the presence of fluid and ions in the rock and by electrons in minerals at the rock–water interface. For very high temperatures the conductivity of the rock matrix becomes important and the resistivity behaves as described for mineral conduction.

Porosity and permeability

Porosity is defined as the ratio between the pore volume or voids to the total volume of a material, in this case soil or rock (Heath, 1983). There are primarily three types of porosity: 'intergranular', where the pores are formed as spaces between grains or particles in a compact material like sediments and volcanic ash; 'joints–fissures' or fractures, where the pores are formed by a net of fine fissures caused by tectonics or cooling of the rock (igneous rocks, lava); and 'vugular porosity', where big and irregular pores have been formed due to dissolution of material, especially in limestone. In all types of porosity, there are some isolated voids, called storage pores, and finer connecting pores called fracture pores.

It has been observed through different laboratory tests that resistivity of water-bearing rocks varies approximately as the inverse square of the porosity (Archie, 1942). This is an empirical law called Archie's law which describes how resistivity depends on porosity if ionic conduction in the pore fluid is the dominating conduction mechanism in the rock (salinity of the pore fluid is high and surface conduction is negligible):

$$\rho = \rho_w a \phi_t^{-n} \tag{3.67}$$

Where ρ is bulk (measured) resistivity; ρ_w is resistivity of the pore fluid; ϕ_t is fracture porosity as a proportion of the total volume; a is an empirical parameter, which varies from < 1 for intergranular porosity to > 1 for joint porosity, usually around 1; and n is cementing factor, an empirical parameter, usually 1-2.

Permeability represents a measure of how fluids flow through a porous solid. A rock may be highly porous, but if pores are isolated, it will have no permeability and the rock may not conduct electricity. Effective porosity represents the degree to which pores within the solid are interconnected. Usually, permeability is directional in nature, but secondary porosity like fractures, frequently have a significant impact on the permeability of the material. In addition to the characteristics of the host material, the viscosity and pressure of the fluid also affect the rate at which the fluid will flow (Lee et al., 2003).

Water rock interaction and alteration are discussed in the next section.

3.2 Resistivity structure of high-temperature geothermal areas

Resistivity of geothermal areas is governed not only by presence of fluid and temperature, but also by hydrothermal alteration products, since they contain clays (Gasperikova, 2011). High-temperature geothermal fields in volcanic areas in the world have in general a similar electrical resistivity structure.

The primary minerals in the host rock matrix are transformed into different minerals because of water–rock interaction and chemical transport by the geothermal fluids. The formation of alteration minerals depends on temperature and the type of primary minerals and the chemical composition of the geothermal fluid (Flóvenz et al., 2012). Porosity and permeability also control the intensity of the alteration.

A correlation between resistivity structure and hydrothermal alteration of rocks in geothermal systems is discussed in Árnason et al. (1986); Árnason et al. (2000); Hersir et al. (2009); Flóvenz et al. (2005) and Flóvenz et al. (2012). A typical resistivity cross section taken from the Nesjavellir high-temperature geothermal system in SW Iceland is given in Figure 16. The rocks in the area are mostly composed of basalts (as lavas, scoria layers, hyaloclastite, or intrusions). No correlation was found between resistivity and lithology in the boreholes. A low resistivity cap ($< 10\,\Omega$m) surrounding a resistive core usually characterizes the resistivity structure of high temperature fields in volcanic rocks. There are a medium to high resistivity near surface layers representing unaltered cold rocks, below which a low resistivity cap delineates the smectite-zeolite zone originally formed at temperatures of 100 - 220 °C. In the temperature range of 230 - 240 °C the zeolites disappear and smectite is gradually replaced by the more resistive chlorite in the so-called transition zone or mixed-layer clay zone. Below this transition section is the more resistive epidote-chlorite zone originally formed at temperatures exceeding 250 °C, also called the resistive core where the resistivity is dominated by surface conduction.

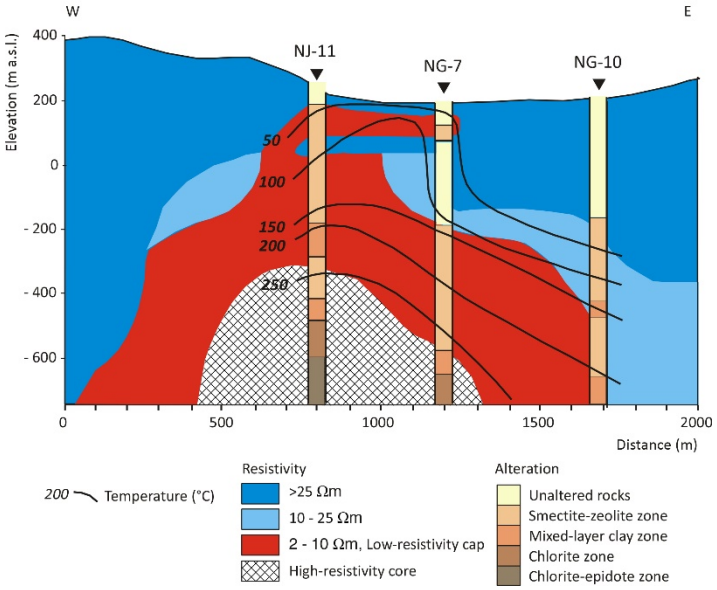

FIGURE 16: Typical resistivity structure of a high-temperature geothermal area (Nesjavellir geothermal field). The Figure shows a clear correlation between the subsurface resistivity structure and the alteration mineralogy in three wells and true formation temperature (from Árnason et al., 1986)

An overview of the relationship between subsurface resistivity, hydrothermal alteration, temperature, and conduction mechanism is summarized in Figure 17. Flóvenz et al. (2012) mention that the change from a smectite to chlorite-type alteration is reported to occur at temperatures close to 230 °C in basaltic geothermal systems. The change to illite seems to occur at somewhat lower temperature, or 180 °C.

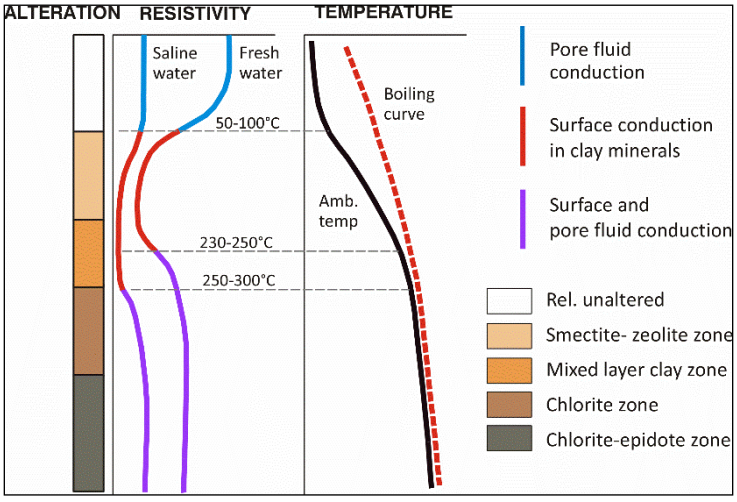

FIGURE 17: The general resistivity structure and alteration of the basaltic crust in Iceland (from Flóvenz et al., 2012)

Revil et al. (1998) and Kristinsdóttir et al. (2010) mention how due to surface conduction, resistivity will mostly depend on the alteration mineralogy for high-temperature reservoirs. Flóvenz et al. (2005) also conclude that for almost all freshwater saturated high-temperature fields the surface

conduction is dominant, both in the chlorite and the smectite zone. From previous discussions we also know that CEC of the involved minerals is the dominant actor for surface conduction, but the electrical conduction mechanism depends on the stage and amount of the hydrothermal alteration of the rocks. The observed increase in resistivity at the top of the mixed clay/chlorite zone in many high temperature geothermal reservoirs worldwide is most likely due to much higher cation exchange capacity in the smectites (0.8–1.5 meq/g) than in the alteration minerals below like chloride (0.01 meq/g) (Flóvenz et al., 2005; Lévy et al., 2018). Chloride presents up to two orders of magnitude lower CEC than smectite. In more silica-rich geological environments like Borinquen Geothermal area (Molina et al, 2016), the smectite tends to be replaced by illite with typically lower CEC than that of smectite, often around 0.2–0.30 meq/g (Flóvenz et al., 2012).

If the alteration and temperature are in equilibrium, the subsurface resistivity structure reflects not only the alteration but also which temperature to expect. As mentioned by Hersir and Árnason (2009) this was an important finding, because if the temperature that produced the alteration mineralogy still prevails, then the resistivity structure can be used to predict temperature, in most cases it can be regarded as a ‘maximum thermometer’. But if cooling occurs, the alteration remains and so does the resistivity structure and consequently we could be overestimating the temperature of the subsurface. It has also occurred that alteration minerals have indicated lower temperature than measured in the wells. This has been interpreted as being due to a young system being heated up and the alteration is lagging behind, still not in equilibrium with the temperature (Hersir and Árnason, 2009).

4 GEOLOGICAL SETTING OF THE STUDY AREA

4.1 Tectonics and geology

Central America (CA) is characterized by an internal magmatic arc developed as result of subduction. Here, the Cocos plate subducts the western Caribbean plate boundary along the Middle America Trench (MAT) at a convergence rate of 8.5 cm/yr (DeMets, 2001) (Figure 18). DeMets et al. (2010) indicate rates from 67 mm a^{-1} in Guatemala to 80 mm a^{-1} in southern Costa Rica (CR). Collision of the Cocos Ridge, a 2 km high aseismic ridge standing on >20 km thick oceanic crust, is the largest geodynamic force acting on the Caribbean plate, driving crustal shortening directly inboard and tectonic escape of the Central American forearc (CAFA) northwest of the ridge axis (Kobayashi et al., 2014). The Central Costa Rica Deformed Belt (CCRDB; Figure 18), a seismically active zone of distributed deformation, has been proposed to mark the southeast margin of the CAFA.

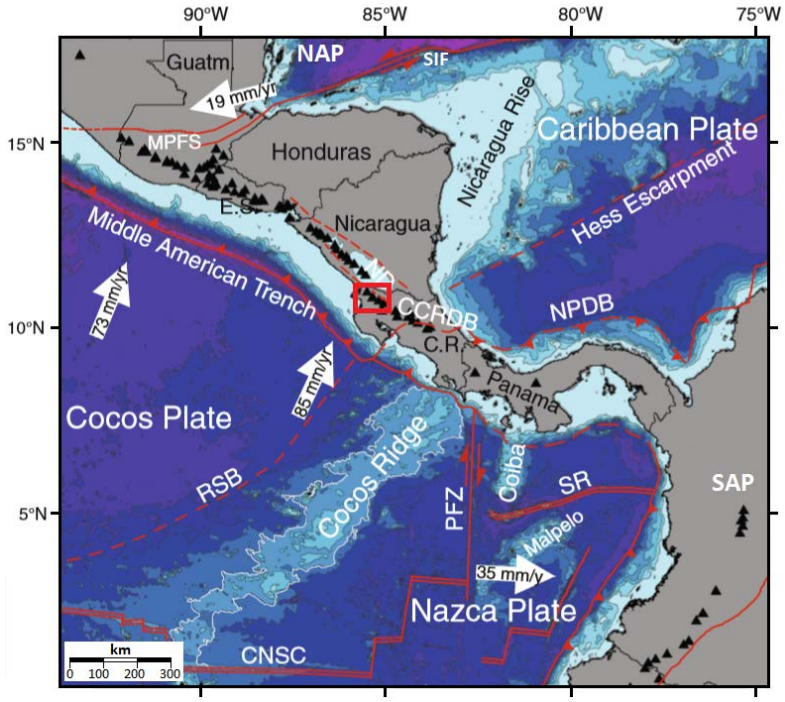

FIGURE 18: Tectonic map of Central America showing the location of the study area (red square), the North American and South American Plates (NAP & SAP), the Central Costa Rica Deformed Belt (CCRDB), Cocos-Nazca spreading centre (CNSC), North Panama Deformed Belt (NPDB) and the Panama Fracture Zone (PFZ), plate boundaries and major tectonic structures (red lines) and the main Quaternary volcanoes (black triangles). Black lines denote the coastline and international boundaries (modified from Lücke, 2012)

The most prominent geotectonic features near Costa Rica on Figure 18 are: (a) the subduction trench, a product of the subduction of the Cocos plate under the Caribbean plate; (b) subduction of a major topographic seafloor feature called Cocos Ridge, a submarine volcanic range from the Galapagos hot spot, extending along much of south CR, where the trench apparently has been plugged by the anomalously buoyant oceanic crust; (c) the Panama Fracture Zone, which forms one arm of a triple junction between the Cocos, Nazca, and Caribbean plates off the coast of south CR; (d) the motion of the Central America fore arc and Panama block (PB). The last one is discussed in Kobayashi et al. (2014) and a driving mechanism for motion of the Central America forearc (CAFA) is proposed there.

In CR, the Quaternary volcanic rocks associated with the magmatic arc are distributed as shown on Figure 19. The Costa Rican crust itself (about 40 km thick) is quasi-continental. This type of crust is

not as thick, old or crystalline as typical continental crust, but rather thickened compared to normal oceanic crusts. It shows an acidic evolution through time and P-wave velocities (V_p) similar to typical, true continental crust, indicating an increase in maturity of the arc (Alvarado et al., 2017). The distribution of other older volcanic as well as intrusive rocks is clearly showing this NW-SE trend due to the subduction process (Figure 19).

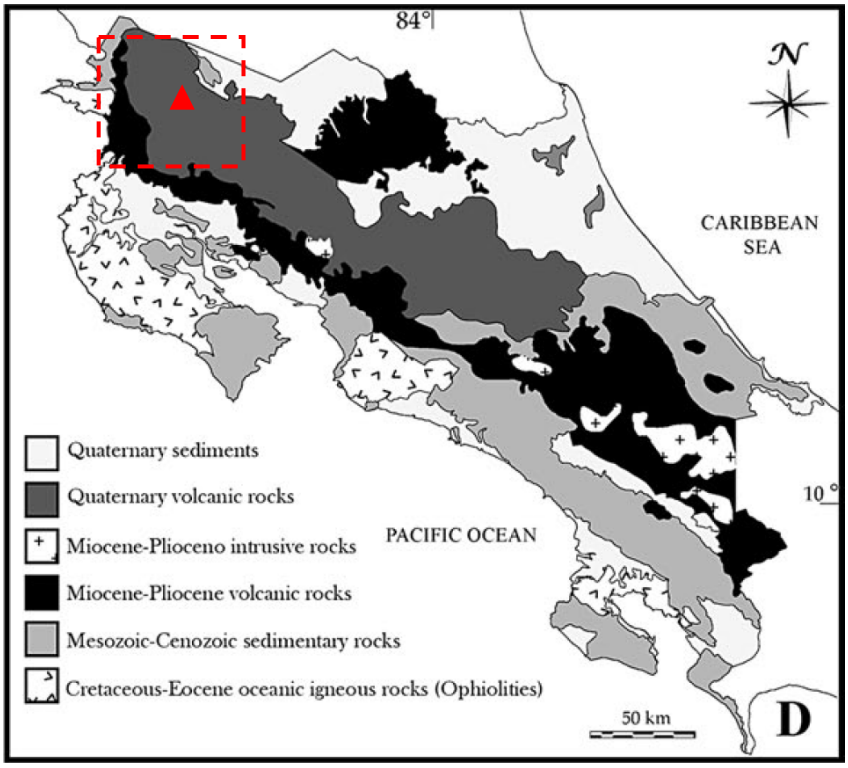

FIGURE 19: Simplified geological map of Costa Rica showing the area of interest (inside the red dashed square) and the approximate location of Rincón de la Vieja Volcano (red triangle) (modified from Alvarado et al., 2017)

This tectonic activity on the Pacific coast of the Central American region takes place along the "ring of fire", and consequently the creation of the volcanic arc along the Pacific Rim has facilitated the formation of geothermal reservoirs. Various geothermal power plants already exist and contribute significantly to the countries' energy mix generation. Just over 500 MWe are currently installed in the region. The geothermal potential for power generation in Central America is estimated to be between 3,000 and 13,000 MWe (Sander, 2015). In El Salvador for example, ~25% (204 MWe) of the generated power derives from geothermal resources. In Costa Rica geothermal development and exploration for electric power generation purposes has increased considerably during the last years. Currently, two geothermal fields where 7 power plants with a total installed capacity of ~253 MWe are operated by ICE (*Instituto Costarricense de Electricidad*). Sánchez and Vallejos (2015) point out that by 2013 geothermal represented 7.98% of the installed capacity but 14.96% of the total energy generated. Once Reventazón hydropower plant began operation in 2016 adding ~305 MWe to the electric power generation (also developed by ICE), the percentage of contribution from geothermal changed to ~13%. In June 2019, Pailas II Geothermal Power plant (Figure 20) began the production adding 55 MWe more making a total of ~253 MWe raising the contribution from geothermal to ~16% of the electricity required by the country.

4.2 Guanacaste volcanic mountain range

Geothermal exploration studies were carried out during the 70s and the 80s in Costa Rica (CR). The most prominent geothermal prospects are in the northwest part of the country, on the slopes of the

Rincon de la Vieja, Miravalles and Tenorio volcanoes (Moya and Yock, 2007). *Borinquen Geothermal Field (BGF)* is located on the western flank of Rincon de la Vieja volcanic complex, twenty kilometres to the north of Liberia City, in Guanacaste province (Figure 20).

Guanacaste Volcanic mountain range represents the most important feature of the Central America volcanic arc in the northwest part of CR with an extension of ~75 km, where four Quaternary andesitic stratovolcanoes were formed (Figure 20): Orosi (OV) – Cacao (CV), Rincon de la Vieja (RVV) - Santa María (SMV), Miravalles (MV) and Tenorio – Montezuma (TMV). The formation of the volcanic range was preceded by different periods of intense explosive silicic volcanism, generating several hundreds of cubic kilometres of ignimbrites and related deposits, which were emplaced in the period 6–0.65 Ma (Vogel et al., 2004). These products extended mainly towards the Pacific coast and formed the "Santa Rosa Ignimbrite Plateau" (Chiesa et al., 1992; Molina et al., 2014).

The two geothermal fields produce presently on this mountain range ~253 MWe (Miravalles GF ~163 MWe and Las Pailas GF ~90 MWe; Figure 20). The production in Mivalles (MGF) started in 1994 with 50 MWe and in Las Pailas Geothermal Field (PGF) in 2011 with 35 MWe. Las Pailas II started to generate 55 MWe in June, 2019. Borinquen I is planned for 55 MWe by 2023 and Borinquen II will add 55 MWe more by 2030 (ICE, 2018a). Figure 20 shows the location of the main geological structures presented in Molina et al. (2014) that have influence on BGF, the location of seven deep wells (red stars), two of these in PGF and five in Borinquen GF as a reference for the next maps. All the maps are given in UTM (Z16, WGS84) coordinates.

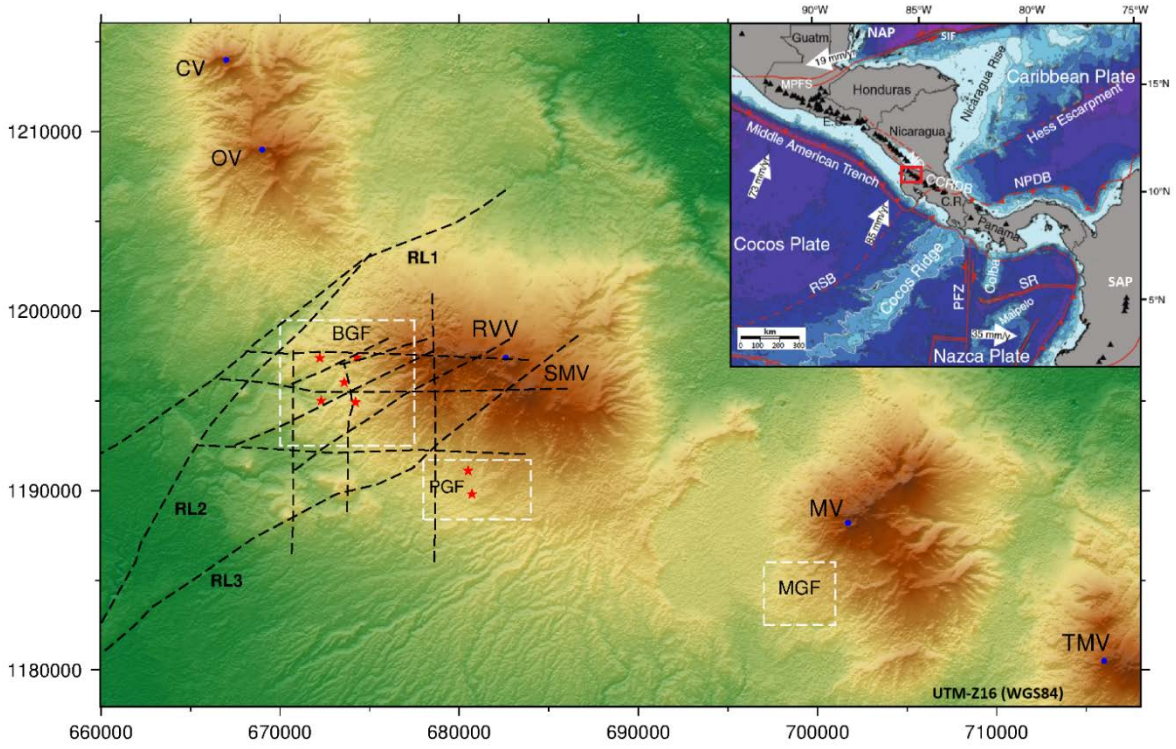

FIGURE 20: Location of Borinquen Geothermal Field (BGF) as well as Miravalles (MGF) and Las Pailas Geothermal Fields (PGF) (white dashed squares), Quaternary volcanoes Orosi (OV) – Cacao (CV), Rincon de la Vieja (RVV) - Santa María (SMV), Miravalles (MV) and Tenorio – Montezuma (TMV) (blue dots), geological structures (black dashed lines, adopted from Molina et al.,2014) and wells (red stars). Coordinates are UTM-Z16 (m), generated from SRTM data

4.3 Geology of study area

Kempter (1997) identified in the surroundings of the study area at least three caldera structures - Cañas Dulces, Guachipelín, and Guayabo – based on the spatial distribution of the deposits and by comparing the stratigraphy. This activity is associated with different caldera collapse events and it is probably responsible for these ignimbritic eruptions, their ages are 1.7 Ma, 1.5 Ma, and 1.4–0.6 Ma, respectively.

Kempter (1997), Zamora et al. (2004) and more recently Molina et al. (2014) and Molina et al. (2016) discuss the origin and formation of the Cañas Dulces Caldera (CDC) (Figure 21). In the last two works, they combined information from deep boreholes drilled by ICE (ICE, 2018b) together with new geological work and radiometric dating to describe its stratigraphy, structure and volcanic evolution of the area.

The stratigraphy of the Borinquen Geothermal area is summarized from Molina et al. (2014) as follows:

The Bagaces group

This forms most of the ignimbrite plateau of Santa Rosa (SW of the volcanic arc) consisting of sequences of andesitic lavas, crystal tuffs and lithic tuffs, with a predominance of explosive products. It extends from the base of the current volcanic edifices to the Pacific coast and is overlaid by the Liberia Formation. In PGB01 (Figure 21 and Figure 23) it first occurs at a depth of 1850 m (-1150 m a.s.l.) and reaches a thickness of 749 m (without reaching the base), whereas in Las Pailas it reaches a maximum thickness of 1077 m (PGP05). Its age ranges from 8.75 to 1.43 Ma. These rocks are very permeable and a total loss of drilling fluid often occurs (i.e. when the drilling system loses fluid at a flow rate of 50 L/s).

The Liberia Formation

This formation is mainly constituted of massive pyroclastic flow deposits, dacitic to rhyolitic in composition, characterised by corroded quartz and biotite phenocrysts. It usually occurs below 250 m a.s.l. and has a maximum thickness of 1692 m (PGB2, Figure 21) inside the caldera. This formation corresponds to the products of the eruption that generated the CDC about 1.43 Ma ago, a massive eruption of about 200 km^3 of rhyolitic magma largely responsible for the formation of the Liberia ignimbrite. Liberia Formation is radially distributed around the south-western flank of Rincon de la Vieja volcano in the area of the Borinquen and Las Pailas geothermal fields. Field mapping shows that the Liberia Formation extends mainly on the Pacific side of the Rincon de la Vieja–Santa María volcanoes. These deposits have a characteristic white colour but are slightly reddish-to-pink in some places.

The Cañas Dulces Formation

This includes a group of seven dacitic domes containing phenocrysts of plagioclase, green hornblende, clinopyroxenes and orthopyroxenes, minor biotite, and opaques in a devitrified groundmass, emplaced on the periphery of the southwestern border of the Cañas Dulces depression. The last dated ages for these domes range from 1.41 to 0.8 Ma (Molina et al., 2014) and seem to be consistent with the relative stratigraphy and the new ages given for the Liberia Formation.

The Pital Formation

This unit includes dacitic pyroclastic sequences interbedded with minor epiclastic, lacustrine deposits and andesitic lavas, which constitute the post-caldera infill of the CDC. It was deposited 1.43–0.8 Ma ago and has a maximum thickness of 445 m (PGB5, Figure 21). Kempter (1997) describes this as a succession of pumice-rich dacitic fallout and pyroclastic density current deposits containing

some minor epiclastic and lacustrine deposits, as well as some andesitic lavas, and it is restricted to the interior of the CDC.

Deposits from the Rincón de la Vieja volcano

This is the uppermost stratigraphic unit and consists mainly of andesitic lava flows with subordinated pyroclastic deposits ranging in age from 1.14 ± 0.03 Ma ago to present (Carr et al., 2007). They outcrop at the surface with a maximum thickness of 450 m (PGB5). Some pyroclastic and debris avalanche deposits are found in the uppermost part of this sequence dated with an age of 3490 ± 105 yr (Melson, 1988).

Molina et al. (2014) conclude that the Liberia Formation corresponds to a caldera forming eruption. It is suggested that CDC was probably formed under strong structural control dominated by two parallel NE-SW regional faults, RL2 and RL3 (Figure 21), followed by the construction of the Rincon de la Vieja-Santa Maria volcanic complex. According to age and stratigraphic relationships it is proposed that the Cañas Dulces dacitic domes were emplaced immediately after the formation of the caldera through the same fault system that controlled the caldera collapse. The present model for the CDC is shown in Figure 21 including the geological map of the study area.

Two geological cross sections A-A' and B-B' shown on the map of Figure 21 with thin dark grey dashed lines are presented in Figure 22 and Figure 23 largely sustained from well logs drilled by ICE. Those results show the concentration of the Liberia Formation inside the hypothetical caldera and important displacements in the Bagaces group as well as the location of some of the domes in the caldera borders.

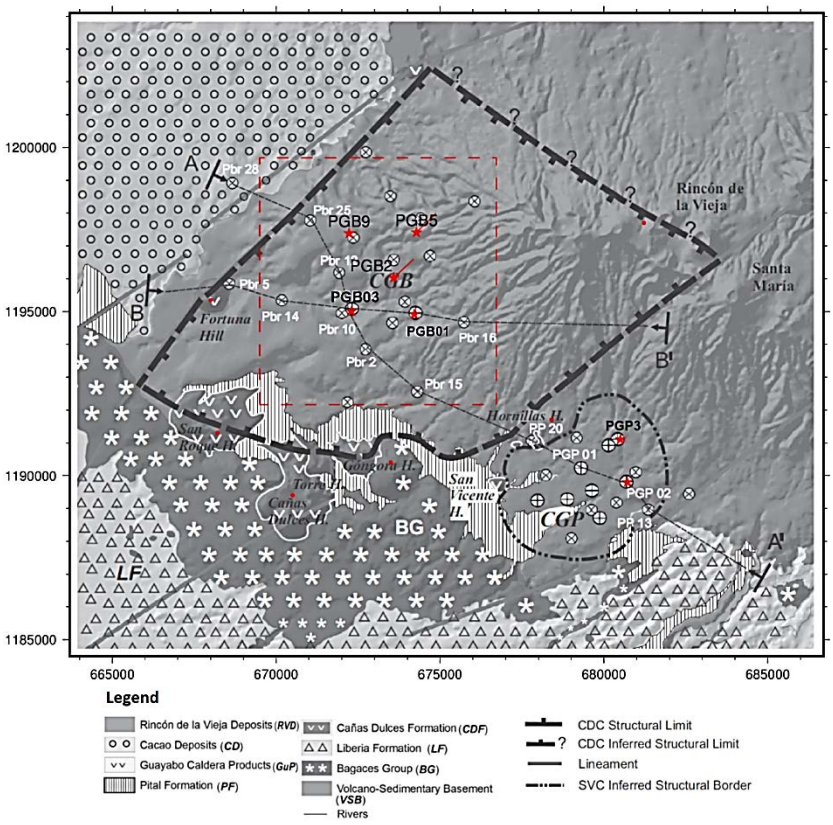

FIGURE 21: Geological map of the study area showing the location of Borinquen Geothermal Field (red dashed square), deep wells (red stars) and inferred Cañas Dulces (CDC) and San Vicente (SVC) caldera boundaries (black dashed line) (modified from Molina et al., 2014). Coordinates in UTM-Z16 (WGS84)

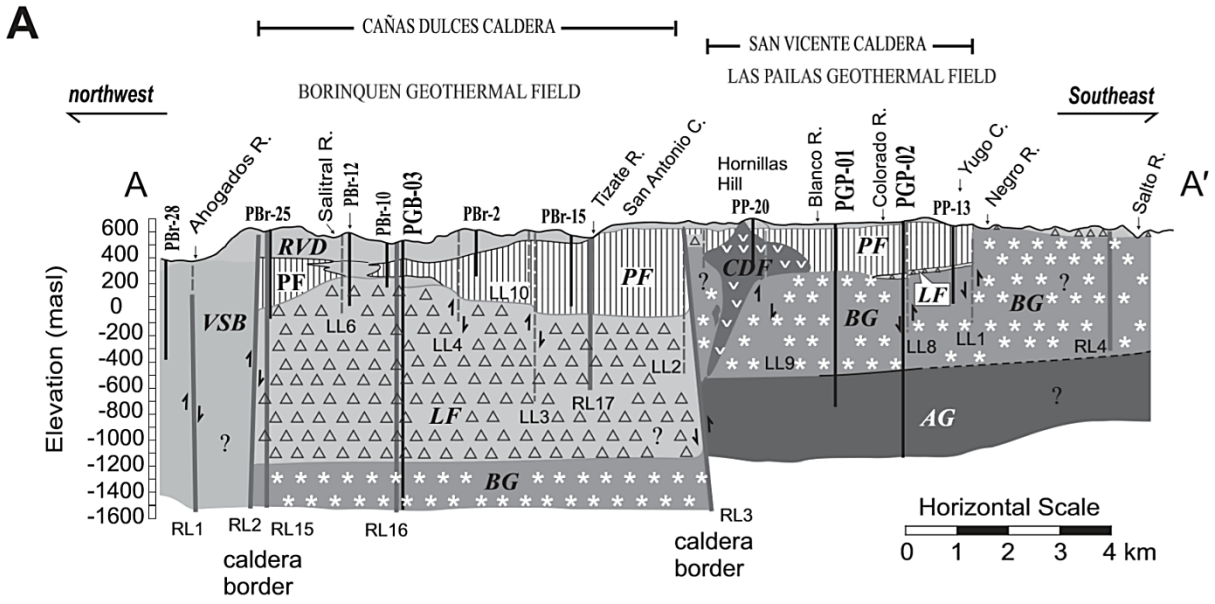

FIGURE 22: Geological cross section (A-A') of the Borinquen and Las Pailas Geothermal areas (from Molina et al., 2014) (Refers to Figure 21 for legend)

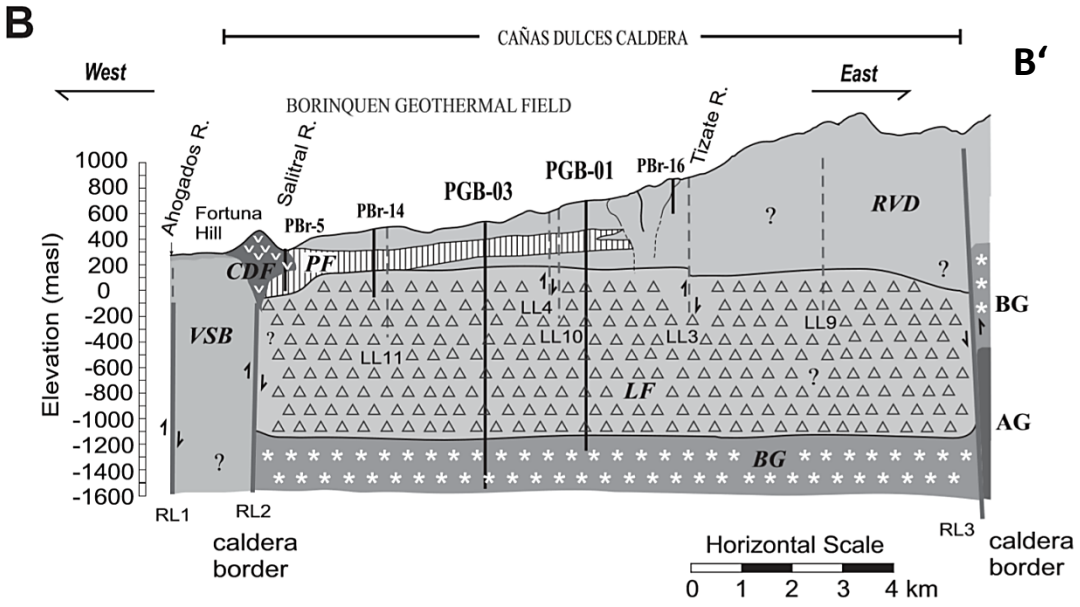

FIGURE 23: Geological cross section (B-B') for the Borinquen and Las Pailas Geothermal areas (from Molina et al., 2014). (Refers to Figure 21 for legend)

The north and northeast boundaries for the Cañas Dulces Caldera are still unknown in these previous works. This is mainly because those boundaries are buried below post-caldera deposits and there is no clear morphological or structural expression on the surface.

4.4 Main geological structures and geothermal manifestations in the study area

The main geological structures and geothermal manifestations are presented in Figure 24 as a result of analysing and combining well logs, geological and remote sensing data (adopted from Molina et al., 2014). They also used results from structural data published in previous studies (Denyer and Alvarado, 2007; Denyer et al., 2009) to compare with the thermal and gravity anomalies to define the geological structures presented below. The north-east boundary of the proposed Cañas Dulces Caldera has question marks due to that it has not been identified. The other caldera boundaries are adopted from Molina et al. (2014) and represented by the thick dark grey dashed lines and the proposed San Vicente Caldera structure (Molina, 2000) is represented by the black dashed semi-circular shape to the southeast.

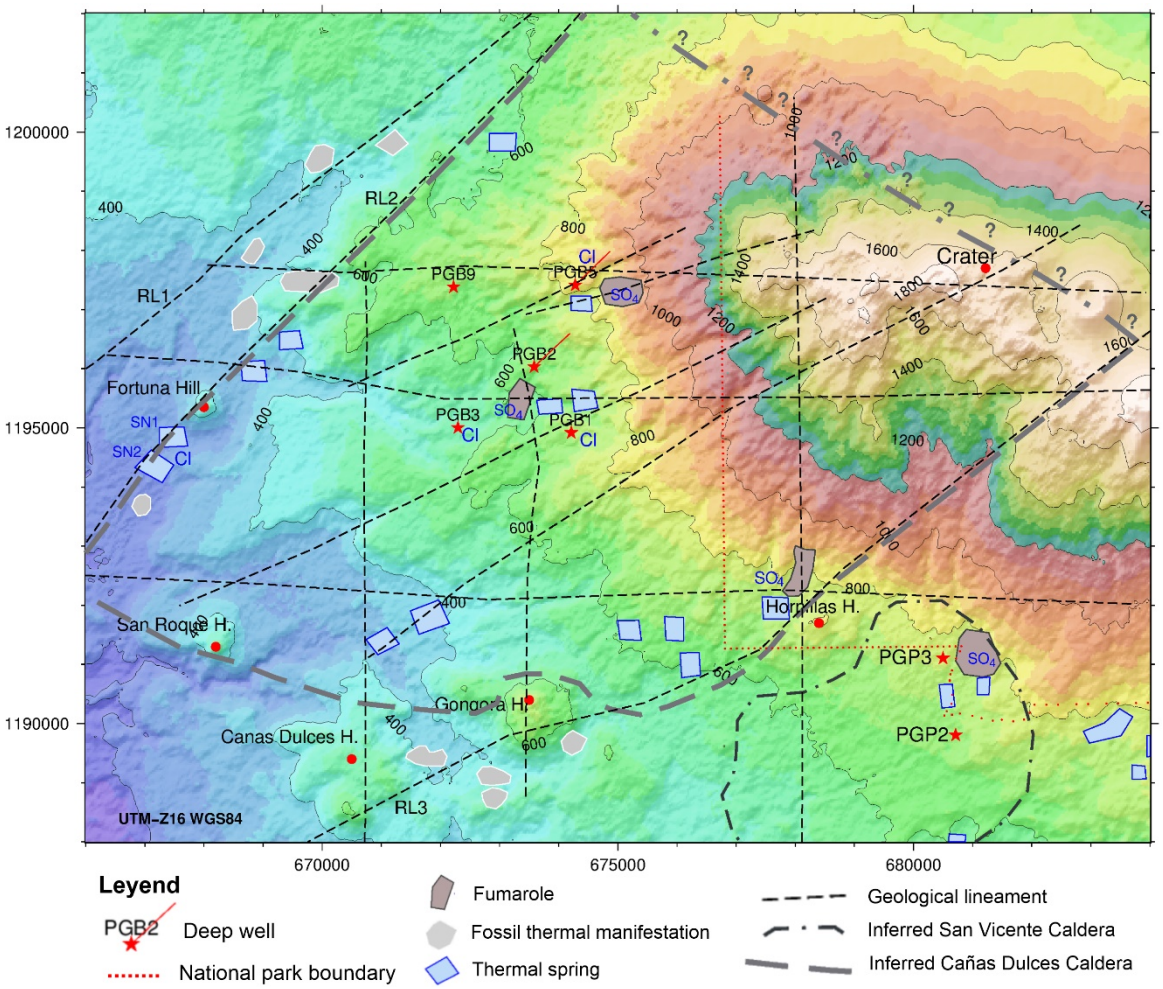

FIGURE 24: Main geological lineaments, geothermal manifestations (modified from Molina et al., 2014) and topography in the background. Deep wells (red star) with a red line represent directional wells azimuth. SO_4 and Cl waters are with blue labels. Landmarks in red dots. Coordinates are in UTM-z16

4.5 Other geoscientific data

4.5.1 Resistivity surveys

Resistivity data from Las Pailas and Borinquen Geothermal Areas were collected using MT and TDEM. Internal reports have been done by the Department of Geophysics for specific surveys in the area but an integration with other geoscientific information including the most recent resistivity data for BGF (refers to section 5.1) was missing. West Japan Engineering Consultants, Inc (West Jec) through the collaboration of Japan International Cooperation Agency (JICA) worked on developing a conceptual model for Las Pailas and Borinquen (JICA, 2012). At that time (~2011) the EM data from BGF were about half of the current data and most MT sounding data lacked static shift correction. A 3D resistivity model was created. Three main resistivity discontinuities were proposed NR2, NR3 and NR4 shown in Figure 25. Discussion about the wells in Borinquen GF and contributions to the development of Las Pailas GF (Figure 20) are a result of that work.

4.5.2 Gravity

Gravity data were mostly collected before and around 2000. The results from the Bouguer gravity map reduced for a density of 2.3 g/cm^3 by Herrera and Lezama (2002) are used in this work to create the map shown in Figure 25. The map contains the same reference landmarks as in the previous maps as for example the deep wells in Borinquen GF and in Las Pailas GF. From these results we can see:

- ✓ A negative anomaly is dominating most of the central part in the Figure.
- ✓ A positive EW laying anomaly west of the Gongora Hill is mainly associated to the presence of the dacitic domes (Molina et al., 2014).
- ✓ The Bouguer gravity gradients are comparable to the resistivity discontinuities proposed by JICA (2012) in the NW-SE direction (Figure 25).
- ✓ A trend NNE of Fortuna Hill can be seen. It is associated with the geological lineament RL2 (Figure 20 and Figure 25). Thermal manifestations also follow this trend.
- ✓ North-east of wells PGB1, PGB5 and PGP3 there is a change from a negative to positive Bouguer anomaly. A gravity survey performed by Quesada et al. (1995) extending NNW from PGP3 (toward Hornillas Hill) also indicates a positive increase of the Bouguer anomaly which might be due to the dip of the local basement to the southwest.

Three main gravity structures are suggested by red dashed lines in Figure 25. One structure is NW-SE aligned to the gradient in the central part, one SW-NE according to the gravity gradient and with a resistivity discontinuity found in this work, and one structure surrounding the main low gravity anomaly. The last one is proposed by following the mean contour value of the Bouguer Anomaly, the results of the geoelectrical strike and the resistivity discontinuities proposed in this work, information from previous geological studies (for instance evidence to the west in geological cross sections, Figure 22 and Figure 23), connection to the geothermal manifestations and the resistivity gradient NR2.

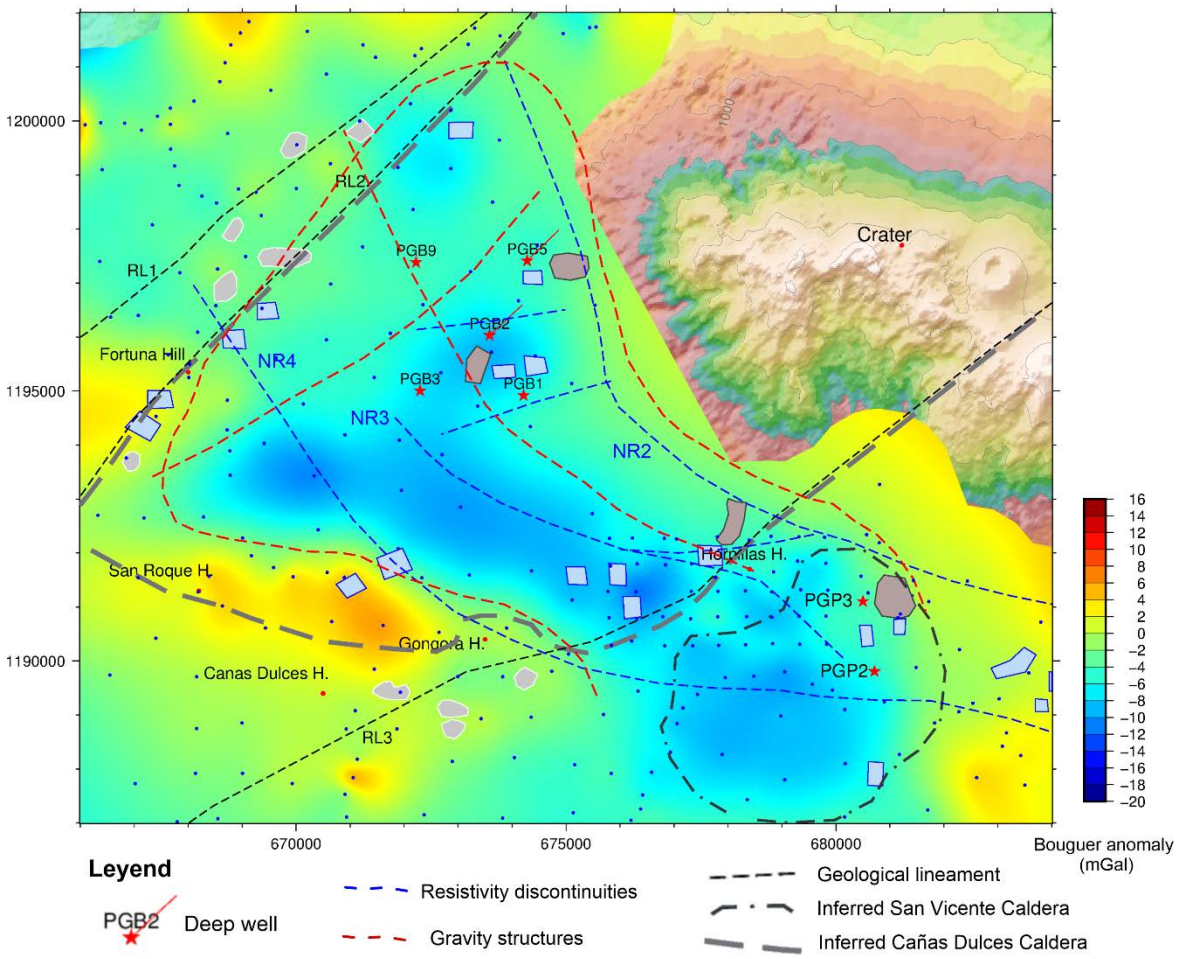

FIGURE 25: Bouguer gravity map (reduction density = 2.3 g/cm^3) showing proposed gravity structures (red dashed lines, this work), gravity stations (blue dots), geothermal wells (red stars), geological lineaments RL1, RL2, RL3 (black dashed lines), inferred caldera structures, geothermal manifestations (refers to Figure 24 for legend) and resistivity discontinuities from JICA (2012) (blue dashed lines). Coordinates are in UTM-Z16

4.5.3 Well log data

Five deep wells have been drilled in BGF (see Table 1) besides 17 shallow temperature gradient holes. Thermal gradient of the BGF area was estimated by Molina et al. (2016) after analysing the temperature profiles obtained from the gradient wells with depths ranging from 300 to 670 m. The result is shown on Figure 26. It indicates thermal gradient values varying from 6 °C/100 m (PBr-28 located in the NW part) to 56 °C/100 m (PBr-7 is located in the south part). The sector with the highest thermal gradient is located around PBr-7, where borehole PGB1 reached a maximum temperature of 277 °C at a depth of 2570 m. At this point, the thermal anomaly seems to be related to the ascending heat plume as suggested by the surface geothermal manifestations that reach boiling point (Molina et al., 2016). The thermal anomaly extends to the north and widens to embrace a larger area which is oriented E-W (TL3). According to these results PGB3 could be outside of the main thermal anomaly.

The information presented in Table 1 and other well data was obtained from Molina et al. (2016) and Molina et al. (2018). Internal reports (ICE, 2018b) from the Geology Department (CSRG) at ICE were also used.

TABLE 1: Deep wells in BGF

Well	Elevation (m a.s.l.)	Depth (m)*	Max Temperature (°C)	Technique
PGB1	699	2594	277 (at 2570 m depth*)	Vertical
PGB3	533	2082	210 (at the bottom)	Vertical
PGB2	664	2106	260 (at the bottom)	Directional, az 45°
PGB5	844	2310	250 (at 1000 m depth*)	Directional, az 45°
PGB9	658	-	On progress	Directional, az 90°

*Depth represents the true vertical depth (TVD)

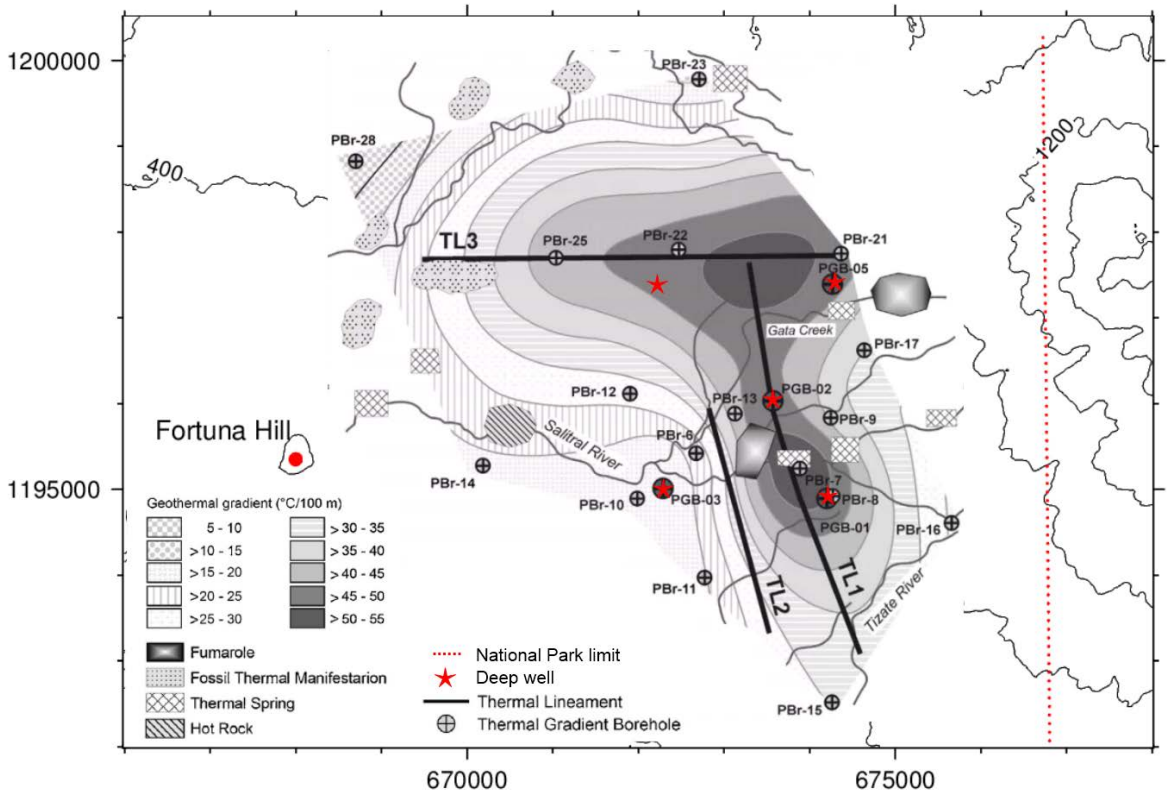

FIGURE 26: Thermal gradient in Borinquen GF (modified from Molina et al., 2016) showing the deep wells (red star), the geothermal surface manifestations and the gradient boreholes (black circle with a cross). Coordinates are in UTM-Z16

4.5.4 Geochemistry

The most important facts summarising the hydro geochemistry of the area are presented in Molina et al. (2016). SO_4, Cl and HCO_3 concentrations allowed to identify three types of water. These results are presented in Figure 24.

Sulphated waters with temperatures of 57–97 °C and pH values of 2.40–5.43 that originate from fumaroles (see SO_4 label in Figure 24) and consist of immature waters that have not had enough residence time to reach chemical equilibrium with the rock. They originate from groundwater with high oxygen content, and react with H_2S of magmatic origin, then oxidise and form SO_4. They are associated with areas of fluid rise (upflow) and do not come into direct contact with a high enthalpy geothermal reservoir.

Bicarbonate waters come from hot springs. They are slightly acidic-to-neutral (pH 5.0–7.57) with temperatures of 30.5–50 °C and originate in shallow aquifers with short residence time in the subsurface (Mg concentrations of 4.8–65 mg/L). They are heated or mixed with steam condensation and are supposedly unrelated to a geothermal reservoir.

Chloride waters (mature waters) are slightly acidic-to-neutral (pH 4.01–6.43) with temperatures of 36.6–73.0 °C. Samples from hot springs, Salitral Norte SN1 and SN2 and from the geothermal wells PGB1, PGB2, PGB3 and PGB5 were analysed (Figure 24). Their concentrations of Na, K and Mg suggest that the waters from spring SN have reached equilibrium with the rock at a temperature of nearly 235 °C. This indicates that they are related a high enthalpy reservoir. The temperatures for the samples from the deep wells were of the order of 280 °C, which is consistent with the maximum temperature measured directly in the PGB 01 (277 °C).

The Cl/B ratio suggests that waters from SN1 (97.9) and SN2 (95.5) samples and wells PGB1 (102.6), PGB2 (105.6) and PGB5 (101.9) are related but unrelated to those from PGB3 (79.6) as mentioned by Molina et al. (2016). This genetic link is confirmed by the $\delta 18O$ and δ D concentrations in samples from SN and wells PGB 01 and PGB 02 through a dilution line.

5 BORINQUEN AREA: MT AND TDEM DATA ACQUISITION AND PROCESSING

5.1 MT and TDEM surveys

The Borinquen geothermal area has been studied intermittently by ICE (*Instituto Costarricense de Electricidad*). The department of geophysics has collected MT sounding data since around the year 2000 when the company bought the first electromagnetic instruments and TDEM data since 2009 when it got the first instrument for this technique. The reason for the discontinuous exploration in Borinquen using EM methods has been the need to carry out surveys in other geothermal areas like Miravalles, Las Pailas and Pocosol but also due to all the management related to permissions for accessing specific areas including the national park. The last two campaigns in Borinquen area took place between the years 2012 to 2015. They focussed on:

- ✓ Completing areas where electromagnetic data are lacking
- ✓ Complementing MT stations that were missing AMT information
- ✓ Improving the data quality
- ✓ Collecting TDEM sounding data to correct for the static shift.

This new data package is the one used in this work together with other older EM data. The total number of stations used in this work is 97 co-located MT/TDEM soundings. The location of the sites is shown in Figure 27. All the magnetotelluric data were collected for frequencies ranging from 10400 Hz to 0.0001 Hz. The recording time for all the stations was always at least 20 hours to guarantee enough samples for the low frequencies (reflecting deep lying resistivity structures). The separation between the different sites varies from 300 m and up to 700 m, with an average of about 500 m.

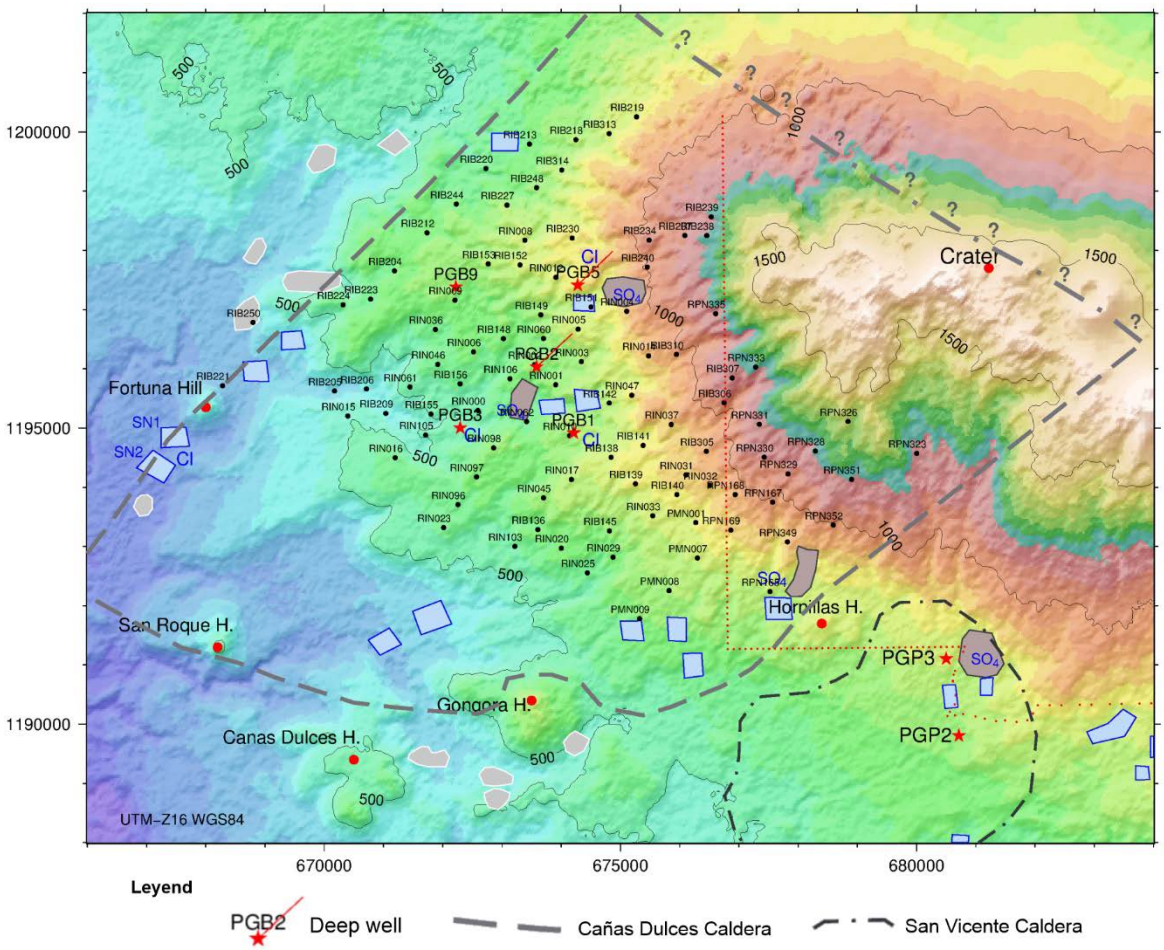

FIGURE 27: MT/TDEM stations in the prospect area (black dots), the previously inferred caldera structures, the hydrothermal manifestations (Refers to Figure 24 for legend), deep wells (red star), landmarks in red dots and national park boundary (red dotted line)

The area is characterized by rain and dry forest together with very irregular topography and mostly dense vegetation (Figure 28). Therefore, the access to the sites was very exhausting and the possibility to set up a precise grid was almost impossible. That is why the location of the soundings was not always the one planned with the field crew. Moreover, sometimes a sounding was repeated more than once due to different reasons like for instance animals biting the wires during the night causing distortion in the signals, unexpected electrical storms and battery failure.

FIGURE 28: The rough conditions in Borinquen Geothermal area

For all these field campaigns we used instruments manufactured by Phoenix Geophysics Ltd for both, MT and TDEM. The first receiver used to collect MT data was the V5 in the year 2000. By 2008, ICE got two MTU-5A units to replace the V5. The most recent A/MT data which were collected were acquired using only MTU-5A units. For the TDEM campaigns the V8 multi-function receiver was used. All these instruments automatically record the coordinates for each sounding as they are synchronized by GPS. A Garmin 60 handheld GPS was used to confirm the coordinates.

The MT data were acquired using a typical field configuration for MT as shown in Figure 3. Five channels were recorded: two for the electric field (Ex, Ey) using dipoles measuring the electric potential through the difference between two pairs of electrodes and three for the magnetic field (Hx, Hy, Hz) consisting of three coils that act as magnetic induction sensors. For all the sites we used the same standard field set up: electrodes separated by a horizontal distance of 100 m, connected by a shielded wire and buried 30 - 40 cm, one dipole aligned to the magnetic north (N-S direction) and the other one in E-W direction. Magnetic sensors were oriented one N-S, one E-W and one vertical (Figure 3). The horizontal magnetic sensors were buried 40 cm (approx.) and the vertical was always buried at least half of its total length. The magnetic sensors are buried to avoid temperature changes affecting the electronics, distortion/damage by wild animals and the stability also reduce the noise by vibrations. The acquisition unit was grounded using one more electrode and a 12 V - 35 Ah battery supplied the power. Using a compass, we aligned the measurement axes such that the x and y directions were orthogonal to each other for both the electric dipoles and the magnetic sensors and using a level we set the x and y coils to be horizontal and vertical for z component (Figure 29). Wires for the different sensors were usually buried to reduce wind noise effects due to vibration. Interference caused by the power lines (60 Hz) was very low because this area has limited development and additionally the instruments have a notch filter to suppress this frequency.

FIGURE 29: ICE technical staff placing, aligning and levelling the magnetic coils

A five component MT station was installed as a remote reference station. It was located around 30 km away from the survey area and was used to reduce the effects of local cultural noise. This is based on the fact that the magnetic signal tends to be the same over a large area and that disturbances at the local station may not necessarily be recorded at the remote site (Gamble et al., 1979). However, the results from the remote station were too noisy and instead of improving the data they caused some disturbances. As the data were good enough (acceptable coherency) it was decided to continue without the reference station because the time was running short and more data needed to be collected.

The field set up for all the TDEM sites was the typical one shown on Figure 7. A V8 receiver, T3 transmitter, RXU-TMR controller and respective transmitter and receiver loops were used. All of them manufactured by Phoenix Geophysics. A single turn 100 m by 100 m transmitter loop was used, or two turns 50 m by 50 m in some cases when topography did not allow a large loop. Two sides for the square of the transmitter loop were aligned to the magnetic north and the other two in E-W direction. As a magnetic sensor we used a small loop of approximately 1 m diameter consisting of a 100 turns coil (effective area ~100 m^2) and three 12 V - 35 Ah batteries supplied the power, two for the current injection in the transmitter (power stage) and one for the controller and the receiver units. Data were collected for two different frequencies (30 and 5 Hz). The acquisition time was on average 10 min.

5.2 MT data processing

The earth natural electric and magnetic field components are measured by sensing the very small voltage and current signals in the subsurface (Figure 3). Data are recorded as time series for the 5 components (Figure 4). Once the recording time is finished, data are downloaded from the MT instrument and backed up into a database. The first step is to review the time series. This is done with Synchro-Time Series Viewer program provided by Phoenix Geophysics (Phoenix Geophysics, 2005). This program allows viewing the raw time-series of the five recorded channels (Figure 4), power spectra derived from the time series and coherence between pairs of orthogonal electric and magnetic components. After this, the time series are transformed from the time domain to the frequency domain using the SSMT2000 program (Phoenix Geophysics, 2005) whose interface is shown on Figure 30. In order to review or process data we need to have calibration files for the receiver and also for each coil sensor. All sensors and instruments are calibrated before the campaigns started.

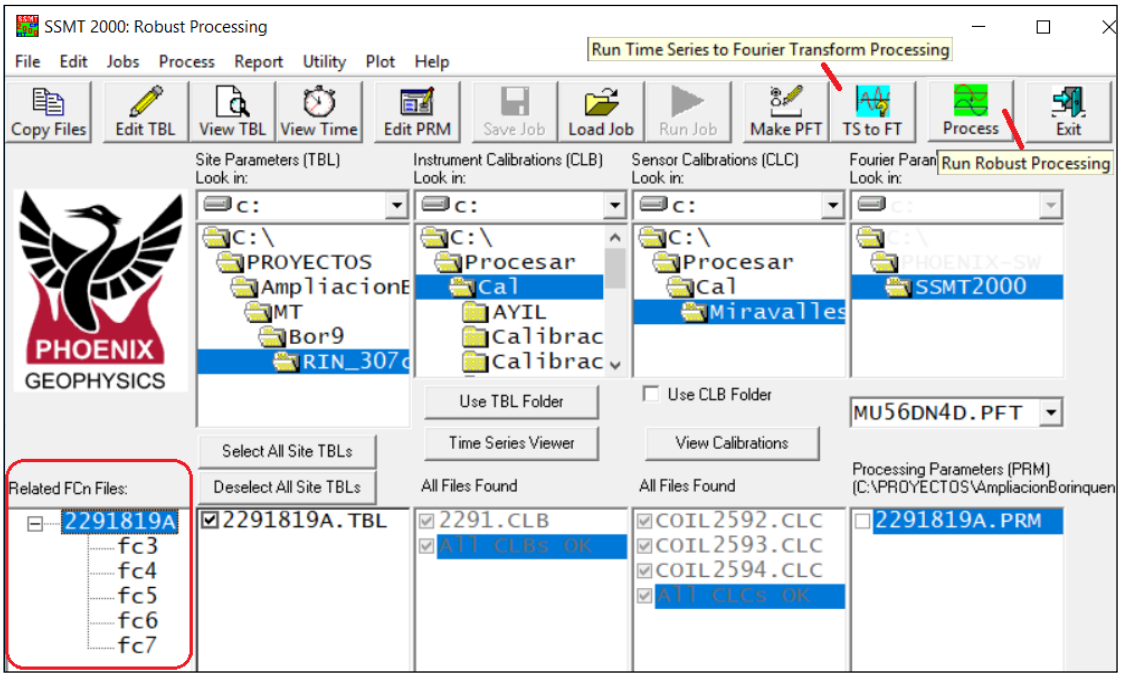

FIGURE 30: The SSMT2000 software. The main menu during the processing of MT sounding data

Once data are transformed into the frequency domain we can run the so-called robust processing or a simple cross-power processing. Robust processing is a variety of routines that can substantially reduce the effect of noise present in the data files. It calculates the impedance tensor from the natural electric and magnetic fields. Two files are created containing the cross-powers. Cross-powers are the number of equal-sized segments (maximum 100) into which the time series are divided when calculating data points for each frequency (Phoenix Geophysics, 2005). The software MTeditor from Phoenix Geophysics is the one used to edit the cross-powers. The aim is to remove outliers from both xy and yx modes, for both resistivity and phase. The last step in this processing is to export the data into the industry-standard format EDI file (Wight, 1987) that contains the necessary information which are used for geophysical interpretation/inversion software.

We calculated the rotationally invariants from the impedance tensor mentioned in equations (2.47), (2.48) and (2.49) and the content of every EDI file was plotted as presented in Figure 31 to ensure the information was in the files. On Figure 31a we have the curves for ρ_{xy}, ρ_{yx}, ρ_{det} and ρ_{ave} and on Figure 31b the phase for the same cases, respectively. A change in resistivity is directly associated with a change in phase. Figure 31c shows the plot of the impedance strike angle which is often related to the geological strike but has the 90° ambiguity (Zhang et al., 1987) and in Figure 31d we have the coherency and skew. From the skew curve (black dotted curve) we can see that the values are below 0.1 for high frequencies (shallow part) and increase below 1 Hz (deep structure) meaning that the resistivity structure is more complex at the deep part for this specific site (~3D earth) as explained in section 2.2.7. From the coherency curves we can see how data are affected by the MT dead band (frequencies ranging from 0.5 to 5 Hz; Simpson & Bahr, 2005). In BGF, the component Hz was always measured in the field meaning that we can also plot the Tipper value and Tipper strike angle which can help to solve the Zstrike angle ambiguity.

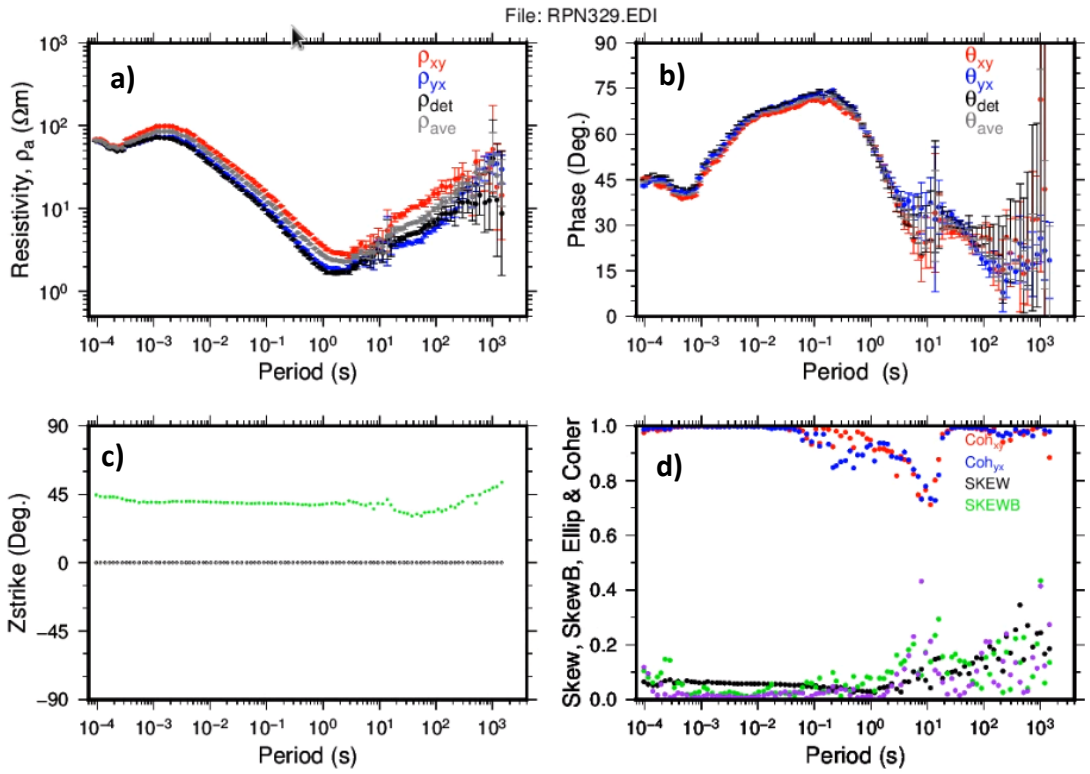

FIGURE 31: Elements of an EDI MT data file. a) Apparent resistivities and b) phases for xy and yx modes (red and blue curves) and for the rotationally invariants (ρ_{det} and ρ_{ave}, black and grey curves, top panels). In c) the Zstrike (green dotted curve) and d) skew and coherency (red and blue dotted curves)

5.3 TDEM data processing

As for the MT data, we downloaded and backed up each TDEM sounding data and stored in a database. After downloading the information, we used the windows-based program TemPro (Phoenix Geophysics, 2005) that allows one to export the raw data files into Universal Sounding Format (USF) file format (Stoyer, 2010). It is also a way to decide if the quality of the sounding data is good enough. We can also remove the outliers using TemPro but this process was done using Linux based programs. First, we need to read the usf-file using the program TemX (Árnason, 2006a) as shown in Figure 32 where the plots for the sounding can be visualized and to the right we have an example of how data look like on the terminal. After the outliers are masked (if necessary) the processed data are exported into an *inv*-file format. Before writing into the file, TemX averages groups with the same frequency but different antenna effective area and calculates apparent resistivity as Discussed by Árnason (2006a). These files are used later for the 1D joint inversion.

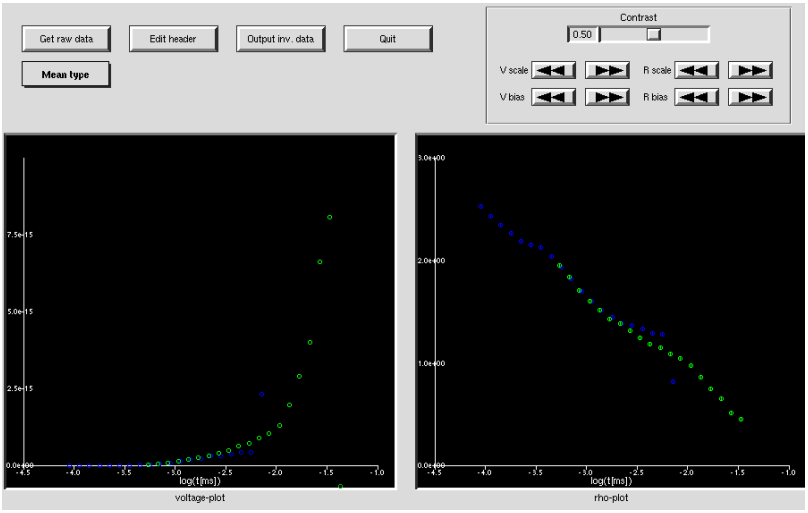


```
Set: 2 Comp:Z Stk:1 Rx:50.0 Tx:2500.0 Toff(us):400
Ch    t(ms)  V(mV/Am^2)   V*t^(5/2)  Rhoa(Ohmm)
 1   0.5365  6.9170e-09  4.6114e-17  9.0557e+01
 2   0.6754  5.7441e-09  6.8098e-17  6.9831e+01
 3   0.8503  5.0157e-09  1.0574e-16  5.2077e+01
 4   1.0704  4.0662e-09  1.5244e-16  4.0807e+01
 5   1.3476  3.1017e-09  2.0678e-16  3.3302e+01
 6   1.6966  2.3662e-09  2.8052e-16  2.7175e+01
 7   2.1358  1.5238e-09  3.2126e-16  2.4826e+01
 8   2.6888  1.1142e-09  4.1771e-16  2.0840e+01
 9   3.3850  7.8215e-10  5.2144e-16  1.7975e+01
10   4.2615  5.4281e-10  6.4352e-16  1.5623e+01
11   5.3649  3.4586e-10  7.2915e-16  1.4375e+01
12   6.7541  2.4257e-10  9.0940e-16  1.2406e+01
13   8.5029  1.5716e-10  1.0477e-15  1.1289e+01
14  10.7045  1.1232e-10  1.3316e-15  9.6212e+00
15  13.4761  9.4868e-11  2.0000e-15  7.3359e+00
16  16.9655  7.7698e-11  2.9129e-15  5.7094e+00
17  21.3582  6.0550e-11  4.0367e-15  4.5933e+00
18  26.8884  5.6152e-11  6.6570e-15  3.2907e+00
19  33.8505  3.8379e-11  8.0911e-15  2.8894e+00
20  42.6153 -7.8828e-12 -2.9553e-15  1.0000e-20

Finshed reading raw data form file: RPN323.usf
```

FIGURE 32: Graphical display of TDEM data in TemX. The left panel displays normalised voltages multiplied by $t^{5/2}$ against log-time. The central panel displays apparent resistivity against log time. The panel to the right shows an example of raw data

The example on Figure 32 is Phoenix V8 data recorded with a ~100 m^2 receiver coil on high frequency (30 Hz, blue data points) and low frequency (5 Hz, green data points).

6 INTERPRETATION OF EM DATA

In this chapter the geoelectrical strike analysis of MT data is performed. Thereafter, the code and processes for the 1D joint inversion of TDEM and MT data are explained. The respective results from the static shift correction, resistivity cross sections and depth slices are presented. Then, the code for the 3D inversion of MT data and the processes involved in order to execute the inversion are also explained. We compare the results for the different initial models by using resistivity slices. Lastly, we present the 3D resistivity inversion results through resistivity cross sections and depth slices for one of the three initial models.

6.1 Geoelectrical strike analysis

Geoelectrical strike analysis of MT data can indicate the directions of resistivity contrasts that could be used to infer geological features that are not necessarily seen on the surface. In a geothermal environment it could be associated with geothermal fluid paths. As mentioned in section 2.2.5 the Zstrike suffers from the 90° ambiguity and the strike direction can't be uniquely determined using MT impedance strike data alone. This can be solved by using information from the Tipper vector if the vertical magnetic field (Hz) was measured. As discussed in in section 2.2.6 the Tipper is a parameter that relates the vertical component of the magnetic field to its horizontal components as shown in equation (2.53).

For a homogeneous medium, the Tipper function is zero due to no induced vertical magnetic field, H_z. On the other hand, there is an induced vertical magnetic field (H_z) when we are close to a vertical boundary between low and high conductivity structures. For a 2D earth, the coordinate system can be rotated so that the x-axis is in the strike direction, when $\mathcal{T}_{zx} = 0$ and $\mathcal{T}_{zy} \neq 0$. We can do this by minimizing$|\mathcal{T}_{zx}|$.

Strike analysis was performed to get information about the Tipper strike, impedance strike and Induction arrows. Maps for Tstrike and Zstrike were created for frequency ranges based on a logarithm distribution. Induction arrows were generated using the central frequency of those decades. The analysis was done for three different frequencies corresponding to three different depths: shallow, intermediate and great depths. The estimation of the approximated depth was done by using the skin depth formula (equation (2.22)). For shallow depth calculation we used an average resistivity of ~50 Ωm and 0.1 s giving a maximum of ~1 km. For intermediate depths, we used ~1 Ωm and 10 s which gives ~>1 km and for great depths ~1 Ωm and 100 s, giving a minimum depth of ~5 km.

6.1.1 Tipper strike

The Tipper strike (Tstrike) for high frequencies (0.01-0.1 s, shallow depth < 1 km) and for intermediate/low frequencies (10 to 100 s, intermediate/great depth > 1 km) are shown on Figure 33 and Figure 34, respectively. The white dashed lines represent the interpretation for the preferential directions. For high frequency, a NW-SE trend is seen east of PGB5, northeast of PGB1 and to the south and east of the area. A N-S trend next to PBG2 and east of PBG1; a NE-SW trend for the soundings north and northwest of the area (north and northwest of PGB9, for instance); and a E-W trend in the central part as pointed by the white dashed lines in Figure 33.

For the low frequency (Figure 34) the Tstrike shows similar results as for the high frequency. Some of the interpreted preferential directions from the Zstrike map (Figure 35) are placed here as they were created for the same frequency range and also because the Zstrike was constrained by the suggestion of the main Tipper strike and by geological strike suggested in previous geological works.

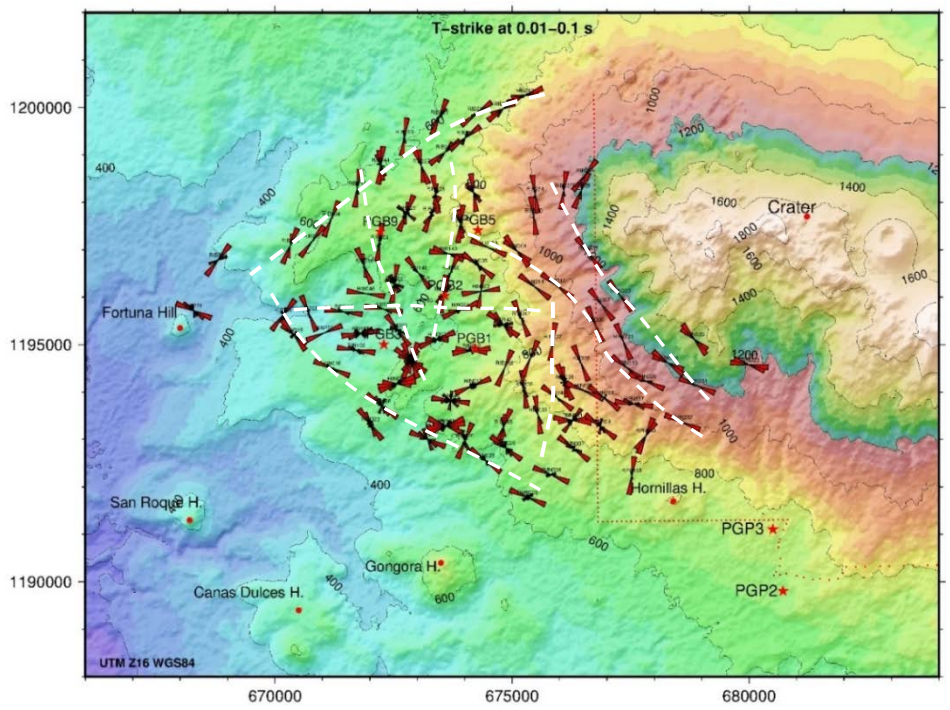

FIGURE 33: Tipper strike for 0.01 to 0.1 s showing the preferential electrical strike direction for high frequencies (100-10 Hz). White dashed lines represent the interpreted preferential directions, deep wells (red star) and landmarks (red dots)

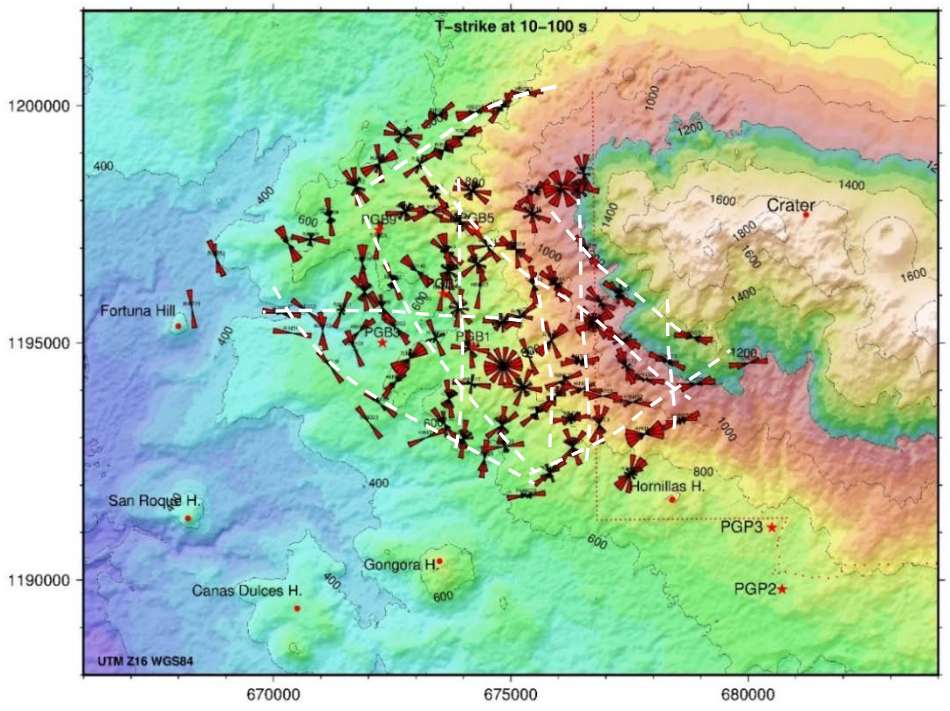

FIGURE 34: Tipper strike for 10 to 100 s showing the preferential electrical strike direction for low frequencies (0.1-0.01 Hz). White dashed lines represent the interpreted preferential directions together with the Zstrike from Figure 35. Deep wells (red star) and landmarks (red dots)

6.1.2 Impedance strike

On Figure 35 and Figure 36 results of the impedance strike for intermediate (> 1 km) and great depth (> 5 km) are shown, respectively. The map for the intermediate part (10 - 100 s) presents NW-SE trends and also N-S indications. These results show more variability for the intermediate part (Figure 35) than at great depth represented by periods from 100 to 10,000 s (Figure 36) where the main trend is clearly NW-SE. This could reflect that the Earth is more ~2D for the deeper part in this area.

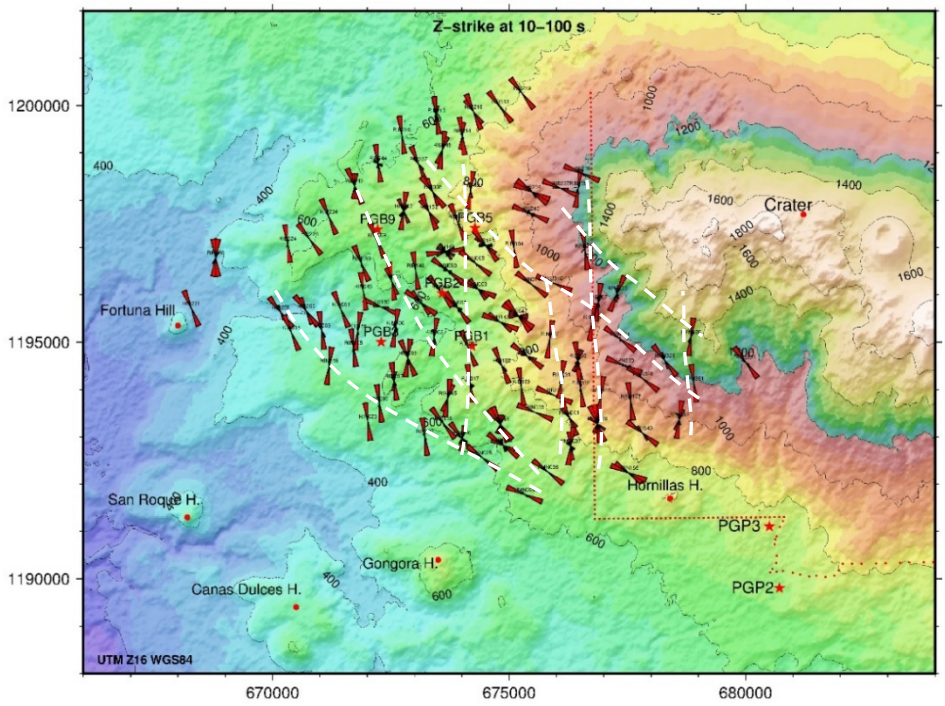

FIGURE 35: Impedance strike (Zstrike) for 10 to 100 s. White dashed lines represent the preferential directions combined with the Tstrike from Figure 34, deep wells (red star), landmarks (red dots) and national park boundary (red dotted line)

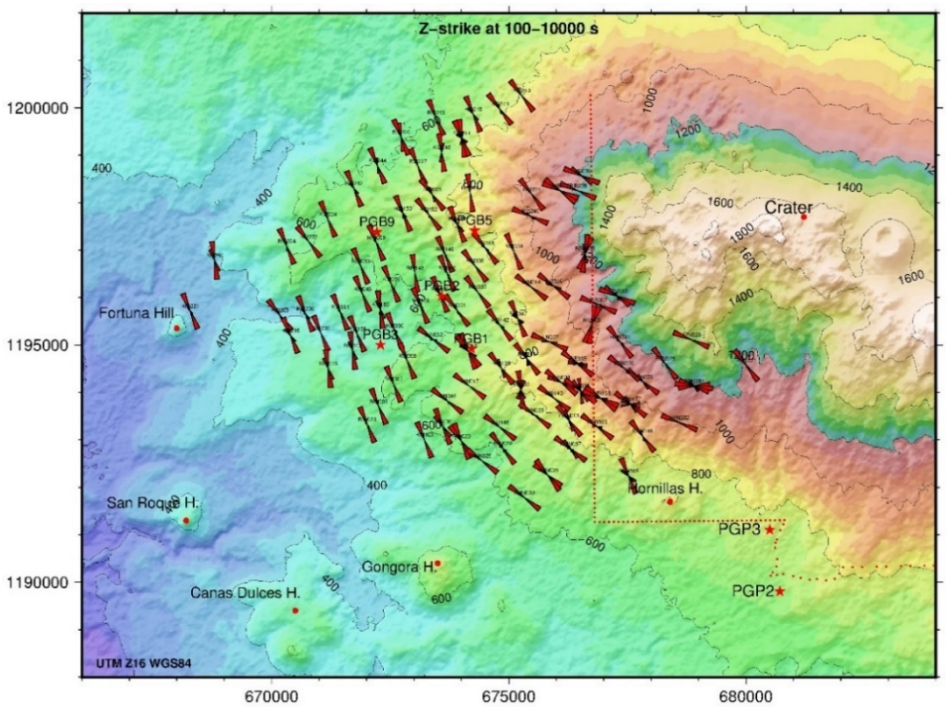

FIGURE 36: Impedance strike (Zstrike) for 100 to 10000 s, deep wells (red star), landmarks (red dots) and national park boundary (red dotted line)

The results from the Tipper strike and Zstrike suggest a regional trend mainly NW-SE that is associated to strike slip faulting systems occurring NW-SE as suggested by DeMets (2001), Barahora et al. (2002), Climent et al. (2014) and JICA (2012) to be mostly right lateral motion. Arias (2002) proposed a large strike slip fault NW-SE connecting BGF and PGF but left lateral motion. Denyer et al. (2009) proposed a fault called Rincon de la Vieja, northeast from the study area with an extension of ~25 km also presenting a possible right lateral strike slip aligned NW-SE. This regional strike is ~parallel to the Middle American Trench and it is suggested in this work to be controlling at a great extend the geothermal activity in approximately a NW-SE preferential orientation, as pointed out by Zstrike at great depths (Figure 36). The presence of N-S faults/fractures as a result of this dextral strike slip motion is also expected in the area as presented in Bakkar (2017), where a recompilation of the main faults and lineaments shows that NW-SE is an important geological strike, also the existence of N-S, E-W and NE-SW faults and lineaments.

6.1.3 Induction arrows

Inductions arrows are another representation of the complex vector, *Tipper* (see section 2.2.6). One for the real part and one for the imaginary. The magnitude of induction arrows depends on both the proximity to the conductor and the conductivity contrast. The bigger the contrast is the longer are the arrows and the closer the conductor is the longer are the arrows. Generally, the real part is more sensitive to broad resistivity contrasts. For 2D Earth the direction of the induction arrow is perpendicular to the true orientation of the regional strike whereas for 3D Earth the direction varies.

In the next two maps we present the induction arrows pointing toward the conductor (Parkinson convention). They were created for the periods of 0.02 s and 200 s to represent information at shallow (~ < 1 km) and great depths (~ > 5 km).

On the map in FIGURE 37 the induction arrows to the northeast point toward the volcano edifice. This is an important indication of a transition to a conductive anomaly (Parkinson, 1959) that could

be associated to magmatic bodies underneath in route to the actual crater. This anomaly is associated with activity at less than ~1 km depth according to the skin depth. On the map in Figure 38 for great depths there are no clear trends but there is a convergence NW from Las Hornillas Hill also present in the HF map. It is consistent with the location of conductive anomalies shown in FIGURE 52.

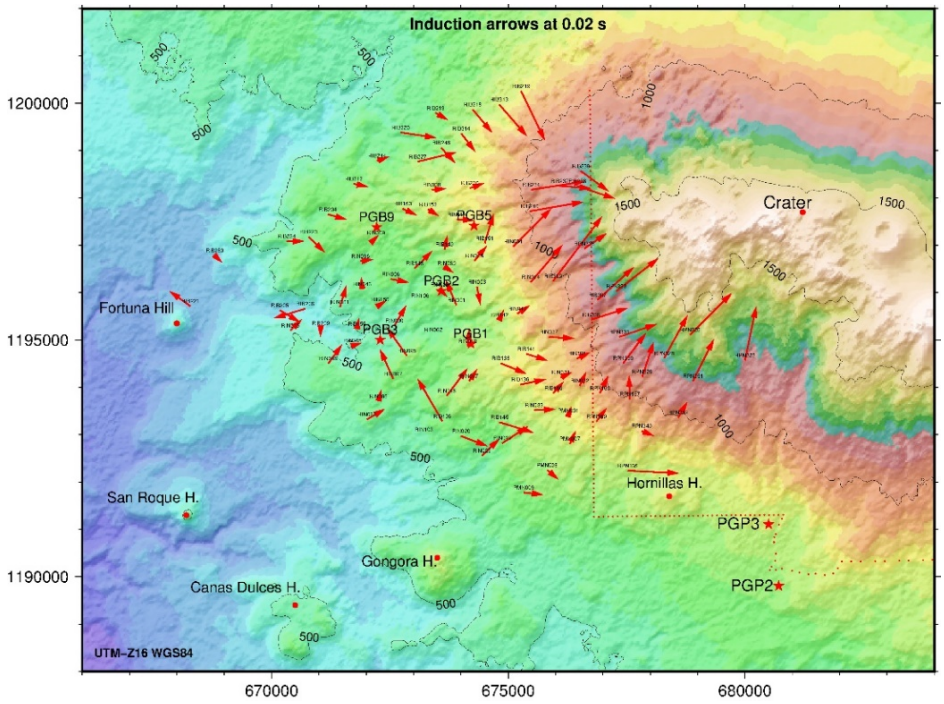

FIGURE 37: Real part of induction arrows for the 0.02 s pointing to the conductor (Parkinson convention). Deep wells (red star), landmarks (red dots) and national park boundary (red dotted line)

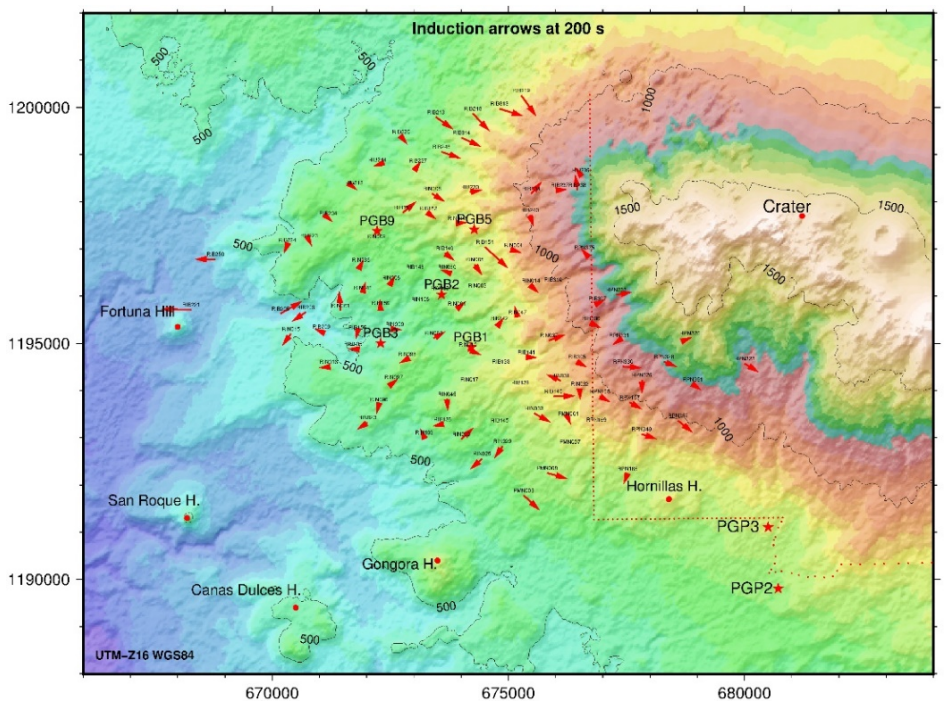

FIGURE 38: Real part of induction arrows for the 200 s pointing to the conductor (Parkinson convention). Deep wells (red star), landmarks (red dots) and national park boundary (red dotted line)

6.2 1D joint inversion of MT and TDEM data

6.2.1 1D joint inversion code

The apparent resistivity and phase from MT sounding data are inverted in order to obtain a resistivity model of the subsurface.

The code used here to perform 1D inversion of the resistivity data is called TEMTD. It is a Linux based code written by Knútur Árnason, geophysicist at Iceland GeoSurvey (Árnason, 2006b). The program performs 1D inversion using horizontally layered earth models. It is done independently for each site. The TDEM program assumes that the source loop is a square loop and that the receiver coil/loop is at the centre of the source loop. The wave form of the electrical current is half-duty bipolar semi-square wave (equal current-on and current-off segments), with exponential current turn-on and linear current turn-off (Árnason, 2006b).

The inversion algorithm used in the code is the non-linear least-square inversion of the Levenberg-Marquardt type (Levenberg, 1944; Marquardt, 1963). The misfit function is the mean-square difference between measured and calculated resistivity data ($\chi 2$), weighted by the standard deviation of the measured values.

The actual function that is minimised is in this case not just the weighted root-mean-square misfit, χ^2, but the "potential":

$$\mathrm{Pot} = \chi^2 + \alpha \cdot \mathrm{DS1} + \beta \cdot \mathrm{DS2} + \gamma \cdot \mathrm{DD1} + \delta \cdot \mathrm{DD2} \tag{6.68}$$

where DS1 and DS2 are the first and second order derivatives of log-conductivities in the layered model

DD1 and DD2 are the first and second order derivatives of the logarithms of the ratios of layer depths.

$\alpha, \beta, \gamma, \delta$ are the relative contributions of the different damping terms and are specified by the user

The program can do inversion of TDEM data, for either voltage (default) or apparent resistivity; inversion of MT data, either phase or apparent resistivity or both; and joint inversion of MT and TDEM data.

6.2.2 1D joint inversion process

The software TEMTD performs the 1D joint inversion of TDEM and MT data by using the *inv* and EDI files as an input. Therefore, it is required to check the EDI files to be sure that they contain all the information needed to carry out the inversion, as for instance the rotationally invariants from the impedance tensor. In this work we use the determinant rotationally invariant of which is based on the four elements of the impedance tensor **Z** (see equation (2.49)).

In the 1D joint inversion, the TDEM soundings are used to correct for the static shift of the MT data. The program was used to perform minimum structure (Occam's) inversion of apparent resistivity and phase for each MT and associated TDEM sounding. In this case, the layer thicknesses are kept fixed, equally spaced on log scale, and the conductivity distribution is forced to be smooth in the minimised "potential" function (Árnason, 2006b). In Figure 39 the MT resistivity data (blue squares curve) is tied to the TDEM resistivity data (red diamonds curve) and the best fitting model for both is generated resulting in a resistivity model (green curve to the right) of the data, the misfit is given below the sounding name, and the static shift factor to the right (left panel).

The 1D joint inversion models for all the TDEM and MT data are given in Appendix A.

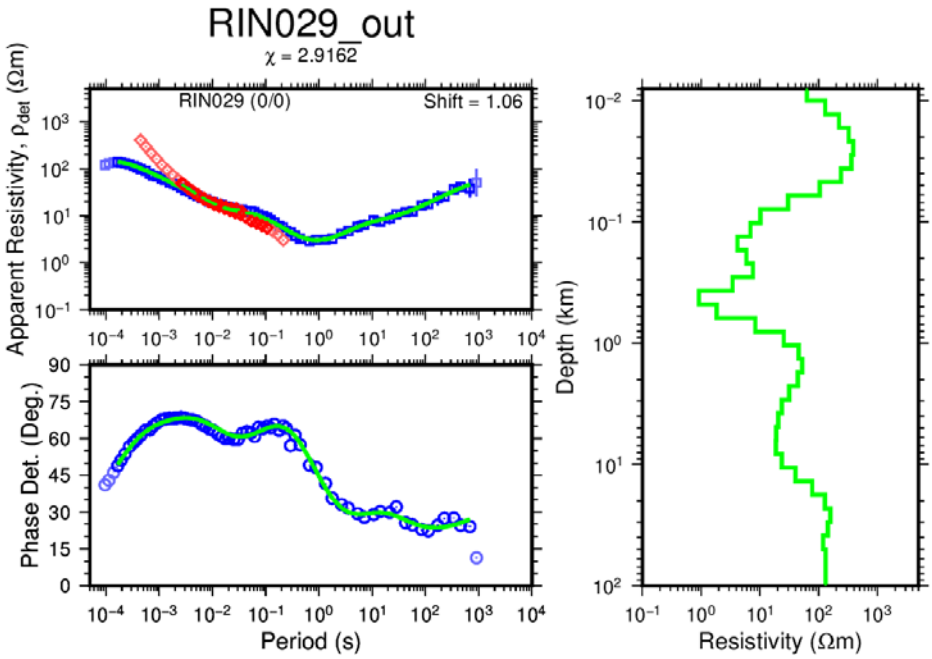

FIGURE 39: Result of 1D joint inversion of TDEM and MT data showing the TDEM apparent resistivities transformed to a pseudo-MT curve (red diamonds) as described by Sternberg et al. (1988), measured apparent resistivity (blue squares) and phase (blue circles) derived from the determinant of MT impedance tensor, and Occam inversion resistivity model (green curve, right panel)

6.2.3 MT static shift correction

In this work, static shift correction has been made for all MT sounding data through joint inversion with TDEM data to provide a more accurate picture of the Earth's resistivity structure as pointed out by Sternberg et al. (1988). It clearly reduces the bias in the inversion models as explained in Árnason (2015).

The results from the static shift correction for the MT sounding data range from ~0,2 to 5,4. The representation of the static shift correction multiplier in Figure 40 shows a normal distribution centred in one meaning that ~14% of MT soundings were not or were slightly affected by static distortions. Moreover, ~31% were shifted up and ~55% were shifted down. The static shift ranges from ~0,2 to ~5, which means that without correction, the interpretation would give in these extreme cases up to five times too low or too high resistivity values and about two times too shallow or too great depths to a resistivity contrast.

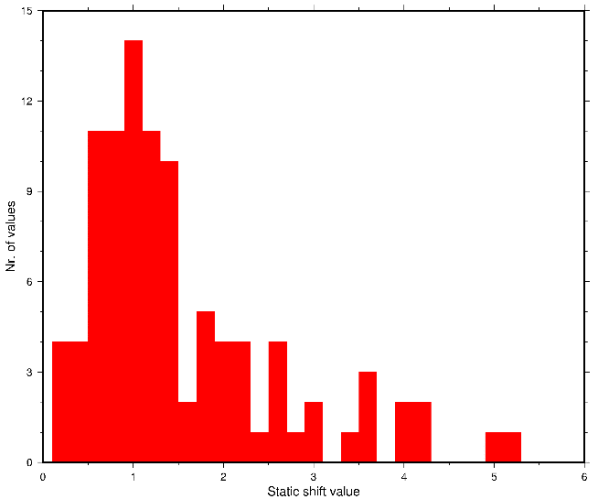

FIGURE 40: Histogram of the static shift for Borinquen Geothermal area

Figure 41 shows the spatial distribution of the static shift correction multiplier in Borinquen Geothermal area. It reflects the irregular distribution of the static shift probably associated with the very rough topography where 86% of the sites required static shift correction.

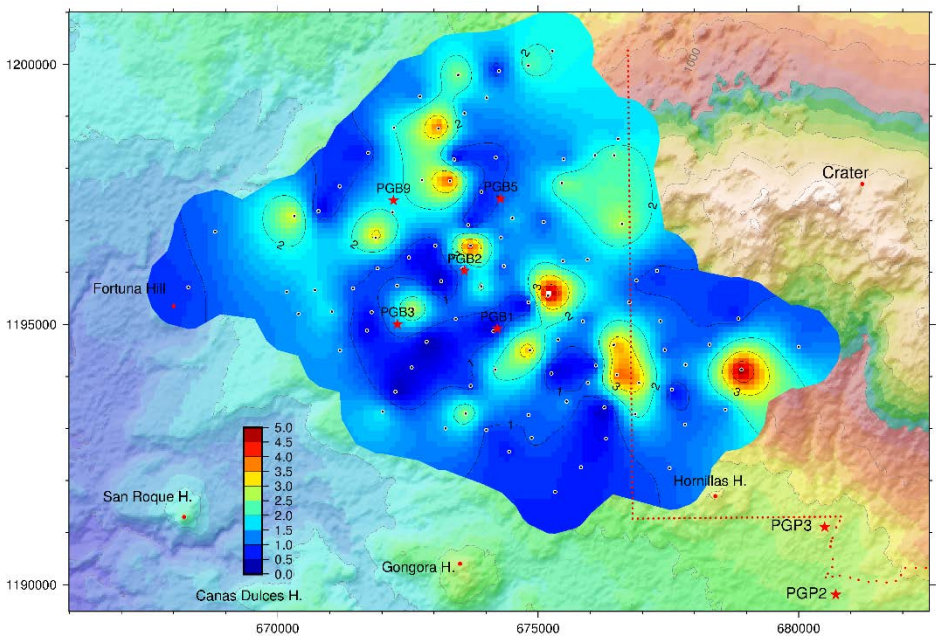

FIGURE 41: Spatial distribution of the static shift multiplier in BGF. MT sites are shown in small black dots. The correction factor scale is located in the left-down corner, deep wells (red star), landmarks (red dots) and national park boundary (red dotted line). (UTM-Z16, m)

6.3 Results of 1D joint inversion

From the 1D resistivity models, cross sections and depth slices down to 3000 m b.s.l. were created to image the distribution of the most important geothermal signatures of the reservoir associated with the conductive layer, transition zone and the resistive core. The orientation of the cross sections was decided by taking into consideration the main trend of the geological and geoelectrical strike. They were designed to pass the deep wells available to project the alteration mineralogy and compare them with the resistivity. Their location is shown on Figure 42.

The cross sections and maps were created by using the Linux based programs, TEMCROSS and TEMMAP. These codes were developed by Hjálmar Eysteinsson, geophysicist at Iceland GeoSurvey (Eysteinsson, 1998).

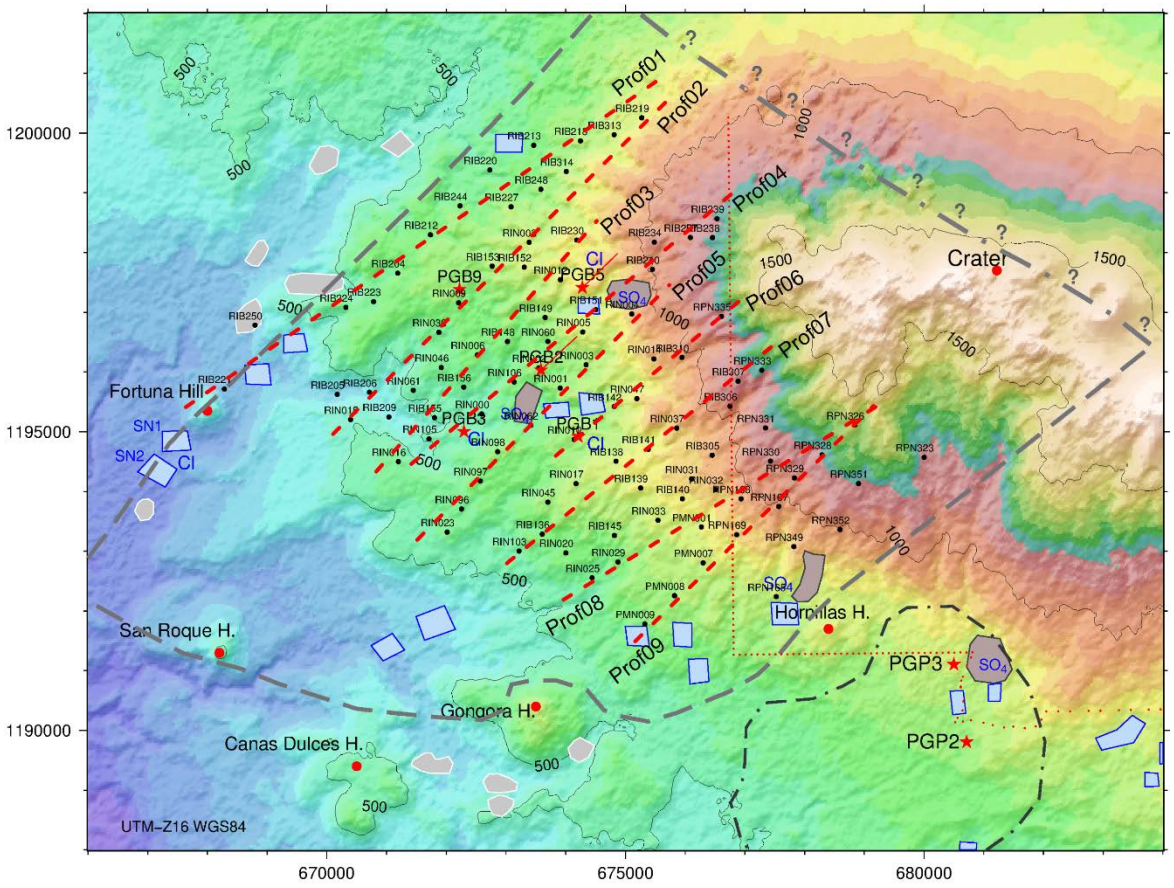

FIGURE 42: Location of the resistivity cross sections (red dashed lines). MT stations are given by black dots, inferred Caldera structures from previous studies and geothermal manifestations (Refers to Figure 24 for legend), deep wells (red star), landmarks (red dots) and national park boundary (red dotted line)

6.3.1 Resistivity cross sections

Figure 43 shows the results for profile 1 located in the northwest part of the study area. The high resistivity surface layer, reflecting un-altered rock formation, is most apparent in the central part of the profile and there it may be up to 200 m thick. Between soundings RIB250 and RIB224, the conductive anomaly (with a high content of smectite) reaches the surface, and that is reflected by the hydrothermal manifestations found in the area as shown on Figure 42. The conductive layer presents an average thickness of ~500 m that seems to be homogeneously distributed on this sector. Below, there is an increase in the resistivity associated with a change in the alteration mineralogy from smectite to a mixed layer clay zone and beneath that a high resistivity core seems to appear.

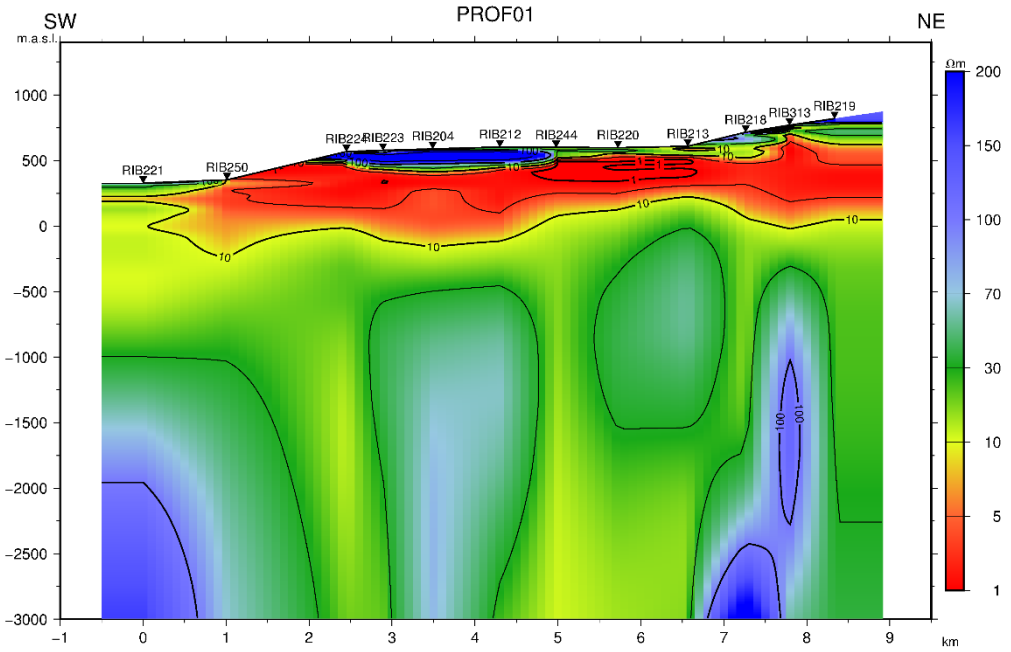

FIGURE 43: Resistivity cross section Prof01. Names of MT stations are given on top, section location is shown on Figure 42

The result for profile 4 is presented on Figure 44. The profile is located close to the central part of the study area and passes through three wells. Below sounding RIB240 and RIB237 there is an evident lateral discontinuity: the thickness of the conductive layer is decreased and presents a displacement as by faulting. The low resistivities reach the surface between sounding RIB151 and RIB240. This coincides with the hydrothermal manifestations (fumaroles) east of PGB5 (see SO_4 label in Figure 42). A high resistive core appears underneath sounding RIN005 and RIB234 below 1 km depth (approximately at 250 m b.s.l). This resistive anomaly is explained by the presence of alteration minerals like illite, chlorite and epidote, suggesting temperatures exceeding ~250 °C as explained by Árnason et al. (1986). This is confirmed by the results of PGB5, where illite/chloride are clearly the dominant alteration minerals at those depths and the measured temperature in the well at 1000 m depth (~-150 m b.s.l.) was ~260 °C. To the southwest we can see how the resistivity doesn't reach values as high as to the northeast, which explains why in well PGB3 the temperature is not as high as expected.

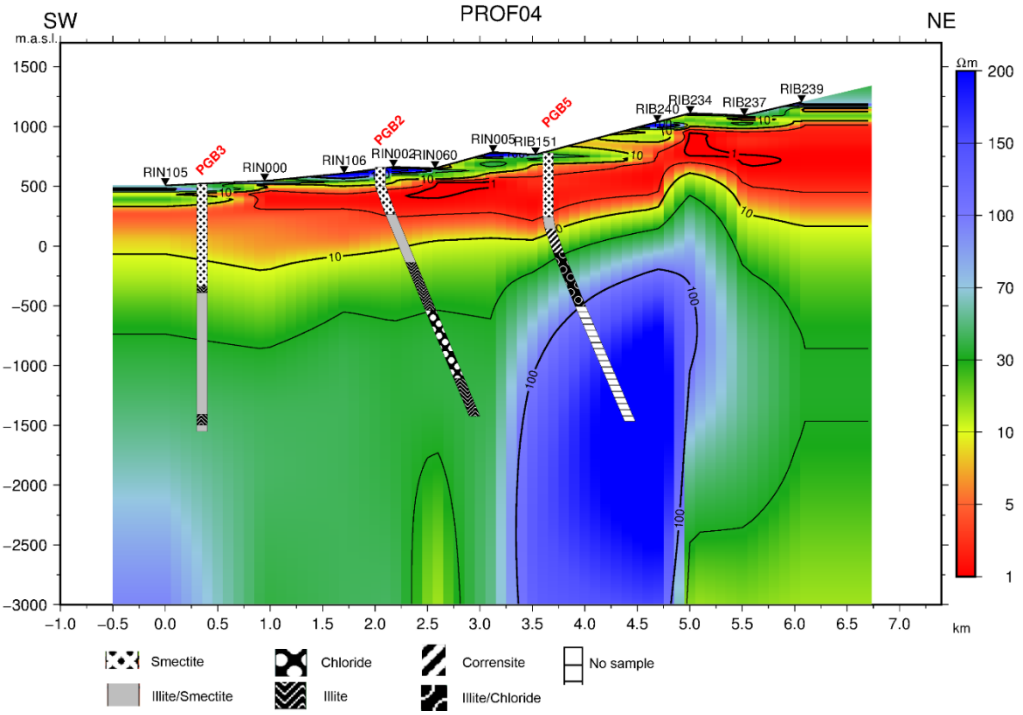

FIGURE 44: Resistivity cross section Prof04. Names of MT stations are given on top, section location is shown on Figure 42 and names of wells are in red. Alteration mineralogy from well logs (ICE, 2018b) is shown

In profile 5 (Figure 45) the resistivity distribution shows a lateral discontinuity that is evident below sounding RIN001 particularly from 500 m b.s.l to 3000 m b.s.l. It coincides with geothermal manifestations on the surface (Figure 42) and might present a connection to the up-flow zone of the geothermal system. There, we can see a decrease in the thickness of the conductive layer. Moreover, the distribution of the highest thermal anomaly and proposed thermal lineament TL1 (Figure 26) are located just at this discontinuity. When alteration mineralogy of the projected wells PGB3, PGB1 and PGB2 are compared with the resistivity, we clearly see how smectite is mostly limited to the conductive layer. Below that, illite starts to appear to create a mixed layer and an increase in resistivity is explained by a reduction of the electrical conduction in illite and chlorite alteration minerals (Weisenberger et al., 2016) found at great depths in wells PGB1 and PGB2.

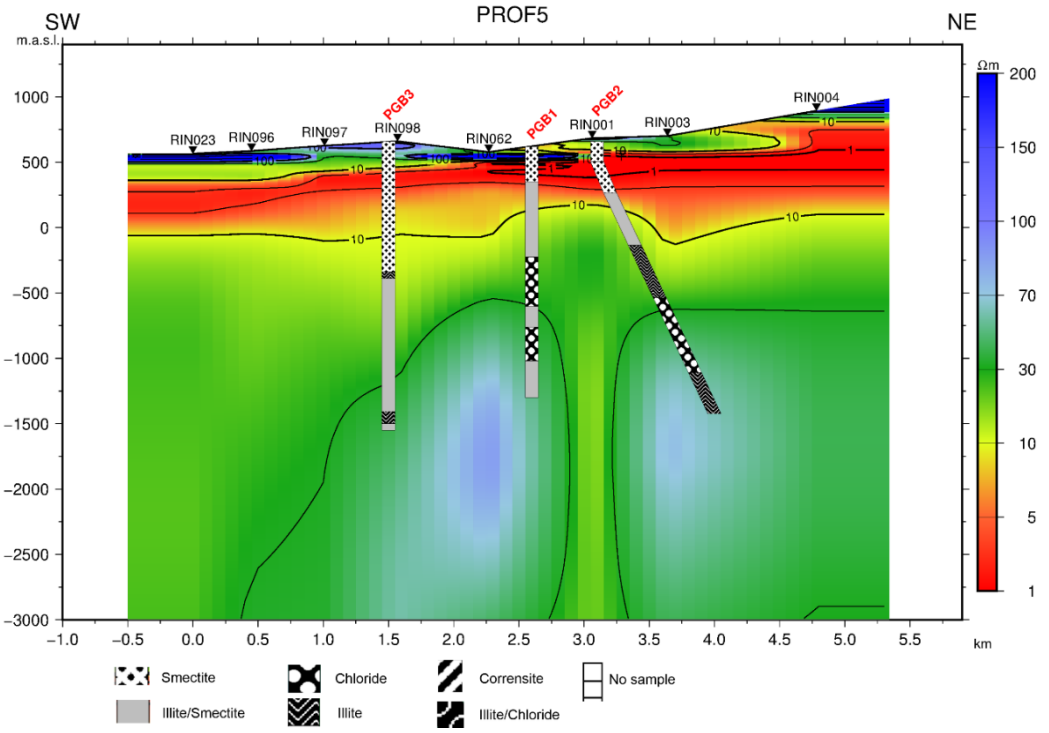

FIGURE 45: Resistivity cross section Prof05. Names of MT stations are given on top, names of wells are in red. Alteration mineralogy from well logs (ICE, 2018b) is also shown and section location is given on Figure 42

In profile 7 (Figure 46) just underneath sounding RIB138 there is a lateral resistivity discontinuity that could be related to the one mentioned before on profile 5, but also this could be an effect of distortion of the model because the anomaly is mostly represented by one sounding and the static shift in this sounding is questionable. Between sounding RIB306 and RPN333 there is a displacement in the conductive layer as by faulting that could be associated with a resistivity discontinuity aligned NW-SE. The resistive bodies located between sounding RIB141 and RPN333 and below sea level are associated to temperatures exceeding 250 °C.

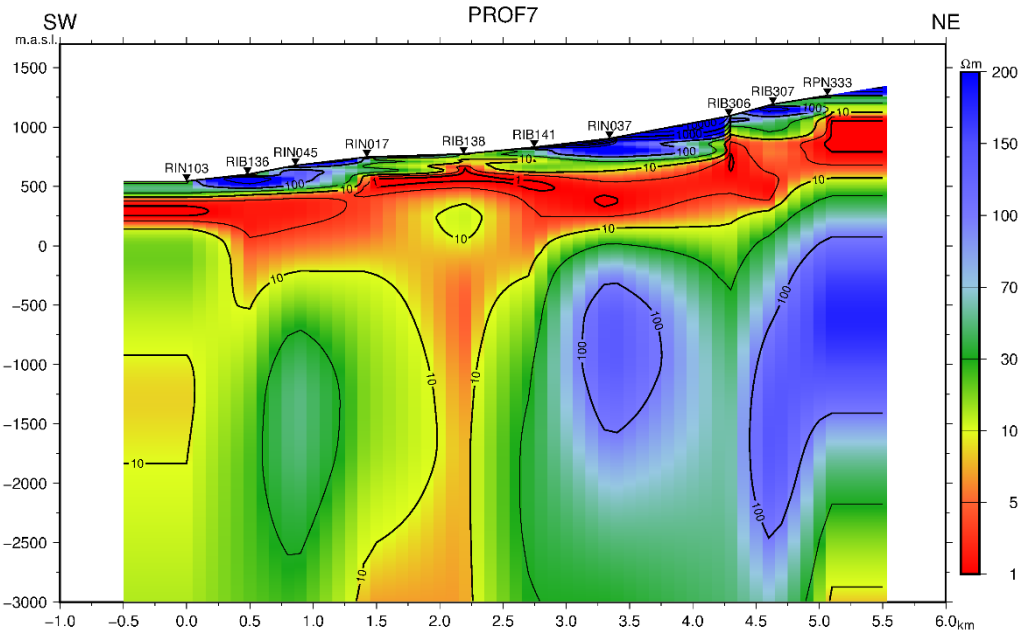

FIGURE 46: Resistivity cross section Prof07. The name of the MT stations is given on top and names of wells are in red. Section location is given on Figure 42

The resistivity profiles based on 1D joint inversion show the typical resistivity structure of a high temperature geothermal system in volcanic environment. It comprises near surface layers of unaltered rocks (high resistivity) followed by a conductive layer that presents resistivity less than 10 Ωm caused by the high content of smectite formed at temperatures of ~100 – 220 °C (Árnason et al., 1986; Flóvenz et al., 2005). Below this layer, a transition zone with resistivity values higher than 10 Ωm but less than ~70 Ωm was mapped meaning that smectite is progressively replaced by illite or illite/chlorite formed at temperatures of ~220-250 °C. This transition zone is followed mostly to the NE of the study area by a high resistivity anomaly with values higher than ~70 Ωm meaning that the dominant alteration minerals are illite and/or chloride and temperatures there could exceed ~220 - 250 °C. It happens due to the relation of the resistivity structure of high temperature geothermal areas with the alteration mineralogy (Árnason et al., 1986; Árnason et al., 2000; Hersir et al., 2009; Flóvenz et al., 2005; Flóvenz et al., 2012) and the different electrical conduction mechanisms depending on the stage and amount of the hydrothermal alteration of the rocks (Gasperikova, 2011; Revil et al., 1998; Kristinsdóttir et al., 2010; Flóvenz et al., 2005; Lévy et al., 2018).

The conductive layer, playing the role of a cap rock, presents a thickness varying between ~250 and ~800 m, with an average of ~500 m and the deepest location of the floor of this layer is at ~250 m b.s.l. It tends to disappear to the west (see Profile 01) between sounding RIB221 and RIB250 indicating the limit of the geothermal system which is also suggested by the fossil geothermal manifestations presented in Figure 24. Next to sounding RIN105 and RIB 155 (Profile 3, see Appendix 1) which is close to well PGB3, there is a change in the conductive layer meaning a possible limit of the system to the southwest and this is also reflected in the low temperature of PGB3 with respect to the other wells (see Table 1 and Figure 26).

With the results from the cross sections it is possible to support the relation between resistivity and alteration mineralogy (Árnason et al., 1986; Weisenberger, 2016; Lévy et al., 2018) by comparing the results with well data from BGF, as presented in Figure 44 and Figure 45.

6.3.2 Resistivity depth slices based on 1D inversion

The resistivity slices for the shallow part (<1 km depth) give a good indication of the distribution of the conductive layer and also suggest a NW-SE trend due to possible lateral discontinuities in NE-SW direction as we can see on the resistivity depth slice at 500 m a.s.l. (see black dashed line in Figure 47). To the NE of the dashed line the slice shows the top of the cap layer and to the SW of the dashed line the slice cuts through unaltered surface rocks. The transition from a conductive layer into a more resistive anomaly is seen in the central part of Figure 48 where resistivity higher than 10 Ωm is present.

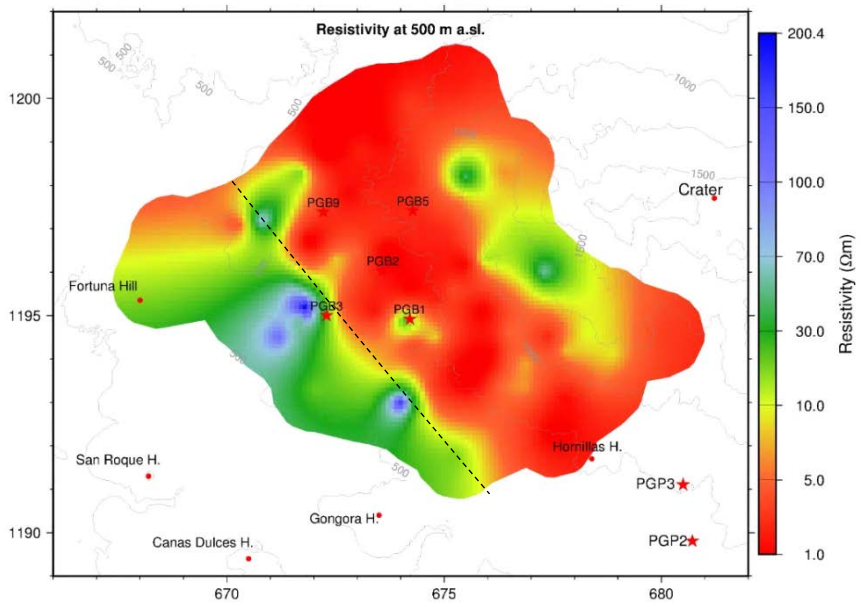

FIGURE 47: Resistivity depth slice at 500 m a.s.l. showing the conductive layer and a NW-SE trend (back dashed line) at resistivity discontinuity, wells (red star) and landmarks (red dot). The coordinates are UTM-Z16 (km)

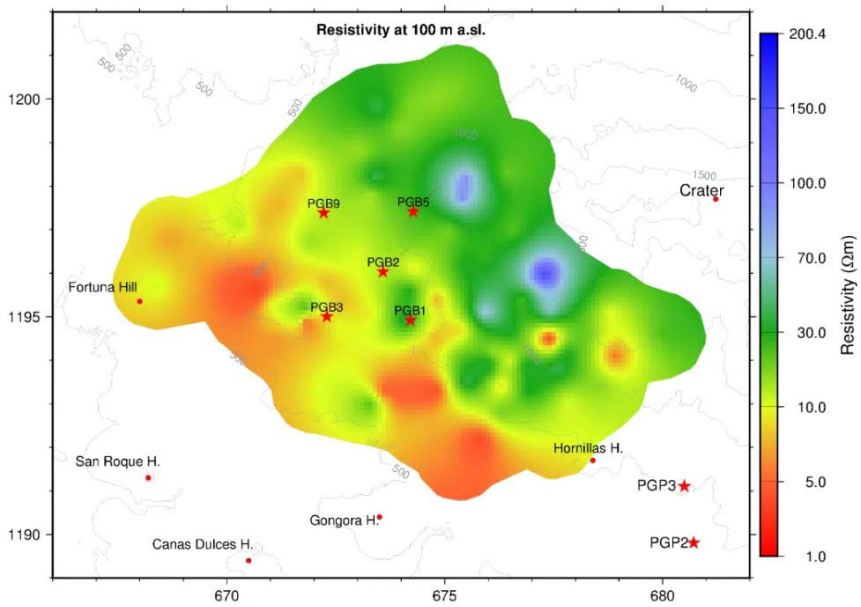

FIGURE 48: Resistivity depth slice at 100 m a.s.l. showing part of the conductive layer as it dips down to the SW and higher resistivity to the NE. Wells are given by a red star and landmarks by a red dot. The coordinates are UTM-Z16 (km)

On the map for 400 m b.s.l. (Figure 49), ENE of PBG1, NE of PGB5 (~1400 m depth at those areas) high resistive anomalies appear which are directly associated with temperatures exceeding 250 °C. At 1000 m b.s.l. (Figure 50) and further below, the resistivity starts to decrease in specific areas, for instance north of Las Hornillas Hill. Deep conductors appear ~3 km EES of PGB1 and PGB5, and NE of PGB5 at a depth of ~2000 m but these are more evident below ~3000 m depth (see Appendix B). This resistivity anomaly is presumably associated with the heat sources at depth.

A similar situation occurs northeast of Las Pailas Geothermal area, where a deep conductor was mapped at approximately the same depth ~3 to ~6 km (Badilla, 2011) suggesting the location of a possible heat source for Las Pailas GF at the proximities (north/northeast) of the inferred northern border of San Vicente Caldera (Figure 24), as proposed by JICA (2012). The different geothermal manifestations associated to up-flow areas (showing a SO_4 content) as presented in Figure 24 were also mapped next to these boundaries.

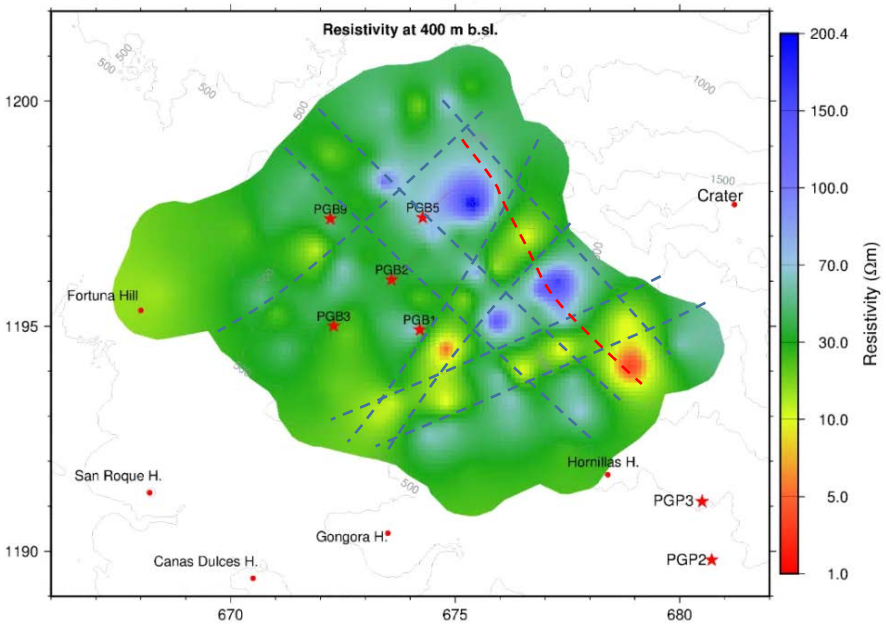

FIGURE 49: Resistivity depth slice at 400 m b.s.l. showing resistivity discontinuities (blue dashed lines) and a discontinuity from the resistivity cross sections (red dashed line). Wells are given by a red star and landmarks by a red dot. Coordinates in UTM-Z16 (km)

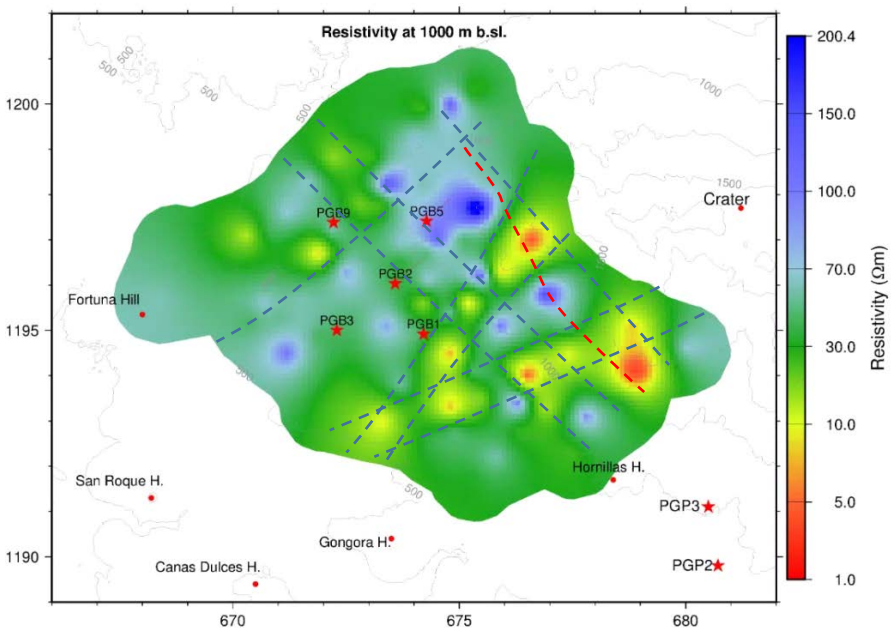

FIGURE 50: Resistivity depth slice at 1000 m b.s.l. showing suggested resistivity discontinuities (blue dashed lines) and a discontinuity from the resistivity cross sections (red dashed line). Wells are given by a red star and landmarks by a red dot. Coordinates in UTM-Z16 (km)

6.3.3 Combination of results based on 1D joint inversion

Figure 51 and Figure 52 present a comparison of the 1D inversion results with the Bouguer gravity map and suggested gravity structures (this work, red thin dashed lines), the resistivity structures proposed by JICA (2012) (blue thin dashed lines, identified as NR2, NR3, NR4), the proposed geological lineaments by Molina et al. (2014) (black thin dashed lines) and an important resistivity discontinuity (red thick dashed line, this work). The trends shown by the Tipper strike for shallow/great depth (Figure 33 and Figure 34) have important coincidence with the orientation of the resistivity and gravity discontinuities.

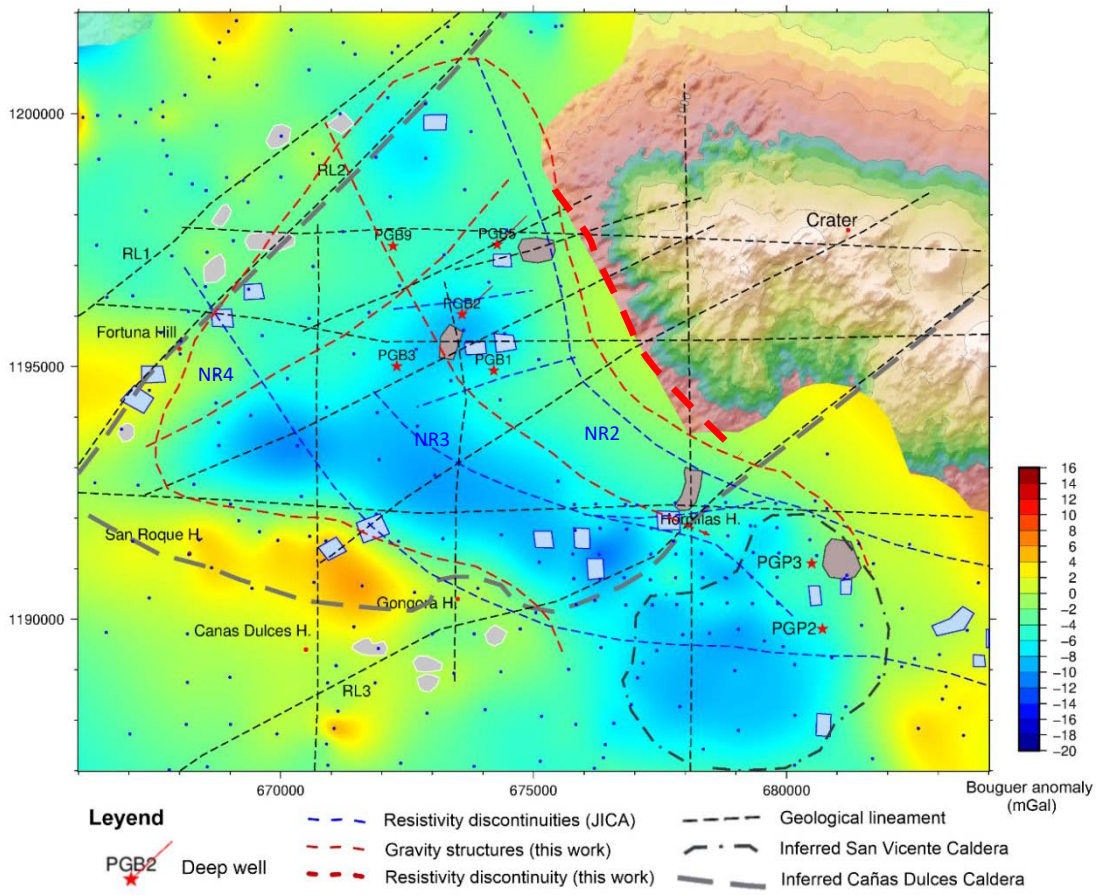

FIGURE 51: Comparison between the Bouguer gravity anomaly, the geological lineaments (black dashed lines, Molina et al. 2014), resistivity discontinuities (red thick dashed line, this work; blue thin dashed lines, JICA, 2012), inferred Caldera structures (previous works) and geothermal manifestations (refer to Figure 24 for legend). Wells are given by a red star and landmarks are red dots. The coordinates are UTM-Z16 (m).

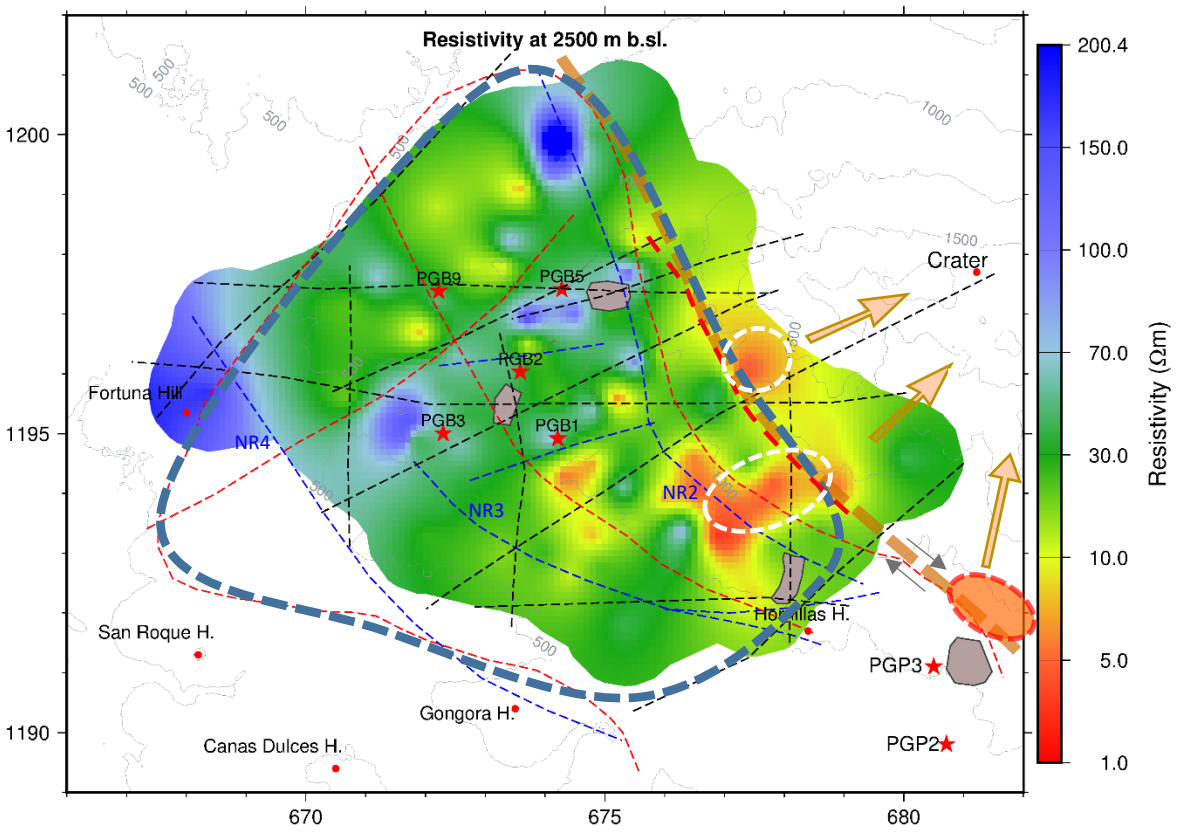

FIGURE 52: Comparison between the resistivity depth slice at 2500 m b.s.l., the gravity structures (red thin dashed lines, this work), geological lineaments (black dashed lines, Molina et al. 2014), resistivity discontinuities (red thick dashed line, this work; and blue thin dashed lines, JICA, 2012), suggested Cañas Dulces Caldera structure (blue dashed shape, this work), and deep conductors mapped in BGF and northeast from Las Pailas GF (orange shape next to PGP3; Badilla, 2011). The orange arrows represent the direction of the possible connections between the proposed heat sources and the active/old craters. Wells are given by a red star, landmarks are red dots, SO_4 hydrothermal manifestations are grey areas. The coordinates are UTM-Z16 (km).

A NW-SE trend is shown by the Tipper and Zstrike NE of well PGB1 (Figure 33, Figure 34 and Figure 35). A resistivity discontinuity is seen in the resistivity cross sections (Figure 52) as for example the one mentioned for profile 4 (~ below soundings RIB240 and RIB234) and for profile 7 (between soundings RIB306 and RPN333). The deep conductors based in the 1D inversion are close to these gradients and lateral discontinuities (white dashed circular shapes; Figure 52). The Bouguer gravity map (Figure 51) presents a negative anomaly at the centre of the area, and also a gradient to the northeast (suggested gravity structure, this work), which is consistent with the resistivity discontinuity NR2 proposed by JICA (2012). Due to the facts above it is proposed in this work that the north and northeast boundaries of the Cañas Dulces Caldera are located on or in the proximities of these anomalies as marked in Figure 52.

The negative gravity anomaly is caused by a substantial amount of low-density material ejected during the formation of the caldera as explained by Hunt (1992). In this case the material corresponds to the Liberia formation (Molina et al., 2014) that fills the caldera as confirmed by the well logs and geological cross sections presented in Figure 22 and Figure 23. The proposed boundaries of the CDC are more symmetric and concentric in shape with the distribution of the negative gravity anomaly compared to what is suggested in previous works and in a better agreement with the different geoscientific information.

The north/northeast boundary of the CDC proposed here could be a part of a large fault- oriented NW-SE that is also connected to the north/northeast boundary of San Vicente Caldera (see orange dashed line in Figure 52). This structure is probably controlling to a great extend the geothermal activity of the south/southwest flank of Rincon de la Vieja – Santa Maria Volcano complex and probably presenting a right lateral strike slip motion as other faults proposed in the area aligned approximately in the same direction (Soto et al., 2003; Climent et al., 2014; Denyer et al., 2009; JICA, 2012). It could explain the existence of N-S lineaments/fractures as shown in Figure 24. N-S structures could have contributed to the movement of the geothermal fluids as shown by the Tipper and Zstrike. The resistivities that could be associated with high temperature areas (Figure 49) are mostly located toward the proximities of this north/northeast caldera boundary. It gives a good suggestion of the most prominent areas associated to the high temperature geothermal resources.

The presumed heat source or even magma accumulation represented by the imaged conductors in BGF (this work) and PGF (Badilla, 2011) could be connected to the old and active craters through the preferential E-W, N-S, SW-NE directions (like RL3, Figure 51). Based on the 1D joint inversion results, the conductors suggest the existence of two possible main magma accumulation anomalies in BGF, one located between ~2 and ~4 km NNW from Las Hornillas Hill or east from BGF as shown in Figure 52 and the other ~3 km east from Las Hornillas Hill. Both are at a depth of ~3 to 6~ km, as found for the conductor of Las Pailas GF.

6.4 3D inversion of MT data

The code used for the 3D forward and inverse modelling is the WSINV3DMT code (Siripunvaraporn et al., 2005). This is a full 3D inversion program for magnetotelluric data. It is extended and implemented from the 2D data space Occam inversion (Siripunvaraporn and Egbert, 2000). The inversion seeks the smoothest minimum structure model subject to an appropriate fit to the data.

Since WSINV3DMT is based on the data space method – all computations depend on the size of data (N), not the size of model parameter (M). The data parameter size N is the total size of the dataset, which is the product of the number of periods N_p, the number of stations N_s, and the number of responses N_r (maximum is 8 for all impedance elements, and 4 for the off-diagonal impedance elements, real and imaginary part):

$$N = N_p N_s N_r \tag{6.69}$$

The model parameter size M is the total number of discretized blocks, which is the product of number of discretization in x (north-south) M_x, number of discretization in y (east-west) M_y, and number of discretization in z (vertical) M_z:

$$M = M_x M_y M_z \tag{6.70}$$

The 3D resistivity inversion requires an iterative minimization process due to non-linearity of the problem. Therefore, the inversion needs to be regularized by imposing constraints on the model as explained in Hersir et al. (2018). It gives interdependence on the model parameters, in such a way that the number of the actually free parameters is reduced. WSINV3DMT uses a combination of minimum structure (Occam inversion) and “prior” model regularization methods. The code minimizes a “penalty function”, which is the weighted sum of 1) the difference between measured data and calculated response (the data misfit), 2) the roughness of the model, and 3) the deviation from the prior model. Initially, the inversion process quickly adjusts the model to reduce severe misfit of the data. Later on, changes that would further reduce the data misfit are rejected because they make the model deviate too much from the prior model.

6.4.1 Data preparation for 3D inversion

6.4.1.1. Static shift

We assumed that in the static distortion the main signal affected is the electric field which suffers the effects of the near-surface resistivity anomalies and topographic effects causing voltage distortion and current channelling as mentioned in Hersir et al. (2018). A joint inversion of TDEM and MT data (apparent resistivity and phase) was performed again for each polarization mode (xy and yx) in order to determine the static shift multiplier to correct the MT data from these distortions. The MT tensor elements were static shift corrected by the equation:

$$\begin{bmatrix} Z_{xx}^{C} & Z_{xy}^{C} \\ Z_{yx}^{C} & Z_{yy}^{C} \end{bmatrix} = \begin{bmatrix} C_x & 0 \\ 0 & C_y \end{bmatrix} \begin{bmatrix} Z_{xx} & Z_{xy} \\ Z_{yx} & Z_{yy} \end{bmatrix} \tag{6.71}$$

$$C_x = \sqrt{\frac{1}{S_{xy}}}\ ; \quad C_y = \sqrt{\frac{1}{S_{yx}}} \tag{6.72}$$

where, Z^c is the corrected and Z the uncorrected tensor, respectively. S_{xy} and S_{yx} are the shift multipliers for apparent resistivity of respectively, the xy and yx polarizations (Árnason et al., 2010).

6.4.1.2. Resampling data

From the spectra we resampled the sounding data according to a defined list of periods (30 periods ranging from 0,001 to 1000 s) to optimize the amount of information involved in the 3D inversion because it is a computational consuming process. We created new resampled EDI files containing five values per frequency decade. The list of periods used for the resampled files is: 1.000e-3, 1.585e-03, 2.512e-03, 3.981e-03, 6.310e-03, 1.000e-2, 1.585e-02, 2.512e-02, 3.981e-02, 6.310e-02, 1.000e-1, 1.585e-01, 2.512e-01, 3.981e-01, 6.310e-01 1.000e00, 1.585e00, 2.512e00, 3.981e00, 6.310e00, 1.000e+01, 1.585e+01, 2.512e+01, 3.981e+01, 6.310e+01, 1.000e+02, 1.585e+02, 2.512e+02, 3.981e+02, 6.310e+02.

6.4.1.3. The model grid

The 3D model consists of resistivity cubes in a 3D grid mesh in the internal coordinate system. The mesh design is mainly based on the spatial distribution of the stations. There is a trade-off between the size of the grid and the computational time it would require to obtain reasonable solutions, because the finer the grid is the more computational time and the larger memory required for the algorithm to converge.

For the area where the MT data are located, it was decided to use grid plane spacing of 250 m in x- and y-direction (cells of 250 m x 250 m side) and increase its size ~exponentially with distance from the dense area (*Figure 53*). Three different grids were created and tested with edges of $\pm$73, $\pm$123 and $\pm$173 km from the origin located at approximately the centre of the area of interest. The study area is located ~23 km away from the coastline which means that the grids include cells ~50, ~100 or ~150 km inside the sea, respectively, being the main difference.

In the vertical direction the horizontal grid planes are dense at shallow depths starting with 25, 50, 50, 75, 100, 100, 100, 150, 150, 200, 200 m, for the first layer's thicknesses, and increasing progressively to a total depth of 75 km.

The total number of vertical grid planes in x-axis and y-axis for the 3D inversion was decided after executing a sensitivity test to evaluate the effects of the conductive seawater on the model response, meaning that the difference between the three grids was in the cells closest to the edges. The test was done by performing a forward modelling using five MT stations symmetrically distributed in the study area (Figure 53). Data for the five MT stations were the same meaning that spectra were

replicated for the list of periods and for the off-diagonal elements of the impedance tensor. An initial homogenous half space model was assessed for 50 Ωm (*Figure 54*).

A global relief model (ETOPO1) from Amante and Eakins (2009) was used to estimate the coastal lines and bathymetry to fix the cells in the sea at 0,3 Ωm.

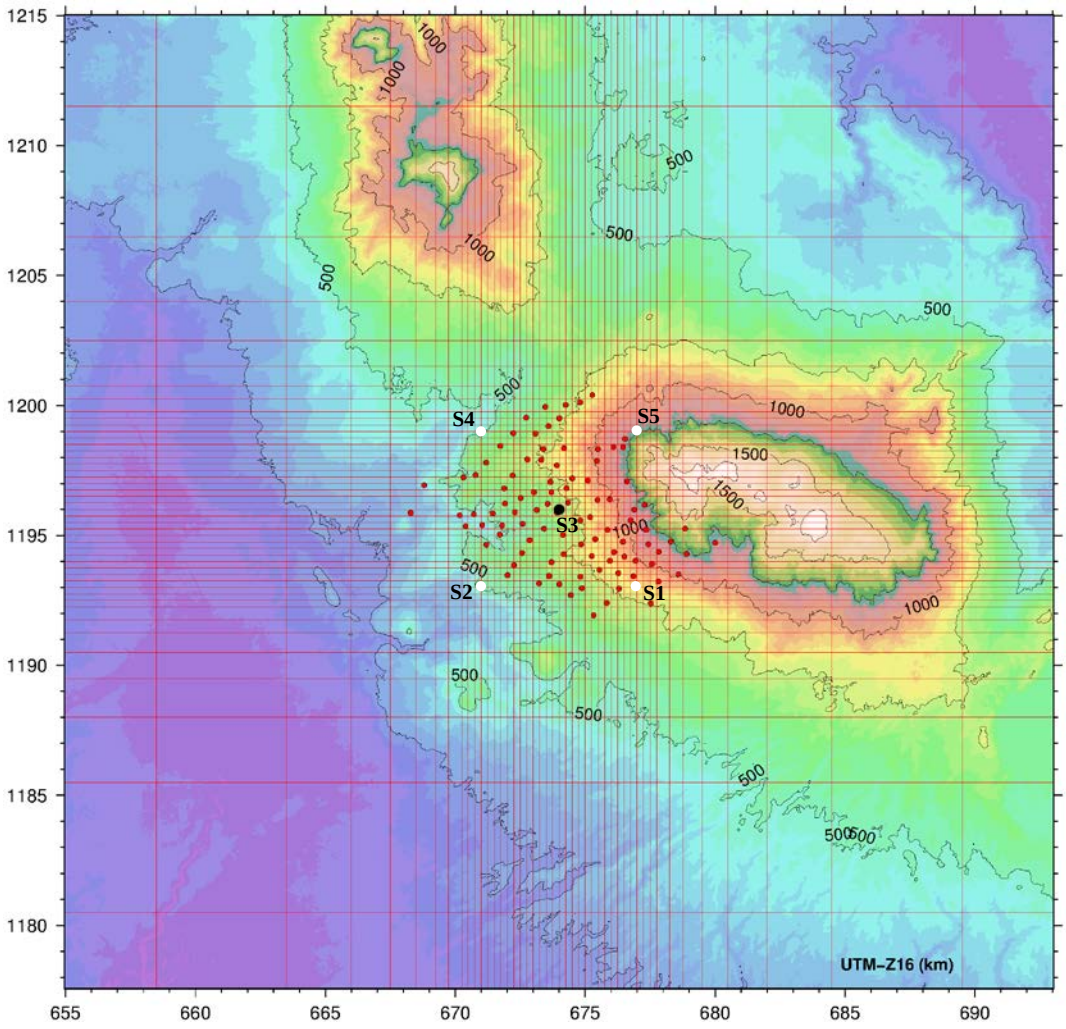

FIGURE 53: Dense grid data coverage. EM soundings are given by red dots. The four white dots plus the black dot at the centre represent the location of the stations used for the forward inversion. Coordinates in UTM-Z16 (km)

The model responses at the five stations for the homogenous half space of 50 Ωm and for the three different grids are shown in Figure 54. The effect of the conductive sea water is mostly seen for low frequencies comprising a period range from 60 to 600 s. It is more marked in the case of ±123 km grid (red dotted curves) due to resistivity curves deviate more from the homogeneous Earth. The most affected polarization mode is the xy. The top view of the final mesh is shown on Figure 55.

Stations 2 (Figure 54) is the most affected one by presenting the largest deviations from the 50 Ωm homogenous half space. This is probably because its location is closest to the coast line (Figure 53), whereas station 5 is less affected probably due to its location farther away from the coastline.

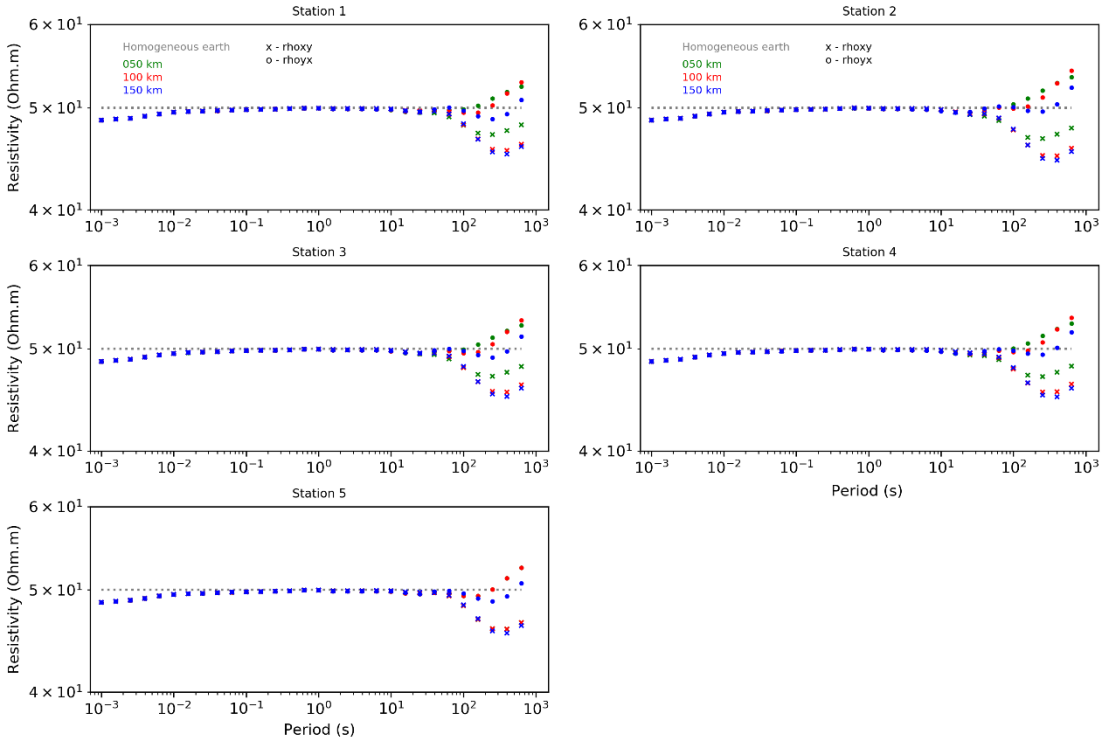

FIGURE 54: Model response for 5 MT stations (Figure 53) using three different grids by fixing the cells in the sea at 0.3 Ωm and for a 50 Ωm homogeneous half space. Results of five stations showing the effects at high and low frequencies from a forward model for the three different grids

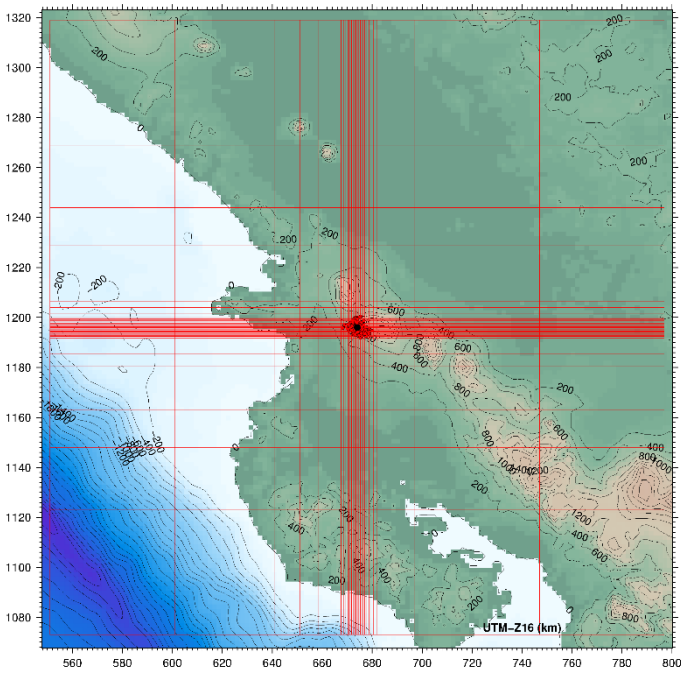

FIGURE 55: Model grid used for the ±123 km edge grid size

6.4.2 Model parameters, initial and prior models

Initially, we tried to use the full impedance tensor for the inversion. It means that we had 97 MT soundings, 30 periods and 8 impedance tensor elements making a total of 23280 data points. We had difficulties with this data set probably due to the size of the problem and the computers were not responding to the inversion. Therefore, we decided to reduce the data set to N = 97x30x4 = 11640 data points.

After defining the grid size, the dimensions of the inversion problem are 54 x 54 x 35, in x, y and z directions, respectively. The numbers of unknowns M consist of 102060 (more than 8 times the number of data points) which shows that it is an undetermined problem. The iterative inversion process is started from an initial model. In order to regularize the inversion, a prior model is used to constrain the deviation of the resulting model from the prior model. Consequently, the resulting model may depend on the initial and prior model.

The influence of the initial model on the resulting model was evaluated by using four different initial models: a homogeneous half-space with resistivity 10 Ωm, 50 Ωm and 100 Ωm; and a model compiled from 1D joint inversion of individual TDEM/MT sounding pairs. In the first case, the inversion only inserts high resistivity where needed and in the second case, the inversion only inserts low resistivity where needed. In all cases the initial model and prior model was the same and the resistivity of the sea kept fixed through the inversion.

6.5 Results of the 3D resistivity inversion

An executable for the parallel processing version of the WSINV3DMT code was created according to the number of data points and model parameter size. The inversion program was executed on a 32-core computer with 132 GB memory using the Message Passing Interface (MPI) parallel computing environment (Siripunvaraporn and Egbert, 2011). The inversion process took on average ~6 hours for each iteration-run and the total computer time for one initial model was of ~2-5 days.

A step procedure was used during all the inversion. Three or four steps/runs for each initial model were required to reduce the data misfit, which is defined as the RMS of the difference between the measured and calculated values, weighted by the variance of the measured values. The fitting of the calculated curves to the measured ones for the 50 Ωm initial model are shown in Appendix C. The misfit of the 3D inversion process is summarized in Table 2.

TABLE 2: Misfit of the 3D resistivity inversion

Initial model	Initial misfit (rms*)	Final misfit (rms*)	Numbers of iterations
10 Ωm homogeneous Earth	14,8	1,12	8
50 Ωm homogeneous Earth	43,9	1,29	11
100 Ωm homogeneous Earth	67,8	1,93	6
1D layered model	35,6	1,26	7

*Refers to root mean square for an error floor of 3

6.5.1 Comparison of different initial models

The results of the 3D inversion based on the four different initial models are compared through a representative example of smoothed elevation corrected resistivity depth slices at 250 m a.s.l. and at 1000 m b.s.l., as presented in Figure 56 and Figure 57. The result from the 1D joint inversion is also compared with the 3D inversion results in these Figures.

In the case of the relatively high resistivity (50 and 100 Ωm) homogeneous half-space initial model, the inversion only inserts low resistivity where needed – lending confidence in low resistivity anomalies in the results. On the other hand, for the relatively low 10 Ωm homogeneous half-space initial model, the inversion only inserts high resistivity where needed – giving confidence in high resistivity anomalies in the final model.

The models in Figure 56 present similar results to the east and northeast where ~high resistivities appear. In the southern, south-western and western part of the Figure we can see how the ~high resistivity is kept in the case of the 50 Ωm homogeneous earth as initial model but is low for the 10 Ωm and for the 1D joint inversion. All models indicate how the low resistivity cap dips towards SW as stated above showing the resistivity discontinuity with NW-SE direction.

In Figure 57 the resulting model for the 10 Ωm homogeneous half-space initial model keeps relatively low resistivity values at 1000 m b.s.l. but the main low and high resistivity anomalies are comparable for the different results.

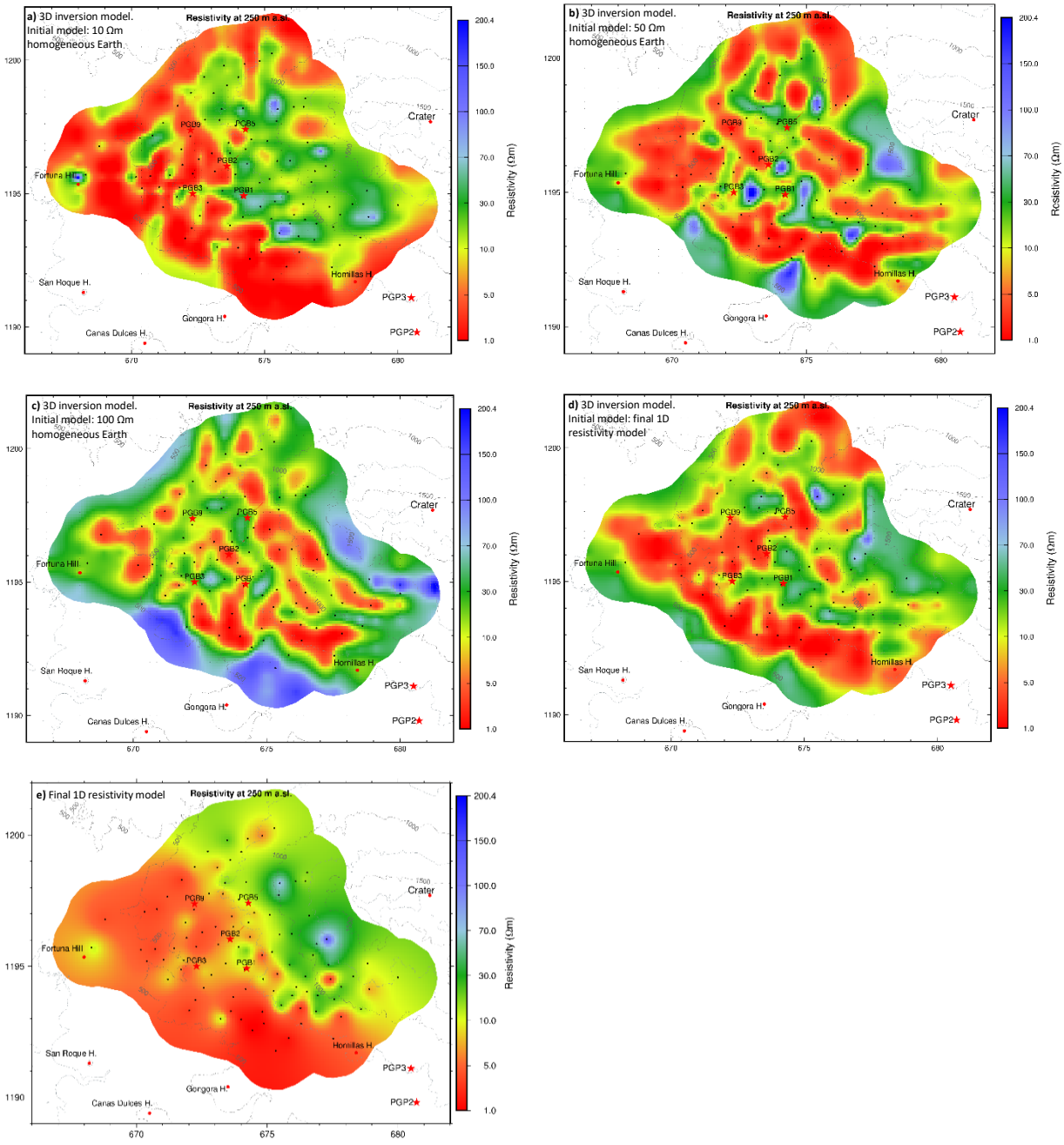

FIGURE 56: Resistivity at 250 m a.s.l. showing comparison between different initial models: a) 10 Ωm homogeneous half-space, b) 50 Ωm homogeneous half-space, c) 100 Ωm homogeneous half-space space and d) 1D joint inversion model. In e) final model from the 1D joint inversion. Black dots represent the EM stations, well locations are given by a red star and landmarks by a red dot

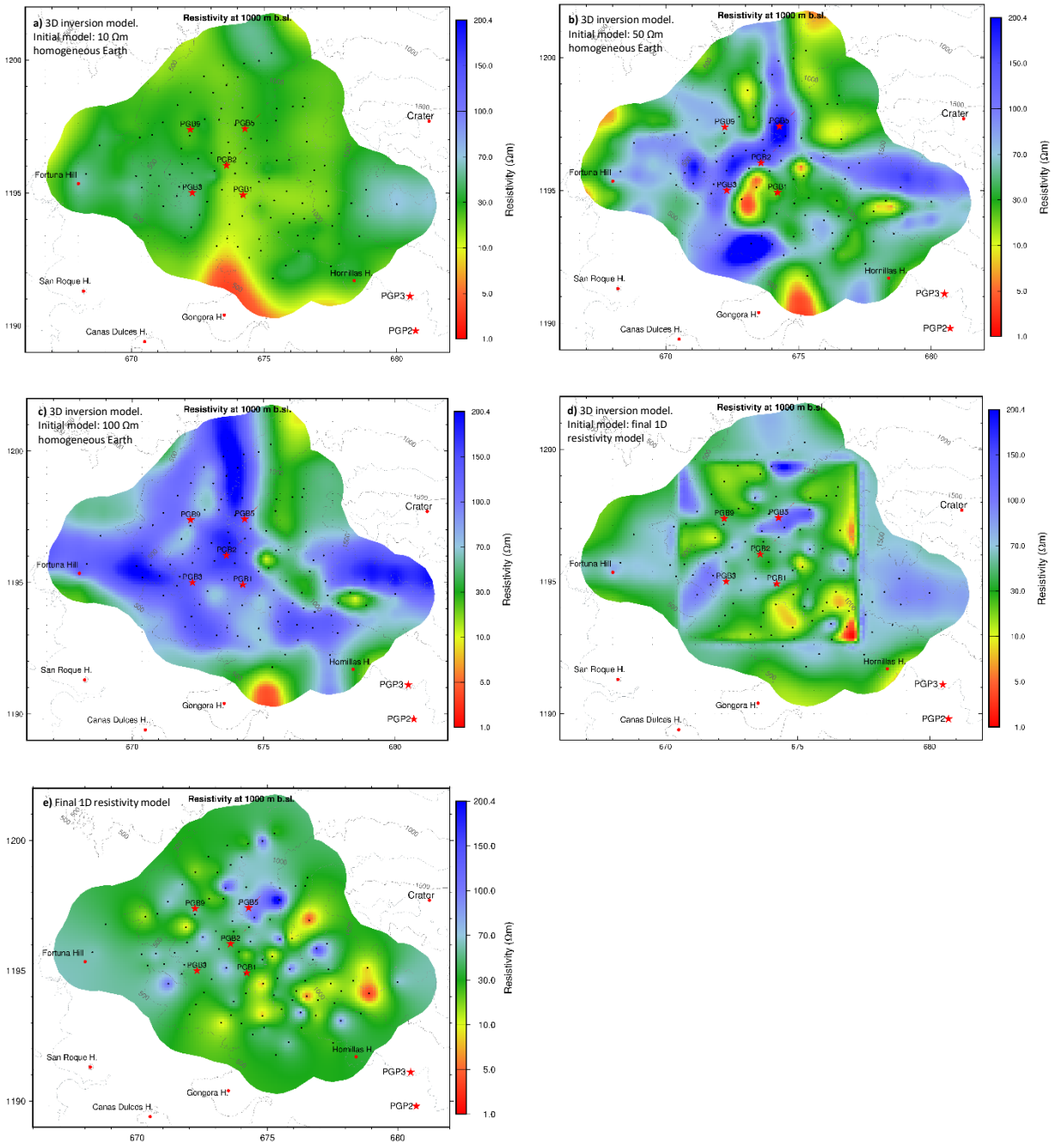

FIGURE 57: Resistivity at 1000 m b.s.l. showing comparison between different initial models: a) 10 Ωm homogeneous half-space, b) 50 Ωm homogeneous half-space, c) 100 Ωm homogeneous half-space space and d) 1D joint inversion model. In e) final model from the 1D joint inversion. Black dots represent the EM stations, well locations are given by a red star and landmarks by a red dot

6.5.2 Resistivity cross sections based on 3D inversion

Six elevation corrected resistivity cross sections based on the3D model using a 50 Ωm homogeneous half-space initial model are presented below. In appendix F we show the other cross sections. They were created down to 4 km b.s.l. to include the anomalies that can affect more directly the geothermal reservoir. The location of the sections is presented in Figure 58.

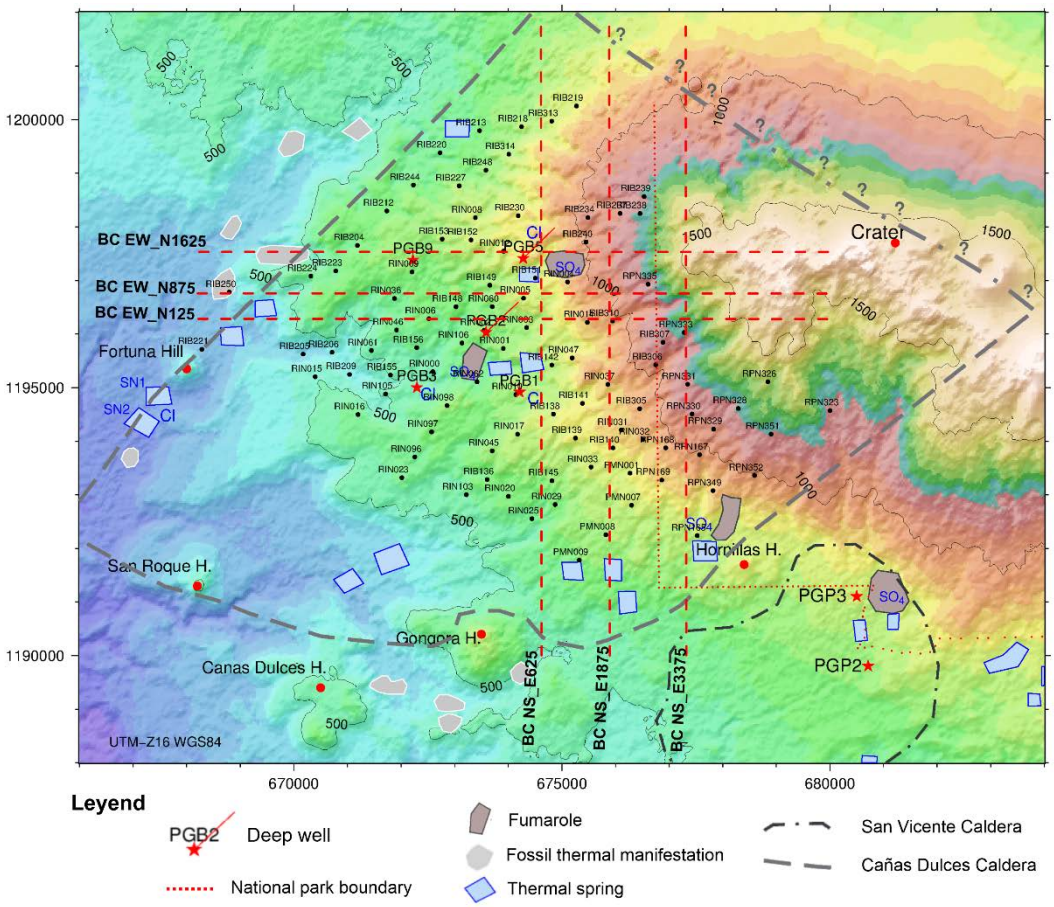

FIGURE 58: Location of the resistivity cross sections. MT stations are given by black dots, inferred Caldera structures from previous studies and geothermal manifestations (refers to Figure 24 for legend), deep wells (red star), landmarks (red dots) and national park boundary (red dotted line)

The cross section on Figure 59 runs N-S in the central part of the area, passing close to the location of PGB1 and PGB5. The vertical pink dashed lines denote the boundary of the dense grid area (Figure 53). The increase in the thickness of the conductive layer to the south is most likely exaggerated due to lack of EM sounding data or by an artefact made by the code. The decrease in the thickness of the layer below MT station RIB151 suggests an up-flow zone and agrees quite well with SO_4 surface geothermal manifestations (Figure 58). The profile presents a domed shape, suggesting shallow location of the geothermal reservoir in the central part of BGF.

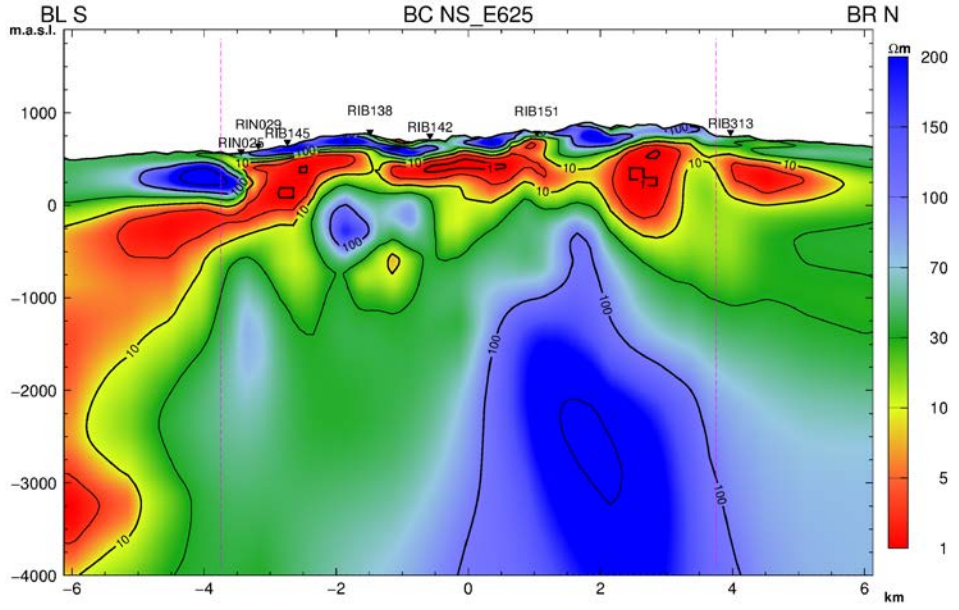

FIGURE 59: Cross section NS_E625. Names of MT stations are given on top, the section location is shown on Figure 58

On Figure 60, also aligned N-S, a lateral discontinuity is seen below station RIB310. It is related to the resistivity discontinuity seen in the 1D profiles that is associated to the north boundary of the caldera structure. The low resistivity at the edge in the north part could be generated by an artefact or just extrapolation of the model.

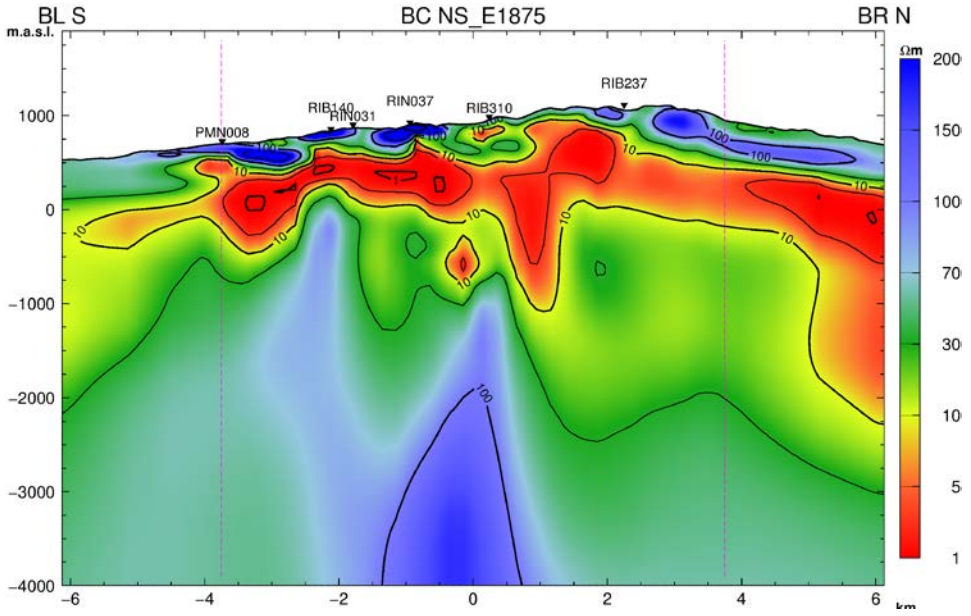

FIGURE 60: Cross section NS_E1875. Names of MT stations are given on top, the section location is given on Figure 58

The profile of Figure 61 presents a deep conductor to the north located 2 km north from the centre of the section and between ~1500 and ~3500 m b.s.l. (~3000 to 5000 m depth). Its continuity further north is partially confirmed by other cross sections (Figure 64) and resistivity maps (Figure 68) and could also be supported by the induction arrows at great depths (Figure 38) pointing to that area. It might indicate the heat source of the geothermal field.

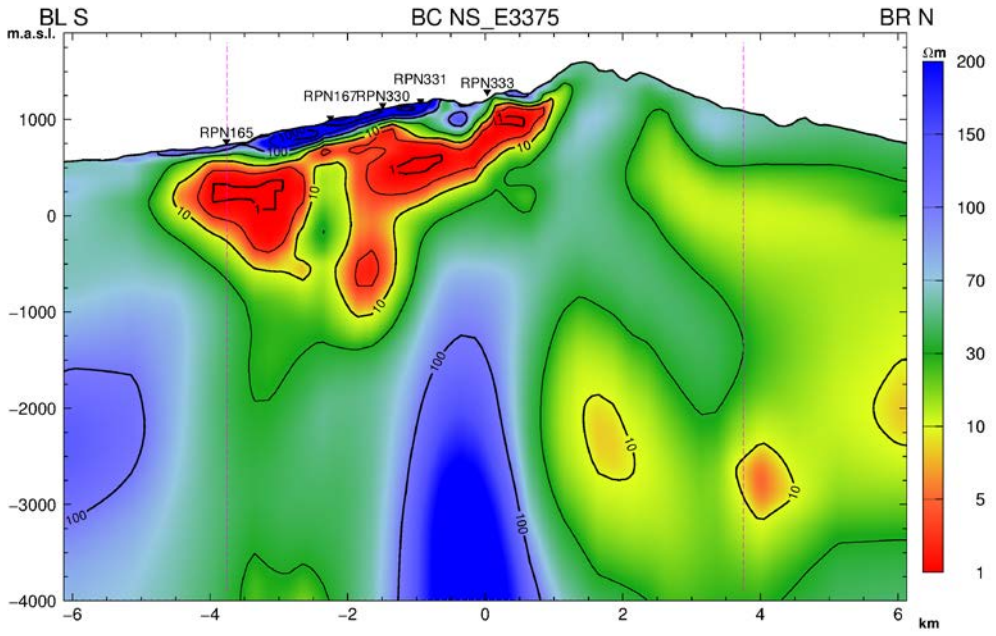

FIGURE 61: Cross section NS_E3375. Names of MT stations are given on top, the section location is given on Figure 58

Figure 62 shows a resistivity profile aligned E-W. It passes approximately through well PGB2. A projection of the well showing the alteration mineralogy is compared with the resistivity structure. The results are quite comparable to the ones discussed in Árnason et al. (1986) and Flóvenz et al. (2012) showing smectite alteration minerals on top directly associated to the conductive layer due to the high CEC of smectite (Weisenberger et al., 2016; Lévy et al., 2018) followed by a mixed layer of smectite-illite where the resistivity increases. Below this, illite and chlorite are the dominant alteration minerals originally formed at temperature of ~220-250 °C, and the resistivity in the subsurface increases as reflected in this cross section. It is consistent with the temperature measured at the bottom of the well (~260 °C; ICE, 2018b). According to this cross section the most prominent geothermal reservoir is located at ~1000 m b.s.l. Underneath sounding RPN333 a lateral discontinuity is revealed confirming the one based on the 1D inversion models (Figure 52).

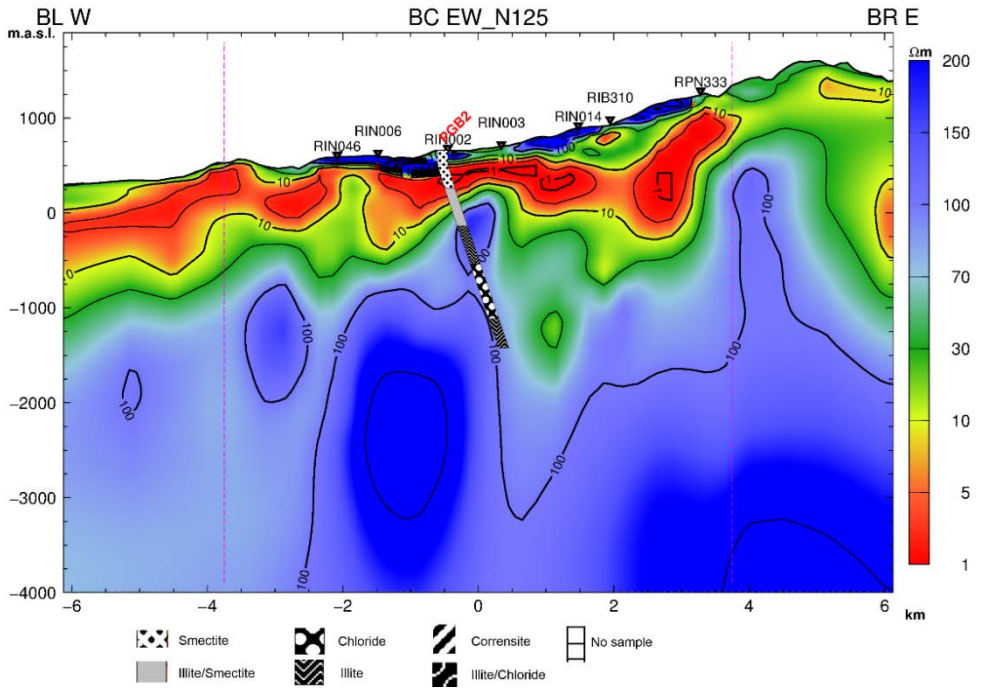

FIGURE 62: Cross section EW_N125. Names of MT stations (in black) and names of wells (in red) are given on top, alteration mineralogy from well logs (ICE, 2018b) is also shown and the section location is given on Figure 58

The cross section presented on Figure 63 shows a lateral discontinuity underneath sounding RPN335. It is attributed to the boundary of the CDC to the NE. The high resistivity at ~1000 m b.s.l is mostly present in the central part.

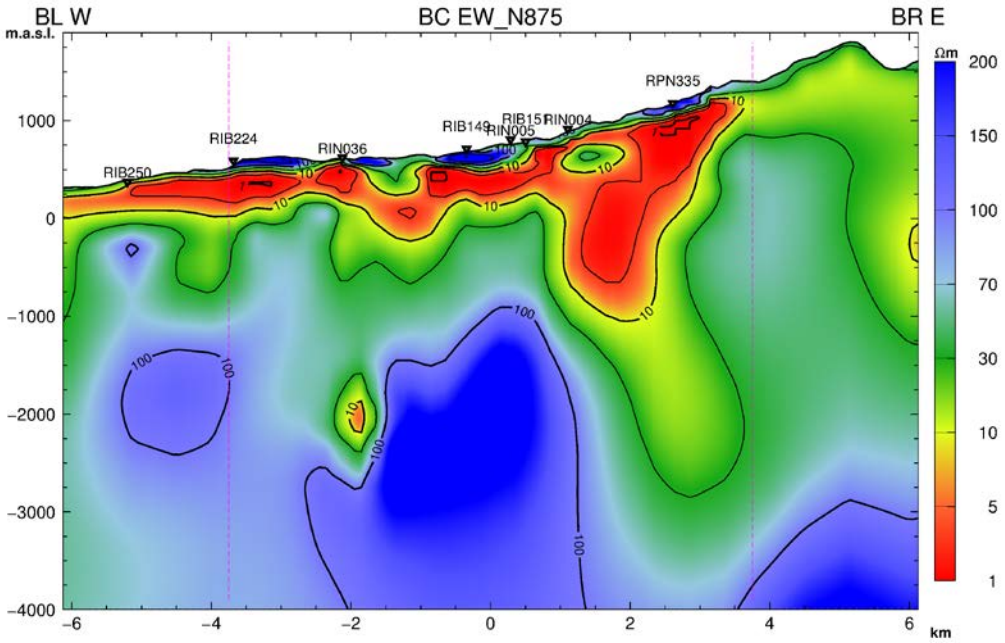

FIGURE 63: Cross section EW_N875. Names of MT stations (in black) and names of wells (in red) are given on top, alteration mineralogy from well logs (ICE, 2018b) is also shown and the section location is given on Figure 58

Figure 64 indicates an important change of the conductive layer between soundings RIN012 and RIB240 which is explained by the geothermal manifestations on surface (SO_4 waters; Figure 58). This might represent an up-flow of the geothermal system. A deep conductive anomaly on Figure 64 is associated with a possible heat source or even magma accumulation that could be connected to the active crater. However, this part of the profile is outside the data coverage and could be an artefact. Its vertical distribution ranges from ~2,25 km to ~ 4 km depth. This model solves the deep conductive anomaly slightly to the north compared to the results based on the 1D inversion.

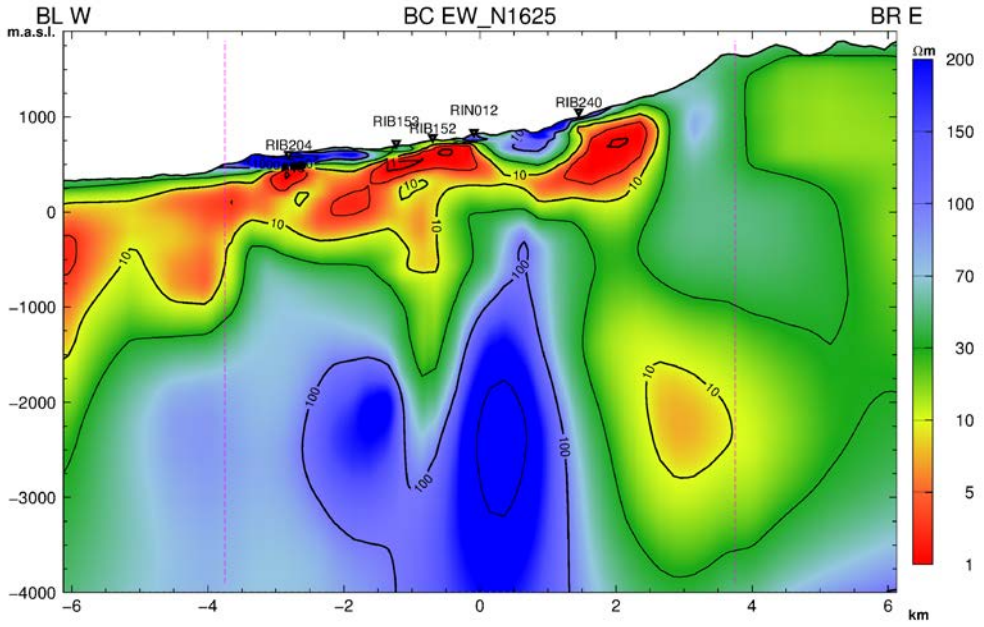

FIGURE 64: Cross section EW_N1625. Names of MT stations are given on top, the section location is given on Figure 58

The cross sections show a similar resistivity structure typical of high temperature geothermal areas as discussed for the 1D joint inversion results, but the horizontal and vertical resolution improves considerably which allows to identify other existing resistivity anomalies and lateral discontinuities. The conductive layer presents a thickness varying between ~250 and ~1 km. The irregular thickness of the cap rock is attributed to faulting/tectonism.

6.5.3 Resistivity depth slices based on 3D inversion

Elevation corrected resistivity slices from the shallow to deeper part of the area are presented in this Section based on 3D resistivity model using an initial model of 50 Ωm homogeneous Earth. The inversion only inserted low resistivity where needed being conservative in this sense as low resistivity anomalies were found in the 1D joint inversion results. The elevations chosen are at sea level, 500 m b.s.l., 750 m b.s.l., 1250 m b.s.l. and 2500 m b.s.l. The subsurface resistivity increases at depth according to the elevation slices presented in Figure 65, Figure 66, Figure 67, Figure 68 and Figure 69.

Heterogeneities in the resistivity models can be explained by a realistic and detailed 3D model representing a complex 3D Earth influenced by much tectonics and geothermal activity. The very rough topography affects directly static shift and it could be the cause of the low quality of some of the TDEM sounding data.

Figure 65 shows the floor of the cap layer to the south and north with resistivity lower than 10 Ωm. In the central part and to the NW it shows the top of the reservoir represented by the higher resistivity.

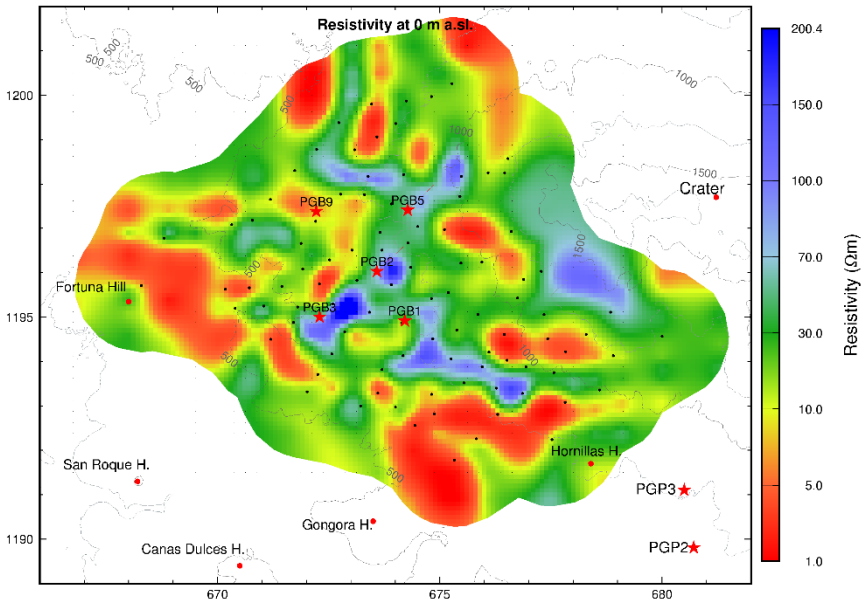

FIGURE 65: Resistivity slice at sea level. Initial model: 50 Ωm homogeneous Earth. Black dots represent the EM stations, well are given by a red star and landmarks by a red dot

Figure 66 created for 500 m b.s.l. shows an increase of the resistivity meaning that we are already below the cap rock for all the area. Low resistivities kept by the model at the edges to the south and to the west is explained by extrapolation or artefacts made by the 3D code as there are no EM data to constrain those anomalies. The low resistivity anomaly close to PGB1 is questionable as this zone is solved with medium to high resistivity values by the other 3D models. Moreover, the well log for PGB1 shows chlorite alteration mineralogy at that depth.

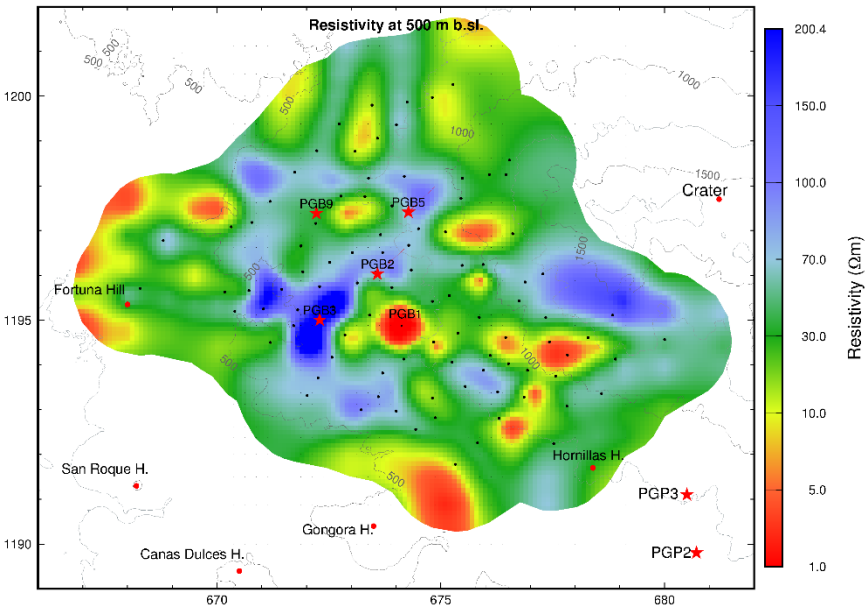

FIGURE 66: Resistivity depth slice at 500 m b.s.l. Initial model: 50 Ωm homogeneous Earth. Black dots represent the EM stations, well are given by a red star and landmarks by a red dot

In Figure 67 and Figure 68 we present the proposed delineation of the Cañas Duces Caldera structure slightly modified to the north in comparison with the presented in Figure 52 after analysing the resistivity cross sections based on the 3D inversion model. The proposed boundaries of the CDC present a ~symmetric shape of ~8 km of diameter. The discontinuity pointed by the red dashed line based on the 1D joint inversion model is quite comparable with the lateral discontinuities seen in the cross sections based on the 3D inversion results.

The resistivity depth slice maps for 1250 and 2500 m b.s.l. are presented in Figure 68 and Figure 69. These Figures show mostly relatively high resistivities which delineate the most prominent geothermal reservoir (Figure 69). The conductive anomaly between PBG3 and PGB1 in Figure 68 is probably caused by the influence of the poor fitting of the MT sounding RIN098 (see Appendix D). Moreover, it is probably influencing the low resistivity anomaly created close to PGB1 (Figure 66). On the other hand, the conductive anomaly marked with a white dashed shape (Figure 68 and Figure 69) to the northeast is resolved quite well and appears in the different 3D resistivity models and even in the 1D joint inversion results.

In Figure 69 the conductive anomaly mentioned above is more evident. No sounding data are there and that could be the cause of this artefact made by the code. It is present in the resistivity cross sections BC NS_E-875, BC NS_E-375 and BC EW_N-1375 in appendix F.

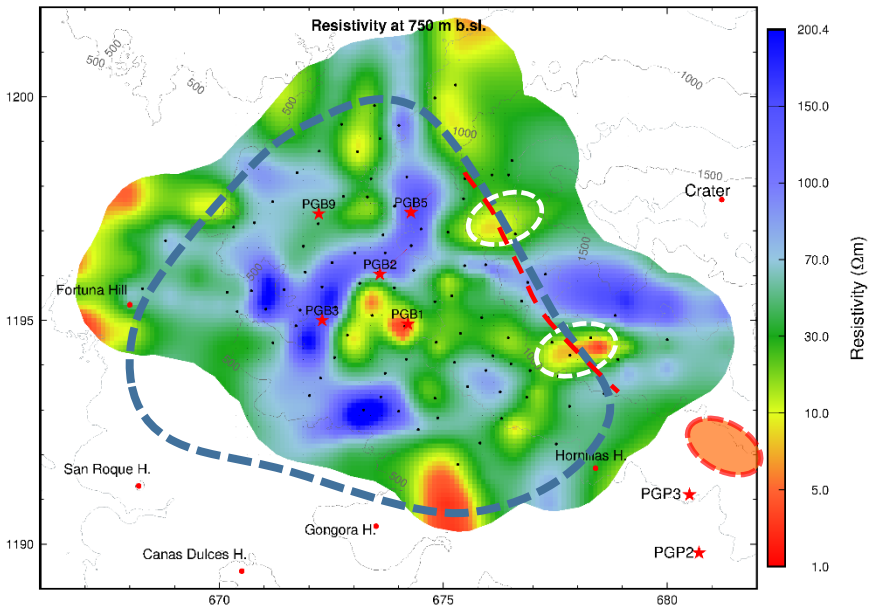

FIGURE 67: Resistivity depth slice at 750 m b.s.l. compared with the resistivity discontinuity based on 1D models (red thick dashed line; this work), the proposed complete delineation of the CDC (blue dashed shape, this work) and the location of possible heat sources (white dashed and orange shapes). Black dots represent the EM stations, well are given by a red star and landmarks by a red dot

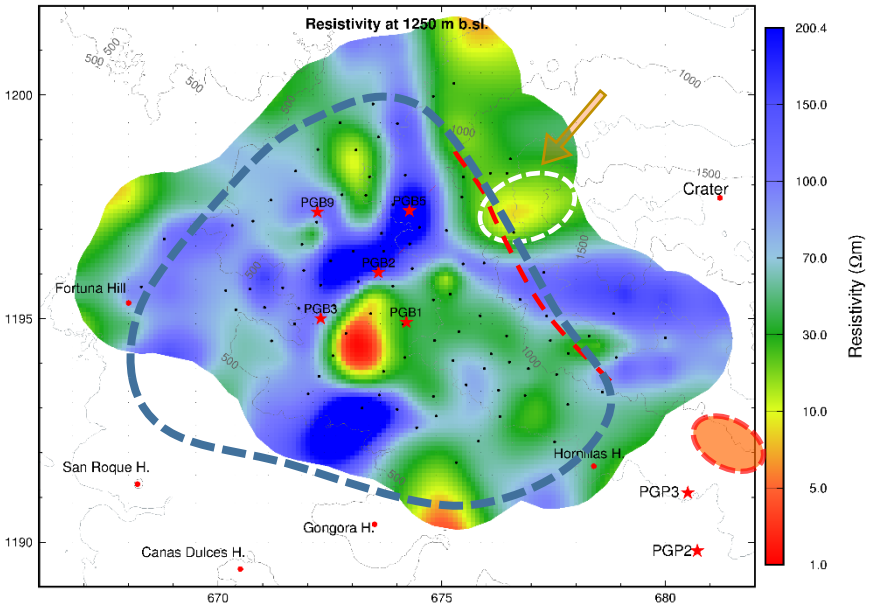

FIGURE 68: Resistivity depth slice at 1250 m b.s.l. compared with the resistivity discontinuity based on 1D models (red thick dashed line; this work), the proposed complete delineation of the CDC (blue dashed shape, this work) and the location of possible heat sources (white dashed and orange shapes). The orange arrows represent the direction of the possible connections between the proposed heat sources and the deep magma source. Black dots represent the EM stations, well are given by a red star and landmarks by a red dot

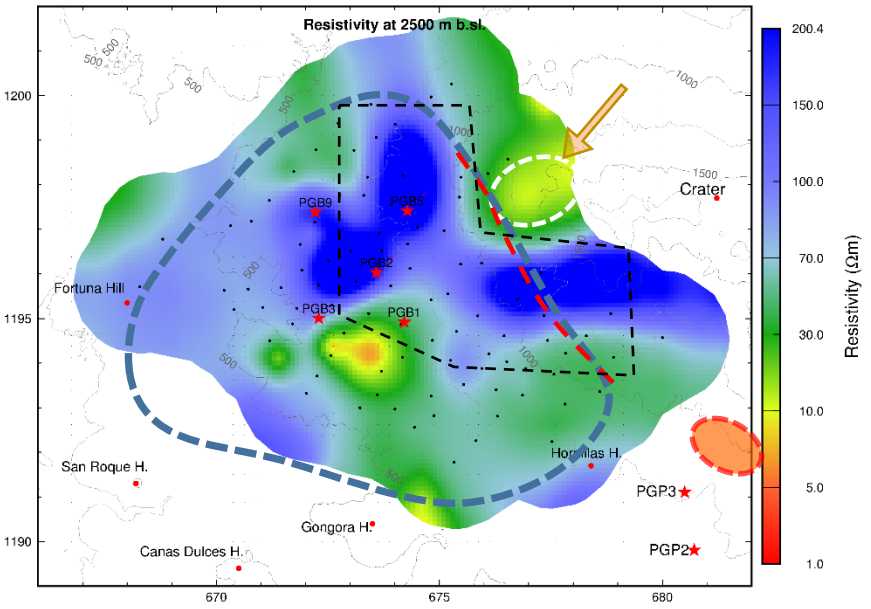

FIGURE 69: Resistivity depth slice at 2500 m b.s.l. (refer to Figure 68 for legend). The black dashed shape delineates the proposed area of the most prominent geothermal reservoir

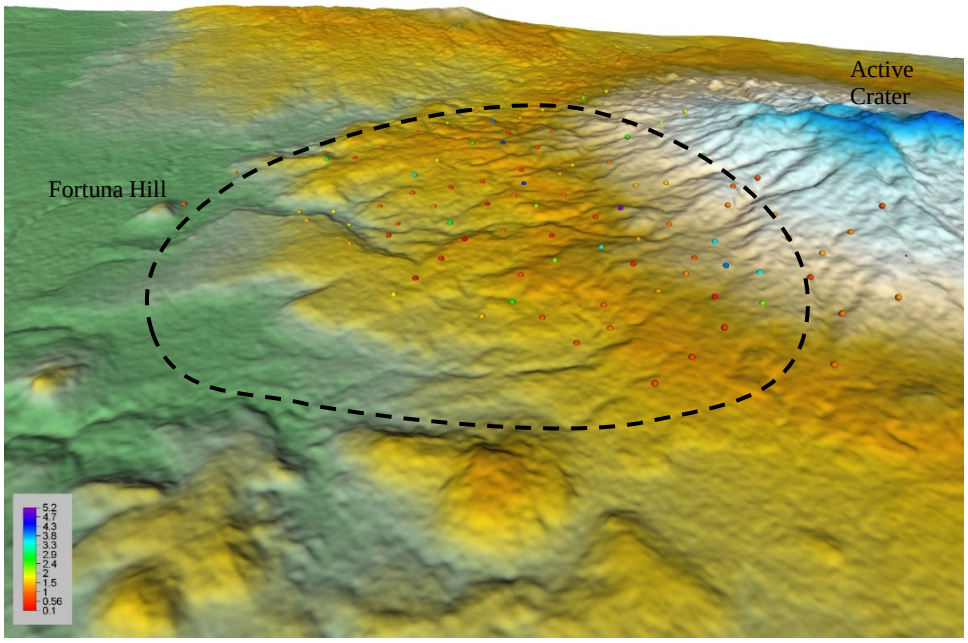

FIGURE 70: Proposed delineation of the Cañas Dulces Caldera

7 CONCLUSIONS AND RECOMMENDATIONS

The main geothermal signatures associated with a high temperature geothermal system in volcanic environment were mapped by using the 1D and 3D resistivity inversion approaches in Borinquen Geothermal area.

The 1D and 3D resistivity inversion models have been compared with well logs and reflect how the temperature dependent alteration of rocks in geothermal systems is directly related to subsurface resistivity.

The conductive layer presents a thickness varying between ~250 and ~800 m, and below the layer, a mixed layer appears where the content of illite/chlorite increases. The resistivity increases especially to the north and northeast delineating the presence of a geothermal reservoir.

The low resistivities present at shallow depths in Borinquen GF forming the cap rock are due to the high CEC of the minerals governing this layer, specifically smectite.

Comparing the resistivity cross sections based on the 1D and 3D inversion and alteration mineralogy, we can conclude that the most likely geothermal reservoir is located at least ~1.5 km depth.

The 3D inversion results give a quite clear image of the resistivity structure allowing to identify more confidently the different stages of alteration mineralogy and lateral resistivity discontinuities.

In this work the total delimitation of the Cañas Dulces Caldera is proposed. It was done by comparing the resistivity inversion results from the present work, the geoelectrical strike, the occurrence of the deep conductors, the Bouguer gravity map and contributions from previous geoscientific works. We propose in this work the caldera boundaries to the north and northeast (Figure 69), and slightly different location of the boundaries to the southwest, south and southeast to the ones inferred before.

The deep conductors (associated to heat source and may indicate magmatic bodies) are formed at the same depth range (~3 to 6 km) in Borinquen and Las Pailas (this work; Badilla; 2011; JICA, 2012).

It is recommended for future works or modelling to improve the quality of the TDEM sounding data in order to do the most realistic static shift correction.

It is recommended to conduct a new 3D resistivity inversion model that integrates all EM data (MT + TDEM) for the Santa María sector, Las Pailas and Borinquen Geothermal areas and interpret the results by comparing with available gravity and magnetic data.

REFERENCES

Arias, O. (2002). Tectocaldera Cañas Dulces-Guachipelín, Costa Rica - 47 págs. Instituto Costarricense de Electricidad, Costa Rica. [Internal report].

Alvarado, G., Benito, B, Staller, A., Climent, A., Camacho, E., Rojas, W., Marroquín, G., Molina, E., Talavera, E., Martínez, S., Lindholm, C. (2017). The new Central American seismic hazard zonation: Mutual consensus based on up to day seismotectonic framework. Tectonophysics. doi.org/10.1016/j.tecto.2017.10.013.

Amante, C. and B.W. Eakins. (2009). ETOPO1 1 Arc-Minute Global Relief Model: Procedures, Data Sources and Analysis. NOAA Technical Memorandum NESDIS NGDC-24. National Geophysical Data Center, NOAA. doi:10.7289/V5C8276M [07-03-2019].

Archie, G.E. (1942). The electrical resistivity log as an aid in determining some reservoir characteristics. *Tran. AIME, 146,* 54-67.

Árnason, K., Haraldsson, G.I., Johnsen, G. V, Thorbergsson, G. Hersir, G.P., Saemundsson, Georgsson, L.S. and Snorrason, S.P. (1986). Nesjavellir: A geological and geophysical survey 1985. Orkustofnun report OS-86017/JHD02 96p. (in Icelandic).

Árnason, K. (1989). *Central-loop transient electromagnetic sounding over a horizontally layered earth*. Orkustofnun, Reykjavík, report OS-89032/JHD-06, 129 pp.

Árnason, K., Karlsdóttir, R., Eysteinsson, H., Flóvenz, Ó.G., and Gudlaugsson, S. (2000). The resistivity structure of high-temperature geothermal systems in Iceland. *Proceedings of the World Geothermal Congress 2000, Kyushu-Tohoku, Japan*, 923-928.

Árnason, K. (2006a). *TemX. A graphically interactive program for processing central-loop TEM data, a short manual.* ÍSOR – Iceland GeoSurvey, Reykjavík, 10 pp.

Árnason, K. (2006b). *TEMTD: A program for 1D inversion of central-loop TEM and MT data, a short manual.* ÍSOR – Iceland GeoSurvey, Reykjavík, 16 pp.

Árnason, K., Eysteinsson, H., Hersir, G. P. (2010). Joint 1D inversion of TEM and MT data and 3D inversion of MT data in the Hengill area, SW Iceland. Geothermics 39, 13-34.

Árnason, K. (2015). The Static Shift Problem in MT Soundings. ÍSOR, Iceland GeoSurvey. Proceedings World Geothermal Congress 2015 Melbourne, Australia, 19-25 April 2015

Badilla, D. (2011). Resistivity imaging of the Santa Maria sector and the northern zone of Las Pailas geothermal area, Costa Rica, using joint 1D inversion of TDEM and MT data. UTP-GTP, Iceland, report 8, appendices, 49 pp.

Bahr, K. (1988). Interpretation of the magnetotelluric impedance tensor – regional induction and local telluric distortion. J. Geophys. (Z. Geophys.), 62(2), 119–127.

Bahr, K. (1991). Geological noise in magnetotelluric data: a classification of distortion types. Phys. Earth Planet. Inter., 66, 24 –38.

Bakkar, H. (2017). Estudios de los procesos sísmicos y volcánicos en el Rincón de la Vieja, Costa Rica. Universidad de Costa Rica.

Barahona, P., Bonilla, E., Cortés R., Guzmán, G., Herrera, P., Hidalgo, P., Martens, U., Méndez, J., Pérez, K., Reyes, K., Sjobohm, L., Vargas, C. & Zamora, N. (2001). Geología - vulcanología del campo geotérmico Borinquen – Las Pailas.- 162 págs. Universidad de Costa Rica [Bachelor thesis.].

Berdichevsky, M. N. and Dmitriev, V. I. (2008). Models and methods of magnetotellurics. Sprinkler, 561 pp.

Cagniard, L. (1953). Basic theory of the magneto-telluric method of geophysical prospecting. *Geophysics, 18,* 605-635.

Carr, M., Saginor, I., Alvarado, G.E., Bolge, L., Lindsay, F.N., Milidahis, K., Turrin, B.D., Feigenson, M.D., and Swisher, C.C. (2007). Element fluxes from the volcanic front of Nicaragua and Costa Rica: Geochemistry Geophysics Geosystems, v. 8, Q06001, doi:1 0. 1029 /2006GC001396

Chave, A., & Jones, A. (2012). *The Magnetotelluric Method: Theory and Practice*. Cambridge: Cambridge University Press. doi:10.1017/CBO9781139020138

Chiesa, S., Civelli, G., Gillot, P.Y., Mora, O., Alvarado, G.E., 1992. Rocas piroclásticos asociadas con la formación de la caldera de Guayabo, Cordillera de Guanacaste, Costa Rica. Rev. Geol. Am. Cent. 14, 59–75.

Christopherson, K., Jones, A. and Mackie, R. (2002). Magnetotellurics for natural resources from acquisition through interpretation. SEG.

Climent, A., Alvarado, G.E., Taylor, W. & Vargas, A. (2014). P.G. Las Pailas II Estudio de amenaza sísmica. - 42 págs. Instituto Costarricense de Electricidad, Costa Rica. [Internal report].

Cumming, W. and Mackie, R. (2010). Resistivity Imaging of Geothermal Resources Using 1D, 2D and 3D Inversion and TDEM Static Shift Correction Illustrated by Glass Mountain Case History. Proceedings World Geothermal Congress, Bali, Indonesia, April 2010, 25-29.

Dakhnov, V.N. (1962). Geophysical well logging. Q. Colorado Sch. Mines, 57-2, 445 pp.

Deering, C., Vogel, T.A., Patiño, L.C., and Alvarado, G.E. (2007). Origin of distinct silicic magma types from the Guachipelín caldera, NW Costa Rica: Evidence for magma mixing and protracted subvolcanic residence: Journal of Volcanology and Geothermal Research, v. 165, p. 103–126, doi:1 0. 1016/ j. jvolgeores. 2007. 05 .004.

DeMets, C. (2001). A new estimate for present-day Cocos Caribbean plate motion: Implications for slip along the Central American volcanic arc: *Geophys. Res. Letters, 28*, p. 4043–4046, doi:1 0. 1029 /2001GL013518.

DeMets, C., R. G. Gordon, and D. F. Argus (2010). Geologically current plate motions, Geophys. J. Int., 181, 1–80, doi:10.1111/j.1365-246X.2009.04491.x

Denyer, P., and Alvarado, G.E. (2007). Mapa Geológico de Costa Rica: San José, Costa Rica, Librería Francesa, scale 1:400,000.

Denyer, P., Montero, W & Alvarado, G. E. (2009). Atlas tectónico de Costa Rica. Editorial Universidad de Costa Rica, San José, 79 pp.

Eysteinsson, H. (1998). TEMMAP and TEMCROSS plotting programs. Iceland GeoSurvey - ÍSOR, unpublished programs and manuals.

Flóvenz, Ó.G., Georgsson, L.S., and Árnason, K. (1985). Resistivity structure of the upper crust in Iceland, J. Geophys. Res., 90-B12, 10,136-10,150.

Flóvenz, Ó.G., Spangenberg, E., Kulenkampff, J., Árnason, K., Karlsdóttir, R., and Huenges E. (2005). The role of electrical conduction in geothermal exploration. *Proceedings of the World Geothermal Congress 2005, Antalya, Turkey*, CD, 9 pp.

Flóvenz, Ó.G., Hersir, G.P., Sæmundsson, K., Ármannsson, H., and Friðriksson, Þ. (2012). Geothermal Energy Exploration Techniques. In: Sayigh A, (ed.) Comprehensive Renewable Energy, Vol 7, pp. 51–9. Oxford: Elsevier.

Gamble, T. D., Goubau, W. and Clarke, J. (1979). Magnetotellurics with a remote magnetic reference. Geophysics, Vol. 44, 53-68.

Gasperikova, E., Newman, G., Feucht, D., and Arnason, K. (2011). "3D MT Characterization of Two Geothermal Fields in Iceland", Geothermal Research Council Transactions, Vol. 35, 1667-1671.

Groom, R. W. and Bailey, R. C. (1989). Decomposition of Magnetotelluric Impedance Tensor in the Presence of Local Three-Dimensional Galvanic Distortion. JOURNAL of GEOPHYS. RES., Vol. 94, No B2, 1913-1925.

Groom, R. W., Kurtz, R. D., Jones, A. G. & Boerner, D. E. (1993). A quantitative methodology to extract regional magnetotelluric impedances and determine the dimension of the conductivity Structure. Geophysical Journal International banner: Volume 115, Issue 3, December 1993, Pages: 1095-1118.

Heath, Ralph C. (1983). Basic ground-water hydrology: U.S. Geological Survey Water-Supply Paper 2220, 86 pp.

Herrera, D. & Lezama, G. (2002). Reducción de datos gravimétricos de las Áreas Geotérmicas Borinquen y Las Pailas. Instituto Costarricense de Electricidad (ICE), internal report, San José.

Hersir, G.P., and Björnsson, A. (1991). *Geophysical exploration for geothermal resources. Principles and applications.* UNU-GTP, Iceland, report 15, 94 pp.

Hersir, G.P., and Árnason, K. (2009). Resistivity of rocks. *Paper presented at the Short Course on Surface Exploration for Geothermal Resources, organized by UNU-GTP and LaGeo, Santa Tecla, El Salvador*, 8 pp.

Hersir, G. P., Árnason, K., Vilhjálmsson, A.M., Saemundsson, K., Ágústsdottir, þ. and Friðleifsson, G. (2018). Krýsuvík high temperature geothermal area in SW Iceland: Geological setting and 3D inversion of magnetotelluric (MT) resistivity data. Journal of Volcanology and Geothermal Research, https://doi.org/10.1016/j.jvolgeores.2018.11.021

Hunt, T. M. (1992). Gravity anomalies, caldera structure, and subsurface in the Rotorua Area, New Zealand. Geothermics, Vol. 21, No. 1/2, pp. 65-74.

ICE (Instituto Costarricense de Electricidad). (2018a). Informe ejecutivo del Plan de Expansion de la Generacion 2018 – 2034.

ICE (Instituto Costarricense de Electricidad). (2018b). Geological reports of Borinquen Geothermal Wells, CSRG [Internal reports].

ICE and GeothermEx Inc., (2001). *Pre-feasibility studies of the Las Pailas geothermal project, Costa Rica*. Instituto Costarricense de Electricidad (ICE), internal report, San José.

JICA. (2012). Preparatory study for Guanacaste Geothermal Power Development Project in Costa Rica [internal report].

Jiracek, G. R., Reddig, R. P. and Kojima, R. K. (1986). Application of the Rayleigh-FFT technique to magnetotelluric modelling and correction: Presented at 8th Workshop on Electromagnetic Induction, Neuchatel, Switzerland.

Kobayashi, D., LaFemina, P., Geirsson, H., Chichaco, E., Abrego, A. A., Mora, H., and Camacho, E. (2014). Kinematics of the western Caribbean: Collision of the Cocos Ridge and upper plate deformation, Geochem. Geophys. Geosyst., 15, 1671– 1683, doi:10.1002/2014GC005234.

Keller, G. V. and Frischknecht, F. C. (1966). *Electrical methods in geophysical prospecting.* Pergamon Press Ltd., Oxford, 527 pp.

Keller, G. V. (1987). Resistivity characteristics of geological targets. In Electromagnetic methods in applied geophysics, pages 13–15, Tulsa, Oklahoma.

Kempter, K. (1997). *Geologic evolution of the Rincon de la Vieja volcano complex, northwestern Costa Rica.* University of Texas, PhD thesis, 159 pp.

Lee, T. J., Song, Y., Uchida, T., Mitsuhata, Y. and Oh, S. (2004). Interpretation of 3D magnetotelluric data including sea effect for geothermal exploration in Pohang, Korea. Proceedings of the 6th Asian Geothermal Symposium, Oct. 26-29, 2004.

Lee Lerner, K., Lerner, B.W., and Cengage, G. (2003). *Porosity and permeability.* World of EarthScience.

Lévy, L., Gibert, B., Sigmundsson, F., Flóvenz, Ó., Hersir, G., Briole, P. and Pezard, P. (2018). The role of smectites in the electrical conductivity of active hydrothermal systems: electrical properties of core samples from Krafla volcano, Iceland. *Geophysical Journal International*, Volume 215, Issue 3, December 2018, Pages 1558–1582, https://doi.org/10.1093/gji/ggy342

Lücke, O. (2012). Moho structure of Central America based on three-dimensional lithospheric density modelling of satellite-derived gravity data. International Journal of Earth Sciences: May 2012. doi 10.1007/s00531-012-0787-y

Manoj, C. (2003). Magnetotelluric data analysis using advances in signal processing techniques. Osmania University, National Geophysical Research Institute, Hyderabad, India.

Melson, W. (1988). Major explosive eruption of Costa Rican volcanoes: Update for Costa Rican Volcanism Workshop, in Meeting held at Skyland, Shenandoah National Park, Virginia, 15 - 17 November 1988.

Molina, F. (2000). Las Pailas Geothermal Area Rincon de la Vieja Volcano, Costa Rica. UNU-GTP, Iceland, report 13.

Molina, F., Martí, J., Aguirre, G., Vega, E. and Chavarría, L. (2014). Stratigraphy and structure of the Cañas - Dulces caldera (Costa Rica). Geol. Soc. Am. Bull., http:// dx.doi.org/10.1130/B31012.1 (published online 23 June 2014).

Molina, F. and Martí, J. (2016). The Borinquen geothermal system (Cañas - Dulces caldera, Costa Rica). Geothermics 64 (2016) 410 - 425.

Moya, P. & Yock, A. (2007). Assessment and development of the geothermal energy resources of Costa Rica. UNU-GTP: Short Course on Geothermal Development in Central America – Resource Assessment and Environmental Management.

Nam, M.J., Kim, H.J., Song, Y., Lee, T.J. and Suh, J.H. (2008). Three-dimensional topographic and bathymetric effects on magnetotelluric responses in Jeju Island, Korea. Geophys. J. Int., 176, 457-466.

Park, S. and Livelybrooks, D. (1989). Quantitative interpretation of rotationally invariant parameters in magnetotellurics. Geophysics, 54 (11), 1483 - 1490. doi.org/10.1190/1.1442612

Parkinson, W. (1959). Directions of rapid geomagnetic variations. Geophysics. J. R. Astr. Soc., 2, 1 - 14.

Pezard, P. (1990). Electrical Properties of Mid-Oceanic Ridge Basalt and Implications for the Structure of the Upper Oceanic Crust in Hole 504B. *J. Geophys. Res., 95*, 9237-9264.

Phoenix Geophysics. (2005). *Data processing. User's guide*. Phoenix Geophysics, Ltd., Toronto, Canada.

Phoenix Geophysics. (2015). *V5 System 2000 MTU/MTU-A User Guide*. Version 3.0 July 2015, Toronto, Canada.

Quesada M., A., Leandro, G., Morales, L. D. (1995). Geophysical exploration of Las Pailas Geothermal Field, Rincon de la Vieja, Guanacaste Province, Costa Rica. Earth Science Series, Vol. 16.

Quist, A.S., and Marshall, W.L. (1968). Electrical conductances of aqueous sodium chloride solutions from 0 to 800°C and at pressures to 4000 bars. *J. Phys. Chem*., 72, 684-703.

Ranganayaki, R. (1984). An interpretive analysis of magnetotelluric data. Geophysics, 49 (10), 1730-1748. https://doi.org/10.1190/1.1441580

Rosenkjaer, G. and Oldenburg, D. (2012). 3D Inversion of MT data in geothermal exploration: a workflow and application to Hengill, Iceland. Proceedings, Thirty-Seventh Workshop on Geothermal Reservoir Engineering. Stanford University.

Rowland, B. F. (2002). Time-domain electromagnetic exploration. Northwest Geophysical Associates, Inc., 6 pp.

Sánchez, E. and Vallejos, O. (2015). Costa Rica Country update. Proceedings World Geothermal Congress 2015, Melbourne, Australia.

Sander, M. (2015). Geothermal Energy Development in Latin America and the Caribbean and the Role of International Development Partners. Proceedings World Geothermal Congress 2015, Melbourne, Australia.

Simpson, F., and Bahr, K. (2005). *Practical magnetotellurics*. Cambridge University Press, Cambridge, UK, 270 pp.

Siripunvaraporn, W. & Egbert, G. (2000). An efficient data-subspace inversion method for 2-D magnetotelluric data, Geophysics, 65, 791-803.

Siripunvaraporn, W., Egbert, G., Lenbury, Y. and Uyeshima, M. (2005a). Three Dimensional Magnetotelluric: Data Space Method, Physics of the Earth and Planetary Interiors, 150, 3-14.

Siripunvaraporn, W. (2011). Three-Dimensional Magnetotelluric Inversion: An Introductory Guide for Developers and Users. Surv Geophysics, (2012) 33:5–27 DOI 10.1007/s10712-011-9122-6.

Spies, B.R., and Frischknecht, F.C. (1991). Electromagnetic sounding. In: Nabighian, M.N., (ed.), Electromagnetic methods in Applied Geophysics. Investigations in Geophysics, Vol. 2A, SEG.

Sternberg, K.B., Wasburne, J.C., and Pellerin, L., 1988: Correction for the static shift in magnetotellurics using transient electromagnetic soundings. *Geophysics, 53-11,* 1459-1468.

Stoyer, C. H. (2010). Universal Sounding Format. Interpex Limited Golden CO.

Swift, C. M. (1967). A magnetotelluric investigation of an electrical conductivity anomaly in the southwestern United States. Geology and geophysics. Ph.D. thesis, Massachusetts Institute of Technology, Cambridge, MA.

Tikhonov, A. (1950). On determination of electric characteristics of deep layers of the earth's crust. Dokl. Acad. Nauk SSSR, 151, 295-297.

Uchida, T. (2005). Three-Dimensional magnetotelluric investigation in geothermal fields in Japan and Indonesia. In: Proceedings World Geothermal Congress 2005 Antalya, Turkey, 24-29 April 2005.

Vogel, T., Patiño, L.C., Alvarado, G.E., and Gans, P.B. (2004). Silicic ignimbrites within the Costa Rican volcanic front: Evidence for the formation of continental crust: Earth and Planetary Science Letters, v. 226, p. 149–159, doi: 10 .1016 /j .epsl .2004 .07 .013.

Von Huene, R., Ranero, C. R. and Weinrebe, W. (2000). Quaternary convergent margin tectonics of Costa Rica, segmentation of the Cocos Plate, and Central American volcanism. Tectonics, vol. 19, No 2, pages 314-334.

Vozoff, K. (1991). The magnetotelluric method. In: Nabighian, M.N. (ed.), Electromagnetic methods in applied geophysics, vol. 2B. Tulsa, OK, USA, 641–711.

Wannamaker, P.E., Hohmann, G.W., and Ward, S.H. (1984). Magnetotelluric responses of three dimensional bodies in layered earth. Geophysics, 49, 1517–1533.

Waxman, M.P. and Smits, L.J.M.: Electrical Conductivities in Oil-Bearing Shaly Sands, Soc. *Pet. Eng., 8,* 107-122, (1968).

Weisenberger, T. B., Ingimarsson, H., Hersir, G.P. and Flóvenz, Ó.G. (2016). *IMAGE Task 3.3 - Physical properties of rock at reservoir conditions: Validation of the influence of cation-exchange capacity (CEC) on resistivity logs within hydrothermal systems.* Iceland GeoSurvey, ÍSOR-2016/044.

Wiese, H. (1962). Geomagnetische Tiefensondierung. Teil II: Die Streichrichtung der Untergrundstrukturen des elektrischen Widerstandes, erschlossen aus geomagnetischen Variationen. Geofis. Pura et Appl., 52, 83–103.

Wight, D. (1987). MT/EMAP Data Interchange Standard. Society of exploration Geophysicists.

Zamora, N., Méndez, J., Barahona, M., and Sjöbohm, L. (2004). Volcano estratigrafía asociada al campo de domos de Cañas Dulces, Guanacaste, Costa Rica: Revista Geológica de América Central, v. 30, 41–58.

Zhang, P., Roberts, R.G., and Pedersen, L.B. (1987). Magnetotelluric strike rules, Geophysics, 52, 267278.

APPENDIX A: 1D joint inversion of MT and TDEM data

The results from the joint 1D inversion of MT and TDEM data are shown here. Red diamonds represent TDEM apparent resistivity transformed to a pseudo-MT curve; blue squares are measured apparent resistivity; blue circles are apparent phase derived from the determinant of MT impedance tensor; green lines to the right represent results of the 1D resistivity inversion model. Above the left panel is the name of the corresponding MT station; the number below the name: χ^2 – is a measure of the fit between the measured and the response data. The number to the left on the left panel is the name of the TDEM station.

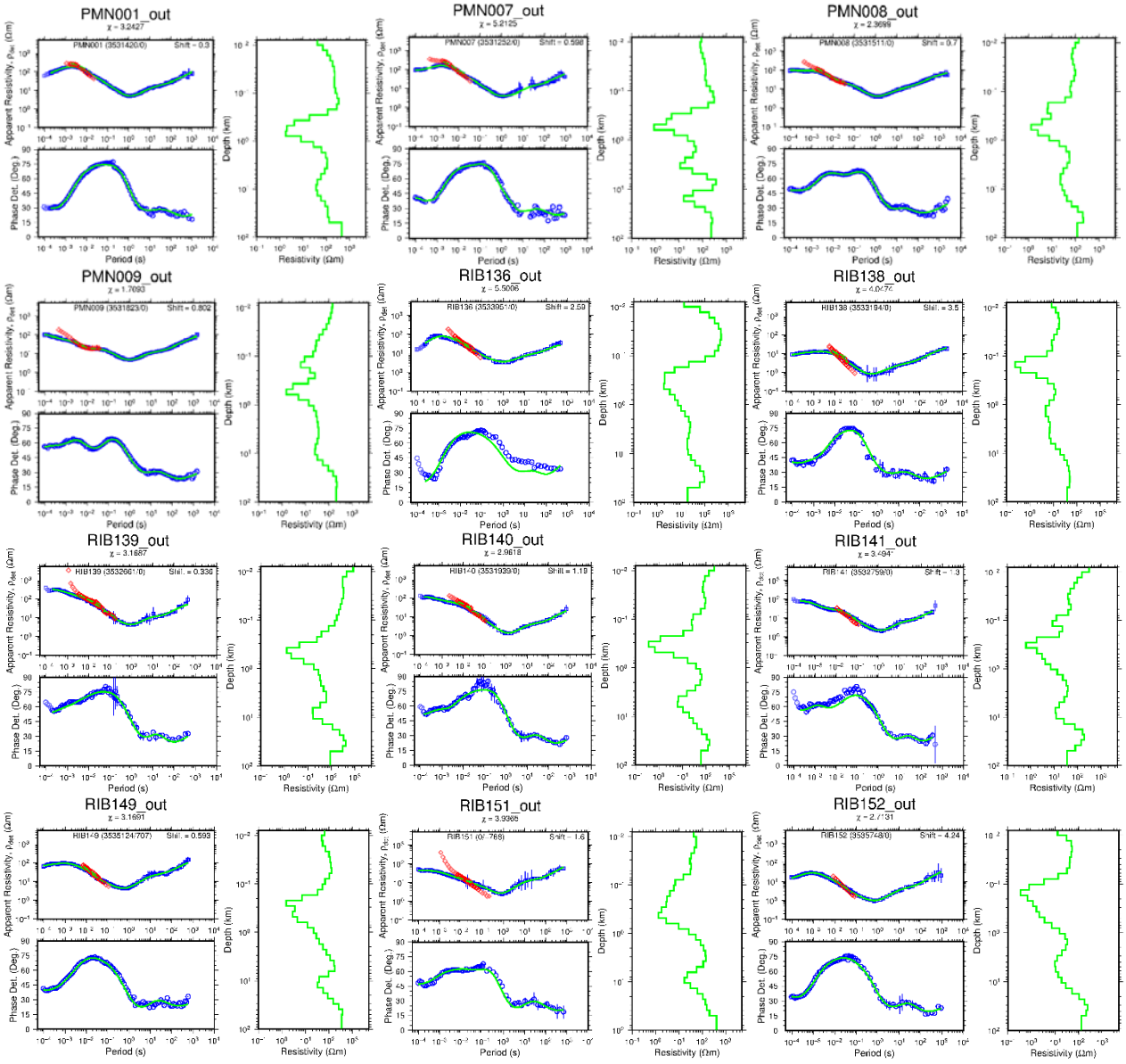

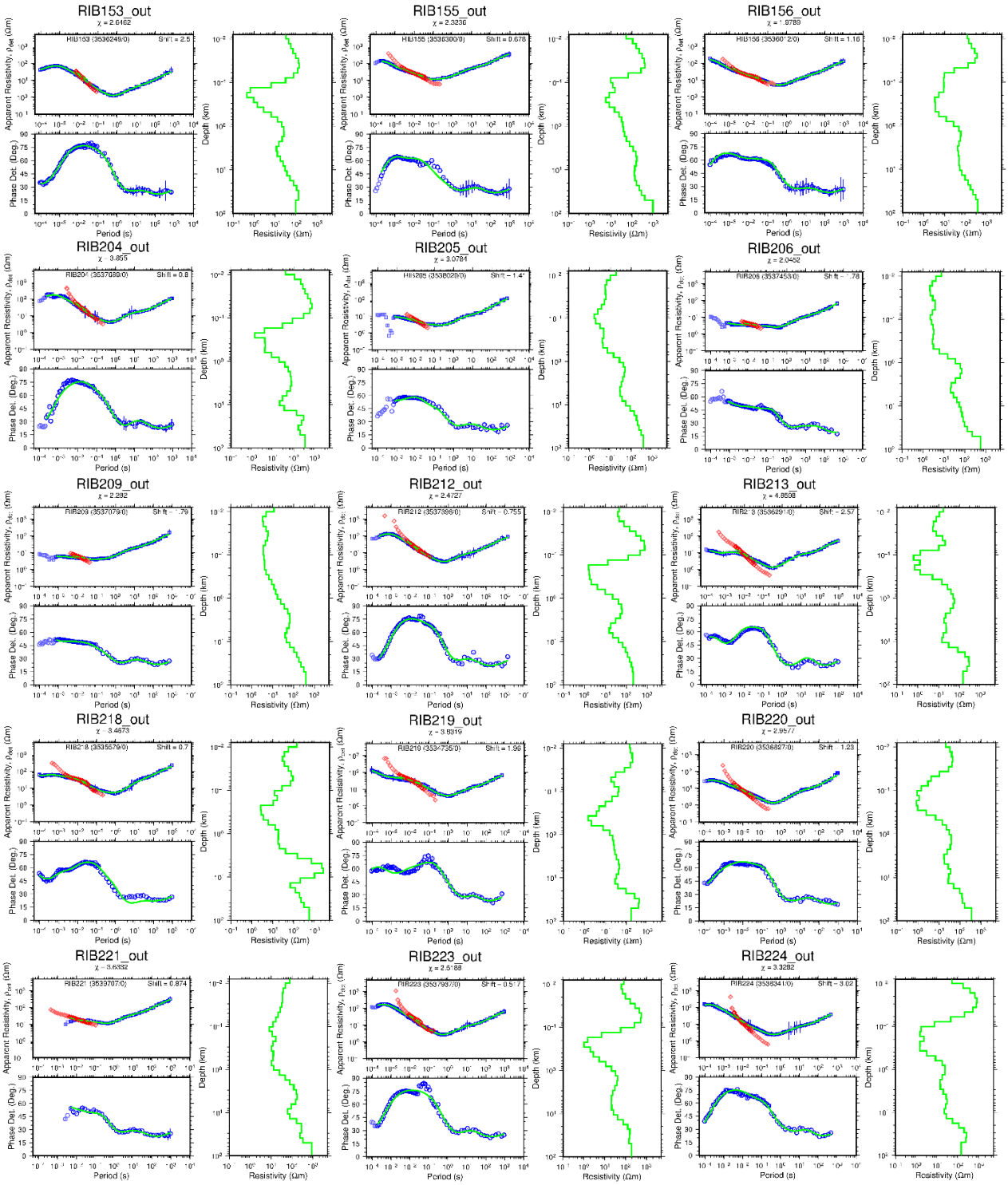
RIB153_out
RIB155_out
RIB156_out
RIB204_out
RIB205_out
RIB206_out
RIB209_out
RIB212_out
RIB213_out
RIB218_out
RIB219_out
RIB220_out
RIB221_out
RIB223_out
RIB224_out
Apparent Resistivity, ρxy (Ωm)
Phase Det. (Deg.)
Period (s)
Depth (km)
Resistivity (Ωm)

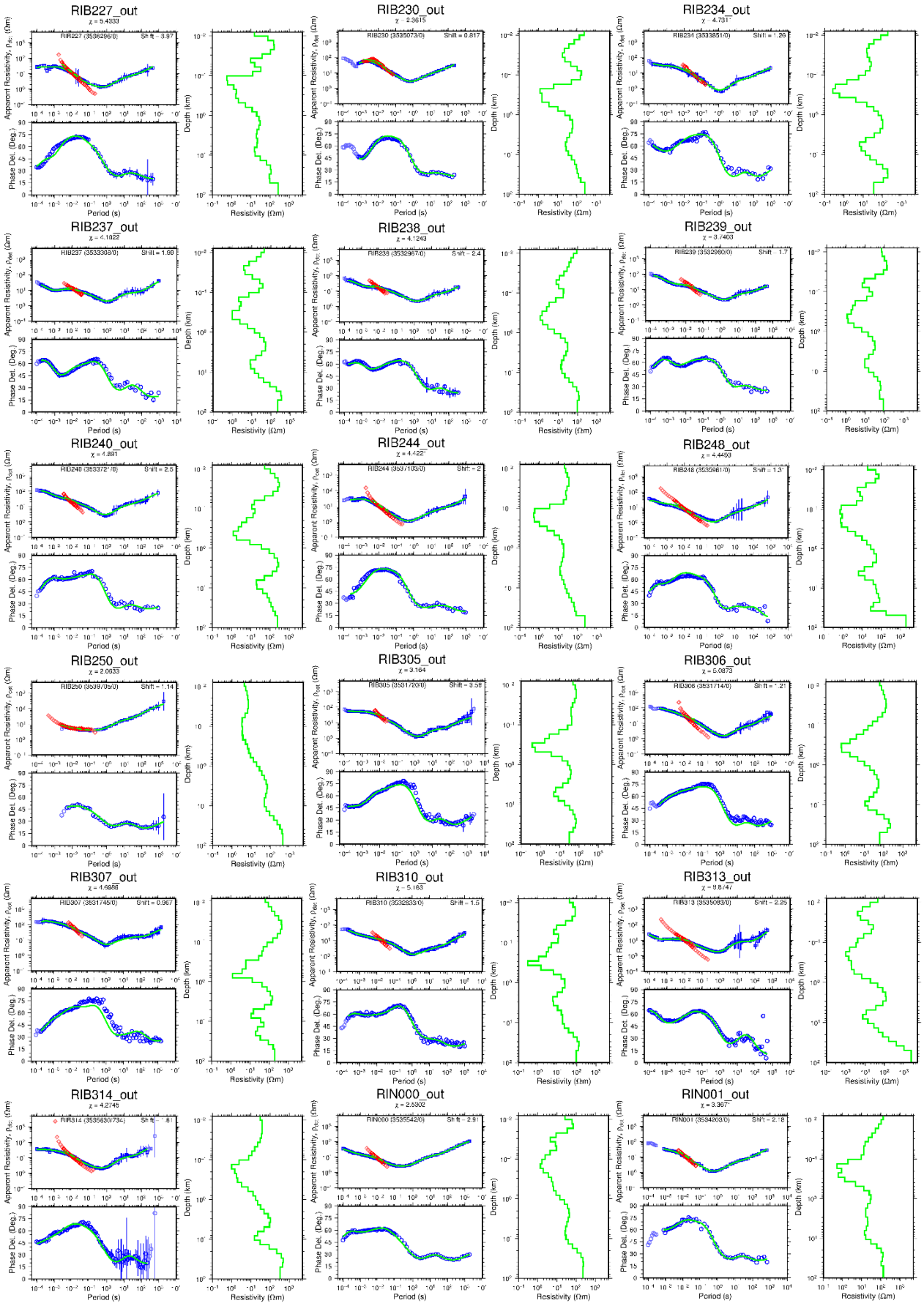
RIB227_out
RIB230_out
RIB234_out
RIB237_out
RIB238_out
RIB239_out
RIB240_out
RIB244_out
RIB248_out
RIB250_out
RIB305_out
RIB306_out
RIB307_out
RIB310_out
RIB313_out
RIB314_out
RIN000_out
RIN001_out
Apparent Resistivity, ρTE (Ωm)
Phase Det. (Deg.)
Period (s)
Depth (km)
Resistivity (Ωm)

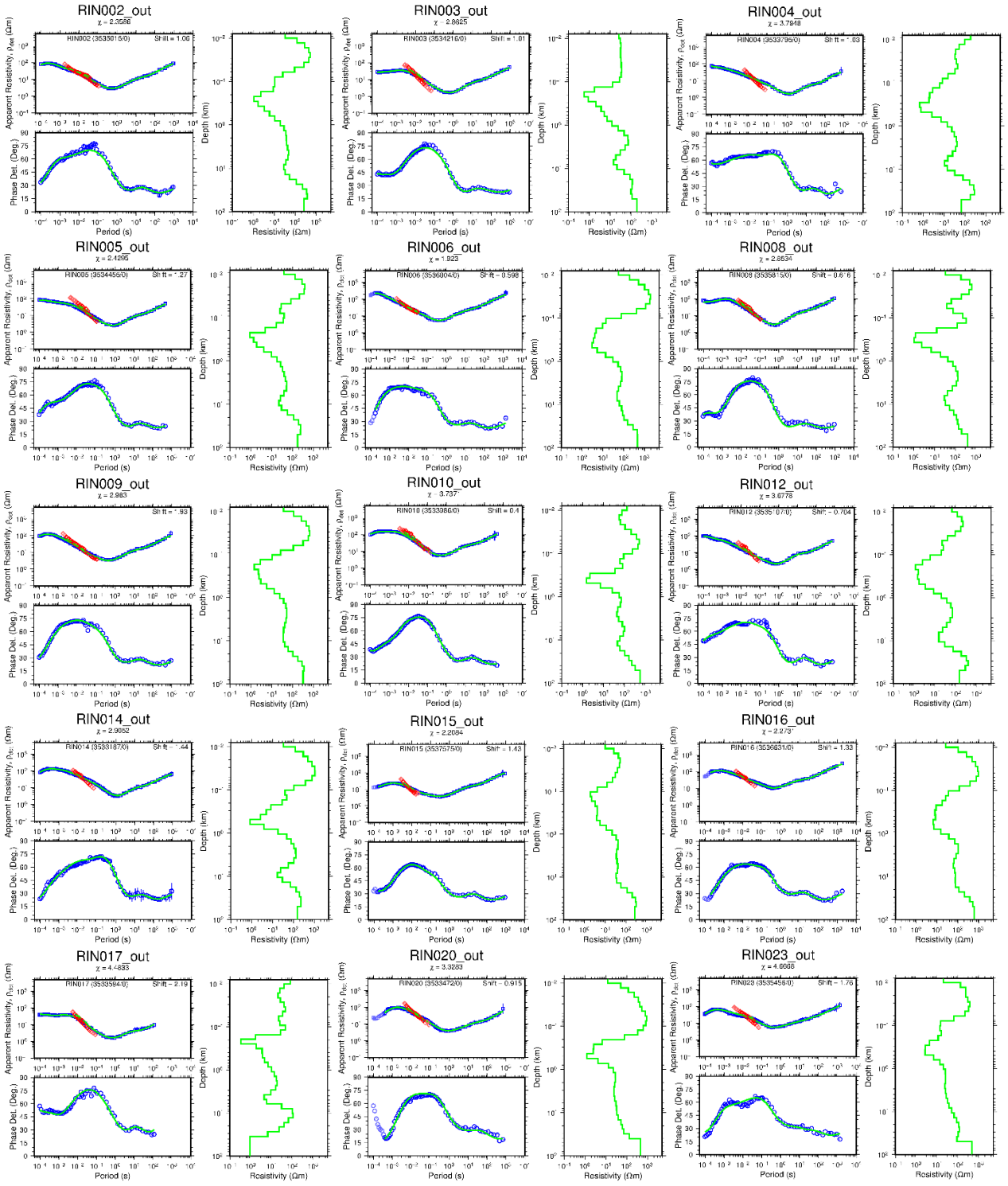
RIN002_out
RIN003_out
RIN004_out
RIN005_out
RIN006_out
RIN008_out
RIN009_out
RIN010_out
RIN012_out
RIN014_out
RIN015_out
RIN016_out
RIN017_out
RIN020_out
RIN023_out
Apparent Resistivity, ρapp (Ωm)
Phase Det. (Deg.)
Period (s)
Depth (km)
Resistivity (Ωm)

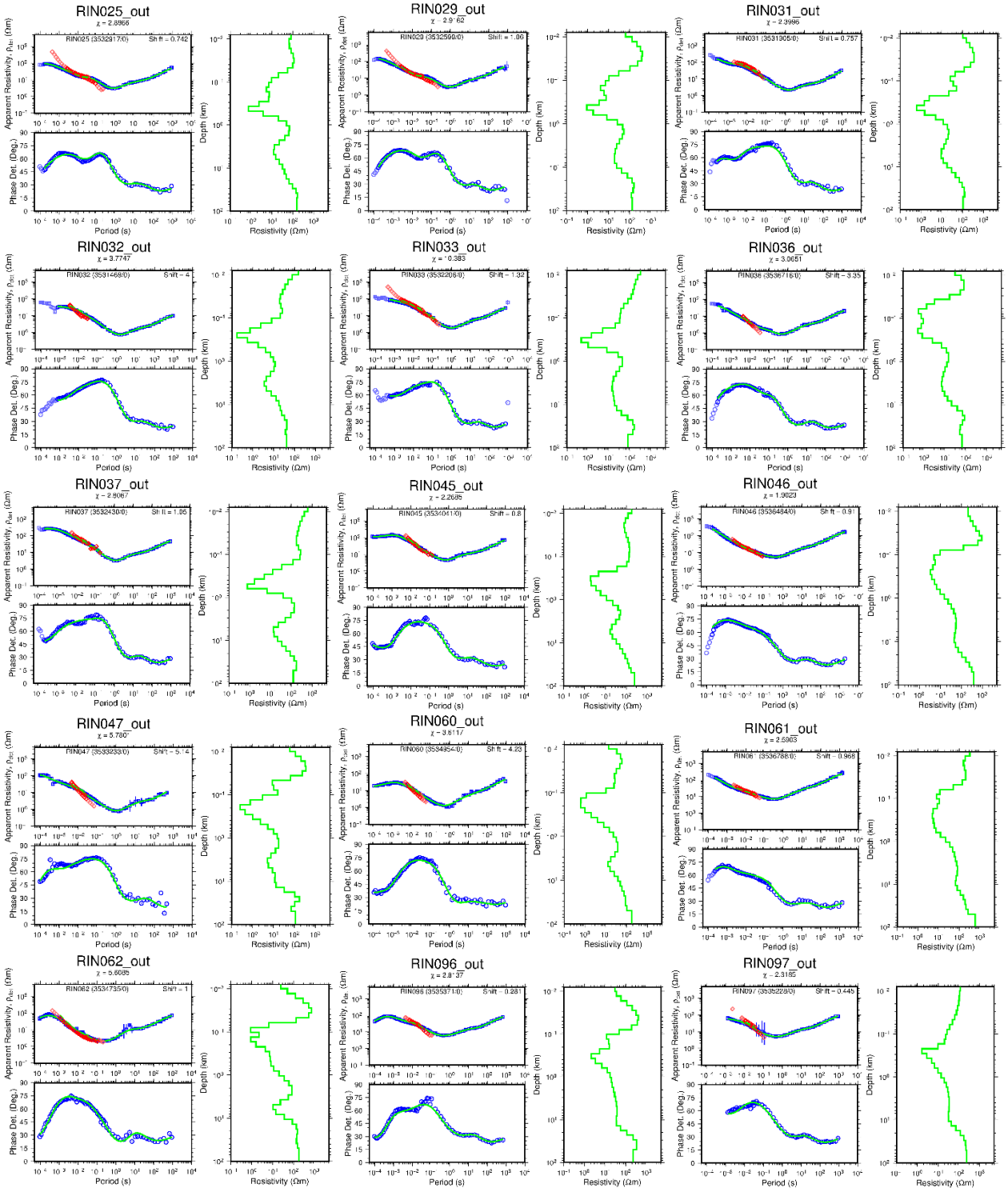
RIN025_out
RIN029_out
RIN031_out
RIN032_out
RIN033_out
RIN036_out
RIN037_out
RIN045_out
RIN046_out
RIN047_out
RIN060_out
RIN061_out
RIN062_out
RIN096_out
RIN097_out
Apparent Resistivity, ρTE (Ωm)
Phase Det. (Deg.)
Period (s)
Depth (km)
Resistivity (Ωm)

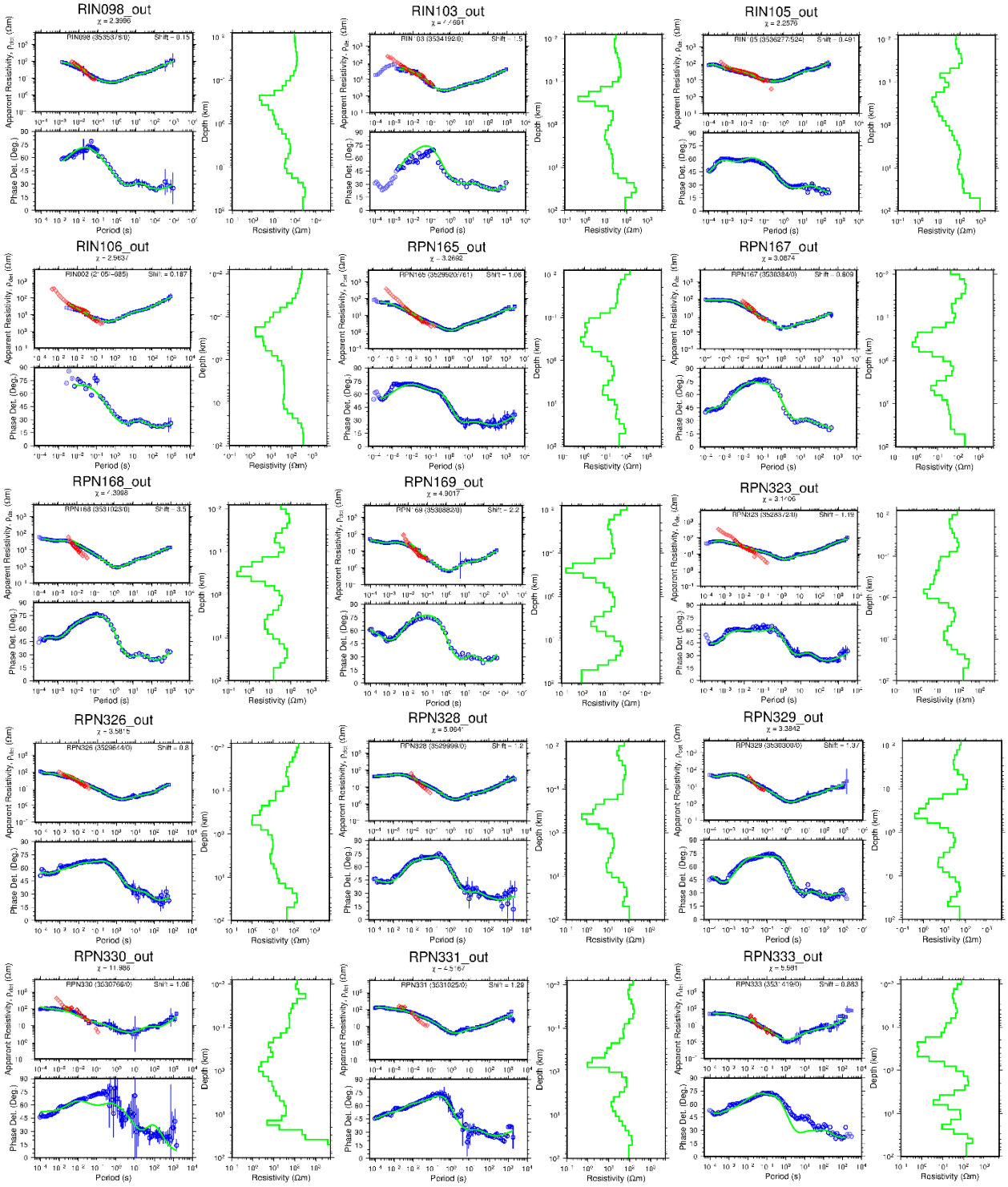
RIN098_out
RIN103_out
RIN105_out
RIN106_out
RPN165_out
RPN167_out
RPN168_out
RPN169_out
RPN323_out
RPN326_out
RPN328_out
RPN329_out
RPN330_out
RPN331_out
RPN333_out
Apparent Resistivity, ρxx (Ωm)
Phase Det. (Deg.)
Period (s)
Depth (km)
Resistivity (Ωm)

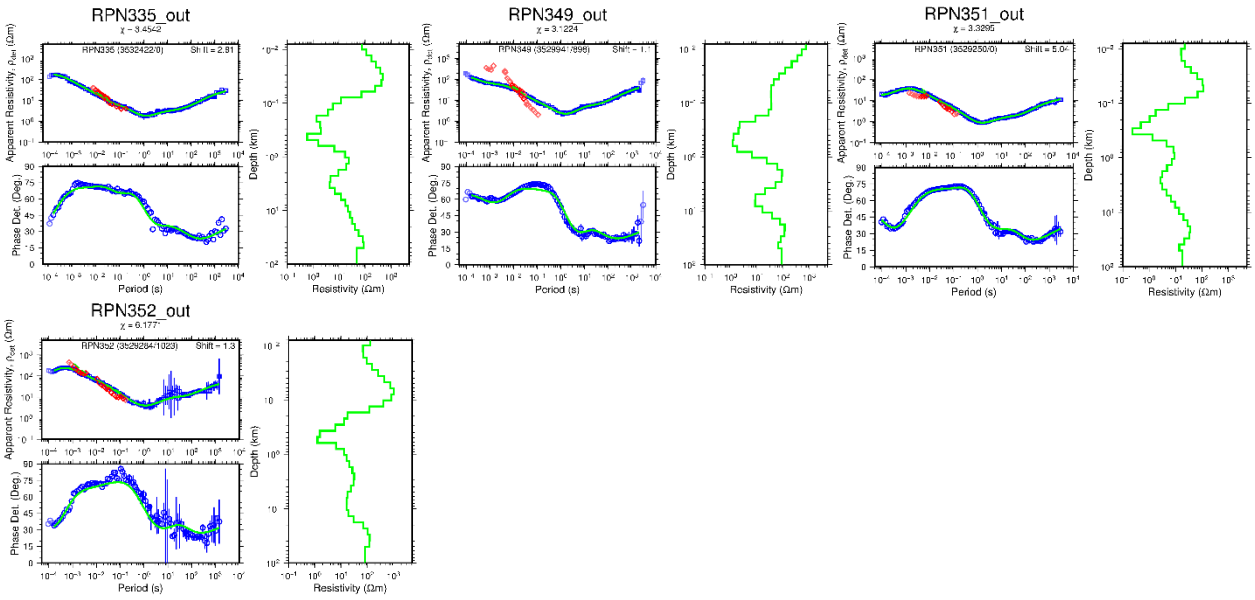

APPENDIX B: Resistivity cross sections based on the 1D joint inversion

The location of the sections is shown on Figure 6.10.

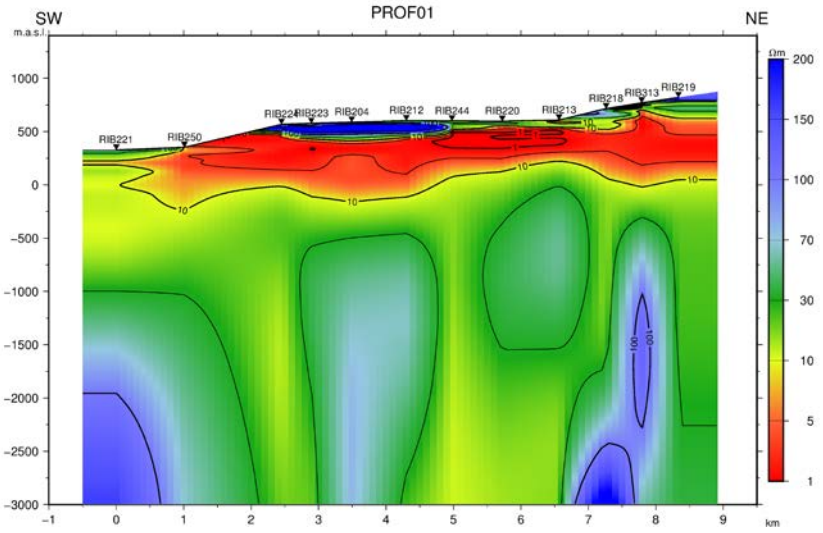

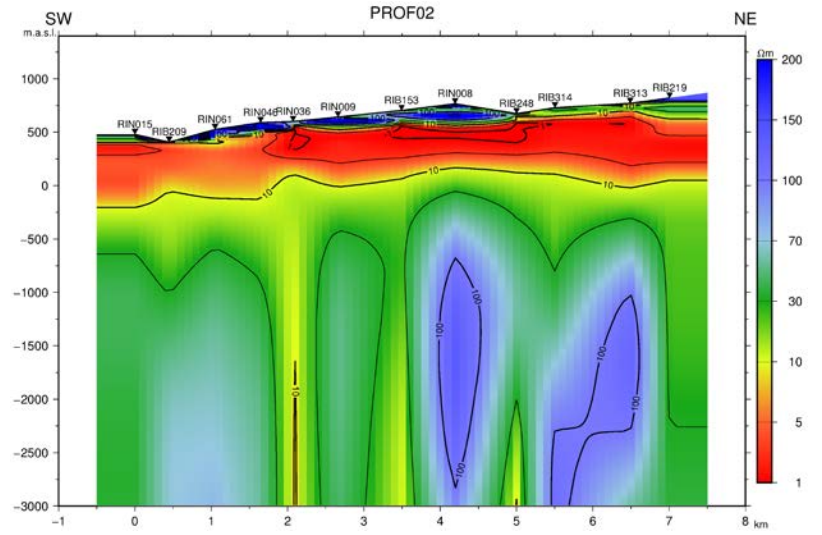
SW
PROF02
NE
m.a.s.l.
Ωm
km
RIN015
RIB209
RIN061
RIN048
RIN036
RIN009
RIB153
RIN008
RIB248
RIB314
RIB313
RIB219

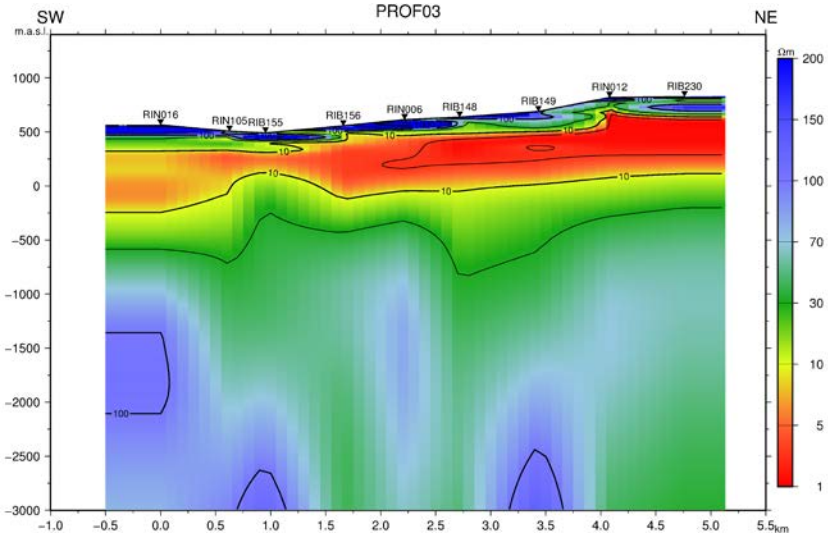
SW
PROF03
NE
m.a.s.l.
Ωm
km
RIN016
RIN105
RIB155
RIB156
RIN006
RIB148
RIB149
RIN012
RIB230

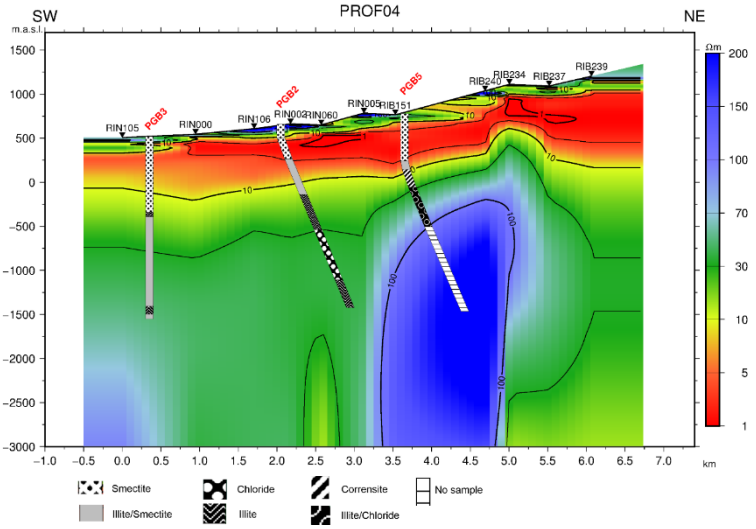
SW
PROF04
NE
m.a.s.l.
Ωm
km
RIN105
PGB3
RIN000
RIN106
PGB2
RIN002
RIN060
RIN005
RIB151
PGB5
RIB240
RIB234
RIB237
RIB239
Smectite
Illite/Smectite
Chloride
Illite
Corrensite
Illite/Chloride
No sample

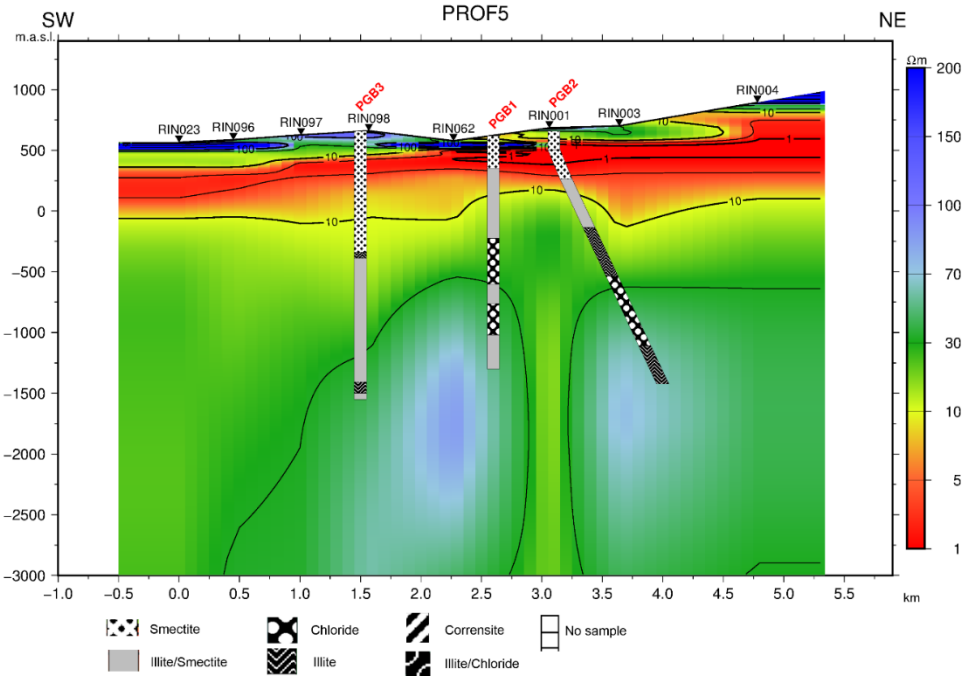
SW
PROF5
NE
m.a.s.l.
Ωm
200
150
100
70
30
10
5
1
km
RIN023
RIN096
RIN097
RIN098
RIN062
RIN001
RIN003
RIN004
PGB3
PGB1
PGB2
Smectite
Illite/Smectite
Chloride
Illite
Corrensite
Illite/Chloride
No sample

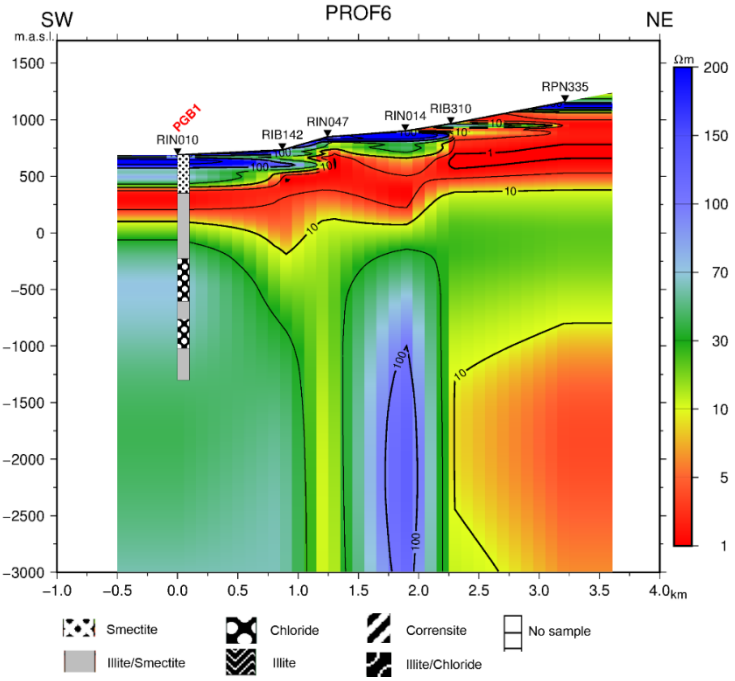
SW
PROF6
NE
m.a.s.l.
Ωm
200
150
100
70
30
10
5
1
km
RIN010
RIB142
RIN047
RIN014
RIB310
RPN335
PGB1
Smectite
Illite/Smectite
Chloride
Illite
Corrensite
Illite/Chloride
No sample

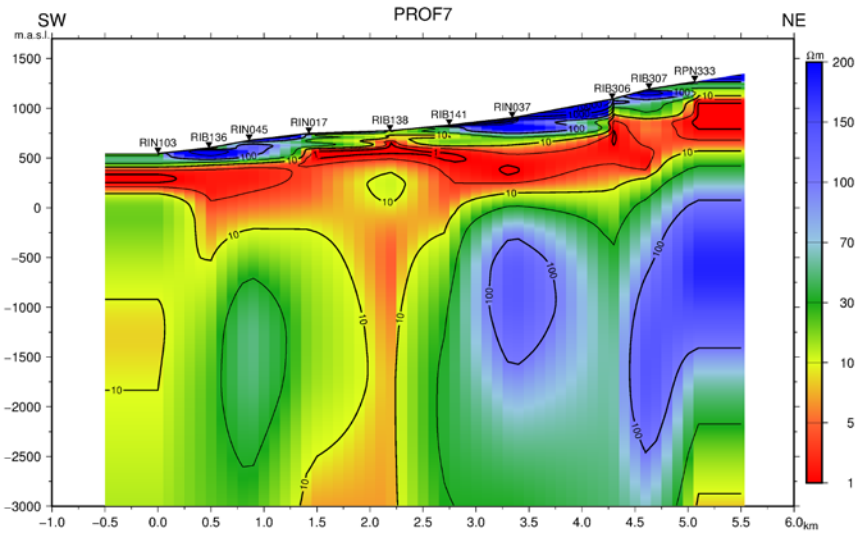
PROF7
SW
NE
m.a.s.l.
Ωm
RIN103
RIB136
RIN045
RIN017
RIB138
RIB141
RIN037
RIB306
RIB307
RPN333

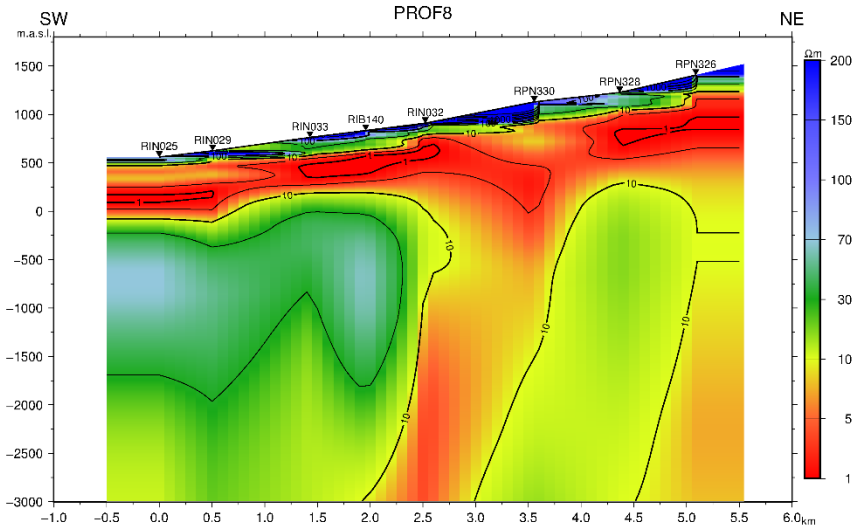
PROF8
SW
NE
m.a.s.l.
Ωm
RIN025
RIN029
RIN033
RIB140
RIN032
RPN330
RPN328
RPN326

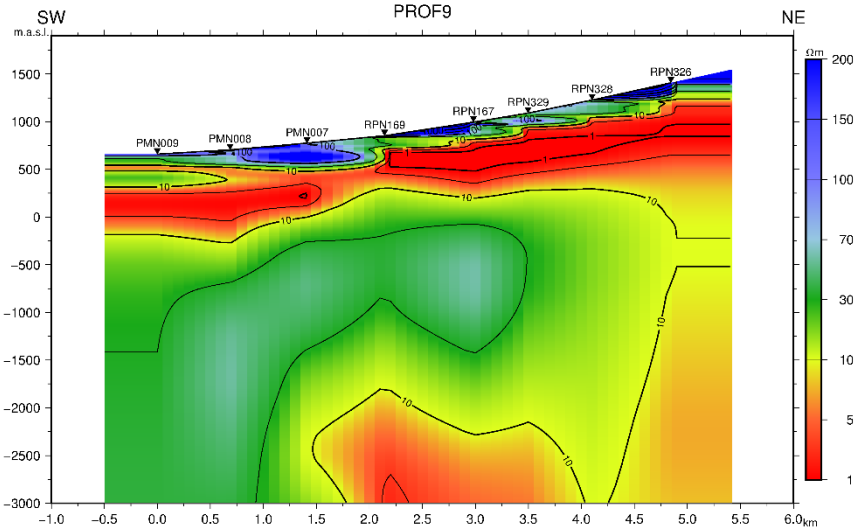
PROF9
SW
NE
m.a.s.l.
Ωm
PMN009
PMN008
PMN007
RPN169
RPN167
RPN329
RPN328
RPN326

APPENDIX C: Resistivity depth slices based on the 1D joint inversion

The coordinates are in km, UTM-Z16.

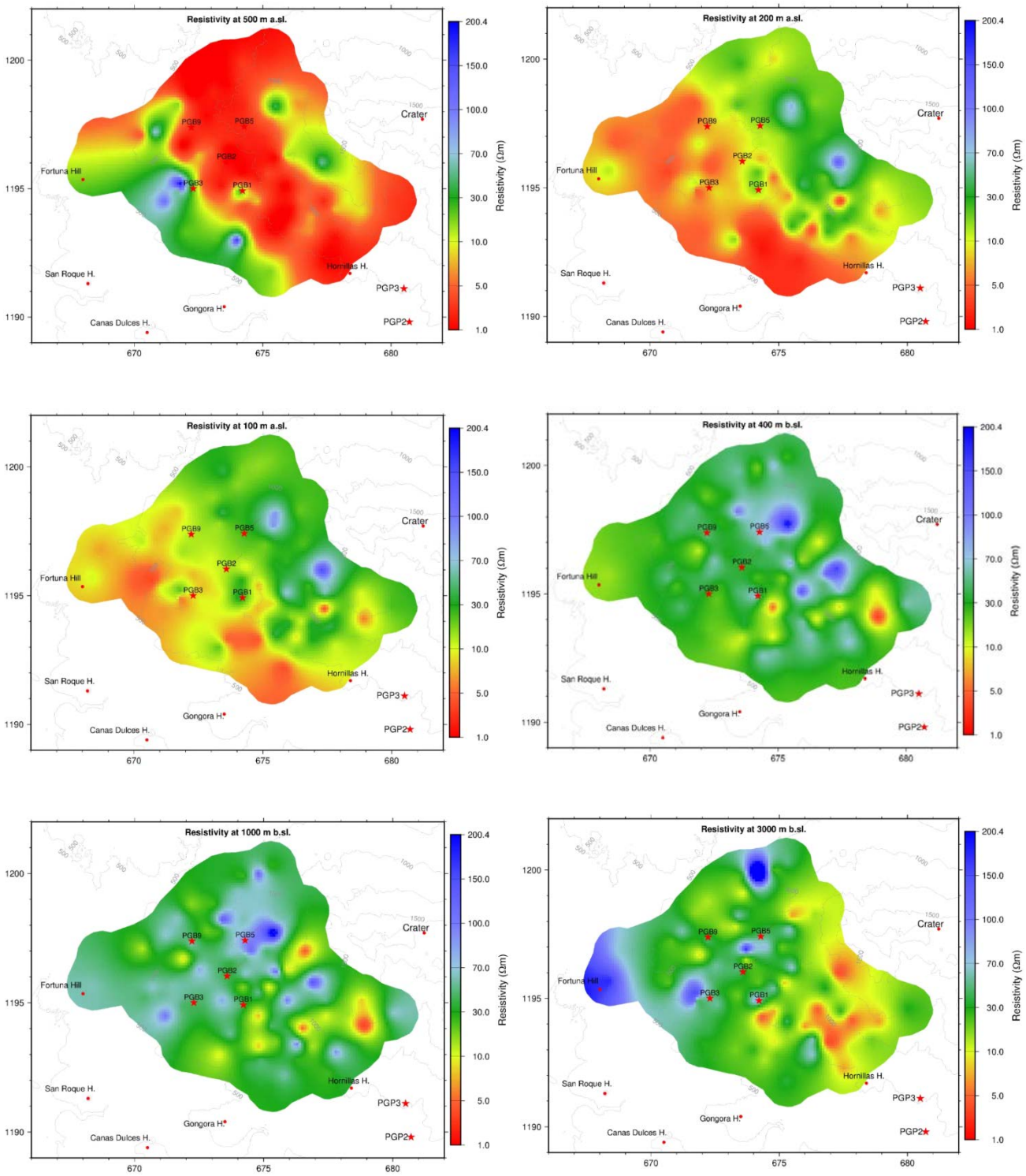

APPENDIX D: 3D inversion data fit

A data fit for all the inverted soundings presented as apparent resistivity and phase and the calculated response of the final model from the 50 Ωm homogeneous half-space as initial model. The data misfit is defined as the RMS (Root-Mean-Square) of the difference between the measured and calculated values of the off diagonal tensor elements (real and imaginary parts). The RMS misfit for the different cases is presented in Table 2.

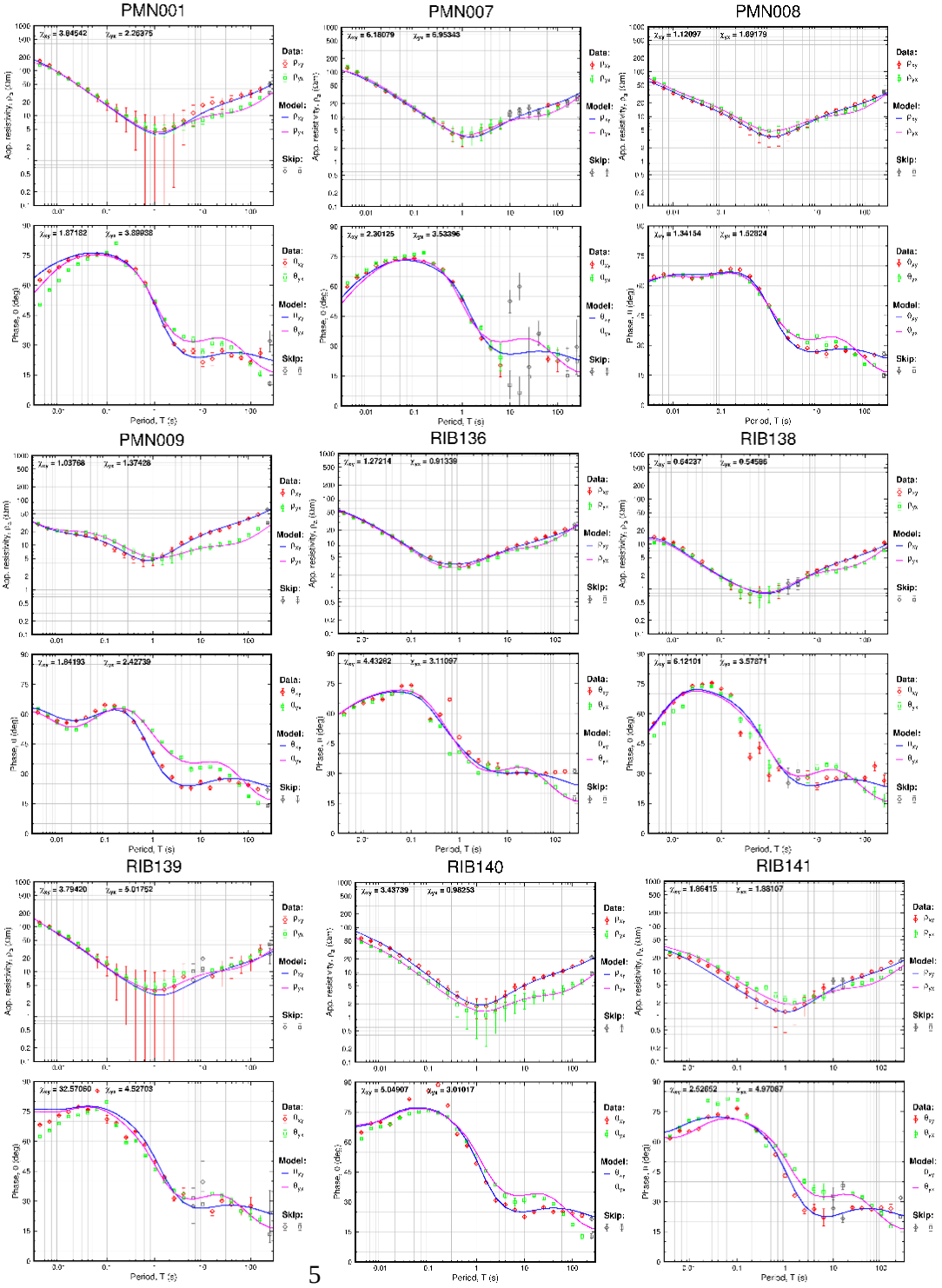

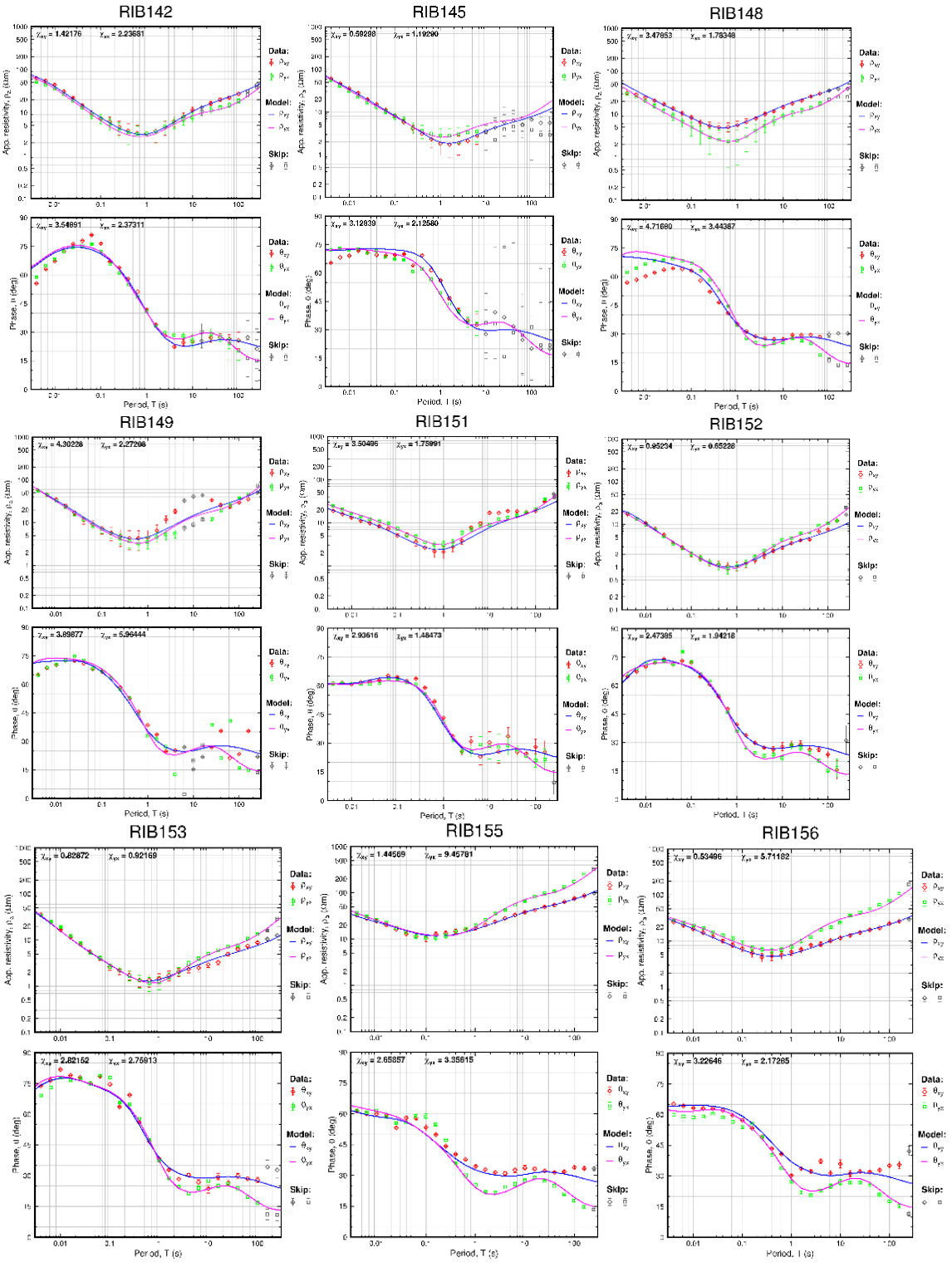
RIB142
RIB145
RIB148
RIB149
RIB151
RIB152
RIB153
RIB155
RIB156
Data:
Model:
Skip:
Period, T (s)
Period, t (s)

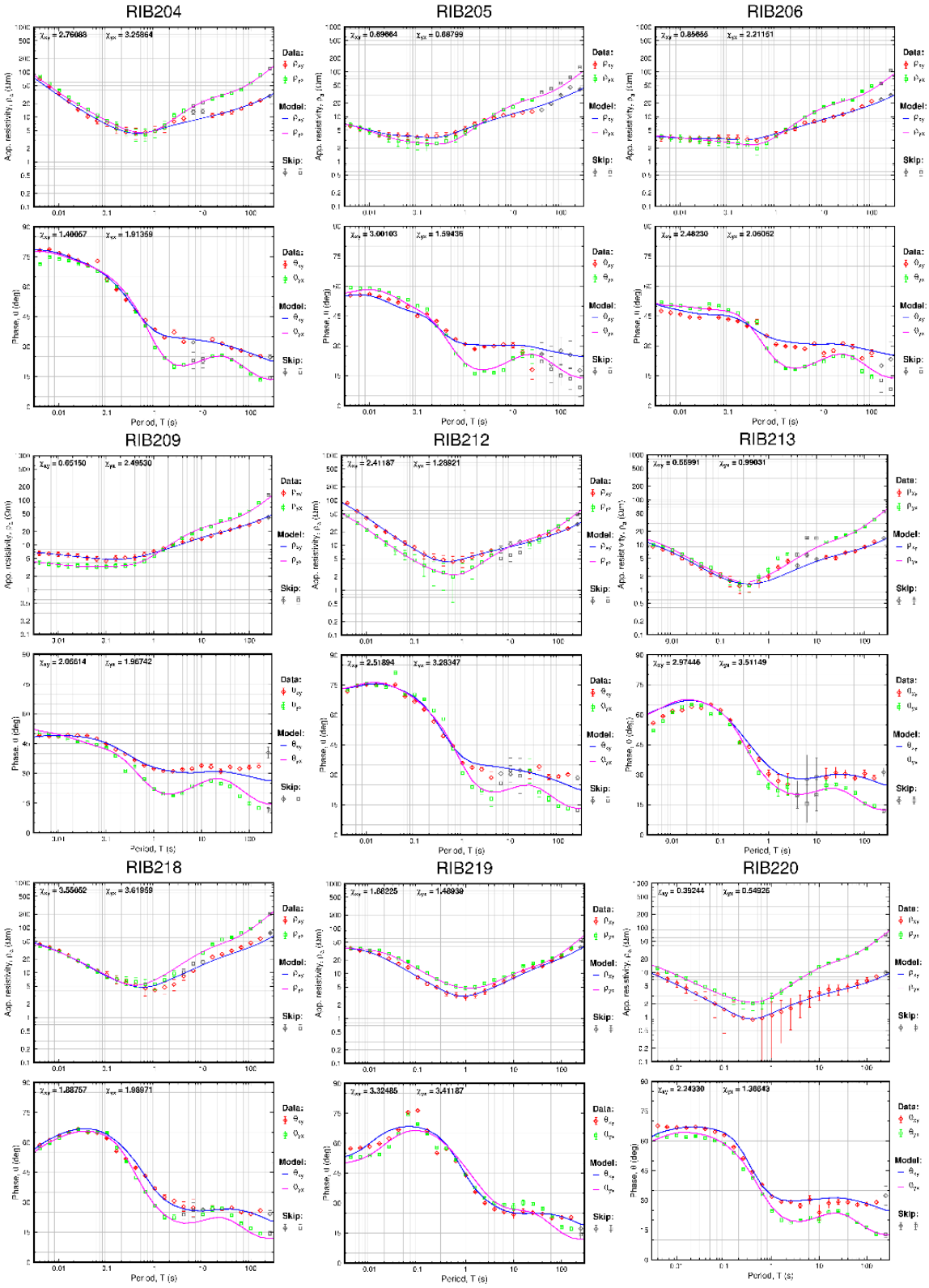
RIB204
RIB205
RIB206
RIB209
RIB212
RIB213
RIB218
RIB219
RIB220
Period, T (s)
Data:
Model:
Skip:

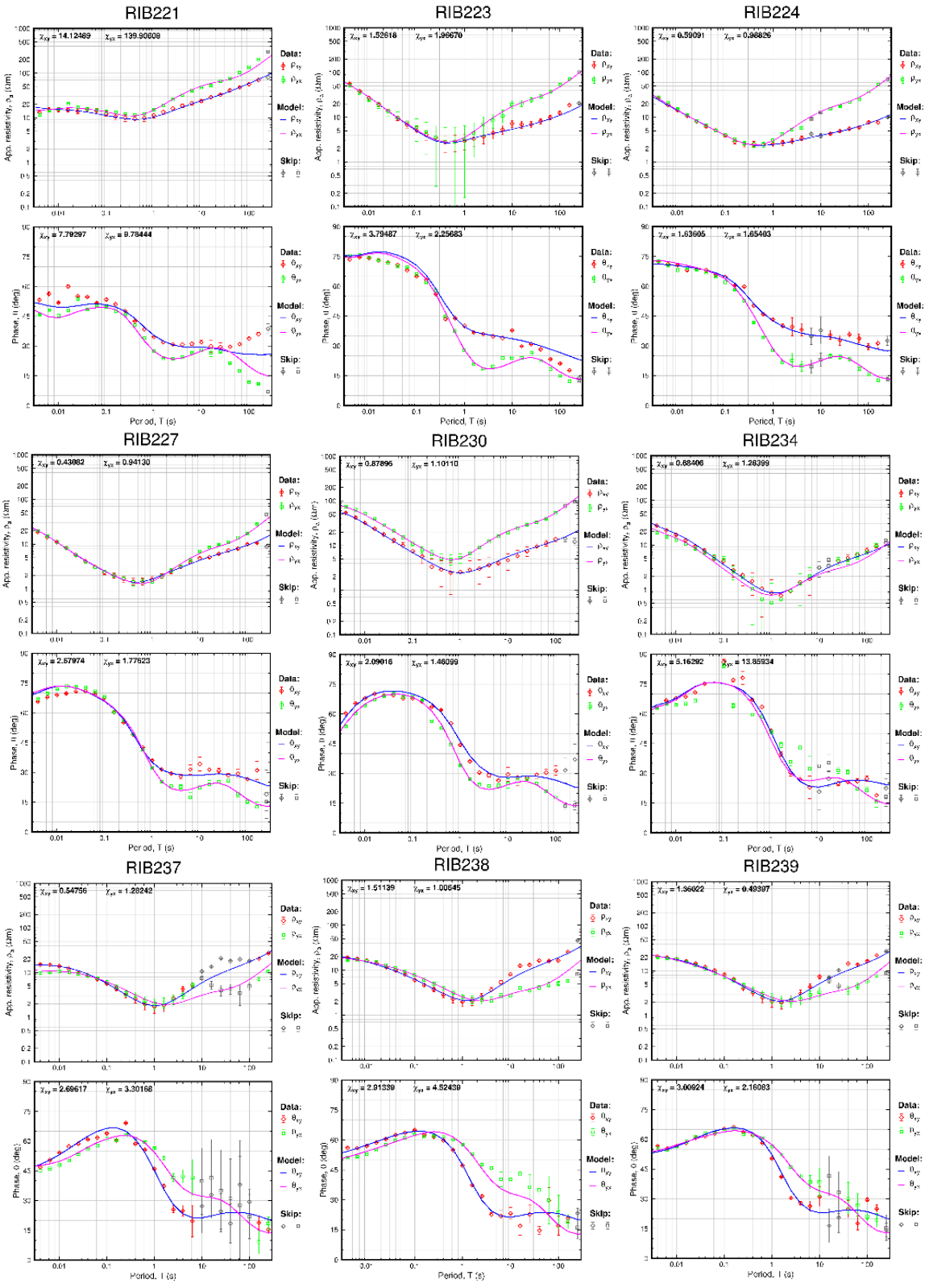
RIB221
RIB223
RIB224
RIB227
RIB230
RIB234
RIB237
RIB238
RIB239
Period, T (s)

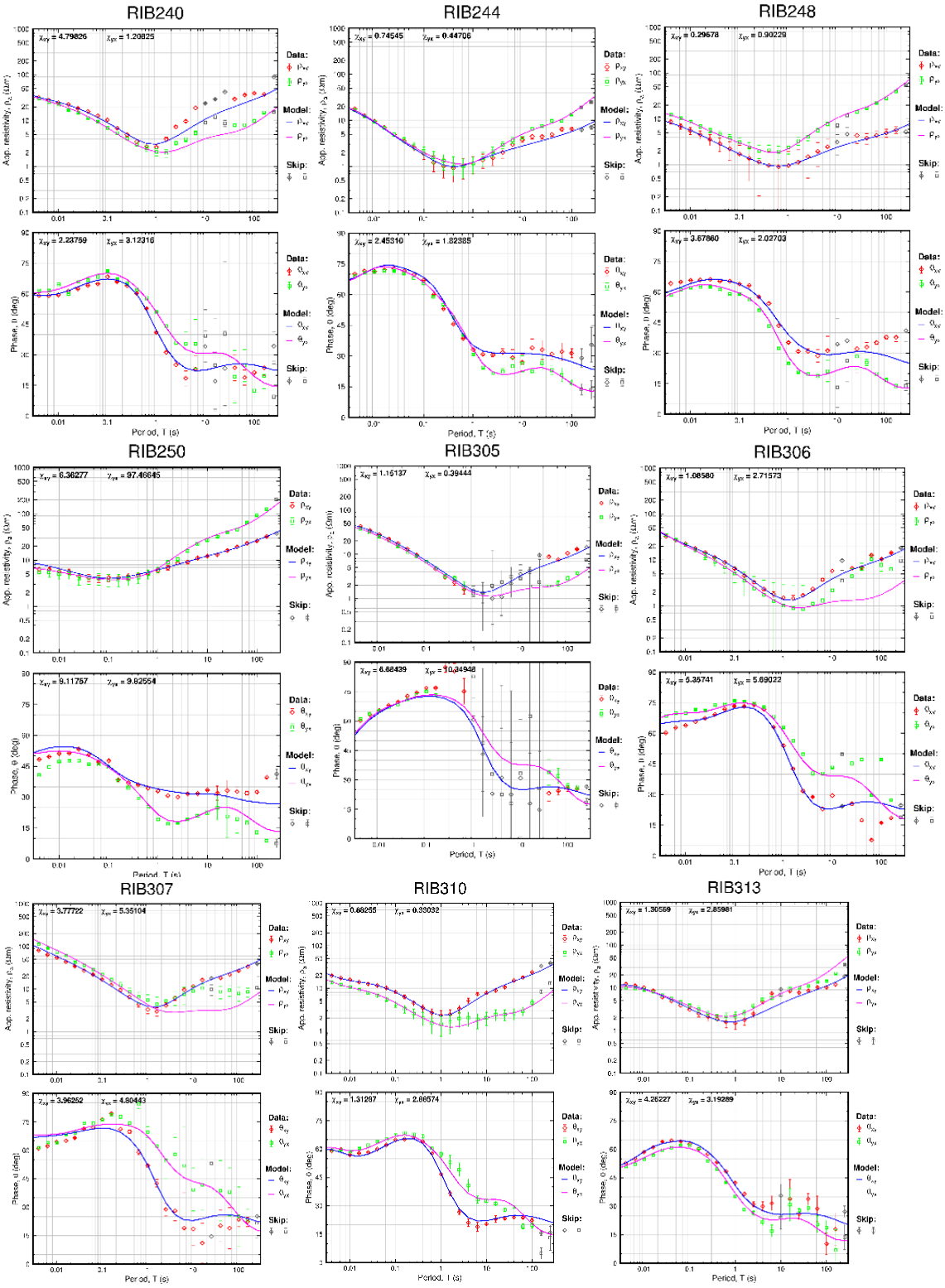
RIB240
RIB244
RIB248
RIB250
RIB305
RIB306
RIB307
RIB310
RIB313
Data:
Model:
Skip:
Period, T (s)

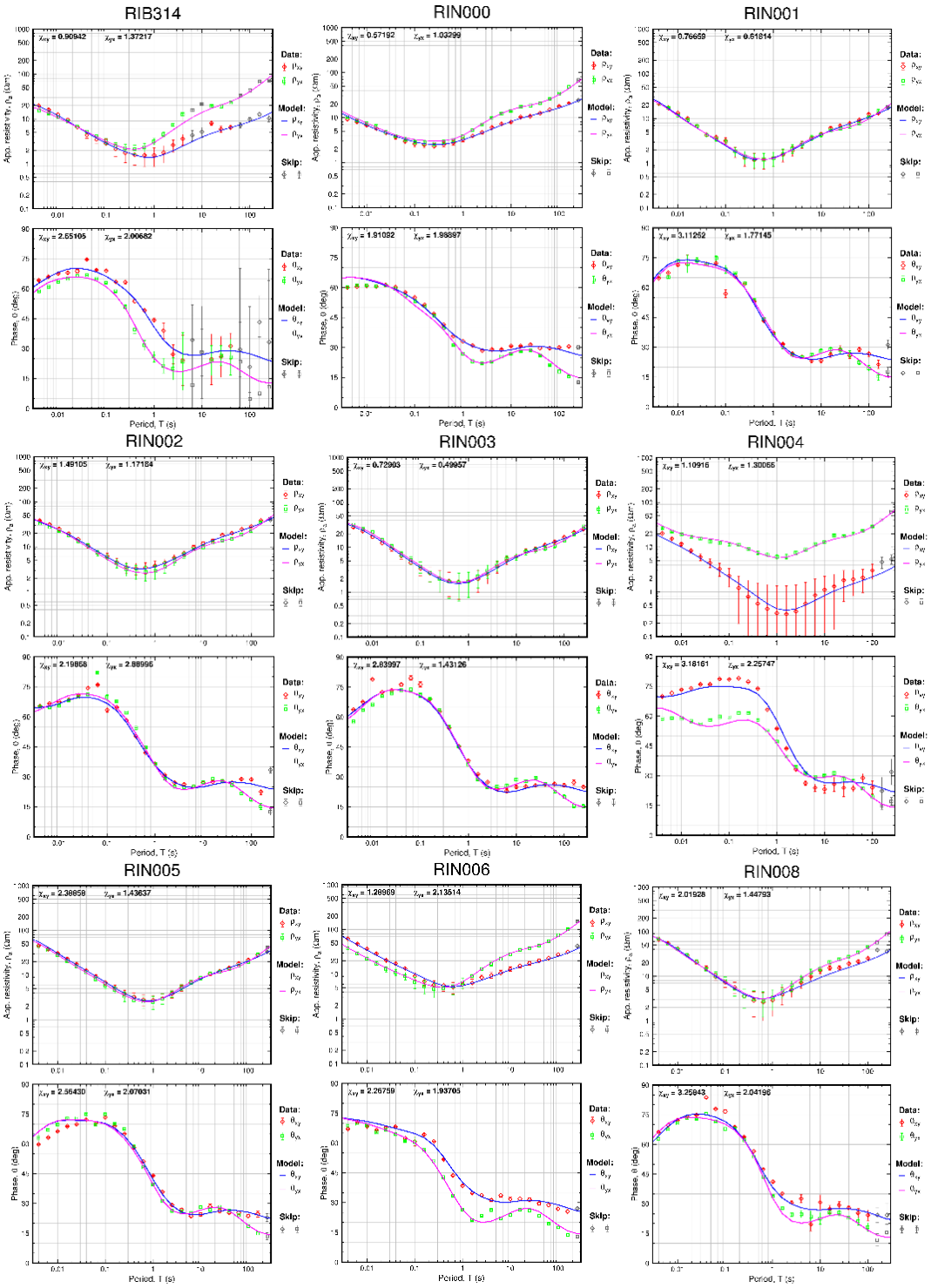
RIB314
RIN000
RIN001
RIN002
RIN003
RIN004
RIN005
RIN006
RIN008
Period, T (s)

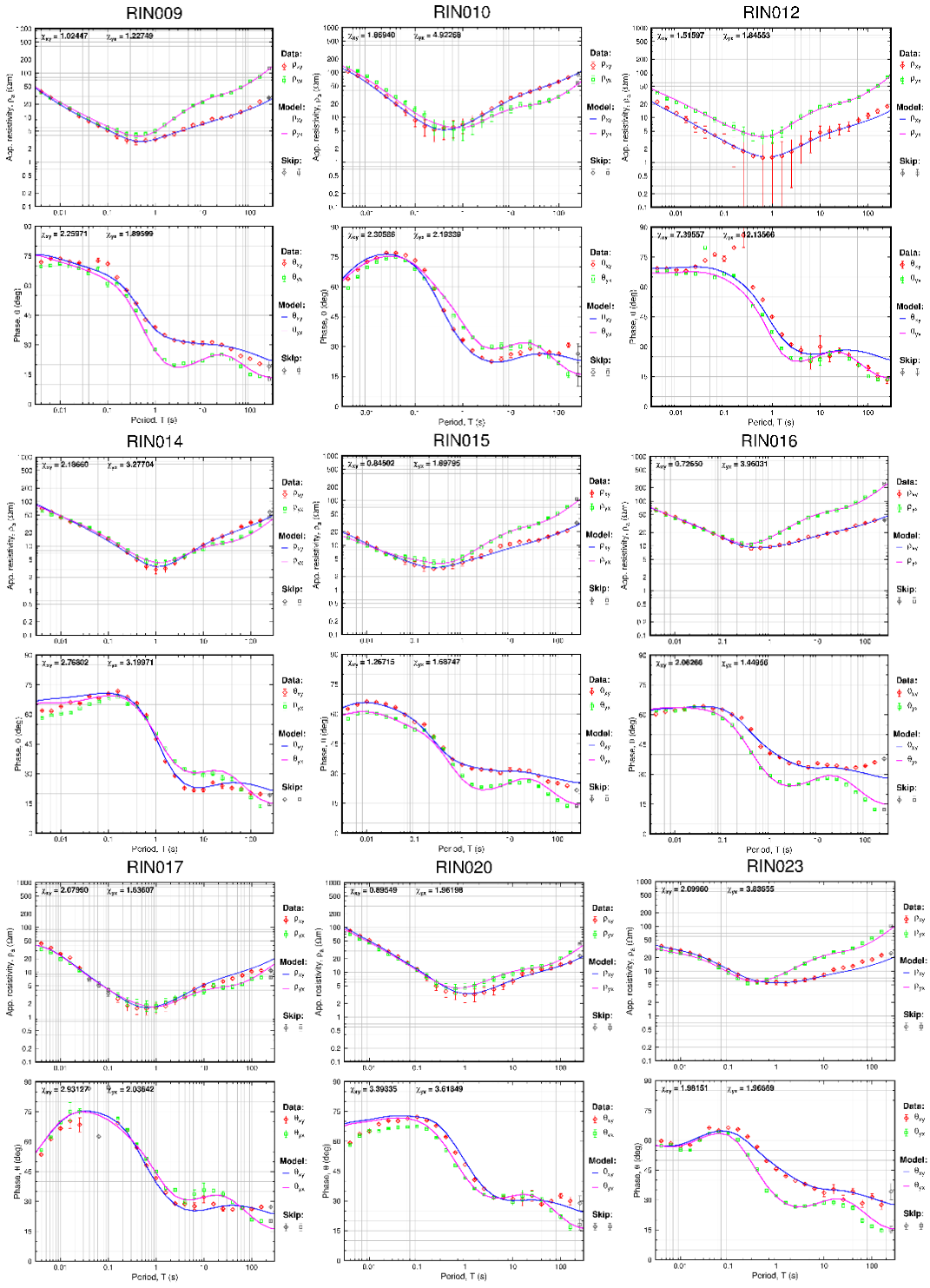
RIN009
RIN010
RIN012
RIN014
RIN015
RIN016
RIN017
RIN020
RIN023
Data:
Model:
Skip:
Period, T (s)

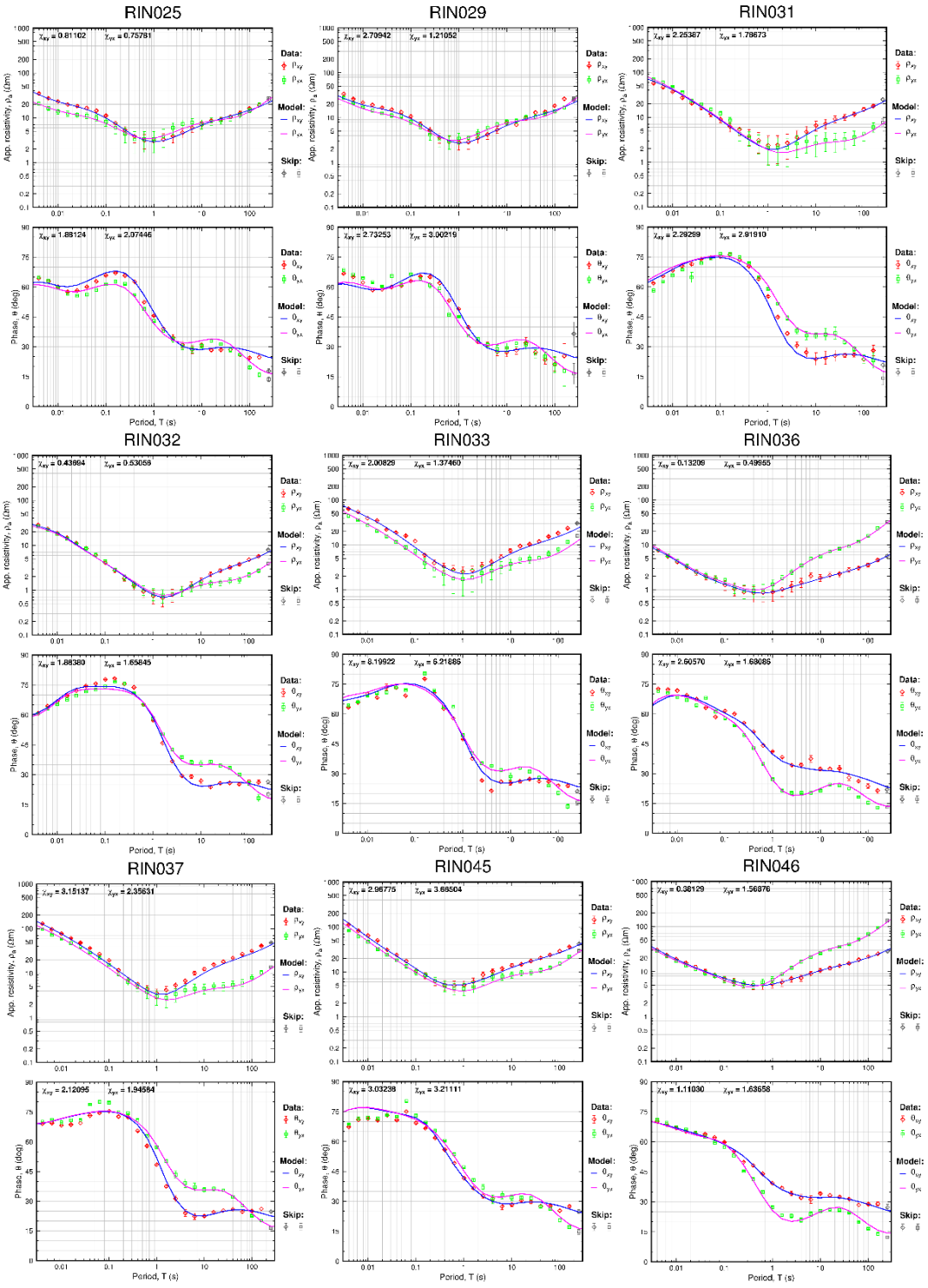
RIN025
RIN029
RIN031
RIN032
RIN033
RIN036
RIN037
RIN045
RIN046
App. resistivity, ρa (Ωm)
Phase, ϕ (deg)
Period, T (s)
Data:
Model:
Skip:

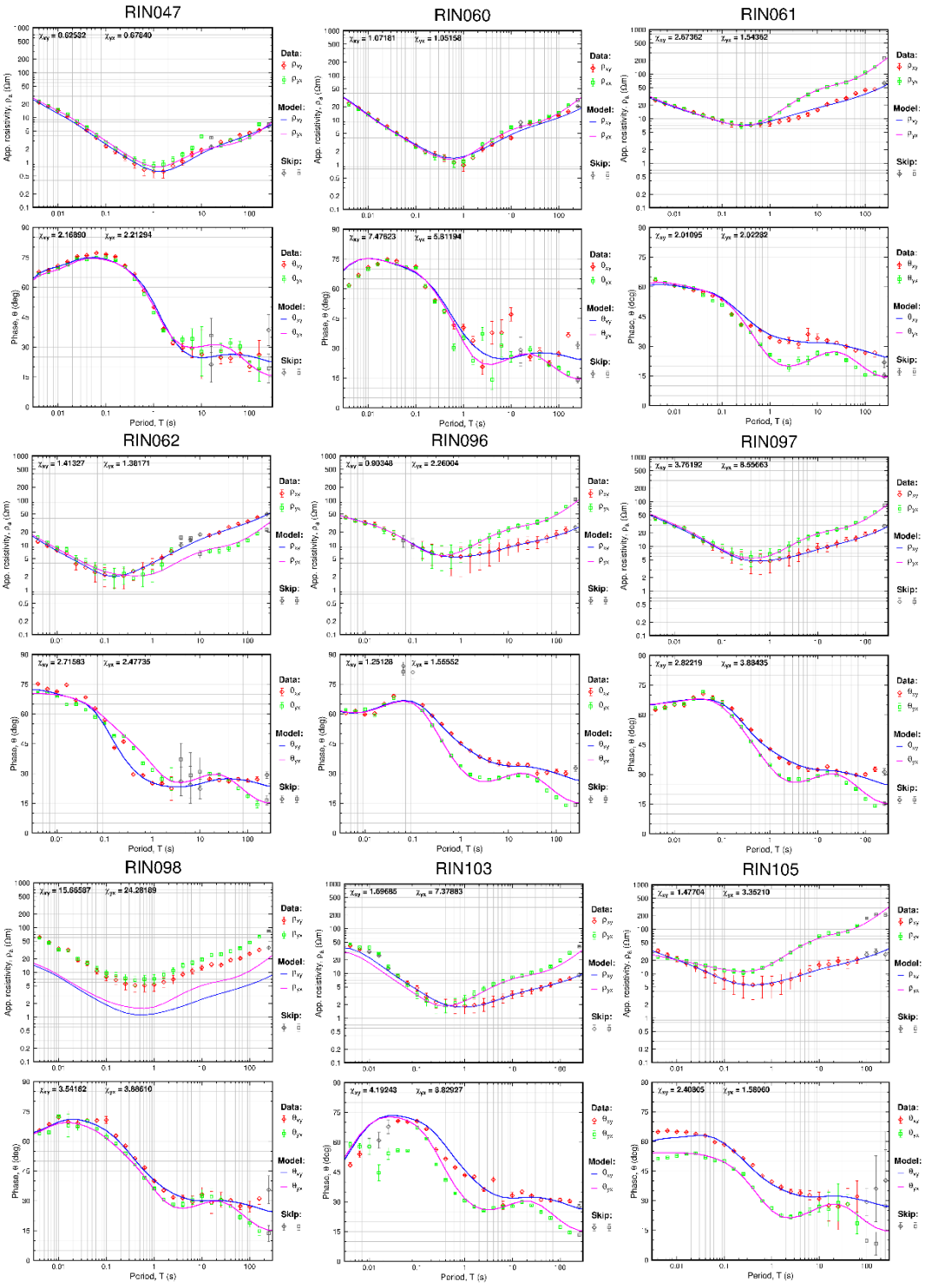
RIN047
RIN060
RIN061
RIN062
RIN096
RIN097
RIN098
RIN103
RIN105
Period, T (s)

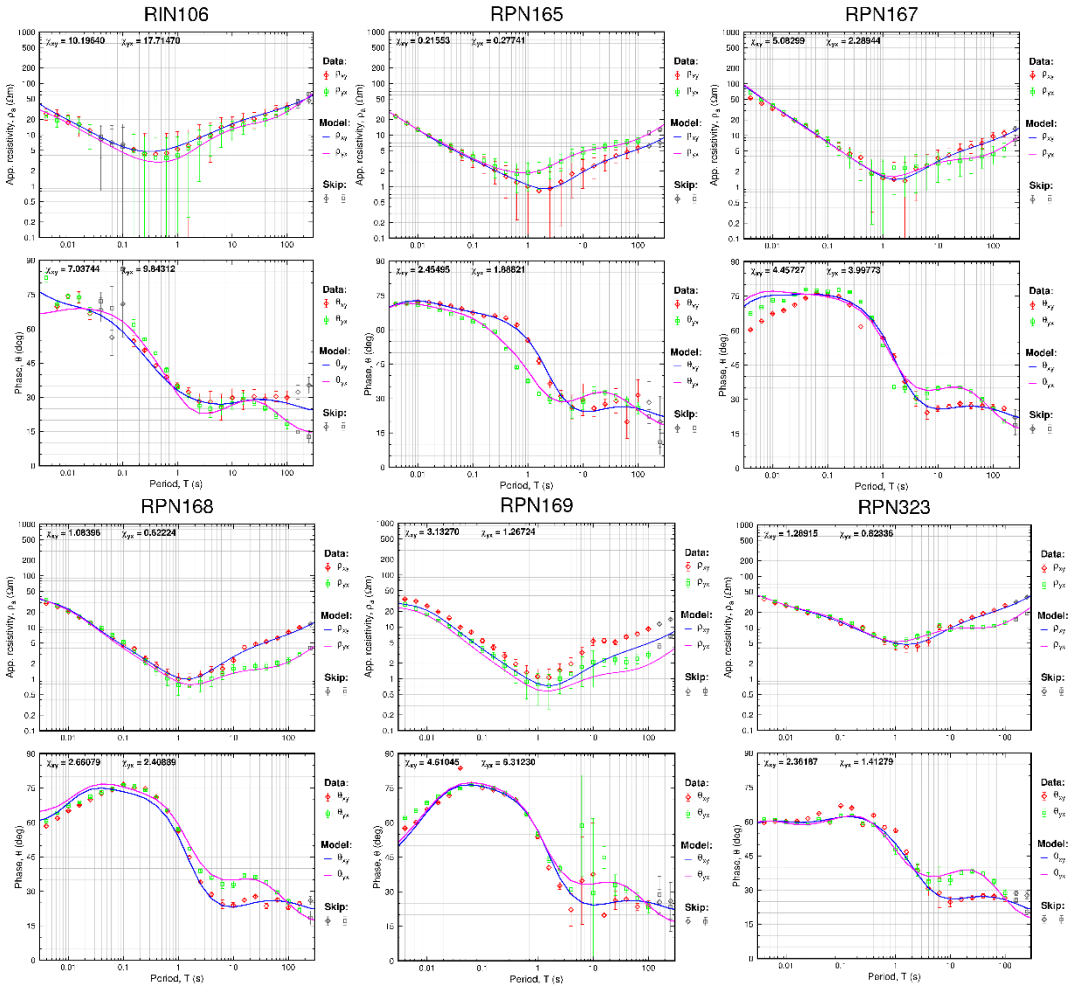
RIN106
RPN165
RPN167
RPN168
RPN169
RPN323
App. resistivity, ρa (Ωm)
Phase, Φ (deg)
Period, T (s)
Data:
Model:
Skip:

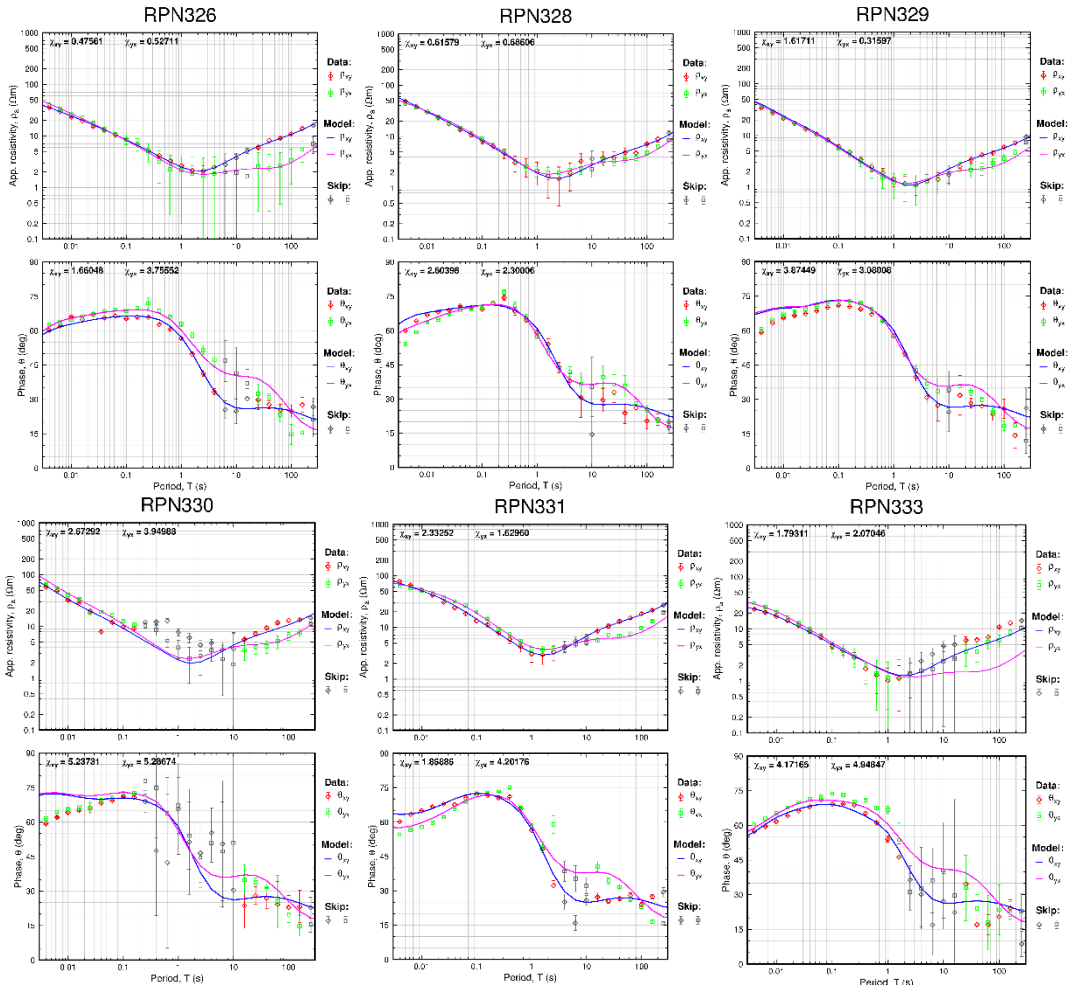
RPN326
RPN328
RPN329
RPN330
RPN331
RPN333
Period, T (s)

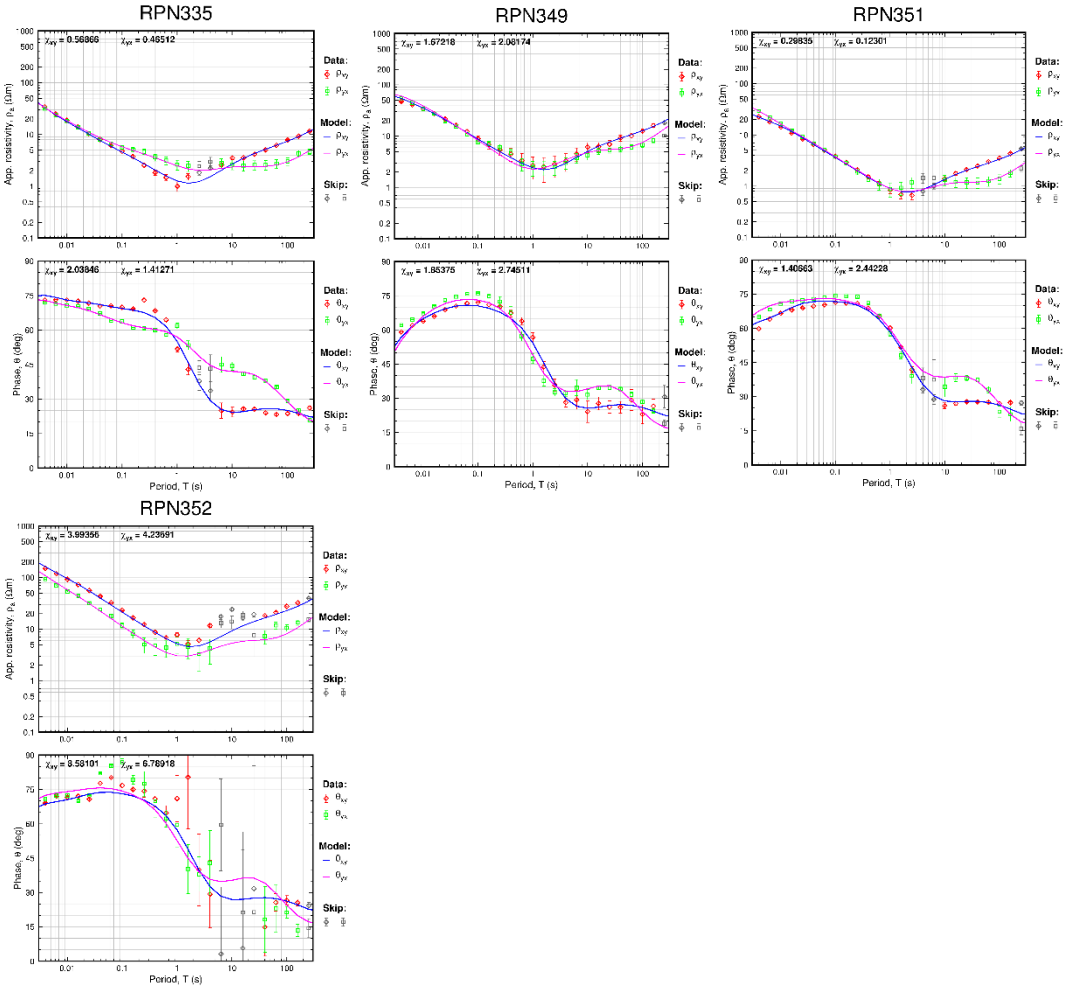

APPENDIX E: Resistivity depth slices based on the 3D inversion

Smoothed elevation corrected resistivity slices through the dense part of the model grid, from the 50 Ωm homogeneous half-space as initial model. The coordinates are in km, UTM-Z16.

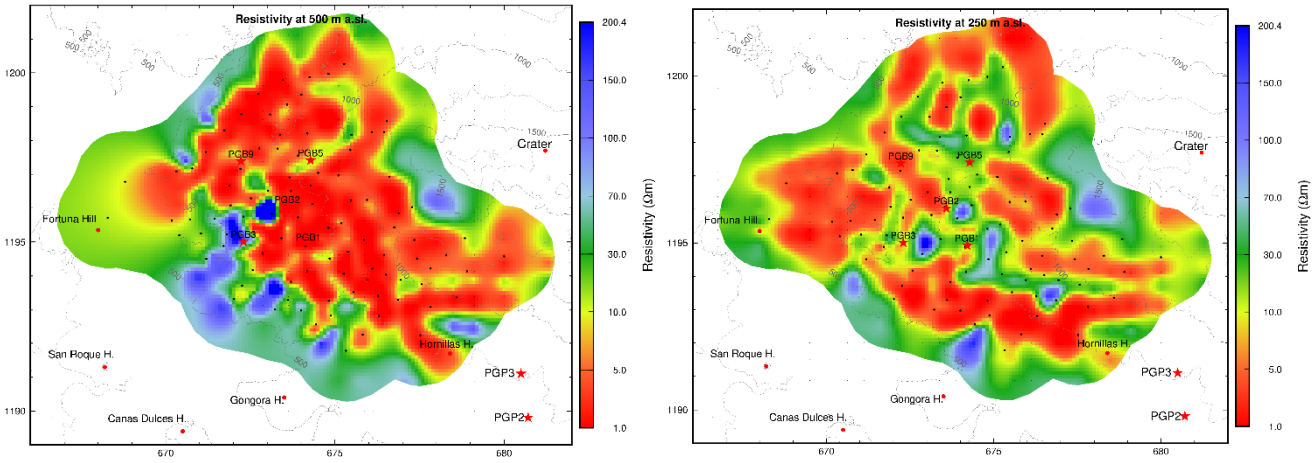
Resistivity at 500 m a.s.l.
Resistivity at 250 m a.s.l.
Crater
Fortuna Hill
San Roque H.
Canas Dulces H.
Gongora H.
Hornillas H.
PGB9
PGB5
PGB2
PGB3
PGB1
PGP3
PGP2
Resistivity (Ωm)
200.4
150.0
100.0
70.0
30.0
10.0
5.0
1.0
1200
1195
1190
670
675
680

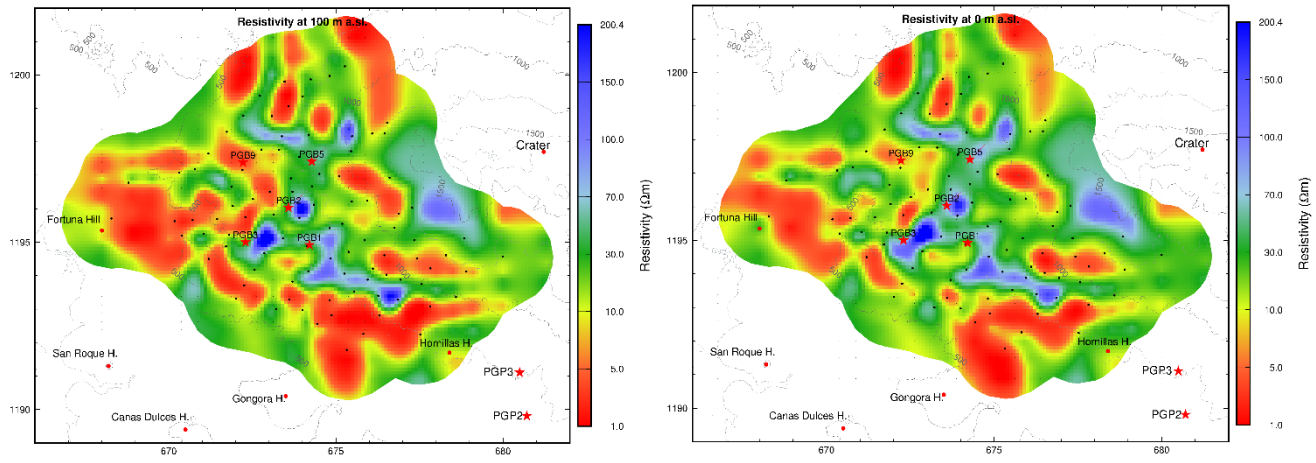
Resistivity at 100 m a.s.l.
Resistivity at 0 m a.s.l.
Crater
Fortuna Hill
San Roque H.
Canas Dulces H.
Gongora H.
Hornillas H.
PGB9
PGB5
PGB2
PGB3
PGB1
PGP3
PGP2
Resistivity (Ωm)
200.4
150.0
100.0
70.0
30.0
10.0
5.0
1.0
1200
1195
1190
670
675
680

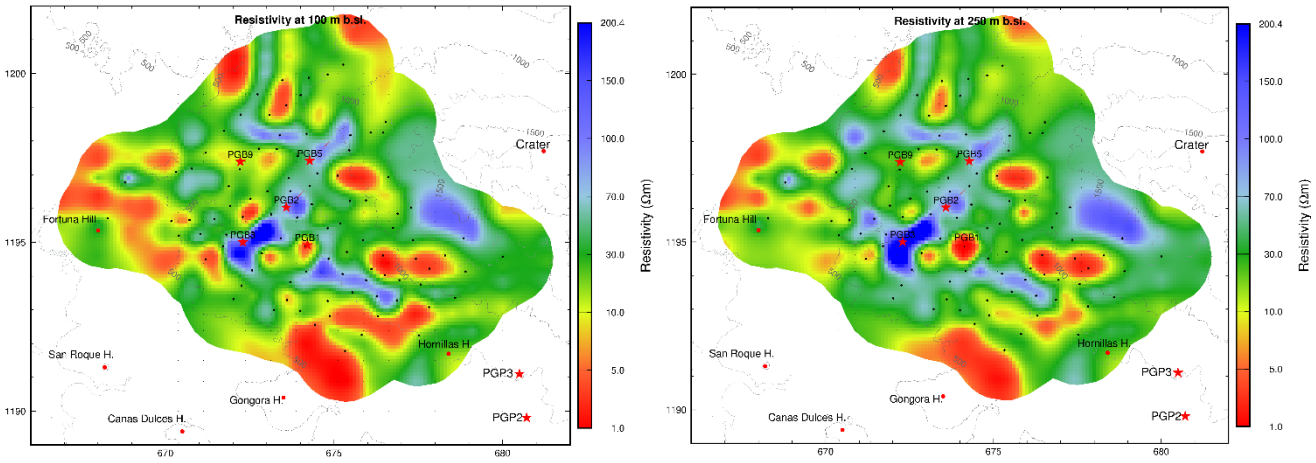
Resistivity at 100 m b.s.l.
Resistivity at 250 m b.s.l.
Crater
Fortuna Hill
San Roque H.
Canas Dulces H.
Gongora H.
Hornillas H.
PGB9
PGB5
PGB2
PGB3
PGB1
PGP3
PGP2
Resistivity (Ωm)
200.4
150.0
100.0
70.0
30.0
10.0
5.0
1.0
1200
1195
1190
670
675
680

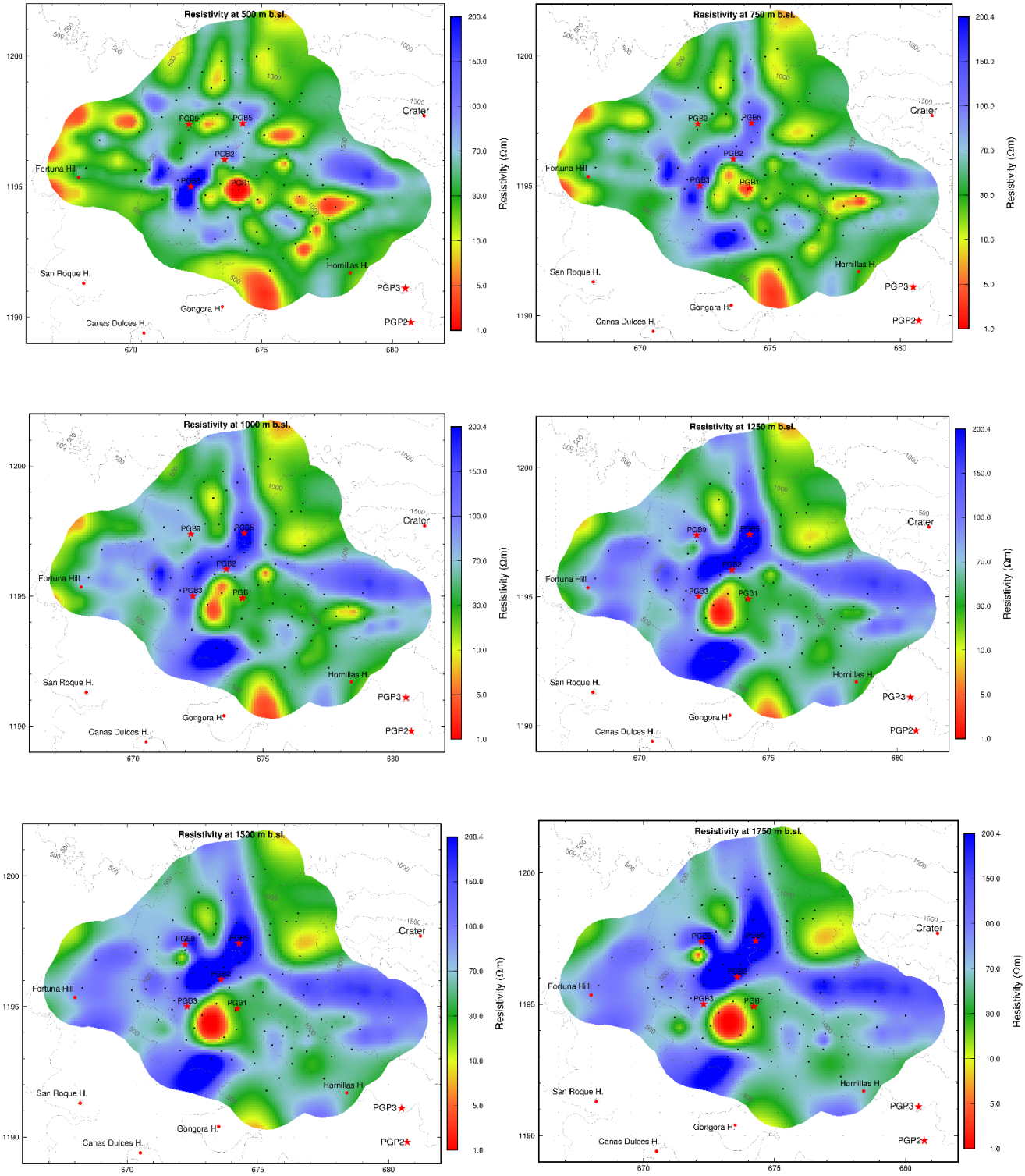
Resistivity at 500 m b.s.l.
Resistivity at 750 m b.s.l.
Resistivity at 1000 m b.s.l.
Resistivity at 1250 m b.s.l.
Resistivity at 1500 m b.s.l.
Resistivity at 1750 m b.s.l.
Crater
Fortuna Hill
San Roque H.
Hornillas H.
Gongora H.
Canas Dulces H.
PGB1
PGB2
PGB3
PGB5
PGB6
PGP2
PGP3
Resistivity (Ωm)
200.0
150.0
100.0
70.0
30.0
10.0
5.0
1.0
1200
1195
1190
670
675
680

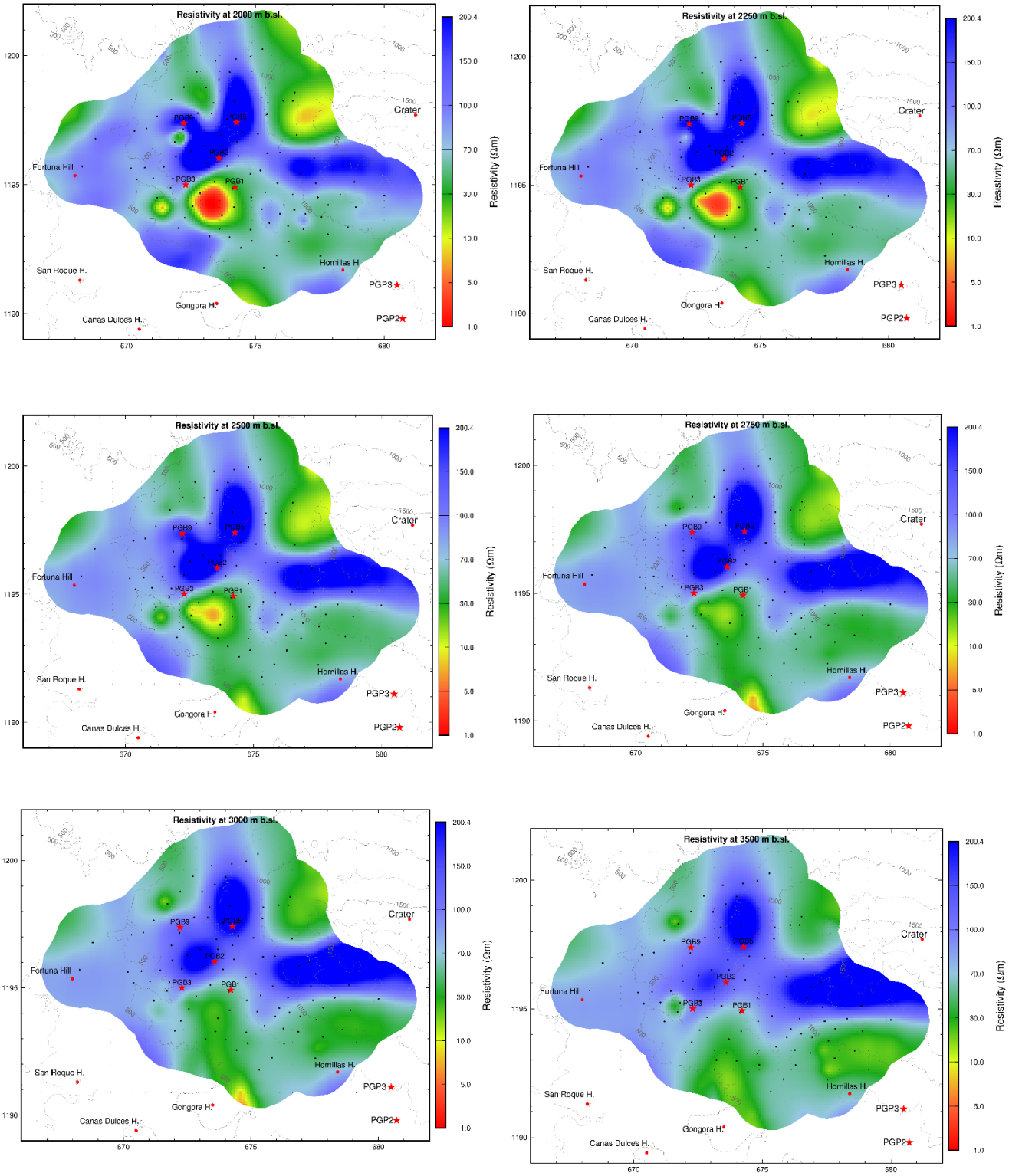
Resistivity at 2000 m b.sl.
Resistivity at 2250 m b.sl.
Resistivity at 2500 m b.sl.
Resistivity at 2750 m b.sl.
Resistivity at 3000 m b.sl.
Resistivity at 3500 m b.sl.
Crater
Fortuna Hill
San Roque H.
Hornillas H.
Gongora H.
Canas Dulces H.
PGB1
PGB2
PGB3
PGB5
PGB9
PGP2
PGP3
Resistivity (Ωm)
200.4
150.0
100.0
70.0
30.0
10.0
5.0
1.0

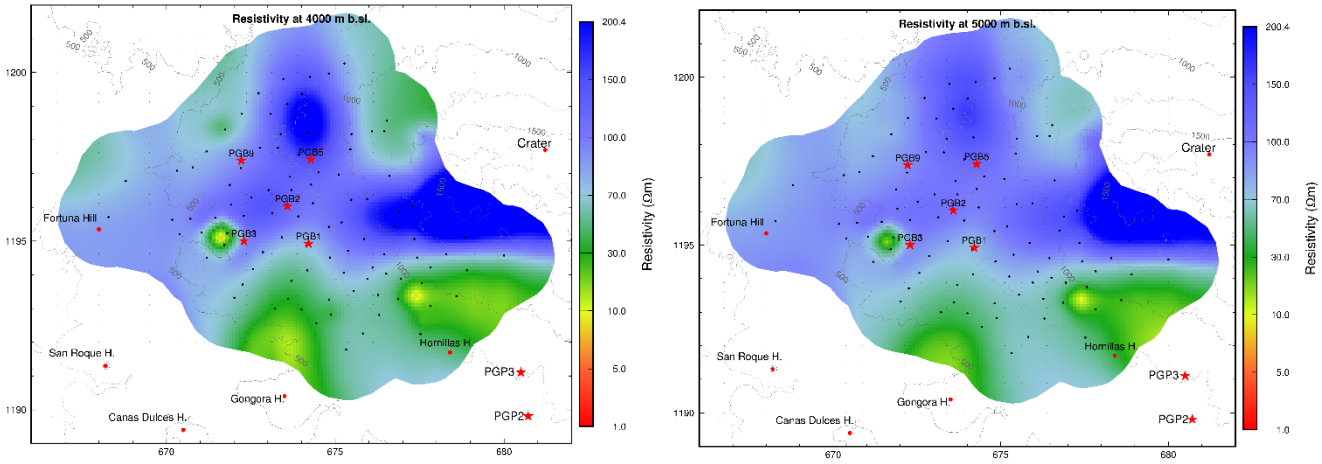

APPENDIX F: Resistivity cross sections based on the 3D inversion

Smoothed elevation corrected E-W and N-S lying cross-sections, through the dense part of the model grid, from the 50 Ωm homogeneous half-space as initial model. They go ~2 km further in each direction. Their locations is given in the next Figure.

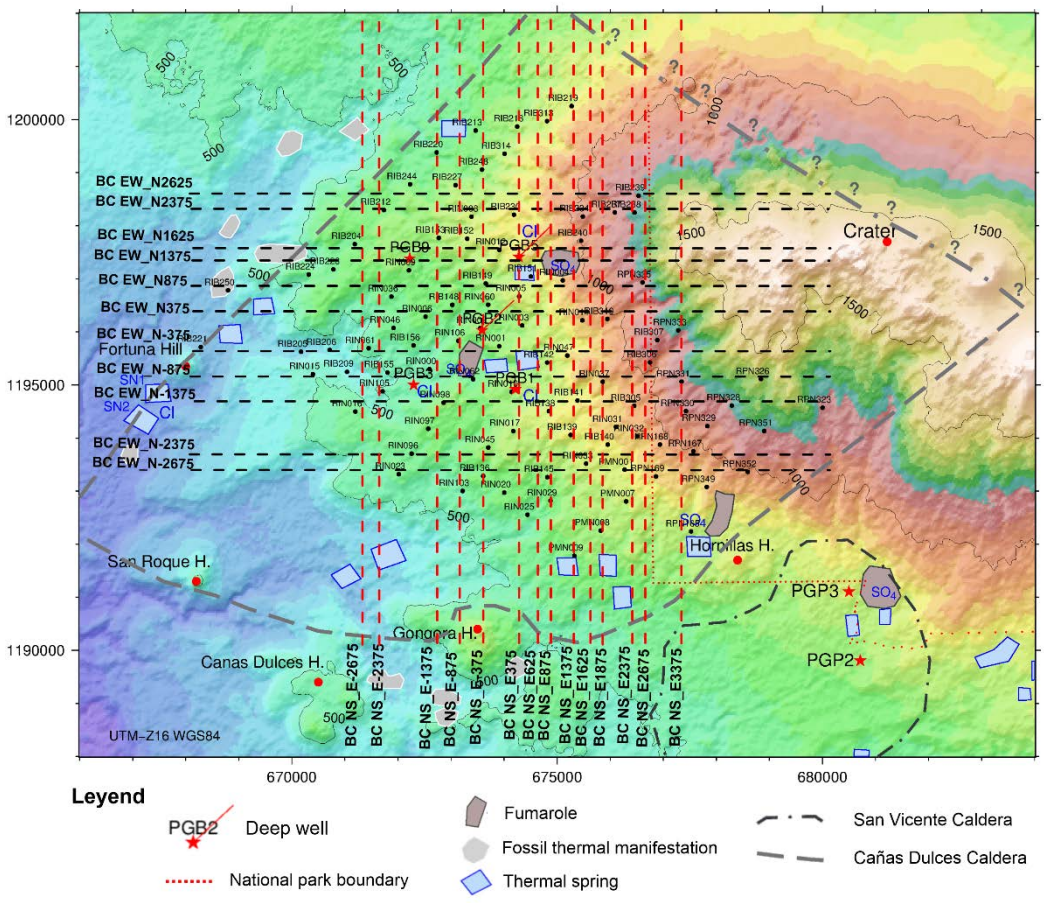

First, the E-W lying cross sections from south to north:

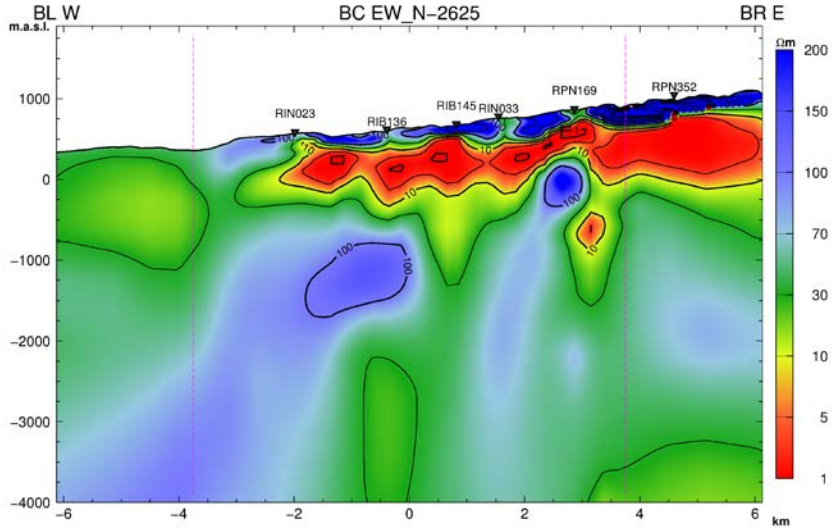

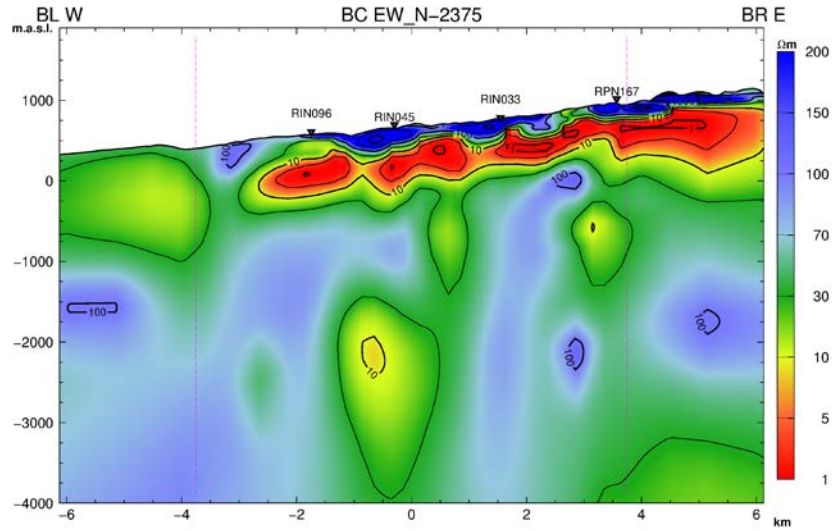

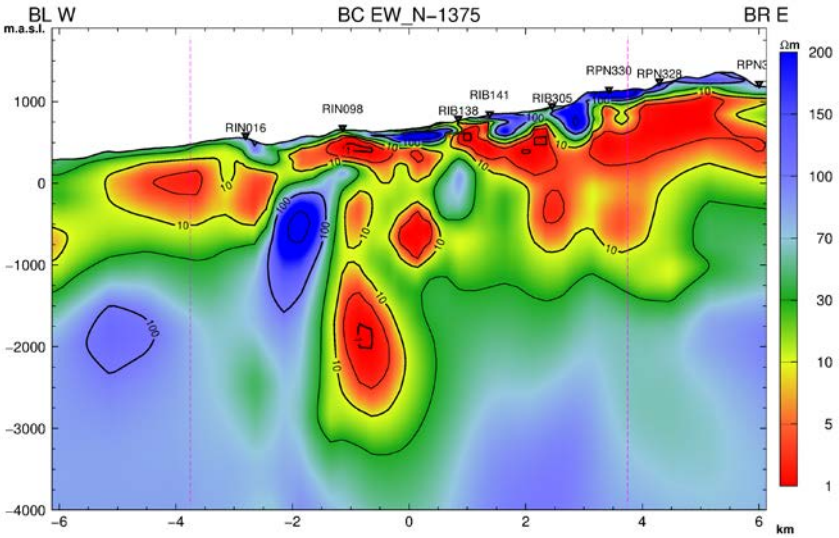

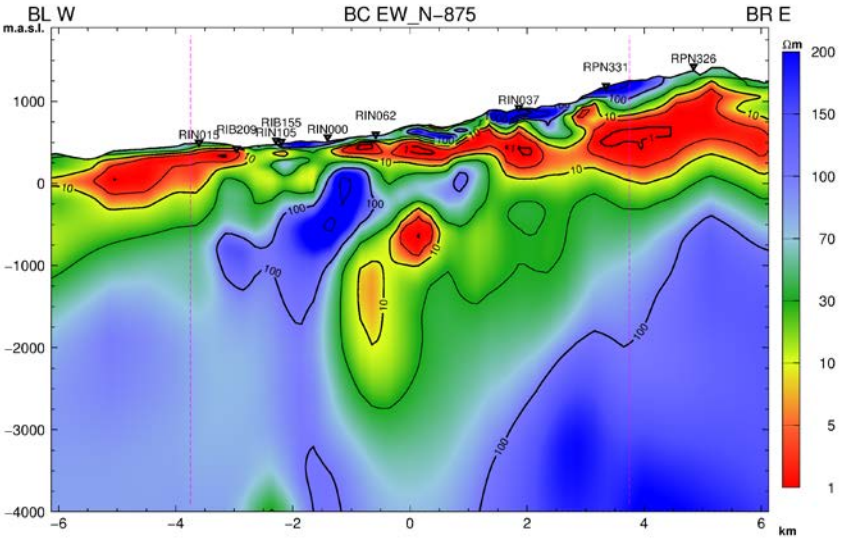
BL W
BC EW_N-875
BR E
m.a.s.l.
Ωm
200
150
100
70
30
10
5
1
km
RPN331
RPN326
RIN037
RIN062
RIB155
RIB209
RIN105
RIN000
RIN015
1000
0
-1000
-2000
-3000
-4000
-6
-4
-2
0
2
4
6

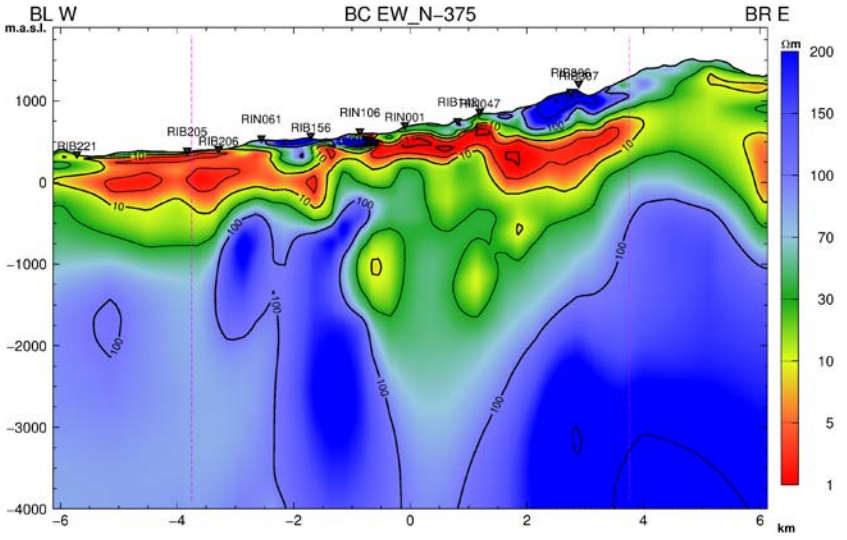
BL W
BC EW_N-375
BR E
m.a.s.l.
Ωm
200
150
100
70
30
10
5
1
km
RIB221
RIB205
RIB206
RIN061
RIB156
RIN106
RIN001
RIB047
1000
0
-1000
-2000
-3000
-4000
-6
-4
-2
0
2
4
6

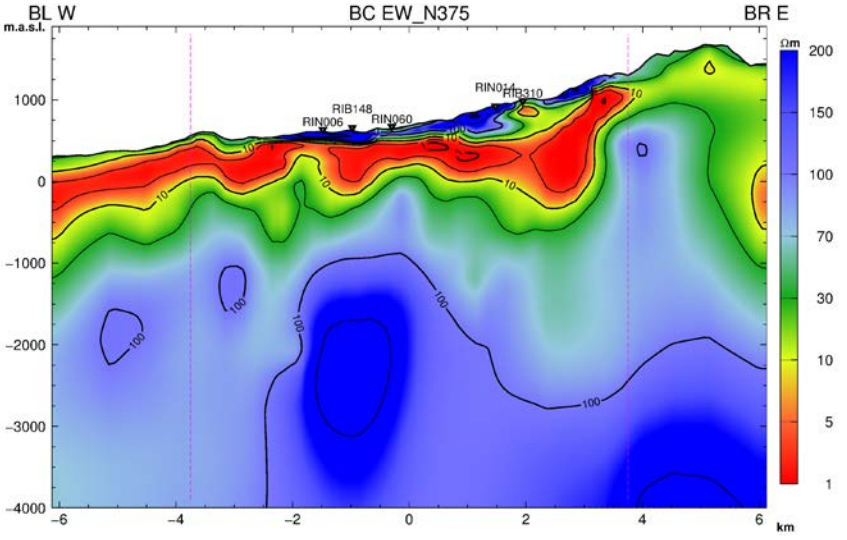
BL W
BC EW_N375
BR E
m.a.s.l.
Ωm
200
150
100
70
30
10
5
1
km
RIB148
RIN006
RIN060
RIB310
1000
0
-1000
-2000
-3000
-4000
-6
-4
-2
0
2
4
6

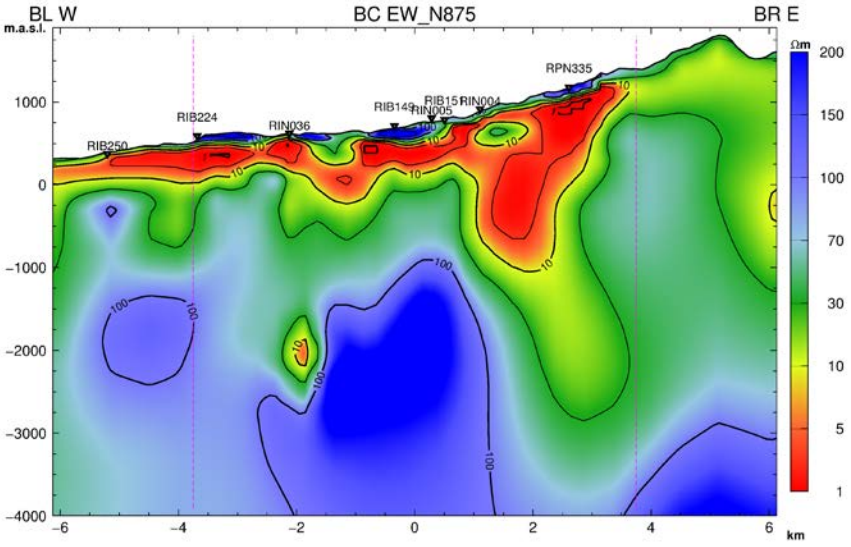
BL W
BC EW_N875
BR E
m.a.s.l.
Ωm
200
150
100
70
30
10
5
1
RPN335
RIB224
RIN036
RIB250
RIB15
RIN004
RIN005
1000
0
−1000
−2000
−3000
−4000
−6
−4
−2
0
2
4
6
km

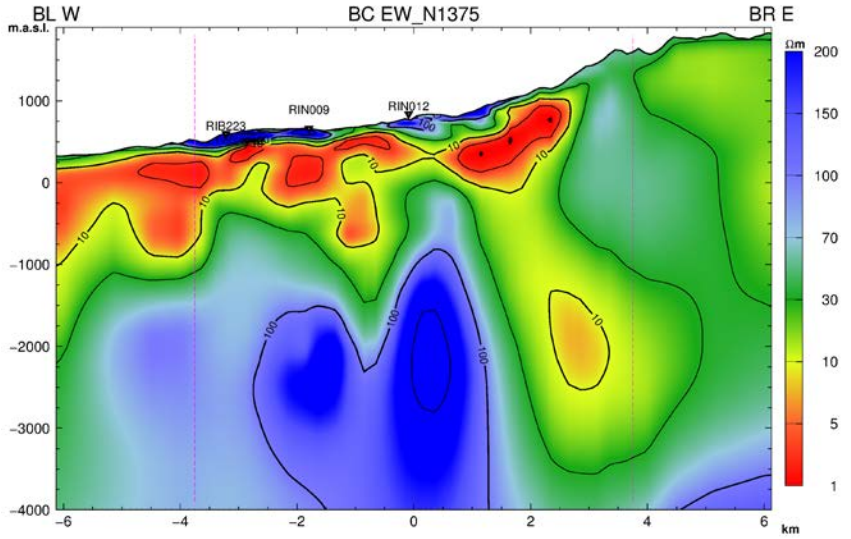
BL W
BC EW_N1375
BR E
m.a.s.l.
Ωm
200
150
100
70
30
10
5
1
RIN009
RIN012
RIB223
1000
0
−1000
−2000
−3000
−4000
−6
−4
−2
0
2
4
6
km

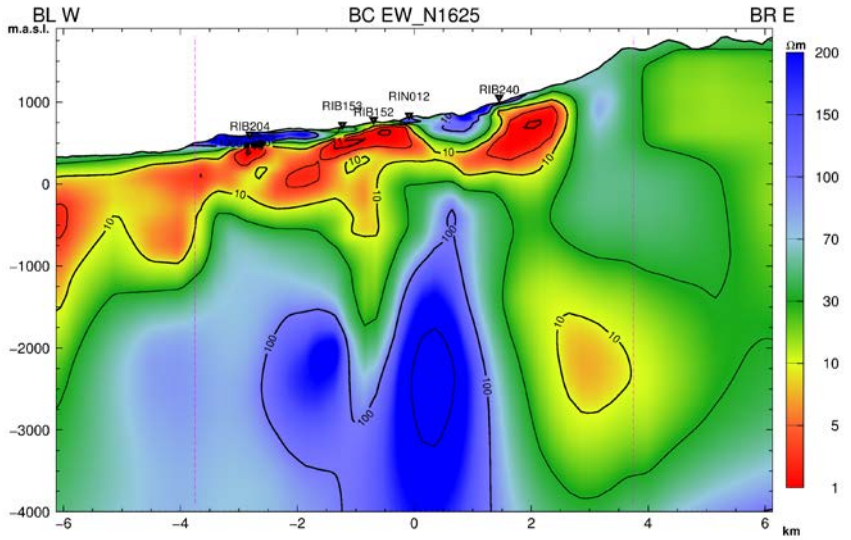
BL W
BC EW_N1625
BR E
m.a.s.l.
Ωm
200
150
100
70
30
10
5
1
RIB240
RIN012
RIB153
RIB152
RIB204
1000
0
−1000
−2000
−3000
−4000
−6
−4
−2
0
2
4
6
km

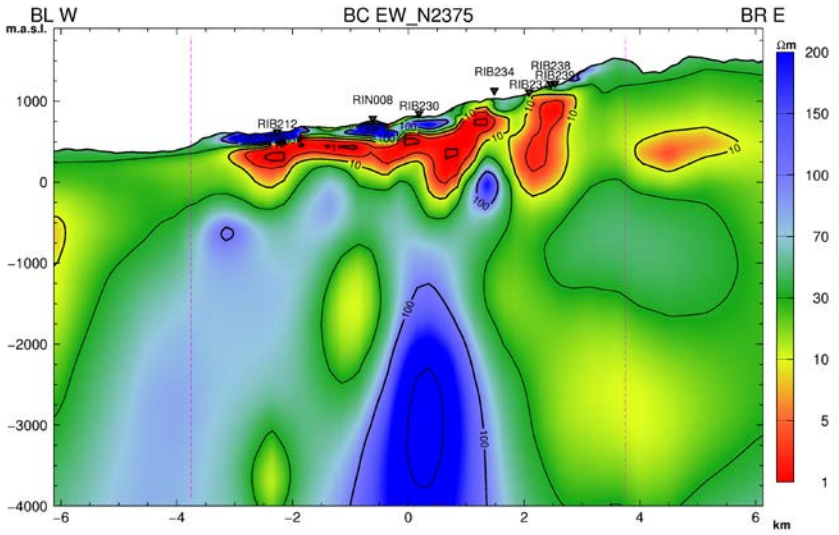
BL W
BC EW_N2375
BR E
m.a.s.l.
Ωm
200
150
100
70
30
10
5
1
RIB212
RIN008
RIB230
RIB234
RIB238
1000
0
−1000
−2000
−3000
−4000
−6
−4
−2
0
2
4
6
km

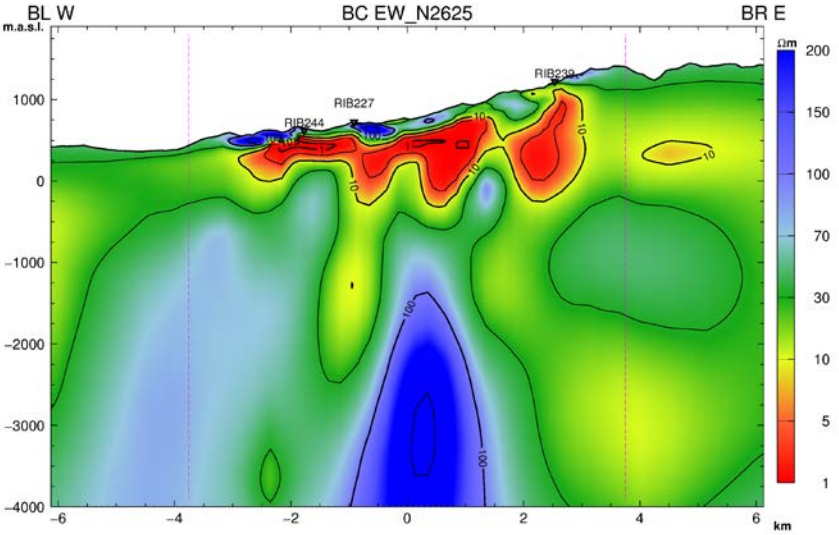
BL W
BC EW_N2625
BR E
m.a.s.l.
Ωm
200
150
100
70
30
10
5
1
RIB244
RIB227
RIB233
1000
0
−1000
−2000
−3000
−4000
−6
−4
−2
0
2
4
6
km

The N-S lying cross sections starting from west are:

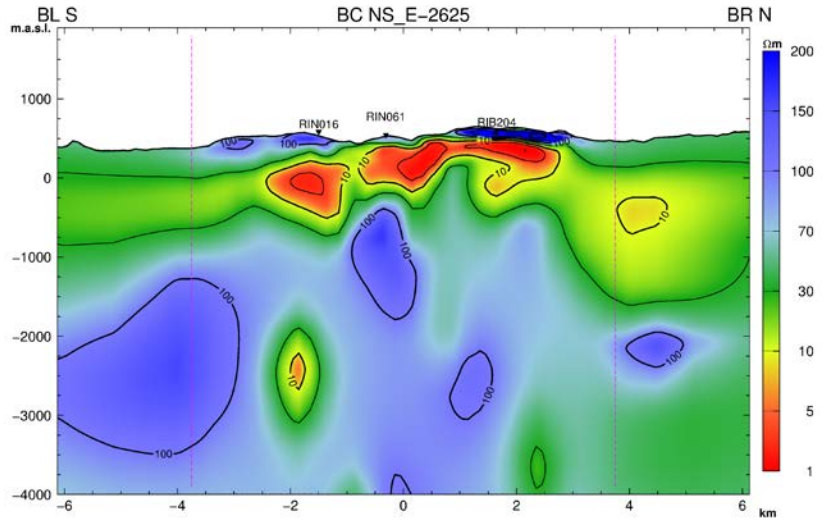

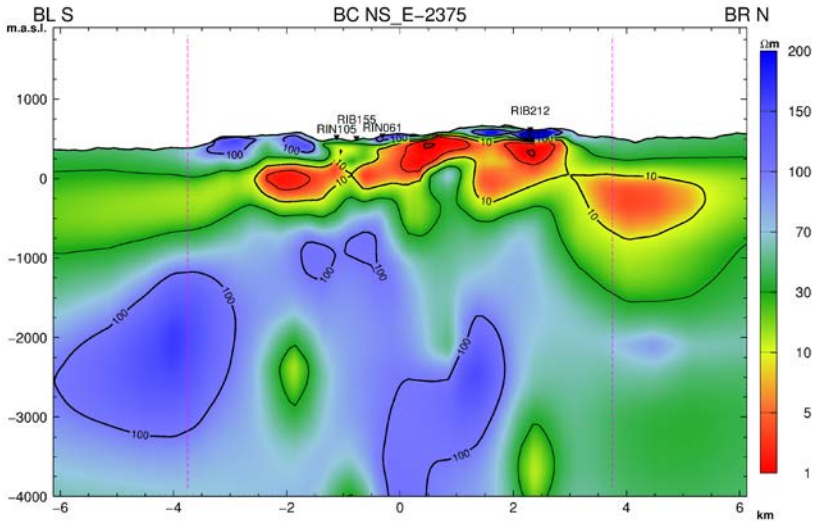

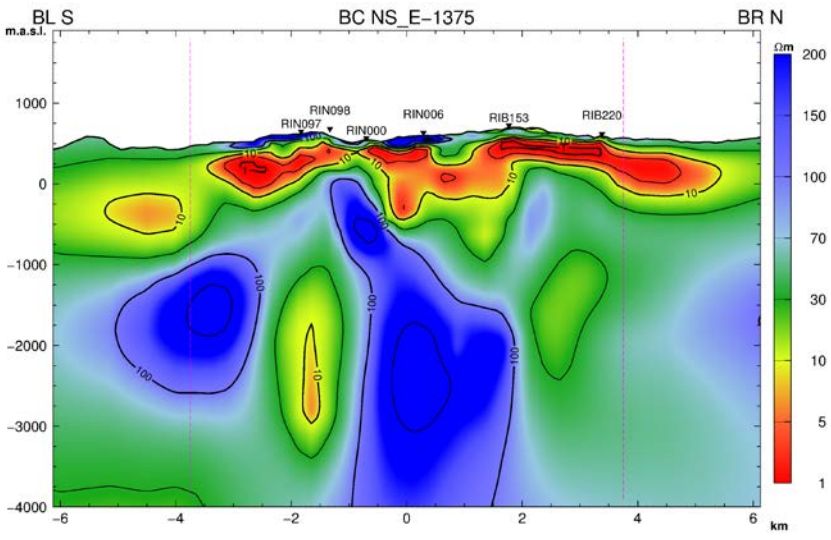

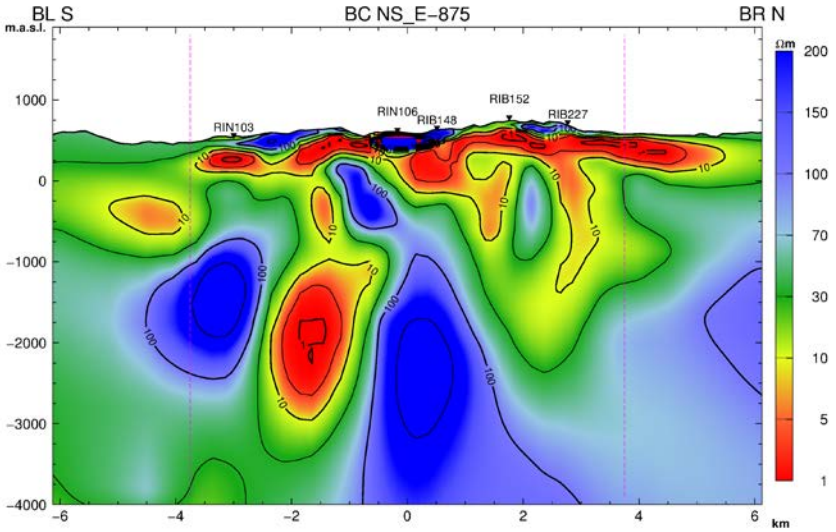
BL S
BC NS_E-875
BR N
m.a.s.l.
Ωm
200
150
100
70
30
10
5
1
1000
0
-1000
-2000
-3000
-4000
-6
-4
-2
0
2
4
6
km
RIN103
RIN106
RIB148
RIB152
RIB227

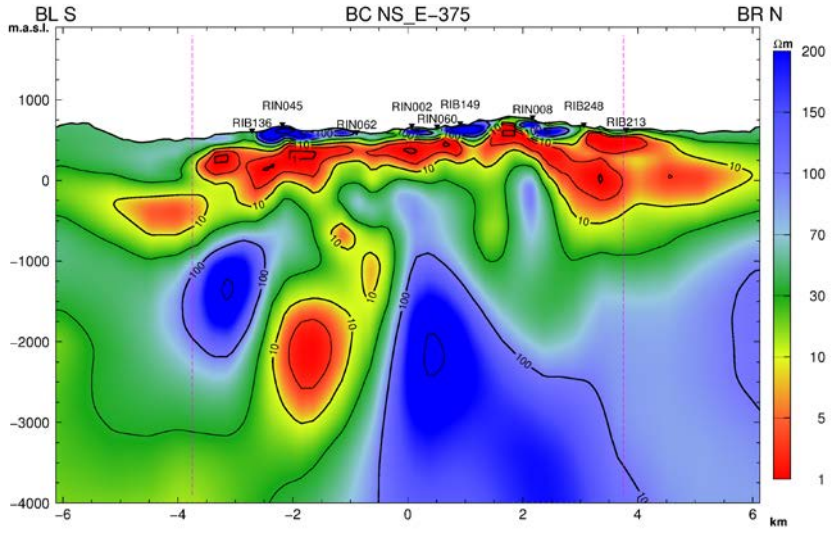
BL S
BC NS_E-375
BR N
m.a.s.l.
Ωm
200
150
100
70
30
10
5
1
1000
0
-1000
-2000
-3000
-4000
-6
-4
-2
0
2
4
6
km
RIN045
RIB136
RIN062
RIN002
RIB149
RIN060
RIN008
RIB248
RIB213

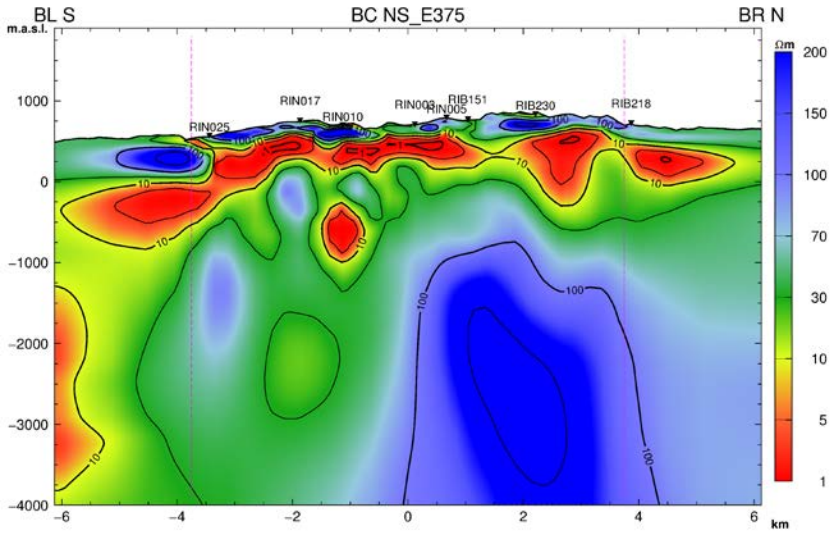
BL S
BC NS_E375
BR N
m.a.s.l.
Ωm
200
150
100
70
30
10
5
1
1000
0
-1000
-2000
-3000
-4000
-6
-4
-2
0
2
4
6
km
RIN025
RIN017
RIN010
RIN003
RIN005
RIB151
RIB230
RIB218

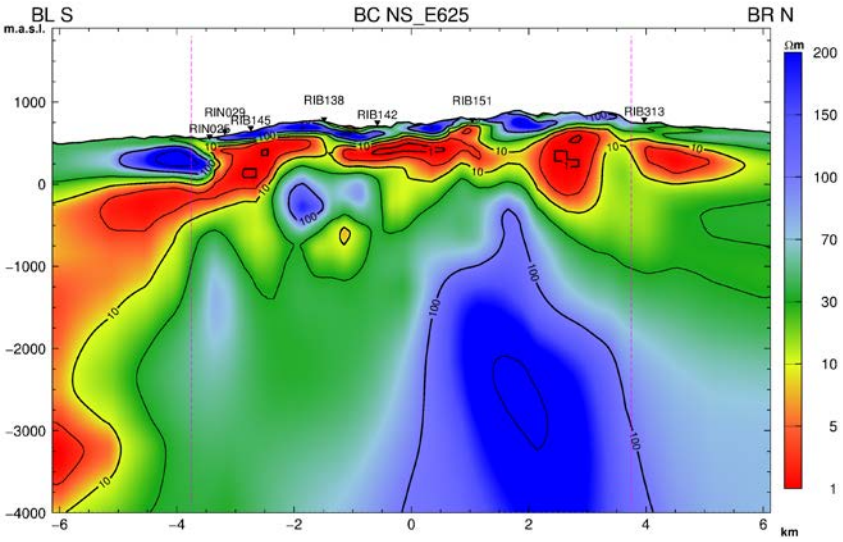
BL S
BC NS_E625
BR N
m.a.s.l.
Ωm
200
150
100
70
30
10
5
1
1000
0
−1000
−2000
−3000
−4000
−6
−4
−2
0
2
4
6
km
RIN029
RIB145
RIN026
RIB138
RIB142
RIB151
RIB313

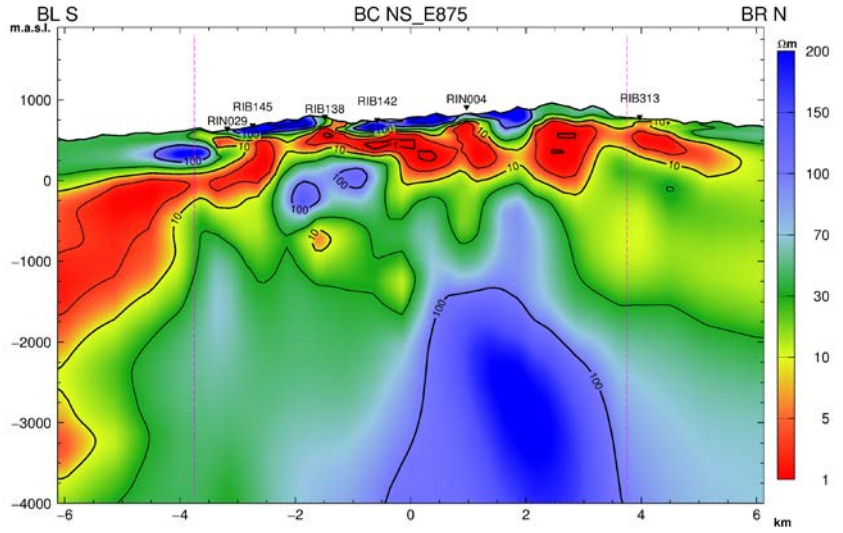
BL S
BC NS_E875
BR N
m.a.s.l.
Ωm
200
150
100
70
30
10
5
1
1000
0
−1000
−2000
−3000
−4000
−6
−4
−2
0
2
4
6
km
RIB145
RIN029
RIB138
RIB142
RIN004
RIB313

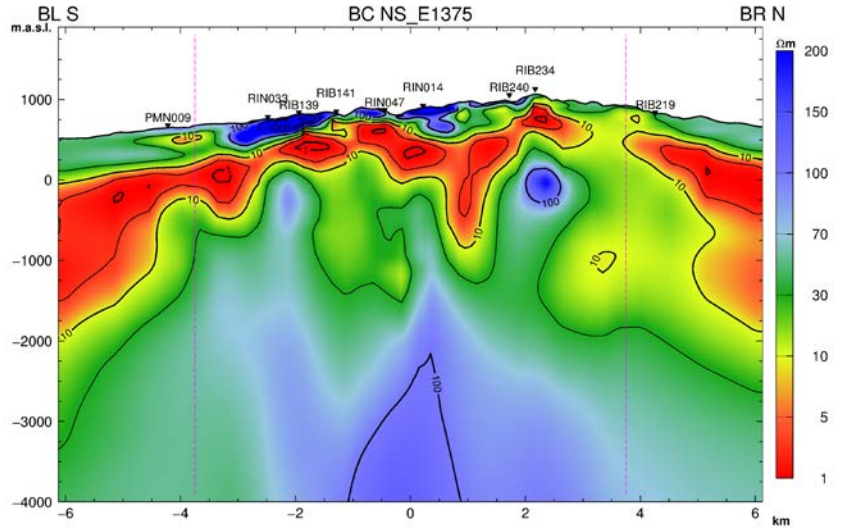
BL S
BC NS_E1375
BR N
m.a.s.l.
Ωm
200
150
100
70
30
10
5
1
1000
0
−1000
−2000
−3000
−4000
−6
−4
−2
0
2
4
6
km
PMN009
RIN033
RIB139
RIB141
RIN047
RIN014
RIB234
RIB240
RIB219

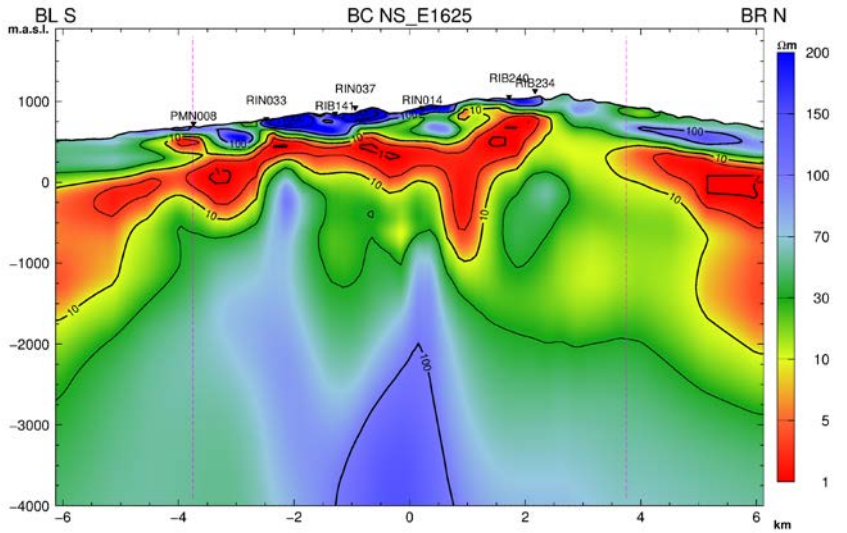
BL S
BC NS_E1625
BR N
m.a.s.l.
Ωm
PMN008
RIN033
RIB141
RIN037
RIN014
RIB240
RIB234
km

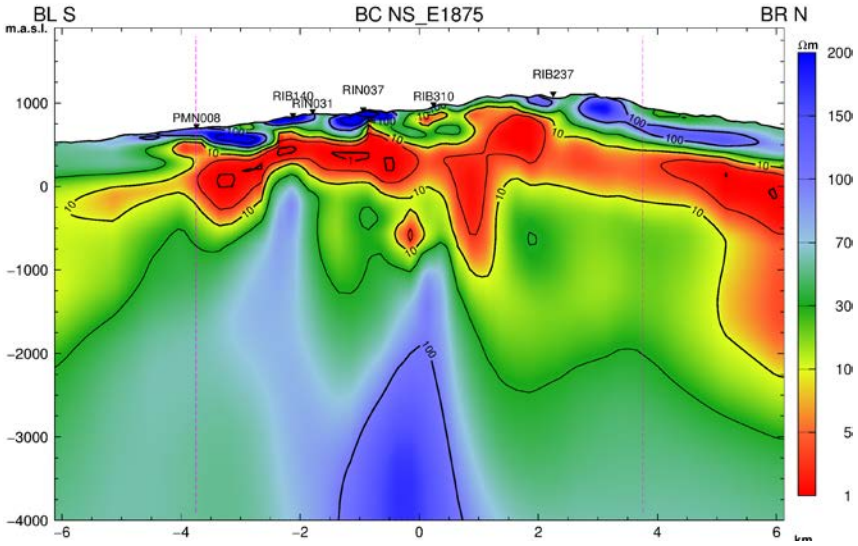
BL S
BC NS_E1875
BR N
m.a.s.l.
Ωm
PMN008
RIB140
RIN031
RIN037
RIB310
RIB237
km

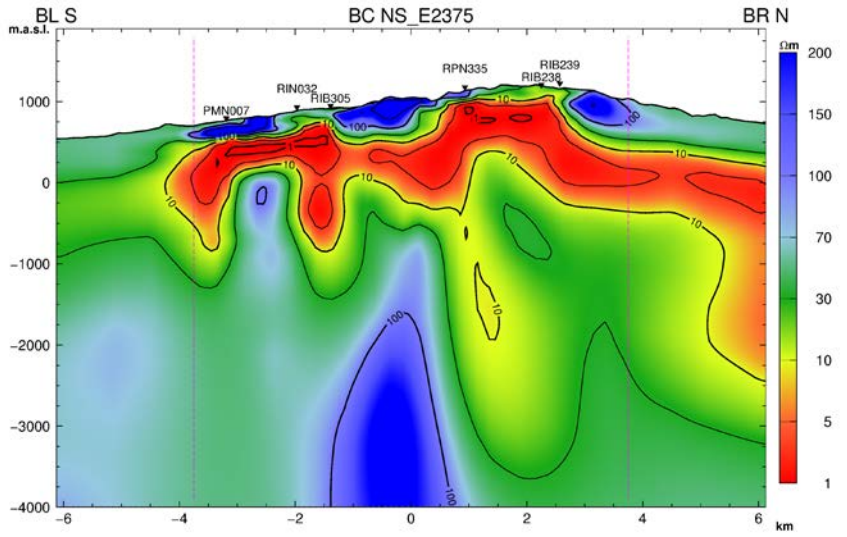
BL S
BC NS_E2375
BR N
m.a.s.l.
Ωm
PMN007
RIN032
RIB305
RPN335
RIB239
RIB238
km

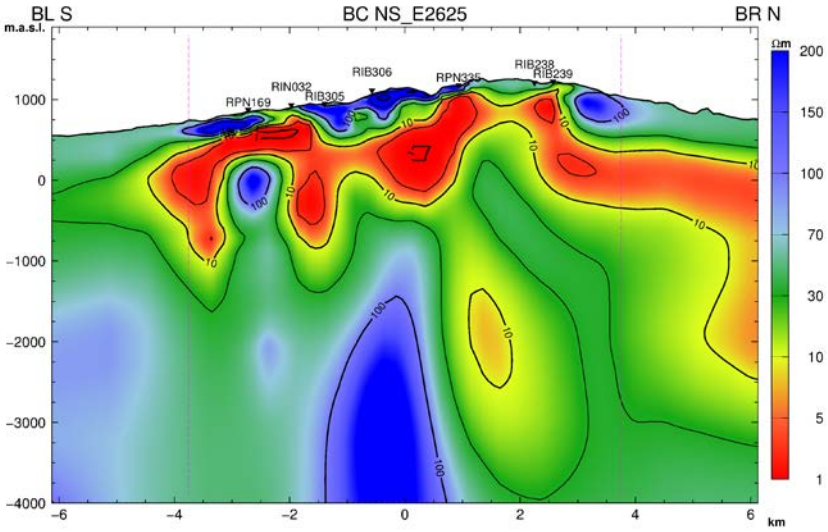
BL S
BC NS_E2625
BR N
m.a.s.l.
RPN169
RIN032
RIB305
RIB306
RPN335
RIB238
RIB239
Ωm
200
150
100
70
30
10
5
1
km

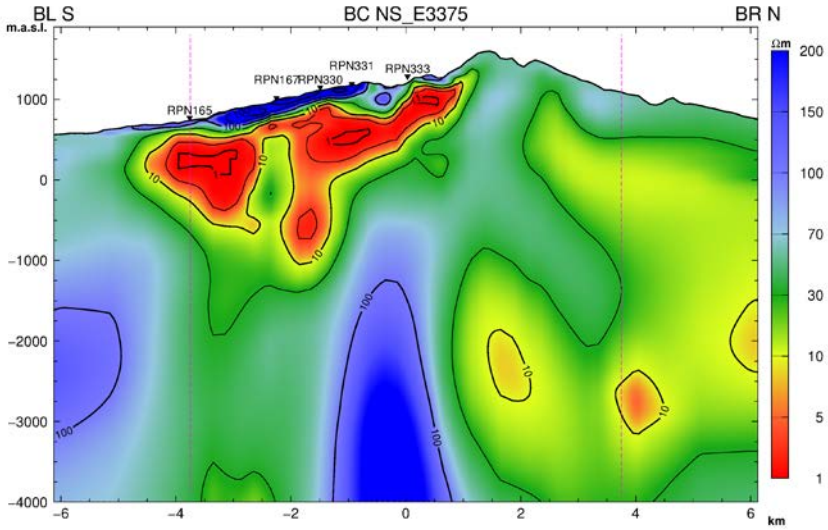
BL S
BC NS_E3375
BR N
m.a.s.l.
RPN165
RPN167
RPN330
RPN331
RPN333
Ωm
200
150
100
70
30
10
5
1
km